Search for $b\bar{b}$ decay of the Stand Model Higgs boson produced in association with a vector boson (W/Z) with the ATLAS detector

By

Yao Ming

A dissertation submitted in partial fulfillment of

the requirements for the degree of

Doctor of Philosophy

(Physics)

at the

UNIVERSITY OF WISCONSIN-MADISON

2016

Data of final oral examination: 11/04/2015

The dissertation is approved by the following members of the Final Oral Committee:

Wu, Sau Lan Yu, Professor, Physics

Smith, Wesley, Professor, Physics

Onellion, Marshall, Professor, Physics

Himpsel, Franz, Professor, Physics

Winokur, Michael, Professor, Physics & Material Science

Acknowledgement

Firstly, I would like to express my deepest gratitude to my advisor Professor Sau Lan WU for the continuous support of my Ph.D study and related research. Her motivation and guidance helped me in all the time of research and writing of this thesis. I could not have imagined having a better advisor and mentor for my Ph.D study.

Besides my advisor, I would like to thank the rest of my thesis committee: Professor Wesley Smith, Professor Marshall Onellion, Professor Franz Himpsel, and Professor Michael Winokur, for their insightful comments and encouragement, and also for the hard questions which incented me to widen my research from various perspectives.

My sincere thanks also goes to Professor Xiaolian Wang and Dr. Kamal Benslama, who provided me an opportunity to join their research teams, and guided me to the world of high energy physics.

I thank my collegues in the HSG5 group at CERN: Giacinto Piacquadio, Heather Gray, Andrew Mehta, Songming Wang, Yuji Enari, Gabriel Facini, Nicolas Morange, for the stimulating discussions, and the sleepless nights we were working together before deadlines. I thank my friends in UW-Madison group: Xiangyang Ju, Hongtao Yang, Fangzhou Zhang, Yang Heng, Fuquan Wang, Wen Guan, Shaojun Shun, Haoshuang Ji, Haicheng Wang, for all the fun we had in Geneva and Madison. In particular, I am grateful to Dr. Ximo Poveda, Dr. Tapas Sarangi, and Professor LianLiang Ma for their guidance and practical advice when I started my search in suppersymmetry particles and higgs boson.

Finally, I would like to express my heart-felt gratitude to my family. I would like to thank my parents and my elder brother, they were always supporting me and encouraging me with their best wishes. Thanks to my daughter Nannan, for being a such wonderful girl who always cherr me up. Lastly, I would like to thank my dear wife Lijia, who has scarified a lot for my graduate career. Thank you for standing with me trough the good times and bad times, none of this would have been possible without your love.

Abstract

This dissertation presents a search for the $b\bar{b}$ decay of the Standard Model Higgs boson. The analysis is performed with the ATLAS experiment, using the full dataset delivered by the LHC and recorded by ATLAS detector during LHC Run 1. The integrated luminosities used are 4.7 fb^{-1} at $\sqrt{s} = 7$ TeV, and 20.3 fb^{-1} at $\sqrt{s} = 8$ TeV. The processes considered in this analysis are associated $(W/Z)H$ production, where $W \to \ell\nu$, $Z \to \ell\ell$ and $Z \to \nu\nu$. Based on the number of leptons (ℓ), the events used in this analysis are divided into zero, one, and two lepton channels. In this analysis, no significant excess is observed above the Standard Model backgrounds. For $m_H = 125$ GeV, a 95% CL upper limit of 1.4 times the Standard Model expectation is set on the cross section times branching ratio for $pp \to (W/Z)(H \to b\bar{b})$. The corresponding expected limit is 1.3 in the absence of signal. The ratio of the measured signal yield to the Standard Model expectation is found to be $\mu = 0.2 \pm 0.5(\text{stat.}) \pm 0.4(\text{syst.})$. This analysis procedure is validated by a measurement of the yield of diboson production(WZ and ZZ), with $Z \to b\bar{b}$. The ratio of observed diboson signal strength to the Standard Model expectation is found to be $\mu_D = 0.93 \pm 0.21$, which is consistent with the Standard Model expectation of $\mu_D = 1$.

This dissertation is organized as follows:

Part I : Introduction.

- Chapter 1 discusses the physics motivations and the goals of this analysis, starting from a basic introduction to the Standard Model and Higgs Mechanism.

Part II : Experimental Apparatus and Physics Objects

- Chapter 2 briefly describes the Large Hadron Collider and the ATLAS detector.
- Chapter 3 discusses the event and object reconstruction for all physics objects used in this analysis.

Part III : Search for the $b\bar{b}$ decay of VH Process

- Chapter 4 briefly summarizes the $VH(H \to b\bar{b})$ analysis.
- Chapter 5 discusses the data and MC samples used in this analysis.
- Chapter 6 describes the selection of the physics objects used, as well as the strategy of event selection in the analysis.
- Chapter 7 discusses the data driven methods used to estimate the background, as well as the background modeling.
- Chapter 8 summarizes the sources of systematic uncertainties affecting this analysis.
- Chapter 9 presents the statistical treatment used in this analysis.

Part IV : Results and Conclusion

– Chapter 10 is the last chapter in this dissertation, which presents the final results of this analysis, including the limit on the cross section times branching ratio for the signal process as well as its compatibility with the Standard Model expectation.

Contents

CHAPTER 1

Physics Motivation

The Higgs Mechanism is a crucial part of the Standard Model, which generate masses for the elementary particles. The Higgs boson, predicted by the Higgs mechanism, is the last piece of puzzle of the Standard Model. After the Higgs Mechanism was developed in 1964, great effort has been made to prove the existence or non-existence of the Higgs boson. In July 2012, the ATLAS [1] and CMS [2] experiments at the LHC [3] reported the observation of a Higgs-like particle with a mass of about 125 GeV [4][5]. In Standard Model, the Higgs boson can directly couple to massive fermions and bosons. The evidences of Higgs coupling to $\gamma\gamma$ [6][7], ZZ^* [8][9], WW^* [10][11] and $\tau^+\tau^-$ [12][13] have been found at both ATLAS and CMS experiments. This dissertation presents the search for the Higgs coupling to a pair of b quarks, and this first chapter discusses the physics motivation of this analysis. Section 1.1 provides an overview of the Standard Model and Higgs Mechanism, while leaving the rich history and beautiful details of the Standard Model to proper references. Section 1.2 discusses the Higgs phenomenology in proton-proton collisions, including the production and decay modes of the Higgs bosons. Section 1.3 covers the history of the Higgs search, as well as the discovery

of a new particle at the Large Hadron Collider. The newly discovered particle is found to be consistent with the prediction of the Higgs boson.

1.1 The Standard Model of Particle Physics

The Standard Model is a theory for particle physics, first built in 1960's, to describe the elementary particles and interactions between them [14][15][16]. Thanks to the interplay between the fundamental theoretical development and experimental discoveries in the latter half of the 20th century, the Standard Model has became a highly predictive theory. In 1973, the existence of top quark and bottom quark was theorized to explain the CP violation [17], they were later discovered by Fermi Lab in 1977 (bottom) and 1995 (top) [18][19].

The Higgs mechanism was an essential part of the Standard Model, developed in 1960s [20, 21, 22, 23, 24, 25]. The goal of Higgs mechanism is to account for the non-zero mass term of elementary particles without breaking the local gauge symmetry of the Standard Model.

Section 1.1.1 discusses the particle content in Standard Model and the interactions between them, and section 1.1.2 provides a brief overview of the Higgs Mechanism.

1.1.1 Particle Content and Interactions

The Standard Model describes all the particles observed so far, as well as three of the four known fundamental interactions. The four known fundamental interactions are strong interaction, weak interaction, electromagnetic interaction and the gravitation. Although the gravitation is not described in the Standard Model, its coupling strength is too small to affect the high energy interactions. The strong interaction

confines quarks into hadrons, electromagnetic interaction binds electrons to atomic nuclei, and the weak interaction is corresponding to the radioactive β decay.

The Standard Model consists of two categories of particles. Fermions of spin 1/2 and Bosons with integer spin, as shown in Fig. 1.1.

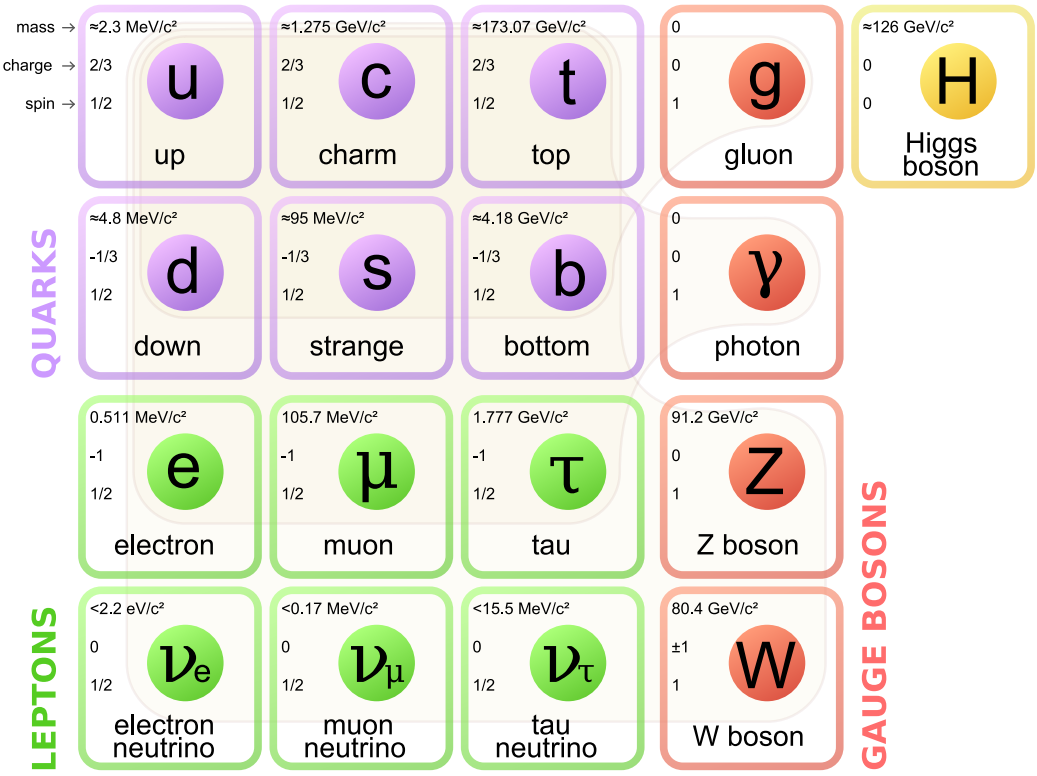

Figure 1.1: The particle content of the Standard Model: 12 fundamental fermions and 5 fundamental bosons [26].

Depending on which kind of interactions they participate in, fermions are further categorized into leptons and quarks. Leptons only participate in electromagnetic interaction and weak interaction, while quarks participate in all three interactions.

There are six types of leptons, known as different flavors in high energy physics,

grouped in three generations. The first generation consists of electrons (e^-) and electron neutrinos (ν_e), the second generation consists of muons (μ^-) and muon neutrinos (ν_μ), the third generation consists of taus (τ^-) and tau neutrinos (ν_τ). Different generations have exactly the same quantum numbers, but the mass of charged leptons increase from 0.5 MeV to 1.7 GeV. Charged leptons decay rapidly from higher mass state to lower mass state, thus electrons are stable and the most easily detected leptons in our universe. Muons and taus can only be found in cosmic rays and high energy collisions.

Leptons	Electric Charge[e]	Mass[GeV]
e^-	-1	0.51×10^{-3}
ν_e	0	$< 2 \times 10^{-9}$
μ^-	-1	105.66×10^{-3}
ν_μ	0	$< 0.19 \times 10^{-3}$
τ^-	-1	1.78
ν_τ	0	$< 18.2 \times 10^{-3}$
Quarks	Electric Charge[e]	Mass[GeV]
u	2/3	2.3×10^{-3}
d	-1/3	4.8×10^{-3}
c	2/3	1.28
s	-1/3	0.1
t	2/3	173.5
b	-1/3	4.18

Table 1.1: The fundamental fermions of the Standard Model and their corresponding mass and electric charge [27].

Similar as leptons, there are also six flavors of quarks, grouped in three generations. The first generation of quark consists of up quark (u) and down quark (d), carrying fractional charge of $\frac{2}{3}e$ (u) and $-\frac{1}{3}e$ (d). The mass of quark increase from 2.5 MeV to 173.5 GeV as generation increases. Since no free quark has been observed, they are set to be confined inside hadrons by strong interaction. In proton-proton collision, the quarks hadronise rapidly into a spray of hadrons, which are then detected as jets. The mass and charge of fermions are summarized in Table 1.1.

In the Standard Model, the fundamental forces are carried by bosons with integer spin. The electromagnetic force is carried by the photons with zero rest mass, which couple to charged particles. The weak interaction force is carried by massive $W^{\pm}$ and Z^0 bosons. Due to the large mass of $W^{\pm}$ and Z^0 boson ($m_W = 80.4\ GeV$ and $m_Z = 91.2\ GeV$) , the weak interaction is suppressed in low energy regions. The strong interaction force is carried by massless gluons with eight different colors, which couple to colored particles, such as quarks.

Bosons	Electric Charge[e]	Mass[GeV]
gluons (g)	0	0
photon (γ)	0	0
$W^{\pm}$	± 1	80.4
Z^0	0	91.2
H	0	125

Table 1.2: The fundamental boson of the Standard Model and their corresponding mass and electric charge [27].

Bosons, which carry fundamental forces, like photons, $W^{\pm}/Z^0$ bosons and gluons are named gauge boson. Besides gauge boson, the Standard Model has a massive scalar boson with spin-0, called Higgs boson. The mass and charge of bosons are summarized in Table 1.2.

A key development in Standard Model took place in 1960s, when electromagnetic interactions and weak interactions were modeled as two different aspects of one same interaction, the electroweak interaction. The two interactions appear differently at low energy scale, but would merge into a single force called eletroweak force when the energy is on the order of 100 GeV. The unification was proposed by Sheldon Glashow, Adbuds Salam, and Steven Weinberg [28][29][30][31].

1.1.2 Higgs Mechanism

The Standard Model is a gauge theory which includes the strong interaction and the electroweak interaction. Since the Standard Model is required to be normalizable, the Lagrangian that describes the dynamics of these interactions has to be invariant under the local space-time transformation specified by symmetry group $SU(3)_c \times SU(2)_L \times U(1)_Y$ [32].

To preserve the local gauge symmetry, additional gauge fields with corresponding gauge bosons are introduced into the Standard Model. The fundamental forces are then mediated by the gauge bosons. There are eight gauge bosons (gluons) corresponding to the $SU(3)_C$ generator, three gauge bosons ($W^{\pm}/Z^0$) for $SU(2)_L$ generator, and one gauge boson for the $U(1)_Y$ generator. All the gauge bosons are required to be massless spin 1 particles to preserve the local gauge symmetry.

This theory works fine with both strong interactions and electromagnetic interactions, where the corresponding gauge bosons have zero invariant mass. However, it is not the case for the weak interaction. Investigation of weak interaction data pointed to a charged massive vector boson acting as the weak interaction carrier [33][34]. In 1964, a method of introducing mass term to weak gauge boson without breaking local gauge invariance was proposed by several groups. In this method, a scalar complex field was introduced to the Lagrangian, known as the Higgs field. The vacuum expectation of Higgs field is not zero. In this way, the Higgs field can give rise to the mass of weak gauge bosons by expanding around its ground state, but still preserve the gauge invariance for the Lagrangian. This method is known as spontaneously symmetry breaking. This mechanism is usually referred to as the Higgs mechanism.

In the Higgs Mechanism, the masses of the weak gauge bosons are set by the

vacuum expectation values through spontaneous symmetry breaking. The existence of massive gauge bosons were then proved by the discovery of the W boson at the SPS Collider at CERN in 1983 [35, 36, 37, 38]. Gauge bosons for strong interaction (gluons) and electromagnetic interaction (photons) remain massless. Fermion masses can also be obtained through the Yukawa coupling [39]. Thus, the fermion masses are not predicted by the Standard Model, but rather input variables to the Standard Model. The coupling strength of a fermion to the Higgs field should be proportional to their invariant mass. The spontaneous symmetry breaking also generate an additional scalar boson, called the Higgs boson. The mass of the Higgs boson is also an input variable of the Standard Model theory, which cannot be predicted. However, the mass is required to be a non-zero value in order to undergo the spontaneous symmetry breaking. Also, in order for the theory to be perturbative, the Higgs mass is considered to be lower than TeV scale.

1.2 Higgs Phenomenology at the LHC

This section discusses the phenomenology of the Higgs boson production and decay modes in proton-proton collisions at the LHC. Section 1.2.1 gives an overview of the proton-proton collisions. Section 1.2.2 discusses the major production modes of Higgs boson at the LHC. Section 1.2.3 covers the decay modes of Higgs boson, in particularly the $H \to b\bar{b}$ decay, which is the topic of this dissertation.

1.2.1 Proton Proton Collision

Particle collision experiments have been playing an important role in high energy physics. Since the latter half of 20th century, varieties of colliders have been built to collide particles with high energy, the outcome of which can then lead to the

observation of new particles. The Large Hadron Collider at CERN is a 27 kilometer circular collider designed to collide two bunches of protons at $\sqrt{s} = 14$ TeV with an instantaneous luminosity of $10^{34}\ cm^{-2}s^{-1}$ [3]. The search for the Higgs boson is one of the most important goals of the LHC physics program.

High energy physics analyses are mostly based on measuring event rate in a certain phase space. Predicted number of events in a collider can be described as

$$N_{events} = \sigma \times \int \mathscr{L} dt \tag{1.1}$$

Here σ is the cross section, and the $\mathscr{L}$ is the instantaneous luminosity.

In proton-proton collision, the calculation can be very complicated if we consider the collision to happen between a collection of the quarks and gluons. The parton model of proton can greatly simplify the calculation by considering the collision as one-on-one parton scattering. This model was first proposed in 1969 by Richard Feynman as a way to analyze the high energy hadron collisions [40]. It was later recognized that partons are actually quarks and gluons in proton-proton collision.

In the parton model, the proton is treated as a collection of point-like partons. In high momentum transfer (Q^2) process, each parton interact independently through Bjorken scaling [41]. In the Standard Model, the strong coupling constant (α_s) decreases as energy increases, as shown in Fig. 1.2, which allows perturbative calculation of QCD processes [42][43].

The cross section depends on both low energy interactions (known as underlying events) and the high energy interactions (known as hard scattering). The factorization theorem is developed to deal with different domains separately [44], making

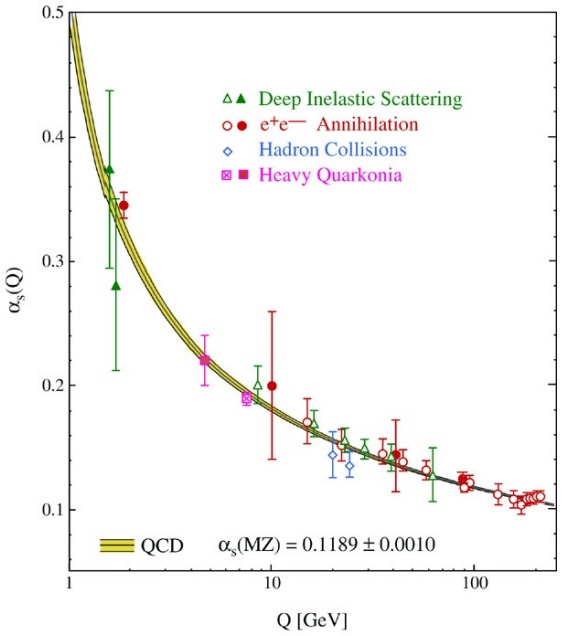

Figure 1.2: Summary of measurements of α_s(Q) as a function of the respective energy scale Q. Open symbols indicate (resummed) NLO, and filled symbols are NNLO QCD calculations used in the respective analysis. The curves are the QCD predictions [45].

use of the parton distribution functions (PDFs) and the partonic cross sections. The PDFs are measured in previous experiments at low energies, then extrapolated to higher energies [46][47]. There are several PDFs sets available at the LHC energy level (14 TeV), such as CTEQ [48], MSTW [49], and NNPDF [50].

The Standard Model and the factorization theorem have successfully predicted cross section for many processes at 7 and 8 TeV [51]. Figure 1.3 shows the predicted cross sections and measured ones for different Standard Model processes using ATLAS Run 1 data. The predicted cross sections agree nicely with the measured ones.

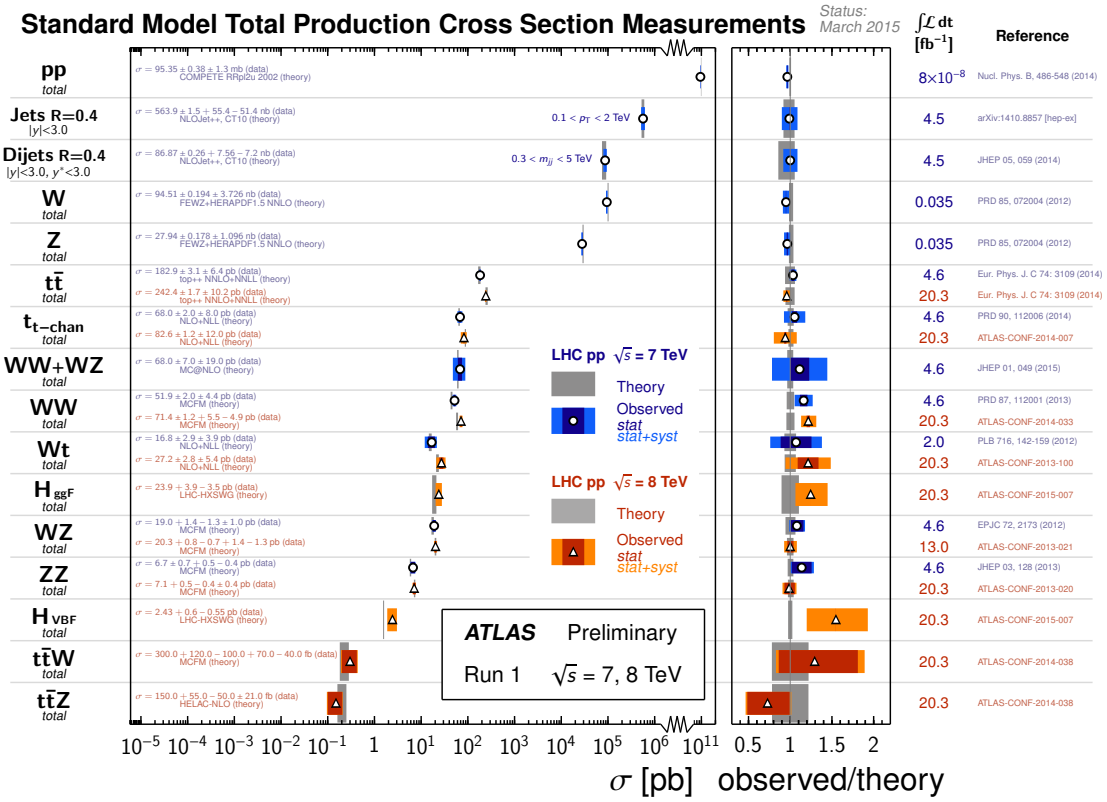

Figure 1.3: Detailed summary of several Standard Model total production cross section measurements, corrected for leptonic branching fractions, compared to the corresponding theoretical expectations. All theoretical expectations were calculated at NLO or higher. The W and Z vector-boson inclusive cross sections were measured with 35 pb^{-1} of integrated luminosity from the 2010 dataset. All other measurements were performed using the 2011 dataset or the 2012 dataset. The dark-color error bar represents the statistical uncertainly. The lighter-color error bar represents the full uncertainty, including systematics and luminosity uncertainties. The data/theory ratio, luminosity used and reference for each measurement are also shown. Uncertainties for the theoretical predictions are quoted from the original ATLAS papers. They were not always evaluated using the same prescriptions for PDFs and scales [51].

1.2.2 Production of Higgs Bosons

One of the main purposes of the Large Hadron Collider is to search for the Higgs boson. In Standard Model, Higgs bosons can be produced in four different processes. This section provides an overview of these four processes, as well as their respective cross sections .

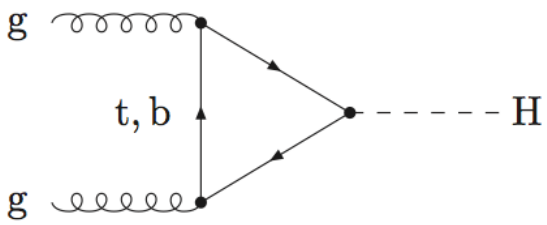

Figure 1.4: Feynman diagram contributing to gluon gluon fusion process at lowest order [52].

The most dominant production mode at the Large Hadron Collider is gluon gluon fusion process (ggF) [52], the leading order Feynman diagram of which is shown in Fig. 1.4. In principle, gluons cannot directly couple to Higgs bosons since gluons are massless. However, the coupling can take place through a quark loop since quarks are both massive and colored, and therefore can couple to both gluons and Higgs bosons. The main contribution arises from the top quark because it is the heaviest quark. Bottom quark, as the second heaviest quark, also contribute to this process. Due to the dominant contribution of gluons in proton's PDF at small momentum fractions, ggF mode makes up about 90% of the total Higgs boson production at the LHC. If the cross section measured at the LHC is consistent with the SM prediction, this can be taken as a proof of Higgs coupling to fermions.

The second largest production mode at the Large Hadron Collider is vector boson fusion process (VBF) [53][54]. In this process, the final state includes objects from the Higgs boson decay plus two additional jets. The leading order Feynman

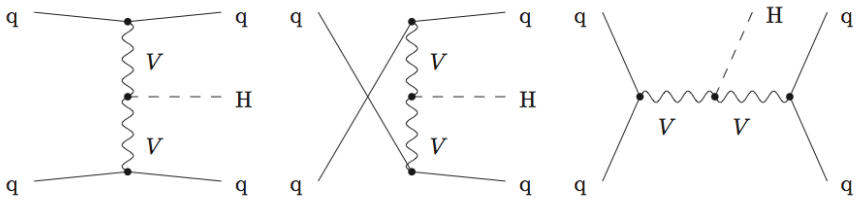

Figure 1.5: From left to right, the three Feynman diagrams shows the leading order topologies of t-channel, u-channel, and s-channel contributions for VBF production, where q denotes any quark or antiquark and V stands for W and Z boson [53][54].

diagrams are shown in Fig. 1.5. In t-channel and u-channel, the two additional jets have a strong tendency to be boosted back-to-back in forward and backward direction, which provide good background suppression. In s-channel, the two additional jets are much softer, thus suppressed after we require a hard jets pair at the analysis level. Evidence of VBF production leads to the conclusion that the Higgs boson does couple to $W^{\pm}/Z$ boson.

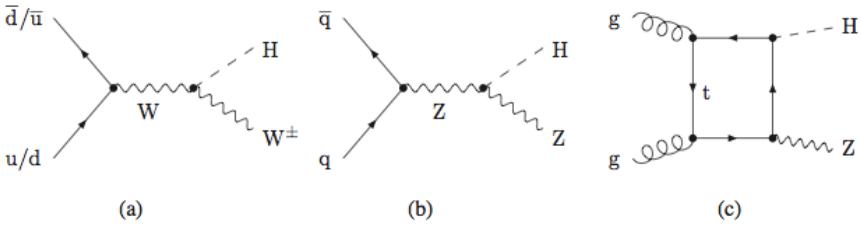

Figure 1.6: (a), (b) Leading order (LO) diagrams for the parton processes $qq \rightarrow VH(V = W^{\pm}/Z)$; (c) diagram contributing to the $gg \rightarrow HZ$ channel [55].

The third largest production modes at the Large Hadron Collider is Higgs boson produced in association with a vector boson (VH) [55]. In this process, the products contains a Higgs boson and a vector boson ($W^{\pm}/Z$). Although the cross section of VH production mode is only about 6% of the ggF cross section, the leptonic decay of the vector boson can be efficiently used for triggering and to reduce the background. This is especially useful for the analysis presented in this dissertation. The leading order Feynman diagrams are shown in Fig. 1.6.

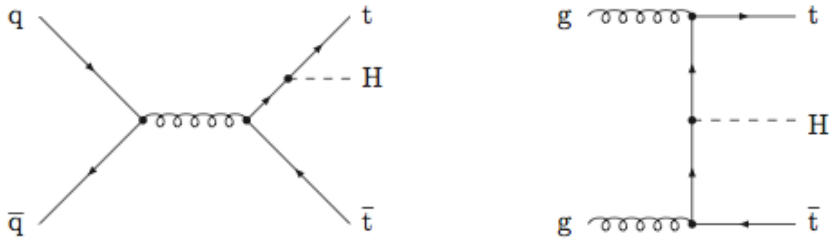

Figure 1.7: Examples of Leading order (LO) Feynman diagrams for the partonic processes qq,gg→ ttH [56][57].

Higgs produced in association with a top quark pair (ttH) is the smallest production mode observable at the Large Hadron Collider[56][57]. Its leading order Feynman diagrams are shown in Fig. 1.7. The ttH production rate can provide relevant information on the Yukawa coupling between top quark and Higgs boson.

In 2010, the Higgs cross section group is founded to provide theoretical calculations and SM predictions of Higgs boson phenomenology to the LHC experiments. The recommendations from this cross-section group are used all through the analysis presented in this dissertation. Fig. 1.8 shows the cross section for each production mode at $\sqrt{s} = 7$ TeV and $\sqrt{s} = 8$ TeV as a function of m_H. Fig. 1.9 shows the sum of the cross sections of these production modes at $\sqrt{s} = 7$ TeV, $\sqrt{s} = 8$ TeV, and $\sqrt{s} = 14$ TeV.

The ggF production mode is controlled by the strong interaction. The leading order calculation of cross section is proportional to ${\alpha_s}^2$. NLO QCD radiative correction increases the cross section by 80% to 100% [58][59][60][61]. Using the heavy top quark limit approximation, NNLO corrections further increase the cross section by 25% [62][63][64][65]. In addition, electroweak corrections are applied; they depend highly on m_H. At m_H=125 GeV and $\sqrt{s} = 8$ TeV, ggF cross section is 19.3 pb [66].

Production mode	σ(7 TeV) [pb]	σ(8 TeV) [pb]
ggF	15.3	19.3
VBF	1.22	1.58
WH	0.572	0.705
ZH	0.316	0.415
VH (WH+ZH)	0.888	1.12
ttH	0.0863	0.129

Table 1.3: The Higgs boson production cross section at $\sqrt{s} = 7$ TeV and $\sqrt{s} = 8$ TeV respectively at the LHC [66].

The VBF cross section is calculated at NLO, both strong coupling and electroweak couplings are took into consideration. The NNLO QCD corrections are expected to be small [67][68][69]. At m_H=125 GeV and $\sqrt{s} = 8$ TeV, VBF cross section is 1.58 pb.

In VH channel, the cross section is calculated at NNLO with electroweak corrections, and the scale uncertainties are of the order of $\pm(1-3)\%$ [70][71][72]. At m_H=125 GeV and $\sqrt{s} = 8$ TeV , $VH(WH + ZH)$ cross section is 1.1 pb.

In ttH channel, the cross section is calculated with NLO QCD correction [73][74][75][76]. At m_H=125 GeV and $\sqrt{s} = 8$ TeV, ttH cross section is about 0.1pb.

Table 1.3 summarizes the cross section for each production mode at the LHC at center of mass energy $\sqrt{s} = 7$ TeV and $\sqrt{s} = 8$ TeV.

1.2.3 Decay Modes of Higgs Bosons

The Standard Model Higgs boson decays rapidly after being produced at the Large Hadron Collider. Thus it can only be observed through the final state objects, with various final states expected.

Higgs boson can directly decay to a massive particle and its anti-particle, such as

$H \to b\bar{b}$, $H \to \tau^+\tau^-$, and $H \to c\bar{c}$. The partial widths at leading order are:

$$\Gamma(H \to ff) = \frac{G_F}{4\pi\sqrt{2}} {m_f}^2 m_H (1 - \frac{m_f^2}{m_H^2})^{\frac{3}{2}} \tag{1.2}$$

In equation above, G_F is the Fermi constant ($\simeq 1/(300\text{GeV})^2$), and m_f is the mass of fermions. The branching ratio to fermions scales with the mass of the fermion, thus decays to heavier fermions are preferred [77][78][79][80].

The Higgs boson can also decay to massless particles through indirect decay: $H \to gg$ and $H \to \gamma\gamma$. The $H \to gg$ decay proceed through quark loops, while $H \to \gamma\gamma$ decay proceed through both quark loops and W boson loops. The partial width of $H \to \gamma\gamma$ decay can be written as Equation 1.3, where F includes contributions from W loops and fermion loops [81].

$$\Gamma(H \to \gamma\gamma) = |F|^2 (\frac{\alpha}{4\pi}) \frac{G_F m_H^3}{4\pi\sqrt{2}\pi} \tag{1.3}$$

The third decay mode is Higgs decay to a particle and its virtual particle, like $H \to WW^*$ decay and $H \to ZZ^*$ decay. The partial widths at leading order are [77][78][79][80]:

$$\Gamma(H \to WW^*) = \frac{G_F}{8\pi\sqrt{2}} m_H^3 (1 - \frac{m_W^2}{m_H^2})^{\frac{1}{2}} (12\frac{m_W^4}{m_H^4} - \frac{m_W^2}{m_H^2} + 1) \tag{1.4}$$

$$\Gamma(H \to ZZ^*) = \frac{G_F}{16\pi\sqrt{2}} m_H^3 (1 - \frac{m_Z^2}{m_H^2})^{\frac{1}{2}} (12\frac{m_Z^4}{m_H^4} - \frac{m_Z^2}{m_H^2} + 1) \tag{1.5}$$

This decay mode becomes dominant at high m_H. In the low m_H range, it is suppressed because one of the resulting vector bosons is off-shell.

The total width and branching ratios are calculated using HDECAY [82][83] and PROPHECY4F [84][85] , with higher order corrections from electroweak and QCD processes. Figure 1.10 shows the branching ratio for different decay modes as a function a m_H. Because of the large mass of bottom quark, $H \to b\bar{b}$ decay is dominant at low m_H. At $m_H = 125$ GeV, the calculated branching ratio of $H \to b\bar{b}$ is 58%. However, the di-jets final states makes it almost impossible to separate the Higgs signal from the Standard Model di-jet background. Instead, searches are performed in VH channel, which has a much smaller cross section ($\sim 6\%$). Fig. 1.11 shows the product of Higgs cross section times branching ratios for different decay modes as a function of m_H at $\sqrt{s} = 8$ TeV.

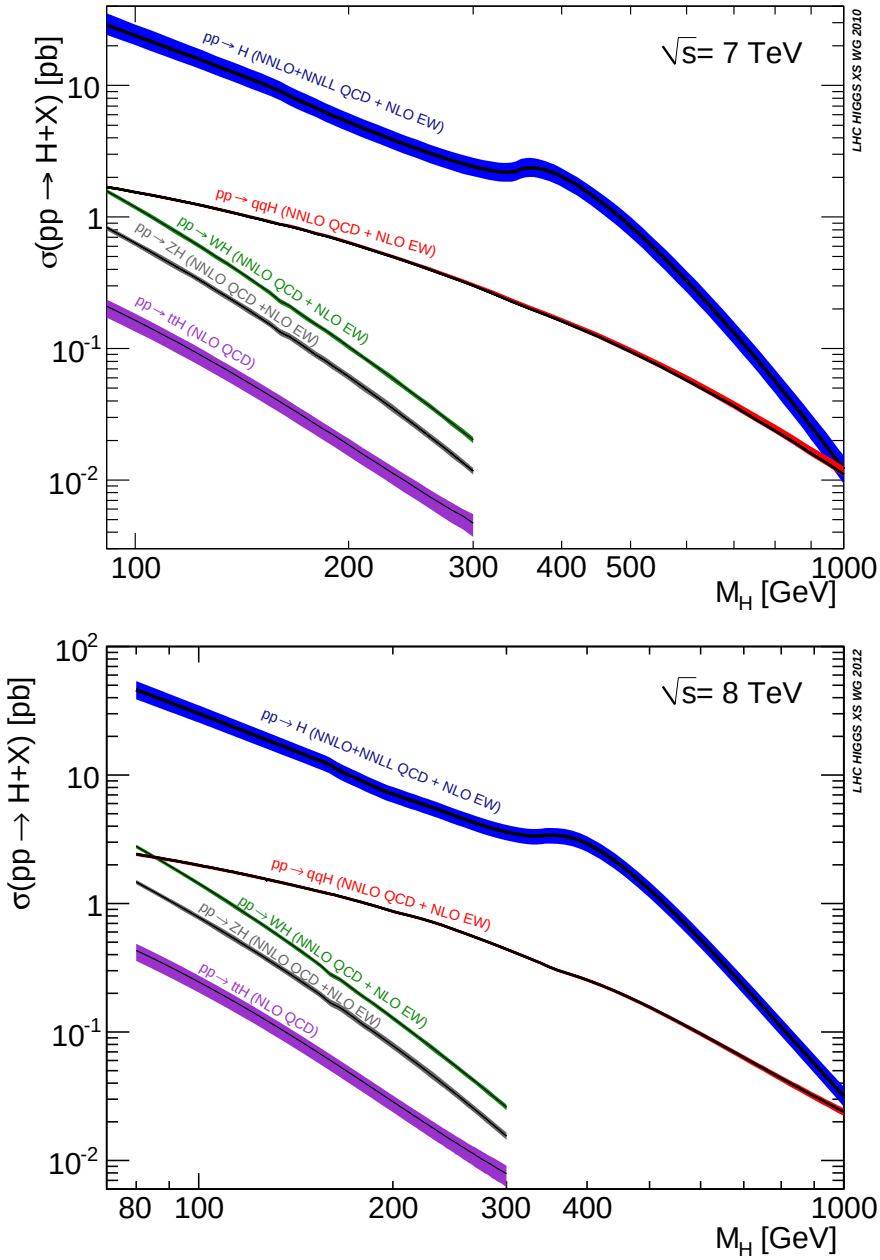

Figure 1.8: Standard Model Higgs boson production cross sections at $\sqrt{s} = 7/8$ TeV as a function of m_H [66].

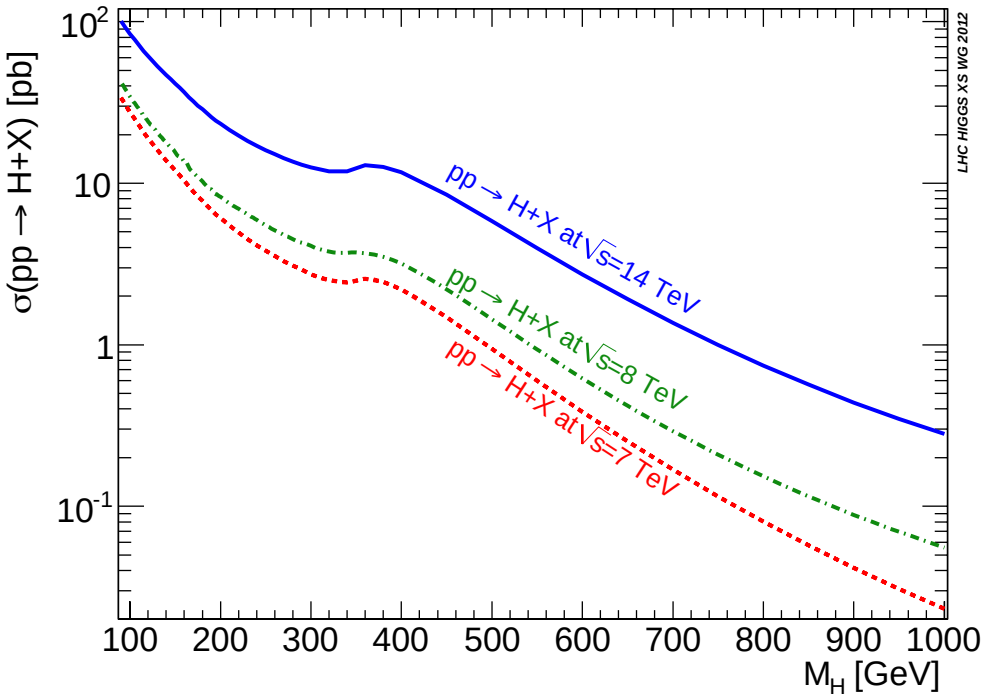

Figure 1.9: Standard Model Higgs boson total production cross section at $\sqrt{s} =$ 7/8/14 TeV as a function of m_H [66].

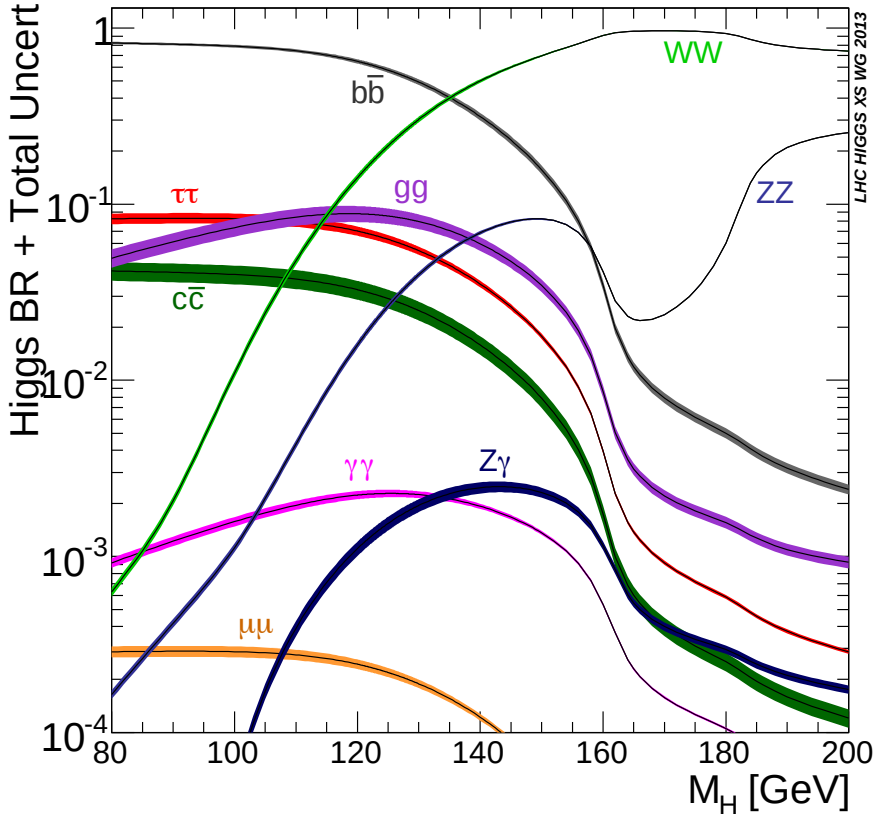

Figure 1.10: Branching ratios of a SM Higgs boson as a function of m_H, the bands indicates the size of corresponding uncertainties [66].

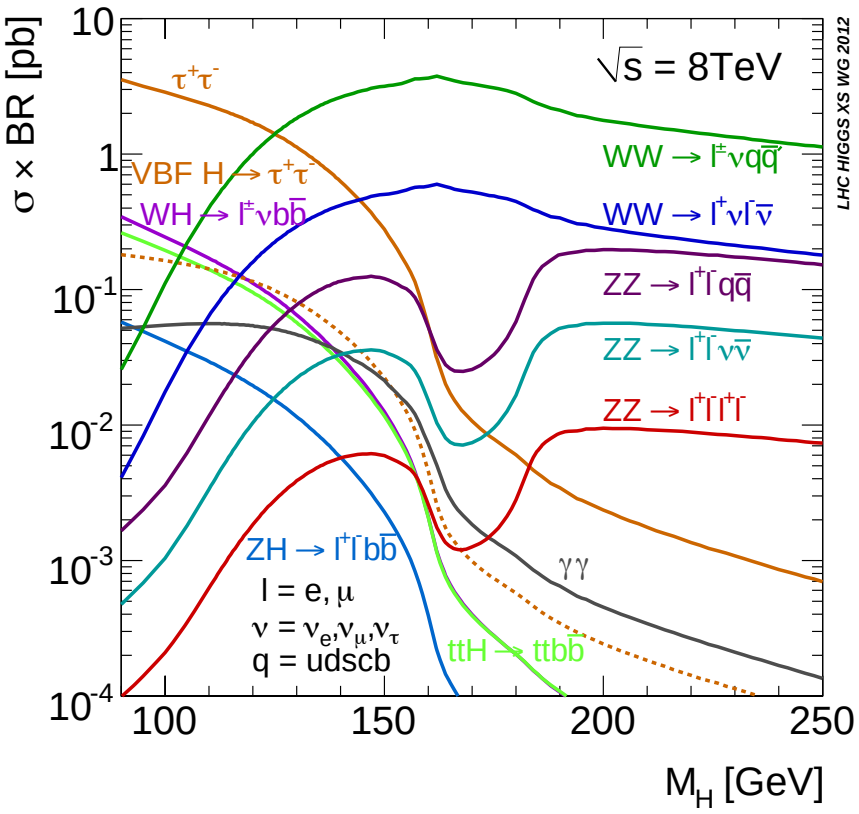

Figure 1.11: Product of production cross section times branching ratios of a SM Higgs boson as a function of m_H at $\sqrt{s} = 8$ TeV [66].

1.3 Experimental Searches for Higgs Bosons

Experimental evidence for the existence of the Higgs boson can be a strong proof for the Standard Model, as well as for spontaneous symmetry breaking. Searches for Higgs-like particles have been performed in different colliders. This chapter gives a brief overview for the experimental search at LEP, Tevatron, and LHC.

1.3.1 LEP

The Large Electron-Positron Collider (LEP) at CERN was a circular lepton collider, which was in operation from 1989 to 2000. It was the most powerful lepton collider ever built on earth at that time. In the end of 2000, the LEP collider energy reached 209 GeV, which accelerated electrons to a Lorentz factor of over 200,000. There were several experiments at LEP, such as ALEPH, DELPHI, L3, and OPAL, performing the search for Higgs bosons. Although no direct evidence of Higgs boson was found, they managed to set a lower bound of 114.4 GeV on the Higgs boson mass at 95% confidence level [86]. In the low m_H region, Higgs boson mostly decays to a bottom quark pair. Thus the most sensitive channel at LEP was 4 jets final state $(H \to b\bar{b})(Z \to jj)$, where Higgs boson was produced mainly in Higgs-strahlung process in association with a Z boson $(e^+e^- \to ZH)$.

1.3.2 Tevatron

Tevatron was a circular proton-antiproton collider at Fermilab, which was in operation from 1983 to 2011. Before LHC, it was the world's highest energy particle collider. In Run II, Tevatron managed to collide proton and antiproton with center of mass energy up to $\sqrt{s} = 1.96$ TeV. There were two experiments at

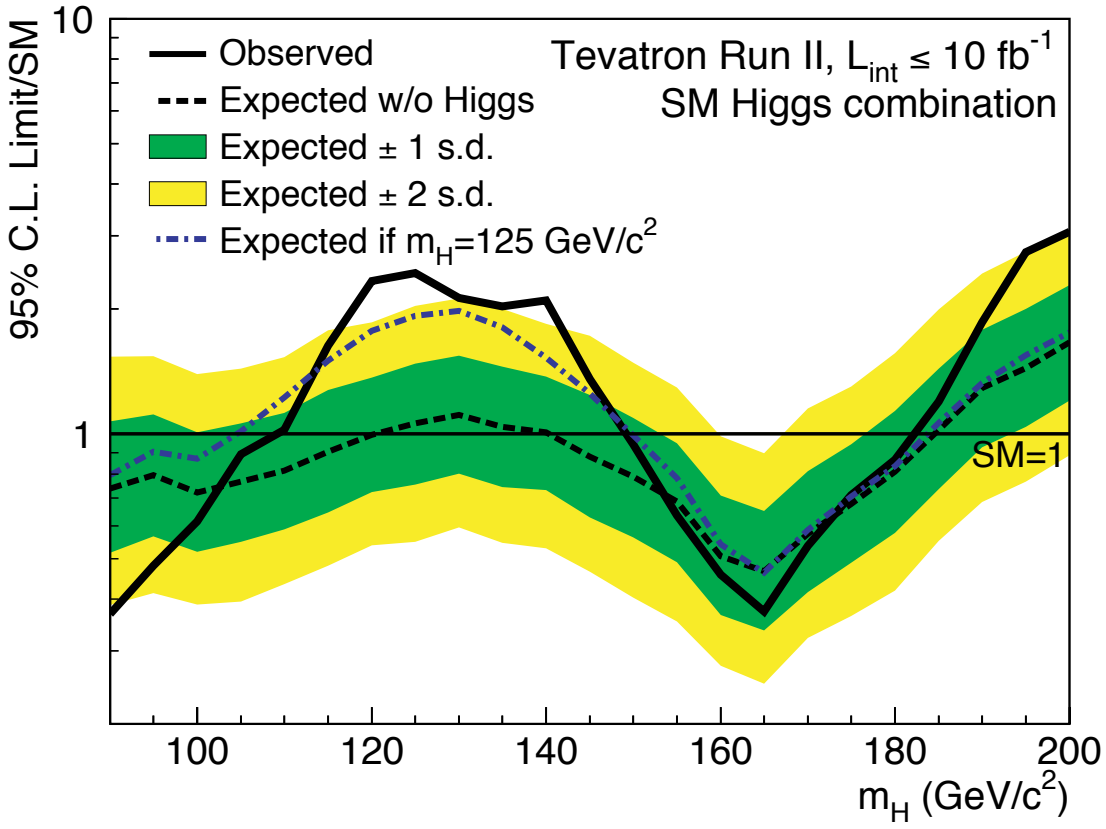

Figure 1.12: Expected and observed exclusion limits on the product of Higgs boson production cross-section and decay branching ratio as a function of the hypothesised Higgs boson mass as resulting from the statistical combination of all search channels studied by the CDF and DØ collaborations [87].

Tevatron performing the direct search of Higgs boson: CDF and DØ experiments. With 10 fb^{-1} data, CDF and DØ were able to exclude the Higgs boson in two different mass ranges with 95% confidence level: 90 GeV $< m_H <$ 109 GeV and 149 GeV $< m_H <$ 182 GeV [87]. Both experiments put special effort on $H \to b\bar{b}$ decay due to the large branching ratio. An excess of data compared to the background expectation was found in a mass range between 115 GeV and 140 GeV with a local significance about 3σ [87].

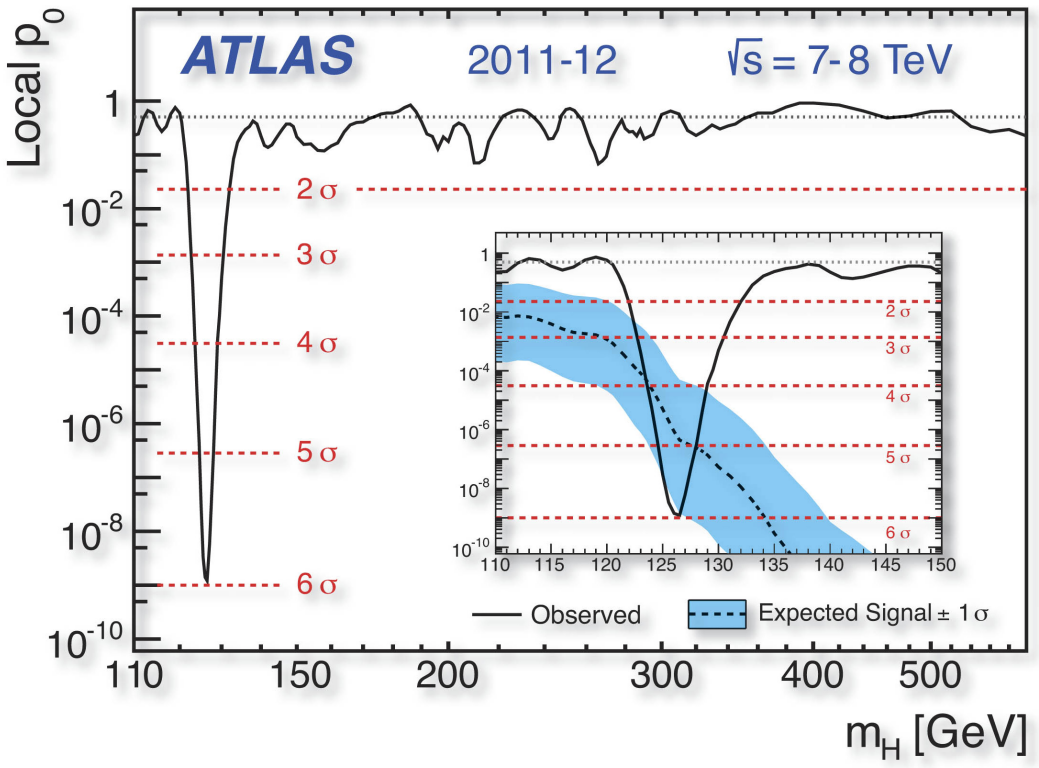

Figure 1.13: Result of a statistical analysis of the ATLAS combined Higgs search. The observed probability (local p0) for background processes to look like the data at mH = 126 GeV corresponds to 1 part in 600 million. This corresponds to a 5.9 sigma observation of a new particle. The plot also shows that no signal is observed at other masses. The inset in the low mass range compares the observed probability with the expectation from theory, showing that the observation at m_H = 126 GeV is consistent with the Standard Model Higgs boson [88].

1.3.3 LHC

The Large Hadron Collider(LHC) is currently the world's largest particle collider, detailed information of which is provided in next Chapter. Search for Higgs boson at the LHC is performed by two general purpose detector: the ATLAS detector and the CMS detector. LHC started proton-proton collision in 2009 with a center of mass energy $\sqrt{s}$ = 900 GeV, and $\sqrt{s}$ = 7 TeV in 2010 with low instantaneous luminosity. In 2011 and 2012, LHC started to collide protons with

high instantaneous luminosity with center of mass energy up to 7 TeV (2011) and 8 TeV (2012). In June 2012, based on the large amount of data collected at 7 TeV ($\sim 5\ fb^{-1}$) and 8 TeV ($\sim 6\ fb^{-1}$), ATLAS and CMS experiments announced the observation of a resonance with mass of about 125 GeV. Fig. 1.13 shows the observed probability by ATLAS for background processes, which is denoted as $p0$. The result presented here is based on the analysis of the $H \to ZZ^*$ and $H \to \gamma\gamma$ decays with contribution from $H \to WW^*$ decay [4]. By the end of 2012, the total dataset collected at LHC is up to $\sim 25\ fb^{-1}$. With the full dataset, detail studies has been performed on the Higgs properties [89][90][91][92] , for example,the mass of Higgs boson was measured by both ATLAS and CMS experiments [93][94]. Until 2015, evidence of Higgs boson has been found on all channels described in 1.2.3 except in the $H \to b\bar{b}$ decay.

CHAPTER 2

LHC and ATLAS Detector

Searching for the new particles requires the use of particle accelerators and colliders. New particles can be generated resonantly from the collision once the center of mass energy $\sqrt{s}$ exceeds the rest mass of the particle. Besides high collision energy, high event rate is also required for the processes with small cross sections. The search for the Higgs boson presented in this thesis is based on the data collected by the ATLAS detector at the Large Hadron Collider. This chapter introduces the accelerator complex used to accelerate and collide protons, as well as the structure of ATLAS detector, while leaving technical details in references [95, 96, 97]. Section 2.1 briefly discusses the structure of the LHC accelerator complex, while section 2.2 provides the key features of ATLAS detector. In the end, section 2.3 summarizes the data taking status in LHC Run 1.

2.1 Large Hadron Collider

Large Hadron Collider is a circular superconducting hadron collider with circumference of 27 km, located at the *European Laboratory for Particle Physics (CERN)* near Geneva, Switzerland. The machine is installed in an underground tunnel, which was initially constructed for the Large Electron Positron Collider (LEP) in 1980s. LHC is designed for proton-proton collisions, proton-Pb collisions, and Pb-Pb collisions. The heavy ion collisions can be used to study the QCD dynamics in extremely hot and dense state, while the proton-proton collisions at high center of mass energy can be used to probe the fundamental interaction between quarks and gluons at high energy scale.

The hadron beams circulate inside LHC in two vacuum pipes. The beams are accelerated through 8 superconducting cavities operating at 400 MHz, which generate electric field to accelerate the beams and compensate the energy loss due to synchrotron radiation. Between the cavities, beams are bent by 1232 super conducting two-in-one dipole magnets, the field strength of which limits the maximum energy of the beam. In the nominal design, the protons can be accelerated to 7 TeV, and the dipoles can provide 8.3 T magnetic field to effectively bend the beam. Compare to the electron beams in LEP, the proton beams have much smaller synchrotron radiation, which not only reduces beam energy loss, but also allows the super conducting dipole magnets to operate under extreme low temperature. Besides the dipole magnets, 392 quadrupole magnets are used to focus the beams. Collisions inside LHC take place at four interaction points, which hosts the four main experiments.

The ATLAS [1, 95, 96, 97] and CMS [2, 98] are two general purpose detectors, aiming at searches for Higgs boson and beyond the Standard Model (BSM) particles,

Figure 2.1: The Large Hadron Collider at the French/Swiss board. The yellow ring indicate the LHC ring, which is 50 m to 100 m underground. Locations of the four main experiments are shown on the plot. The detector for each experiment are inside the LHC tunnel. Location for the SPS and PS are also shown [99].

as well as precision measurements for Electroweak Symmetry Breaking. Besides ATLAS and CMS, there are two other large detectors. The ALICE detector [100], which is built specially for heave ion program, studying the physics of strongly interacting matter and the quark-gluon plasma in heave ion collisions at LHC. The LHCb [101] is an asymmetric detector with excellent vertex detectors, specially designed for secondary vertex reconstruction to study the b-hadron physics.

The LHC ring is only the final stage of series of accelerators. At LHC, protons are initially obtained by ionizing hydrogen gas. After that, they are accelerated by the linear particle accelerator (LINAC2) and grouped to bunches using radio-frequency quadrupoles. Protons leaves LINAC2 with 50 MeV energy, are then boosted by

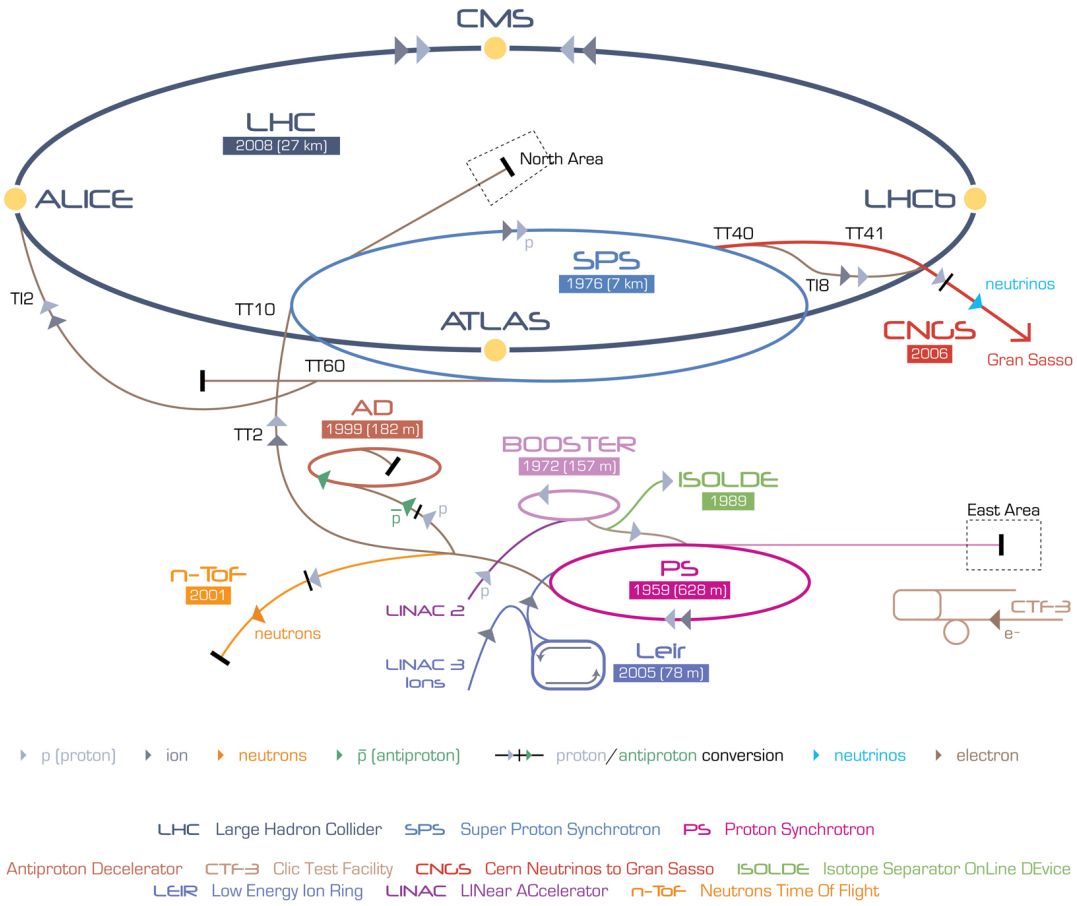

Figure 2.2: Schematic view of the LHC accelerator complex, including the LHC injection chain consisting of the accelerator LINAC2, BOOSTER, PS, and SPS [102].

the Proton Synchrotron Booster (PSB) to 1.4 GeV. The Proton Synchrotron(PS) further accelerates protons to 25 GeV, and group bunches of protons into *bunch trains*. The bunch trains are then fed into the Super Proton Synchrotron(SPS), where the beam energy is increased to 450 GeV, which is the LHC injection energy. Fig 2.2 shows an overview of the LHC complex.

In the nominal design, protons are accelerated to 7 TeV, and collide with a center of mass energy $\sqrt{s} = 14$ TeV with maximum instantaneous luminosity of 10^{34} $cm^{-2}s^{-1}$. In order to reach this luminosity, each beam is designed to have 39 bunch trains, with 345 ns gap between each train. One bunch train consist of 72 bunches

with 25 ns bunch spacing. In each bunch, there are about 115 billion protons.

In 2011 and 2012, LHC operates at different center of mass energies: 7 TeV (2011) and 8 TeV (2012), and the filling schemes used are different from designed ones. Bunch spacing was increased from 25 ns to 50 ns, thus only 36 bunches left in each bunch train, and the total number of bunches decreased from 2808 to 1380. In order to reach the maximum design instantaneous luminosity, the number of protons in each bunch was increased from 115 billion to about 170 billion. In the end, the maximum instantaneous luminosity in 2012 was $7.7 \times 10^{33}\ cm^{-2}s^{-1}$, which is very close to the designed value.

2.2 The ATLAS Detector

ATLAS is a multi-purpose detector with large acceptance and excellent physics performance, located at one of the interaction point (IP-1) inside LHC tunnel. ATLAS detector is designed to cover nearly all of the 4π steradians of solid angle , and provide precise measurement for the final state particles produced by the collisions that happens right at the center of the detector. ATLAS is a barrel-shape detector, about 44 meters long, and 25 meters high, weights about 7000 tons. Fig 2.3 shows the cut away view of the ATLAS detector.

As shown in Fig. 2.3, ATLAS consists of several sub detectors. The innermost detector is the Inner Detector (ID) [103] [104], consisting of Pixel Detector [105], Semi Conductor Tracker [106, 107, 108] and Transition Radiation Tracker (TRT) [109, 110, 111], designed to precisely measure the trajectory and momentum of the charged particles produced in the collision. The whole Inner Detector is surrounded by a solenoid, which can generate magnetic field of 2T [112]. Out of the

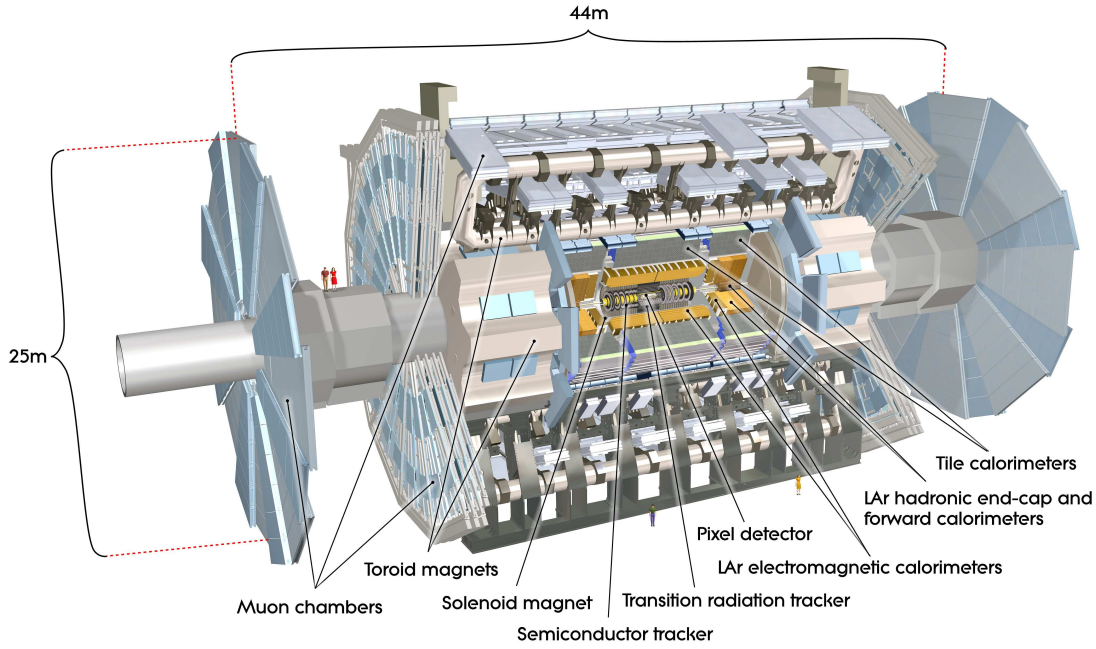

Figure 2.3: Cut away view of the ATLAS detector and the sub-detectors [1] .

solenoid is the Electromagnetic (EM) Calorimeter, using lead as absorber and liquid argon as active medium, designed to measure the energy of electrons and photons [113, 114]. Further outside is the Hadronic Calorimeter, composed of steel and scintillating tiles in the barrel, and liquid argon in the endcap, which can provide precise measurement of the energy deposited by the hadrons [115]. The Hadronic Calorimeter is surrounded by the Muon Spectrometer (MS), consisting of four different technologies to trigger and measure the momentum of muons. The four technologies used are Monitored Drift Tubes (MDTS), Resistive Plate Chambers (RPC), Thin Gap Chambers (TGC) and Cathode Strip Chambers (CSC). The Muon Spectrometer relies on the air core toroid magnet system [116].

2.2.1 Coordinate System

The ATLAS detector uses a right-hand cartesian coordinate. The origin point is the interaction point. The positive z direction is defined along the beam line, pointing

to the counter clock-wise direction viewing from above. The x direction points from the interaction points to the center of the LHC ring, and the y directions points straight up. A spherical coordinate (r, ϕ, θ) is more often used in analysis, where $r = \sqrt{x^2 + y^2}$, and ϕ is the azimuthal angle in the x-y plane to x-axis, θ is polar angle measured to the beam line, defined as 0 when lies along the positive z-axis. In the proton proton collisions, most of the particle produced in the collision have a small θ. In order to get a more flat distribution of particle multiplicity, θ can be replaced by the rapidity:

$$y = \frac{1}{2} ln(\frac{E + p_z}{E - p_z}) \tag{2.1}$$

Since the particles produced in collision carry large energy, the rest mass of the particle can be considered as negligible. Use the approximation of rest mass equals to zero, we get the definition of pseudo-rapidity, usually written as η:

$$\eta = -\ln(\tan(\frac{\theta}{2})) \tag{2.2}$$

According to definition, particles travel in the x-y plane have $\eta = 0$; particles travel along the beam axis have $\eta = \pm \infty$. To describe the angular distance between two particle, ΔR is introduced using the definition below:

$$\Delta R = \sqrt{\Delta\eta^2 + \Delta\phi^2} \tag{2.3}$$

In the Inner Detector, since the tracks of charged particle are bent only in the x-y plane, it is useful to project the momentum and energy of the particles into this plane. The transverse momentum is defined as $p_T = (p_x, p_y)$, and the transverse energy is defined as $E_T = Esin(\theta)$.

In order to describe the distance between reconstructed tracks and the vertices, the transverse impact parameter (d_0) the longitudinal impact parameter (z_0) are introduced. The transverse impact parameter is defined as the closest distance in transverse plane between the track and the primary vertex, while the longitudinal impact parameter is defined as the value of z of the point on the track that determines d_0.

2.2.2 Magnet System

In the ATLAS detector, the magnetic field is used to bend the tracks of charged particles, whose momenta can then be calculated from the curvature of reconstructed trajectory. Since the trajectories of a high momentum particles has smaller curvatures, the corresponding momentum resolution is usually worse comparing to particles with lower momentum.

The magnet system in ATLAS consists of a solenoid and a toroidal system. The solenoid is 5.8 meters long along the beam direction and 2.5 meters in radius, lying outside of the inner detector. It can provide a 2 T magnetic field in positive z direction. The toroidal system consists of three components, one in barrel and two in endcap region. In order to reduce the multiple scattering between muons and the materials that degrades the muon momentum resolution, the toroid is designed as eight separate coils with air between them. The coils are arranged symmetrically in both barrel region and endcap region. In the endcap region, the coils are rotated

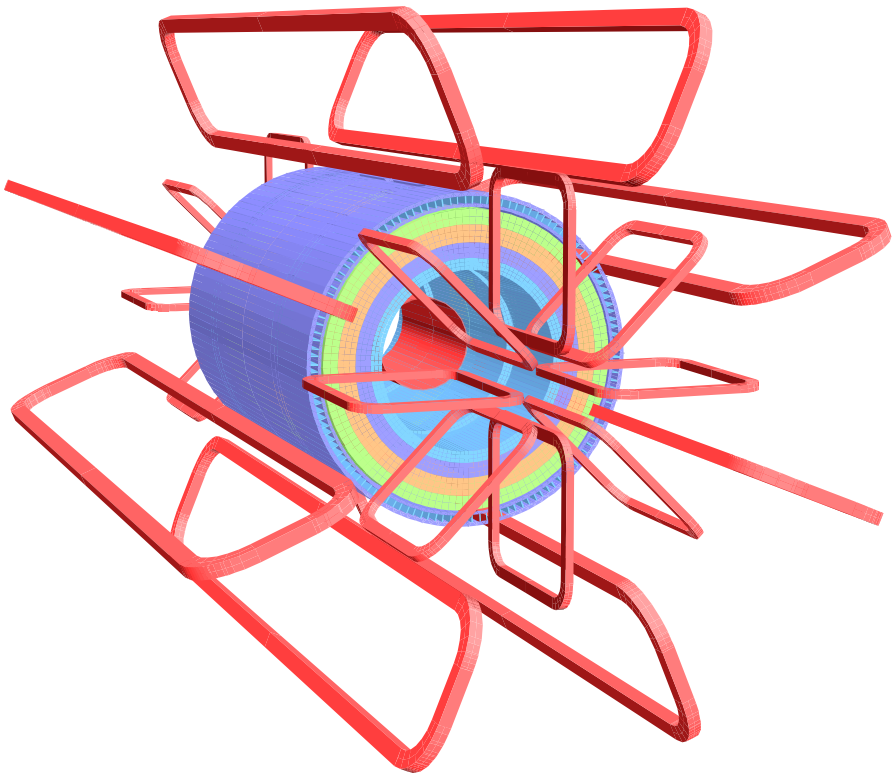

Figure 2.4: Layout of the ATLAS Magnet System. The interior cylinder presents the four layers materials with different magnetic properties which models the tile colorimeter. The solenoid winding lies inside the calorimeter volume. The orange rings present eight barrel toroid coils and the end-cap coils [1].

$\pi/8$ relative to ones in the barrel region to further reduce the scattering effect. Figure 2.4 shows the layout of the ATLAS magnet system.

2.2.3 Inner Detector

The ATLAS inner detector is designed to provide precise measurement of the momentum for charged particles, as well as the tracking information. It is about 6.2 meters long and 2.1 meters in diameter, covering $|\eta| < 2.5$. The entire inner detector is submerged in a 2 T magnetic field pointing to the positive z direction as described above. Besides momentum measurement, the track information can also be used in particle identification, such as photons and electrons. In addition, the

accurate spatial resolution of the inner detector allows high precision measurement of the secondary vertices, which is particularly useful for the analysis described in this dissertation because secondary vertices usually indicates the decay of long lived particles, such as B-hadrons.

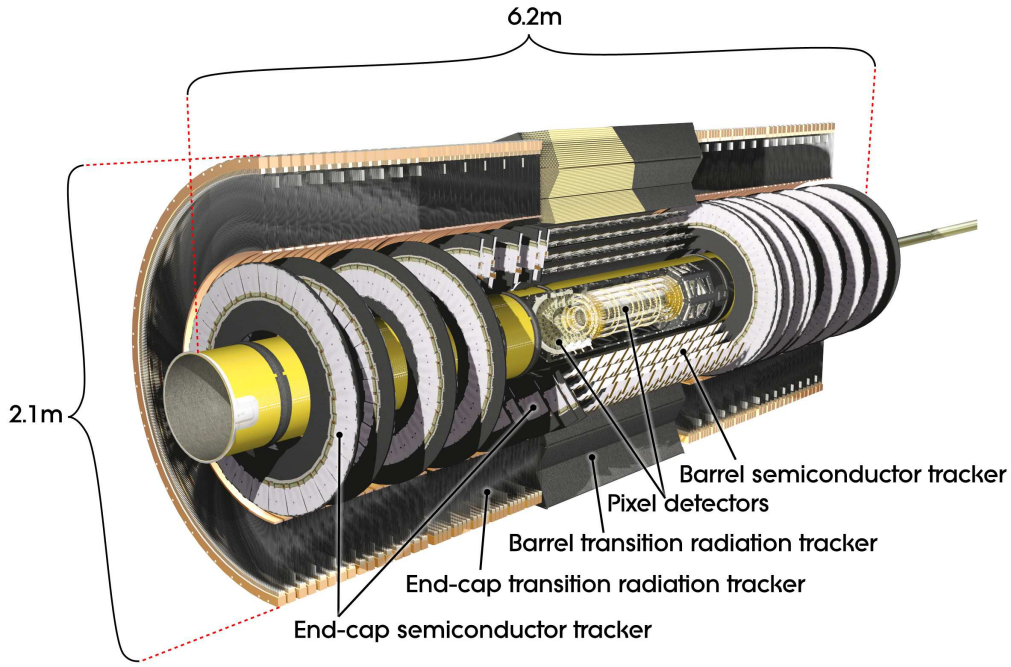

Figure 2.5: Computer generated cross section of the ATLAS inner detector [1].

The inner detector consists of three independent but complementary sub-detectors. From inside to outside: Pixel Detector, Semiconductor Tracker and Transition Radiation Tracker. Sub-detectors have different granularities and provide different number of hit points along the track. The closer to the interaction point, the higher resolution of a given detector has to be, and less number of hit points it can provide. Fig 2.5 shows a computer generated cross section view of the inner detector, a more detailed schematic view of the inner detector is given in Fig 2.6.

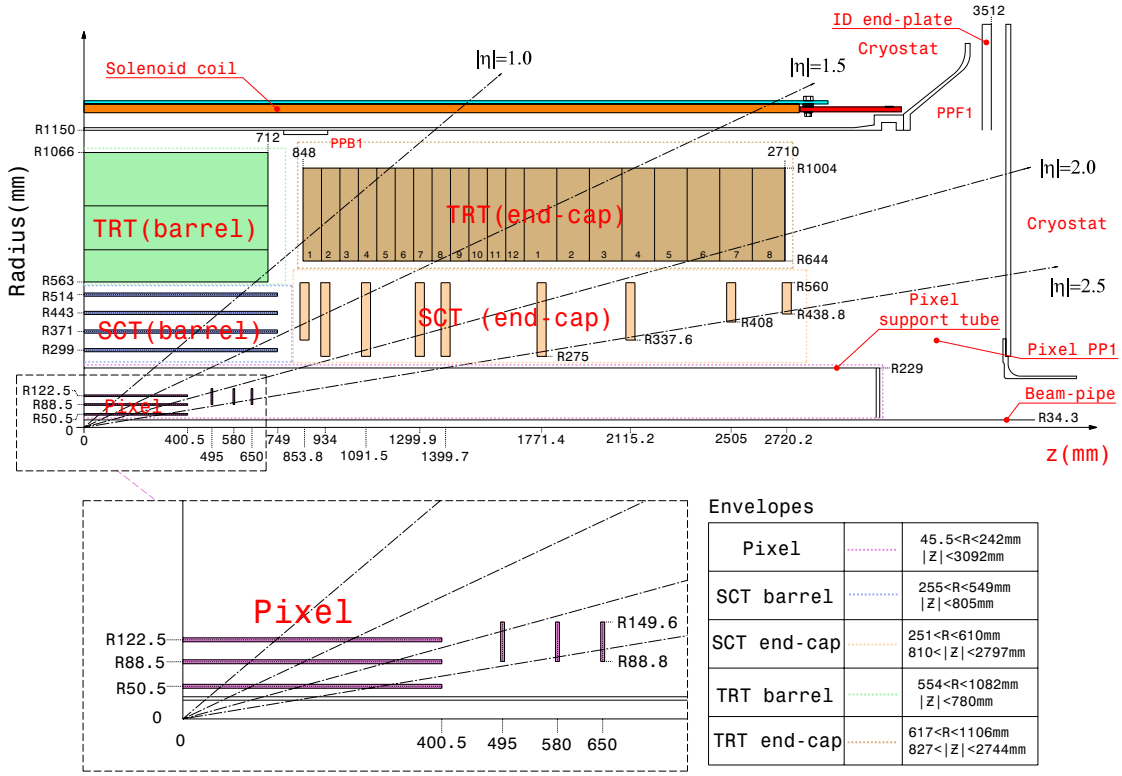

Figure 2.6: Plan view of a quarter-section of the ATLAS inner detector showing each of the major detector elements with its active dimensions and envelopes [1].

Pixel Detector

Pixel Detector is the innermost sub-detector in ATLAS, surrounding the beam line with a distance of about 5 cm. It is designed to provide high precision measurements of space points with coverage $|\eta| < 2.5$, which contributes in reconstruction of tracks and vertices. The Pixel detector has three layers of silicon sensors. The layer close to the beam line is denoted as the B-layer, and is particular important for precise measurement of impact parameters and secondary vertices.

Pixel Detector has barrel region and endcap region. In the barrel region, the silicon sensors are arranged in three concentric layers at R = 50.5 mm, 80.5 mm, and 122.5 mm. In the endcap region, the silicon sensors are arranged in three disks with $z =$ 495 mm, 580 mm, and 655 mm, which are perpendicular to the beam line. The

pixel detector has 1744 sensors, each with 47232 pixels cells. The pixel cells are segmented in R-ϕ and z directions with each cell as small as $50\mu m \times 400\mu m$, which gives typical spatial resolution 10 μm in R-ϕ direction and 115 μm in longitudinal direction.

Semi-Conductor Tracker

The Semiconductor Tracker (SCT) is a silicon strip detector which enclose the Pixel Detector. It consists of four layers of silicon microstrips in the barrel region and nine double-layers structures in the endcap region. In the barrel region, the microstrip layers are located from 299 mm to 563 mm in radius direction, and covers $|z| < 749$ mm in longitudinal direction. In endcap region, the SCT covers 853 mm $< |z| <$ 2720 in longitudinal direction, while the radius size are optimized to provide the same number of hits over the whole η range.

In total, the SCT provides 63 m^2 of active areas, and about 6.3 million readout channels. For each sensor, it has an active area of about $6.36 \times 6.40\ cm^2$, containing 768 active strips. In order to reduce the number of electric readouts, the strips are installed back to back with a small stereo angle of 40 mrad, which breaks the degeneracy along z direction and provides a two dimensional measurement. The overall resolution for the SCT is 17 μm in $R - \phi$ direction, and 580 μm in z direction. On average, the SCT can provide eight space points for one track.

Transition Radiation Tracker

Transition radiation tracker (TRT) is the outermost sub-detector in the inner detector. The concept of the TRT is based on the transition radiation, which takes place when charged particles pass through the boundary between two different dielectric materials. Intensity of the transition radiation is proportional to charged

particle's Lorentz factor. For particles with same momentum, the lighter one has larger Lorentz factor, thus has stronger radiation intensity. It is then possible to discriminate between light and heavy particles, such as electrons and pions. The electronic read out of the TRT is designed with two thresholds, the lower threshold is for particles with larger mass (like hadrons), while the higher threshold is for charged particles with lower masses (like electrons and positrons). By looking at the ratio of high threshold hits and low threshold hits, electrons can be distinguished from hadrons.

TRT consists of about 350,000 drift tubes. The tubes in the barrel region are 144 cm long, aligned with the beam line. The tubes in the endcap region are 37 cm long, aligned in radius direction. Each drift tube has a diameter of 4 mm, filled with a mixture of 70% xenon, 27% carbon-dioxide, and 3% of oxygen with 5 to 10 mbar over-pressure. A wire with 31 μm diameter runs through the tube at the center, which is kept at a high voltage with respect to the shell of the tube. When charged particles pass through the tube, free electrons are generated from the ionization of the mixture of gas and drift to the wire. The drifting process then produces an avalanche of secondary electrons and amplifies the original signal. By measuring the time of arrival of the electrons, TRT can provide 130 μm intrinsic space resolution in $R\phi$ plane. Due to the large length in z(r) direction, TRT can not perform precise measurement in z(r) direction.

In contrast to the Pixel Detector and the Semiconductor Detector, TRT has a smaller coverage of $|\eta| < 2.0$, and much worse intrinsic resolution. However, TRT is able to provide 36 space points over a wide range (563 mm $< R <$ 100 mm in barrel region, and 644 mm $< R <$ 1004 mm in endcap region), which results in a large improvement on the track resolution, as well as the identification between electrons and hadrons.

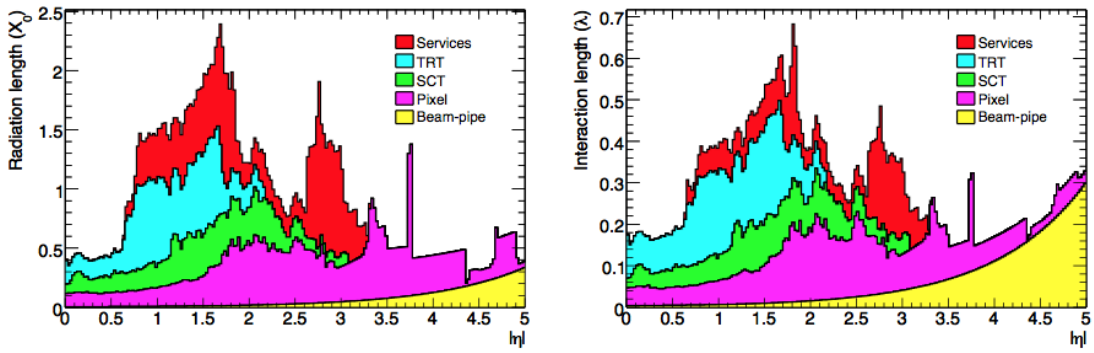

Figure 2.7: The material distribution (X_0, λ) of the inner detector, including the services and thermal enclosures. The distribution is shown as a function of η and averaged over ϕ. The breakdown indicates the contribution of external services and of individual sub-detectors, including services in their active volume [1]. The plot on the left is in terms of radiation length X_0, and the right plot is in terms of interaction length λ.

Combining Pixel, SCT, and TRT together, the transverse momentum resolution of the inner detector for tracks with $p_T > 500$ MeV can be written as:

$$\sigma p_T/p_T = 0.05\% \times p_T/[\text{GeV}] \oplus 1\% \tag{2.4}$$

Since the inner detector is the closest to the interaction point, it was designed to minimize the material budget, which not only degrades the momentum resolution via multiple scattering between particles and detector materials, but also effect the energy measurement in the calorimeters. Fig 2.7 shows the amount of material in the inner detector.

2.2.4 Calorimeter

By reconstructing the trajectory of charged particles, the inner detector is able to provide precise measurement for the momentum of charged particles, as well as the reconstruction of primary and secondary vertices. However, there are also neutral particles with no tracks, such as photon and π^0. To measure the energy of neutral particles, a calorimeter system is needed in ATLAS. The Calorimeter system in ATLAS is intended to provide accurate measurement of particle energies (for both charged and neutral particles), as well as the shower properties, which are then used for particle identification.

The ATLAS Calorimeter consists of three calorimeters: Electromagnetic Calorimeter (ECAL), Hadronic Calorimeter (HCAL), and the Forward Calorimeter (FCAL) [113, 114, 115]. The Electromagnetic Calorimeter is designed to fully absorb and precisely measure the energy of electrons, positrons, and photons, with a coverage of $|\eta| < 3.2$. The Hadronic Calorimeter is intended to fully absorb and measure the energy of hadrons with a coverage of $|\eta| < 3.2$. The Forward Calorimeter is designed to provide additional coverage for both electromagnetic processes and hadronic processes, covering $3.1 < |\eta| < 4.9$. In total, the Calorimeter system provides coverage up to $|\eta| = 4.9$. Fig 2.8 shows the cut-away view of the calorimeter system in ATLAS detector.

All three calorimeters are sampling calorimeters, made of absorbers and active sensors. When a particle hits the absorber, the interactions between the particle and the material generate a shower consisting of secondary particles, the energy of which are then measured by the active sensors as an electric signal. Besides precise measurement of the of particle energy, the calorimeter system is also designed to provide accurate spatial resolution, which can be used for photon reconstruction

and the reconstruction of missing transverse energy (E_T^{miss}).

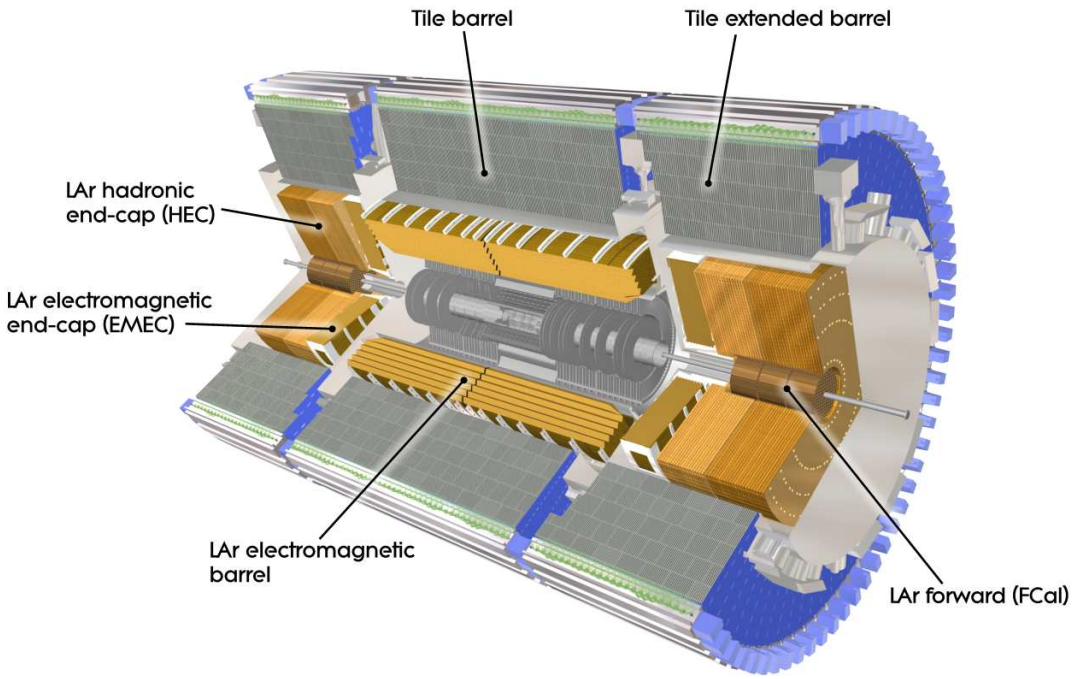

Figure 2.8: Cut-away view of the ATLAS calorimeter components [1].

Electromagnetic Calorimeter

The electromagnetic calorimeter is a finely segmented sampling calorimeter which can provide precise measurement for particle energies, space information, as well as shower properties. The electromagnetic calorimeter is subdivided into a barrel region and two endcap regions. In barrel region, the calorimeter is a cylindrical barrel which has inner and out diameter of R = 2.8 m and 4 m. The barrel region covers full azimuthal angel and $|\eta| < 1.4$ with a small gap of 4 mm at $z = 0$. The endcap region consist of two wheel shape calorimeter, which covers $2.5 < |\eta| < 3.2$ and $1.375 < |\eta| < 2.5$, respectively.

The ECAL is constructed in a accordion shape to interleave the absorber and electrodes. A schematic of the accordion-shaped barrel module is shown in Fig.

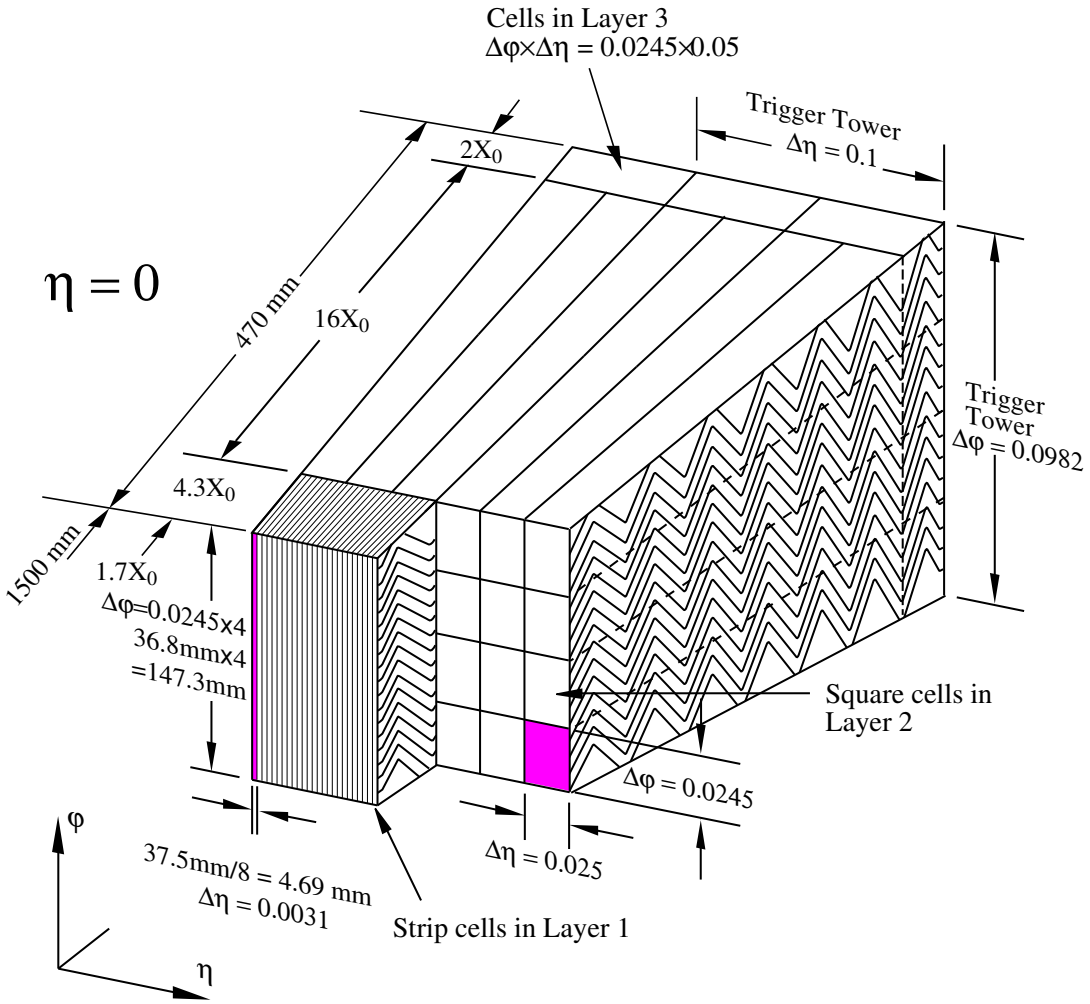

Figure 2.9: Sketch of a barrel module where the different layers are clearly visible with the ganging of electrodes in phi. The granularity in eta and phi of the cells of each of the three layers and of the trigger towers is also shown [1].

2.9. Each module consists of folded layer of lead absorber and electrodes between the layers, liquid argon is filled between the gap of lead and electrodes as the active medium. When electrons and photons pass through the lead layers, an electromagnetic shower is generated through the bremsstrahlung process and pair production of e^+e^-. The created shower ionizes the liquid argon upon going through the active medium to generate free electrons, which then drift to the electrodes to create a signal on the electrodes readout. The sampling time of ECAL is 25 ns, and the readout window is 5 times larger.

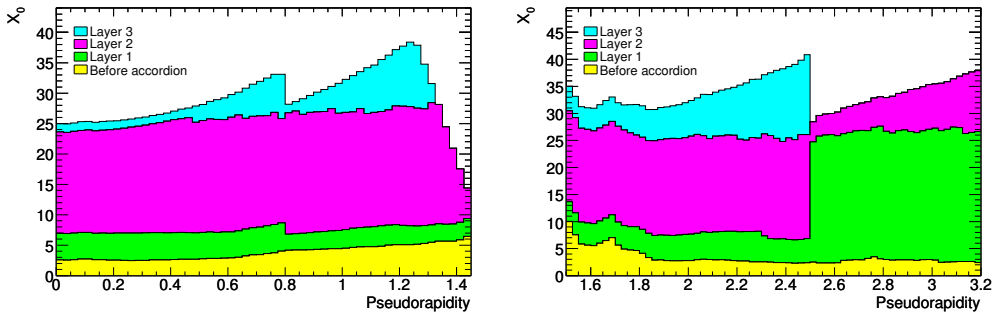

Figure 2.10: Cumulative amounts of material, in units of radiation length (X_0) and as a function of $|\eta|$, in front and in the electromagnetic calorimeters. The plot on the left shows the thickness of each accordion layer as well as in front of the accordion in barrel region. The plot on the right is for endcap region [1]

The resolution of the ECAL depends on the total number of electrons collected on the electrodes, which is proportional to the energy of the incident particle. Thus the energy resolution of the ECAL is a function of the energy of the particles (E).

$$\frac{\sigma(E)}{E} = \frac{10\%}{\sqrt{E/[\text{GeV}]}} \oplus 0.7\% \tag{2.5}$$

In barrel region, the ECAL is segmented into three layers with varying granularity. The inner most layer has finest granularity, which can be used for discriminating converted photons and π^0s. The second layer has a thickness about 16 radiation length (X_0), where particles deposit most of their energy. The third layer is mainly used to distinguish electromagnetic shower and hadronic showers. In $|\eta| < 1.8$ region, there is an additional layer in front of all other layers named pre-sampler, designed to measure the energy loss of the particles before entering the ECAL, the result of which is then used to correct the energy for better resolution. In the endcap region, the ECAL is segmented into two layers with coarse granularity. In total, the thickness of ECAL is larger than 22 X_0 in barrel, and larger than 24 X_0

in endcap. Fig. 2.10 shows the thickness of material, in units of radiation length, in both barrel region and endcap region as a function of $|\eta|$.

Hadronic Calorimeter

The Hadronic Calorimeter (HCAL) is also a sampling calorimeter, designed to fully absorb and measure the energy of hadrons which punch through the Electromagnetic Calorimeter. The Hadronic Calorimeter consist of two sub system covering different region of $|\eta|$. The granularity for each calorimeter is optimized to provide good space resolution for jet direction measurement and shower shape analysis.

The Tile Calorimeter (Tile CAL) [115] is the central barrel of the Hadronic Calorimeter, with a coverage of $|\eta| < 1.7$. The Tile Calorimeter is constructed with steel plates interleaved with tile scintillators. When a hadron passes through the steel absorber, inelastic hadronic interactions between hadrons and absorber initialize a hadronic shower, which then excite the scintillator materials. The photons from scintillator are guided to Photon Multipliers (PMT) to create a electric signal. The Tile Calorimeter consist of three layers with inner radius of 2.8 m and outer radius of 4.25 m.

The Hadronic Endcap Calorimeter (HEC) is located behind the endcap of the ECAL, covering $|\eta|$ range from 1.7 to 3.1. The radiation in this region is much stronger comparing to the barrel region, and liquid argon is used as active medium since it is more resistant to radiation damage compare to scintillating tiles.

The depths of both Tile Calorimeter and Hadronic Endcap Calorimeter are optimized to deposit all the energy of incident hadrons, and to provide enough sampling layers to achieve the required resolution for shower shape analysis. The total depth of Tile Calorimeter is 7.4 λ_0, and the depth of Hadronic Endcap Calorimeter is 10

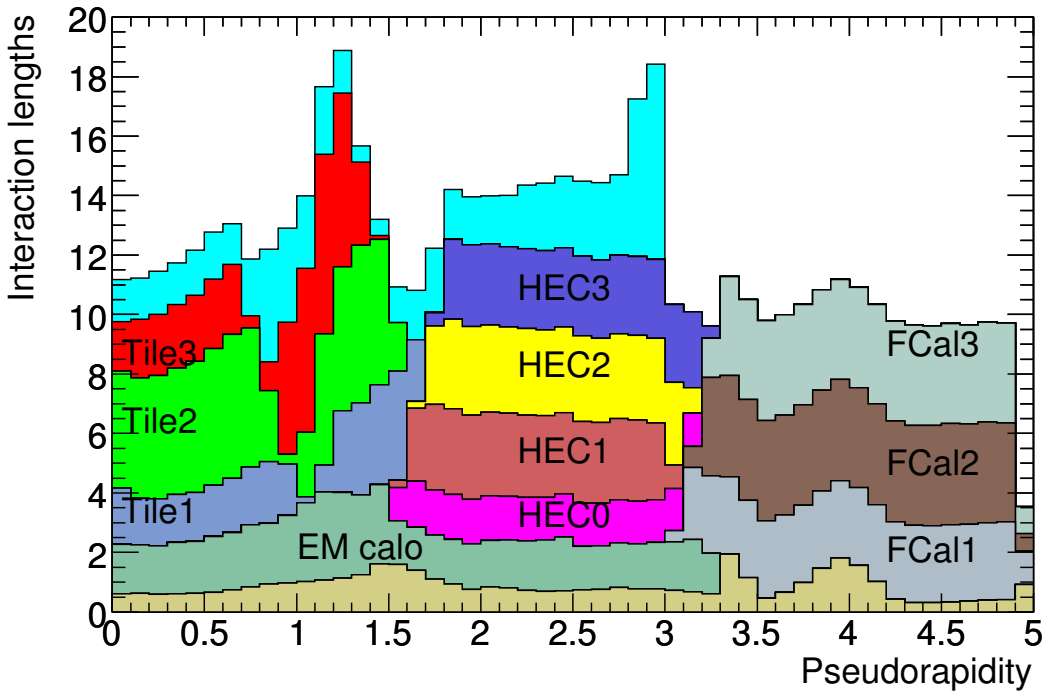

Figure 2.11: Cumulative amounts of material in the Calorimeter of ATLAS detector as a function of $|\eta|$ measured in radiation length (λ_0). Besides the layers of Electromagnetic Calorimeter and the Hadronic Calorimeter, the material in front of the Calorimeter is also shown (olive), as well as the material in front of the muon spectrometer [1].

λ_0. Fig. 2.11 shows the thickness of the HCAL, in units of interaction length, as a function of $|\eta|$.

Similar to the Electromagnetic Calorimeter, the energy resolution of the HCAL is also a function of the energy of the hadrons (E).

$$\frac{\sigma_{barrel}(E)}{E} = \frac{50\%}{\sqrt{E/[\text{GeV}]}} \oplus 3.0\% \tag{2.6}$$

$$\frac{\sigma_{endcap}(E)}{E} = \frac{100\%}{\sqrt{E/[\text{GeV}]}} \oplus 10.0\% \tag{2.7}$$

Forward Calorimeter

The Forward Calorimeter (FCAL) covers range $3.1 < |\eta| < 4.9$. Similar to HEC, FCAL also uses liquid argon as active medium to withstand the strong radiation in high η region. FCAL is designed to provide additional coverage for the reconstruction of jets and E_T^{miss} in the high $|\eta|$ region, as well as a shield to block radiation for the Muon Spectrometer. FCAL consist of three layers, the first layer is optimized for electromagnetic processes, while the other two layers are optimized for hadronic processes.

2.2.5 Muon Spectrometer

The Muon Spectrometer is designed as a independent sub detector at ATLAS, which can provide precise direction measurement and momentum measurement of produced muons.

The Muon spectrometer is the outermost detector at ATLAS. In principle, all particle except muons and neutrinos, such as electron, photons, and hadrons, are stopped by the material in inner detector and calorimeter. Since muons are the only particles that interact with Muon Spectrometer, it allows easy identification. In contrast to Inner Detector, the long lever arm of the Muon Spectrometer allows a much longer trajectory, which provides better resolution for particles with high momentum. By measuring the curvature of the trajectory through toroidal magnetic filed, Muon Spectrometer can provide momentum measurement for muons

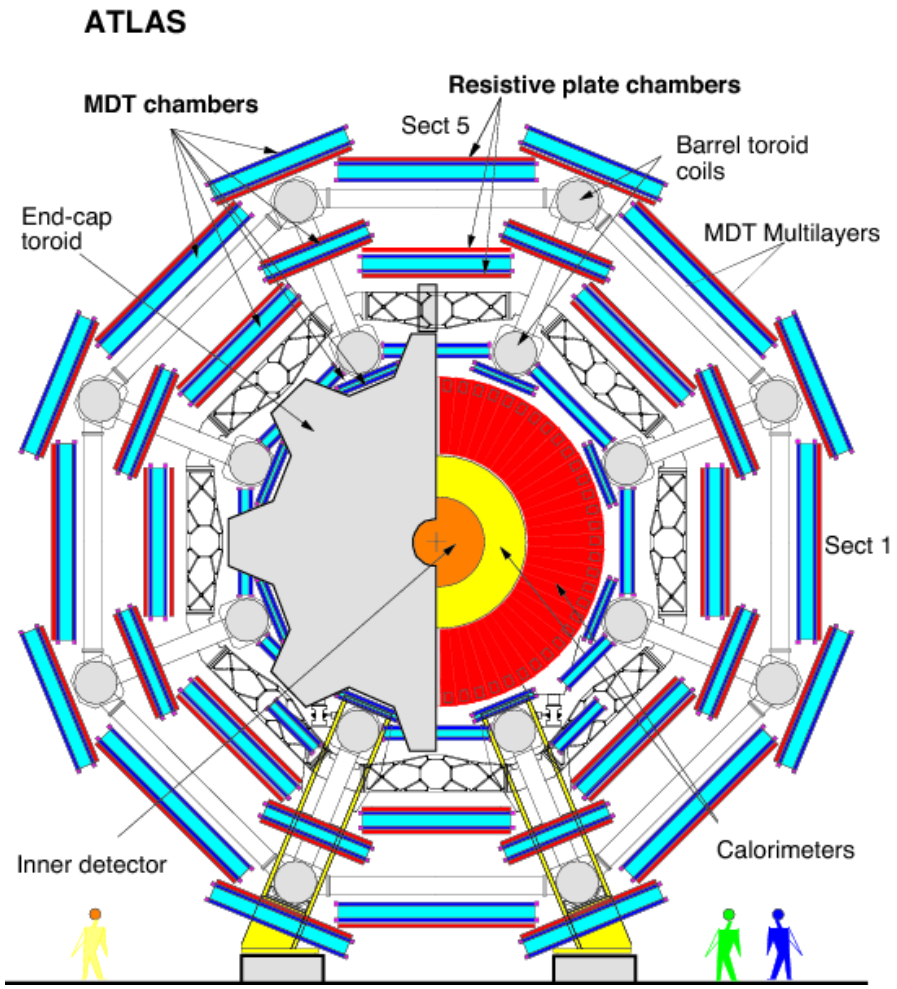

Figure 2.12: Transverse view of one quadrant of the muon spectrometer [116].

with a resolution of at least 10% for 1 TeV muon.

The Muon Spectrometer (MS) consists of four sub-detectors in different η region, as shown in Fig. 2.12 and Fig. 2.13. In total, The MS provides coverage of $|\eta| < 2.7$ for precise momentum measurement, and $|\eta| < 2.4$ for triggering charged particles. To trigger the charged particles, Resistive Plate Chamber (RPC) is used in the barrel region ($|\eta|$ <1.05), and Thin Gap Chambers (TGC) are used in the endcap region ($1.7 < |\eta| < 2.4$). RPC and TGC can also be used to measure the position of hit points in non-bending ϕ direction. The Monitored Drift Tubes (MDT) covers the range $|\eta| < 2.7$, and the drift tubes of which are designed to provide precise

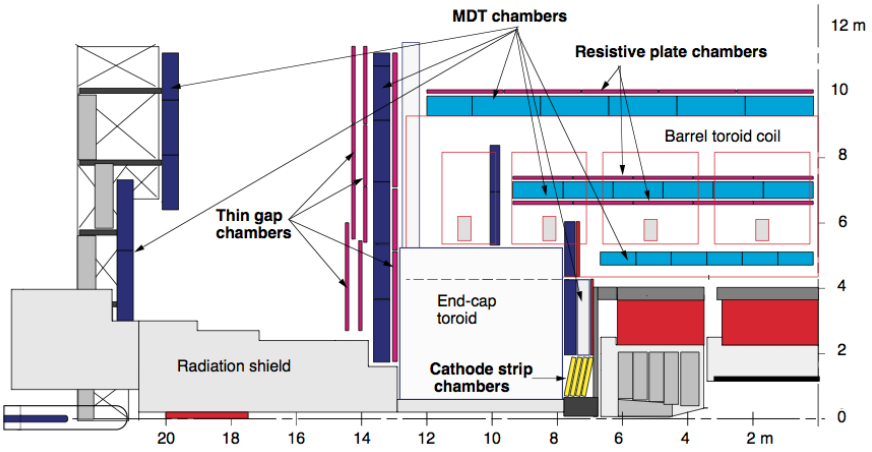

Figure 2.13: Side view of one quadrant of the muon spectrometer [116].

measurement in the bending direction (R-η). In high η region ($2.0 < |\eta| < 2.7$), where the radiation from the beam is much stronger compared to the central region, Cathode Strip Chambers (CSC) are used to keep a good space resolution for the hit points.

The MDT is designed to precisely measure the space points in the bending direction. To achieve the momentum resolution of 10% for 1 TeV muon, a space resolution of 35 μm is required. MDT consist of 3 layers in the barrel region and 4 layers in the endcap region. In the barrel region, where $|\eta|$ <1.05, the drifted tubes are arranged in three cylindrical layers with radius 5 m, 7.5 m, and 10 m. In the endcap region, where $1.05 < |\eta| < 2.7$, the drifted tubes are arranged in four wheels located at $|z|$ = 7.4 m, 10.8 m, 14 m, and 21.5 m. The drifted tubes are 3 cm in diameter, made with aluminum and filled with gas mixture of Ar/CO_2 at about 3 bar. When a drift tube is hit by a muon, the gas mixture is ionized, and the ionized electrons are collected by the wire that runs through the center of the tube. The average drift time is about 700 ns, which can be used to calculate the distance between the hit point and the wire. For one single tube, the space resolution is about 80 μm, By combining information from neighboring tubes, a space resolution of 35 μm

can be achieved.

The CSC is used at the innermost layer of the spectrometer at forward region with $2.0 < |\eta| < 2.7$, where the high-flux environment will degrade MDT's space resolution. The CSC constructed with multi-wire proportional chambers, with orthogonal split cathodes to provide a two dimensional spatial resolution for the hits. Spatial resolution of CSC is 60 μm in bending direction, and 5 mm in the non-bending direction.

The RPC covers $|\eta| < 2.4$, designed to provide fast triggering information for the MDT. The RPC chambers are mounted on either side of the middle layer of the MDT, as well as on the back of the outer most MDT layer. Each chamber consist of two resistive electrode plates, held with a spacing of 2 mm. Inside the gap, a mixture of gas is filled, and an electric filed of 4.9 kV/mm is applied to accelerate ionized electrons to the electrodes. To provide the two dimension measurement, both plates are orthogonally segmented. The spatial resolution of RPC is worse compare to the MDT, at about 10 mm, while the timing resolution is about 7 ns, which is narrow enough to work as a trigger.

The TGC is designed to provide fast trigger at $1.05 < |\eta| < 2.4$, as well as hit information in non-bending direction. The TGC is constructed with multi-wire proportional chambers that extend radially from the beam line, mounted on the inner and middle layers of the endcap wheels of MDT. The TGC has better spatial resolution compared to the RPC, which is several mm in both η and ϕ direction. It also has a narrow timing resolution at 4 ns, which allows the TGC to work as a trigger in the high event rate environment.

2.2.6 Luminosity Detector

The luminosity of a proton-proton collider can be expressed as :

$$L = \frac{\mu \times n_b \times f_r}{\sigma_{inElastic}} \tag{2.8}$$

In equation above, μ is the average number of inelastic interactions per bunch crossing, n_b is the number of colliding bunch pairs, f_r represents the revolution frequency of the beam, and $\sigma_{inElastic}$ stands for the cross section of proton-proton inelastic collision [117, 118].

At the ATLAS experiment, the delivered luminosity is monitored by measuring the observed interaction rate per bunch crossing ($\mu_{observed}$). If we further define $\sigma_{observed} = \epsilon \times \sigma_{produced}$ as the total inelastic cross-section multiplied by the efficiency of a particular algorithm, the total luminosity can be written as :

$$L = \frac{\mu_{observed} \times n_b \times f_r}{\sigma_{observed}} \tag{2.9}$$

The calibration of $\sigma_{observed}$ is performed using dedicated vdM scan as described in [118]. The delivered luminosity can be further written as:

$$L = \frac{n_b \times f_r \times n_1 \times n_2}{2\pi \sum_x \sum_y} \tag{2.10}$$

where n_1 and n_2 are number of protons per bunch in colliding beams, $\sum_x$ and $\sum_y$ describe the horizontal and vertical width of the colliding beams.

Two dedicated detectors are used to measure the luminosity of collision in ATLAS: LUCID and BCM.

LUCID is short for *LUminosity measurement using Cherenkov Integrating Detector*, located at $z = \pm$ 17 m , constructed with aluminum tubes surrounding the beam pipe. Since the number of particles detected by the LUCID is proportional to the number of proton-proton collisions in a bunch crossing, the LUCID can perform measurement for the instantaneous luminosity by counting number of detected particles .

The Beam Condition Monitor(BCM) is located at $z = \pm$ 1.84 m from the interaction point. The BCM consist of four diamond sensors arranged in a vertical pair and a horizontal pair. The signal created in a diamond sensor has a narrow width of 3 ns, which is much smaller compare to the bunch spacing (25 ns). With the short response time, the BCM can be used to measure the particle flux from the beam, and therefore the luminosity.

2.2.7 Trigger System

Inside ATLAS detector, proton bunches collides every 25 ns, the majority of which do not contain events which are considered as valuable in the sense of rare physics processes for further investigation. In general, the valuable events means events produced with large momentum transfer in proton-proton collisions, the final states of which contain objects with high transverse momentum. Fig. 2.14 shows the cross sections of several major processes comparing to the cross section of total proton proton collision.

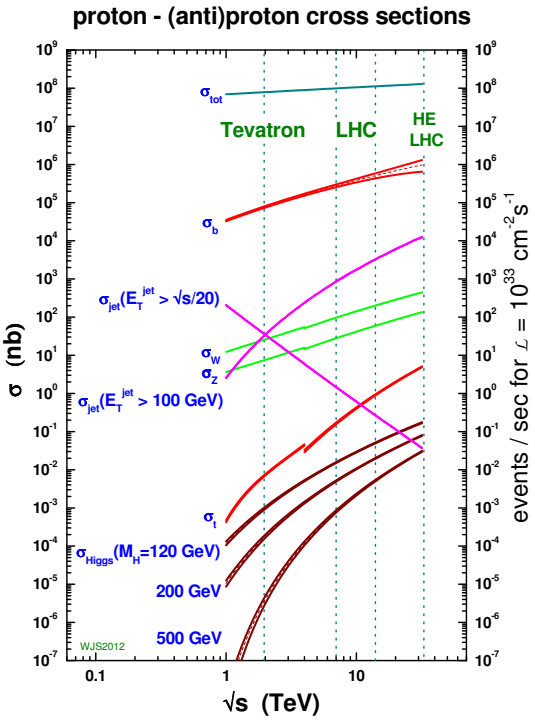

Figure 2.14: Cross section of several major processes comparing to the total cross section of proton proton collision. The total hadronic cross section is based on the parametrization of the Particle Data Group, the cross section for other processes are calculated with either NLO or NNLO QCD correction, where MSTW2008 parton distribution function is used. The discontinuity for some processes at 4 TeV is due to the switch from $p\bar{p}$ to pp collision [119].

Apart from the reason above, it is also not realistic to record all the events due to the limitation of computing and storage resource. To deal with these difficulties, a Trigger system is required to discard most of the produced events, while keeping the valuable ones. In ATLAS, the trigger system can reduce the event rate from 40 MHz to 200 Hz [120]. The trigger system consist of three levels, each of which refines the selection from previous level with more detector information. Level 1 trigger (L1) is the hardware trigger, which reduces the event rate from 40 MHz to 75,000 Hz. Level 2 trigger (L2) and Event Filter Trigger (EF) are high level software triggers that further reduce the even rate from 75,000 Hz to 3,500 Hz, and

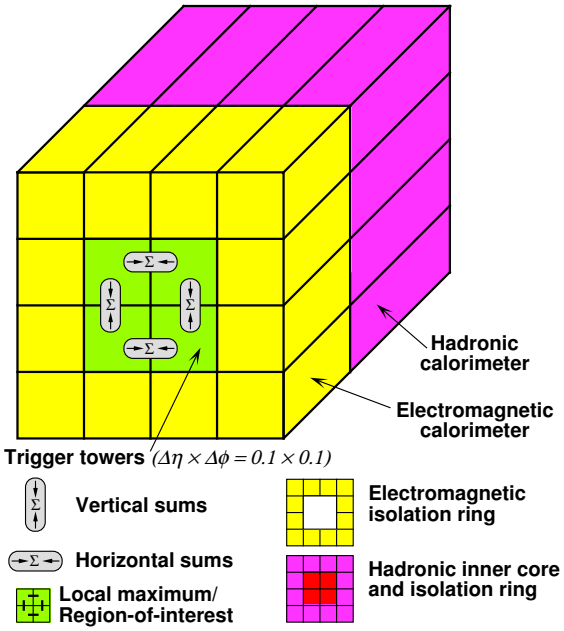

Figure 2.15: L1 Calo trigger algorithm for electron, photon, and τ [1]

from 3,500 Hz to 200 Hz.

The L1 trigger system consists of L1 Calo trigger and L1 Muon trigger, both of which are entirely hardware based, taking decision within 2.5 μs. The L1 Calo trigger uses simplified information from Calorimeter to identify particles such as electrons, photons, and jets. When a collision takes place, the trigger system searches for the local maximum of the energy deposit in the calorimeter. The corresponding

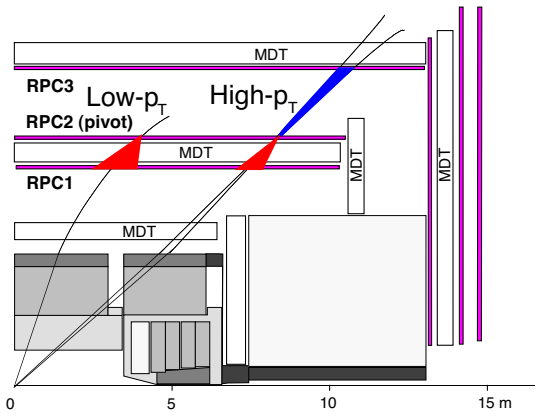

Figure 2.16: Schema of the L1 muon barrel trigger [1].

local maximum is named as *Region of Interest* (ROI). In the triggering process, calorimeter cells are grouped into towers of $\Delta\eta \times \Delta\phi = 0.1 \times 0.1$, denoted as *trigger tower*. Different algorithms are used to select different trigger object. Taking electrons and photons for example, their ROI are defined as a window of 2×2 trigger towers in electromagnetic calorimeter, where the sum of energy in a block of 1×2 trigger towers has to pass a certain threshold, and the neighboring trigger towers of the window has to fulfill an isolation requirement. For the jet objects, a window of 2×2 trigger towers is used in both electromagnetic calorimeter and hadronic calorimeter. The L1 Muon trigger uses the hit information from RPC and TGC sub-detector in the muon spectrometer. When a hit is recorded on the pivot plane (2nd layer of RPC and 3rd layer of TGC), a straight line is fitted between the hit point and the interaction point. Together with coincidences of hits in different layer of RPC and TGC, this line defines a "trigger road". The properties of the trigger road can then define the momentum of the muon by checking the slope of the fitted trajectory [1]. Fig 2.15 shows the L1Calo triggering algorithm, and Fig 2.16 shows L1 Muon triggering process.

Event that passes L1 trigger are then passed to L2 trigger, where additional information from the detector are used to identify the event. At L2 trigger, decisions are made within 40 ms. L2 trigger uses different algorithms for different trigger objects.

At EF level, a full reconstruction is used to identify the event. The trigger objects built in EF level are very similar to the objects used in the offline analysis. In EF level, decisions are made within 4 s.

During Run 1, the development of computing and storage exceeded the expectation. Therefore, the EF output rate was increased to 400 Hz during 2012 [121]. Events passed the EF trigger were then reconstructed at Tier 0 machines and stored all

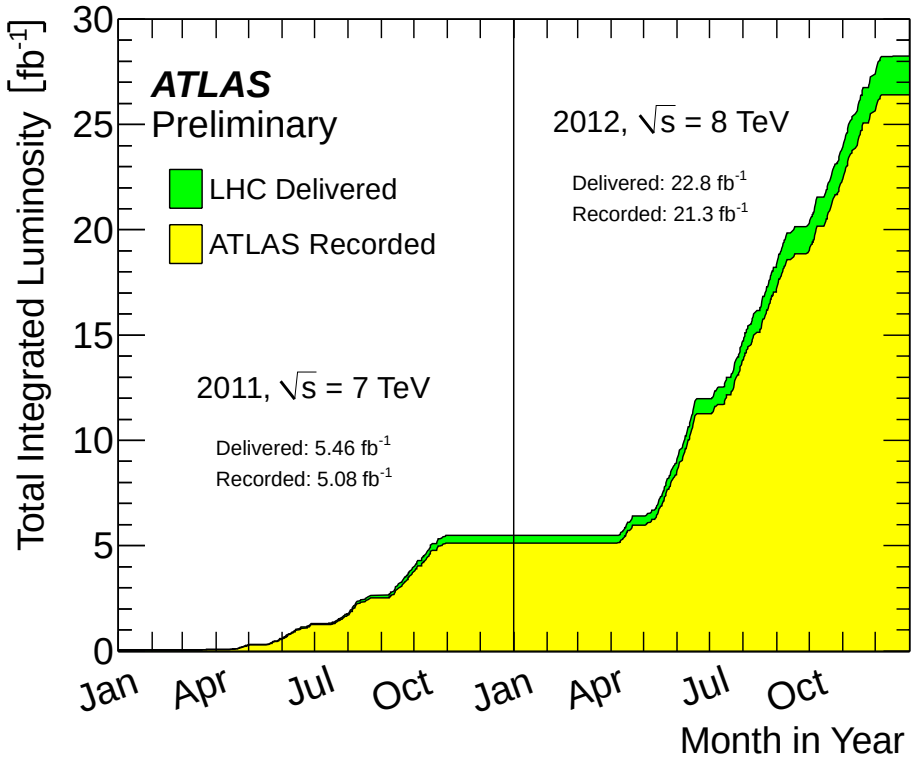

Figure 2.17: Cumulative luminosity versus time for proton-proton collisions at $\sqrt{s} = 7$ and 8 TeV in 2011 and 2012. [122]

over the grid.

2.3 Run 1 Data Taking

Proton-proton collisions were established in LHC since November 2009. In 2009, the injection energy is at $\sqrt{s} = 900$ GeV. In 2010, beam energy increased to $\sqrt{s} = 2.36$ TeV, an integrated luminosity of 48 pb^{-1} was delivered by the LHC, 93.6 % of which is recorded by ATLAS. LHC started to operate with 3.5 TeV beam at the beginning of 2011, the corresponding center of mass energy is $\sqrt{s} = 7$ TeV. The significant increase of the beam intensity in 2011 allows ATLAS to collect 5.2 fb^{-1} data at $\sqrt{s} = 7$ TeV. In 2012, the center-of-mass energy of collisions was further

increased to $\sqrt{s} = 8$ TeV, and the beam intensity also increased. As a result, LHC delivered an integrated luminosity of 23.3 fb^{-1} data with $\sqrt{s} = 8$ TeV, while 21.7 fb^{-1} of which was recorded by ATLAS. Fig 2.17 shows the integrated luminosity as a function of time in 2011 and 2012.

Due to the increase of the instantaneous luminosity, the number of interactions per bunch crossing increased from 5 to 35 during the Run I period. The design value of mean number of interactions, denoted as $< \mu >$, is 17 at ATLAS detector. However, this value reached up to 24 in 2012. The consequence of large number of interaction per bunch crossing is a phenomenon named as *pile-up*. There are two types of pile-up in ATLAS. The first one is known as in-time pile-up, which comes from the fact that more than one pair of protons collides in one bunch crossing under high mean intensity. The second one is know as out-of-time pile-up, which takes place when the energy from the previous collision affects the signal readout for the current collision. Out-of-time pile-up mostly happens in the sub-detectors where the time needed to extract a signal is longer than the time space between two bunches. Fig 2.18 shows recorded luminosity versus the mean number of interactions per bunch crossing for both 7 TeV and 8 TeV data.

ATLAS data taking is organized in Runs, and each run is further divided into *luminosity blocks*. A luminosity block is the smallest unit in data taking, which hold a certain number of data. During data taking, the Data Acquisition system (DAQ) are used to monitor each luminosity block. If there is an detector operation which affect the performance of the experiment, a certain flag is assigned to the corresponding luminosity block. In the end, a *Good Run List* (GRL) is created to contain all the luminosity blocks that can be used in physics analysis, and the total Physics luminosity is calculated based on the GRL.

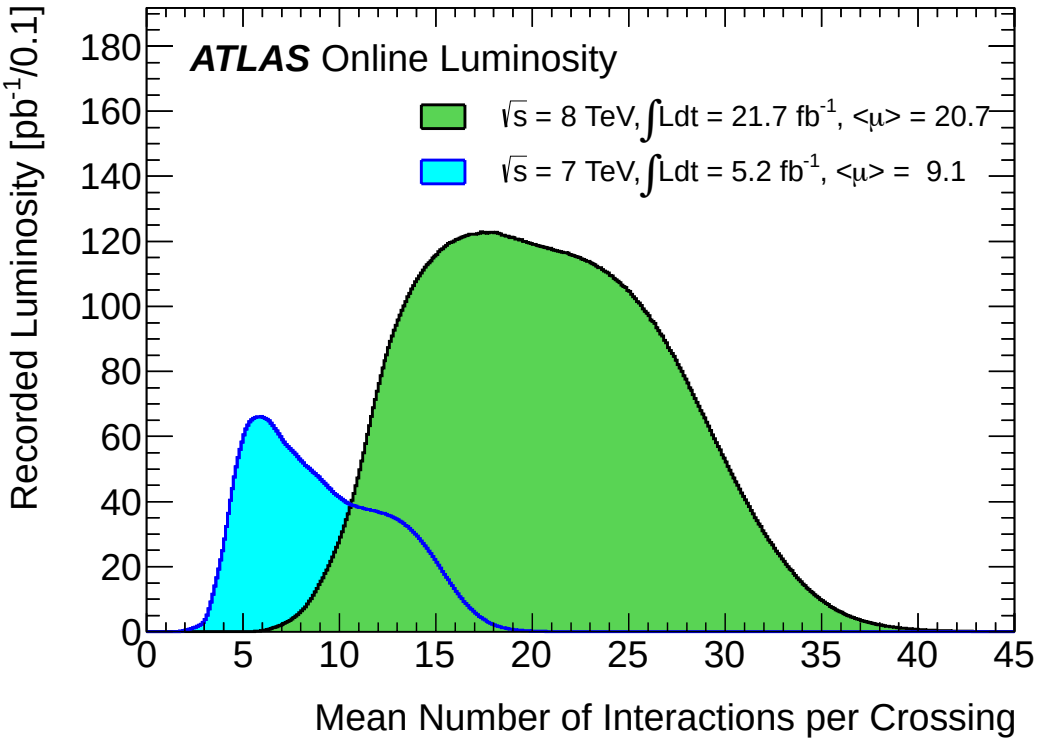

Figure 2.18: luminosity-weighted distribution of the mean number of interactions per crossing for the 2011 and 2012 data. This shows the full 2011 and 2012 pp runs. The integrated luminosities and the $< \mu >$ values are given in the figure. The mean number of interactions per crossing ($< \mu >$) corresponds the mean of the poisson distribution on the number of interactions per crossing calculated for each bunch [122].

CHAPTER 3

Object Reconstruction and Particle Identification

The raw data collected by the ATLAS detector consists of information that can not be directly used in the physics analysis, such as hit information from the tracker and energy information in each cell of calorimeter. Therefore, a construction process is required to rebuild the physics objects, mostly leptons and jets, from the raw data . The reconstruction procedure at ATLAS is a set of dedicated algorithm that converts raw information into readable physics information. During reconstruction, the raw information are first used to build high level objects, such as tracks, vertices, and clusters. These objects are then used to reconstruct and identify physics objects, such as electrons, muons, and jets. In the end, physical properties like four momentum, shower shape, and track quality are calculated and added to the reconstructed physics objects.

The reconstruction chain at ATLAS is implemented in a software framework denoted as ATHENA [123]. Same reconstruction procedure is applied to both data events and Monte Carlo simulated events. During reconstruction, the imperfection of

the simulation may lead to discrepancies in both reconstruction and identification between data and MC. Therefore, further studies are performed to make corrections on the simulation. This chapter provides a summary for reconstruction and identification algorithms used in this analysis. Section 3.1 and 3.2 discuss track and vertex reconstruction in inner detector, section 3.3 discusses cluster reconstruction in calorimeter. Based on these three sections, electron reconstruction process is provided in section 3.4, and muon reconstruction is summarized in section 3.5. Section 3.6 covers jet reconstruction, as well as identification of b-jet. In the end, the reconstruction of missing energy is provided in 3.7.

3.1 Track Reconstruction

Tracks are one of the most important basic objects used in particle reconstruction and identification. In the ATLAS experiment, two tracker systems are built: the Inner Detector and Muon Spectrometer. The Muon Spectrometer are mainly used to reconstruct tracks from muons, which is discussed in detail in section 3.5. This section focuses on the tracks in the Inner Detector, which are then in the reconstruction of electron and jet.

Before reconstruction of tracks, the hit information must be translated into three dimensional space points. For the pixel detector, the hit information directly gives a space point, while the SCT uses a pair of hits to create a space point. In TRT, the timing information is used to create a drift circle centering at the wire. With these space points from the sub-detectors, two algorithms are used to build tracks: inside-out algorithm and outside-in algorithm. The inside-out algorithm is the baseline algorithm for tracks with $p_T > 400$ MeV, which initializes a track candidate with at least two hits from the pixel detectors, and searches for hits

in the remaining layers of the inner detector from inside to outside. With the known magnetic field and material geometry in the inner detector, the position of the hits in next layer can be predicted. The outside-in algorithm is designed for tracks which has less than two hits in the pixel detector, such as the tracks of electrons generated from photon conversions. In the outside-in algorithm, the track candidates are initialized with the TRT, and extrapolated towards the interaction points from outside to inside. More detailed discussion about this two method can be found in [124].

In both algorithms, once a hit is found in the predicted region, the neighboring hit in next layer of detector is being searched for. If no hit is found, a *hole* is marked in the corresponding layer and the search is performed in next layer. If a hit point is used in the reconstruction for more than one tracks, the ambiguity is removed by introducing the track score, which indicates the probability that the track candidate comes from a real trajectory, as well as the quality of the track. Track score favors the track where each hit is associated with the track, and has less holes on it. The shared hit point is then assigned to the track with the highest score.

In the end, both outside-in and inside-out algorithm are used to refit the track with associated space points. Several important properties of the track can be derived from the refit, such as transverse impact parameter (d_0) and longitudinal impact parameter (z_0), which are essentially important in identifying the b-jets by determining whether the track comes from the primary vertices or secondary vertices. Besides the impact parameters, other track properties are also useful for object reconstruction. For example, a minimum number of hits in the silicon detector is required to reject bad reconstructed jets, and the ratio of TRT hits passing the high threshold is used to distinguish electrons from hadrons.

3.2 Vertex Reconstruction

Vertices reconstructed in inner detector indicate the space points where proton-proton collisions or particle decays take place. The vertices are reconstructed with an iterative method named adaptive vertex finding [125]. In this method, tracks with p_T larger than 400 MeV (150 MeV) is selected in 8 TeV (7 TeV) data, and the vertex candidate is defined as (x_0, y_0, z_v), where x_0 and y_0 indicates the original point in transverse plane, and z_v is the mean value of the z_0 distribution of the selected tracks. All tracks in the event are then fitted to this vertex candidate as if they stem from this candidate, incompatible tracks are removed from the vertex iteratively until all tracks associated with this candidate are within 7σ of the z_0 value. This procedure is repeated for the tracks left, until all tracks are associated with a vertex. Vertices with less than two associated tracks are then removed from the reconstruction. Due to the in-time pile-up, the number of reconstructed vertices is usually larger than 1. The *primary vertex* of a event is defined as vertex with the largest $\sum p_T^2$, where $\sum p_T^2$ means the sum of squared transverse momentum of tracks associated to the vertex. All other vertices besides the primary vertex are pile-up vertices. More detail of vertex reconstruction are provided in [125] [126].

3.3 Cluster Reconstruction

Besides tracks and vertices, clusters are also important in particle reconstruction and identification. In calorimeter, an incoming particle initializes a particle shower and deposit energy in many different cells, and the clusters are designed to group the cells back into one object and sum the energy together. The summed energy is then calibrated and corrected to account for the energy loss outside the cluster and

in dead material. In ATLAS, two clustering algorithms are used: sliding-window algorithm and topological algorithm [127].

The sliding-window algorithm groups calorimeter cells in a fixed size rectangular window, whose position is adjusted to find a local maximum energy deposit. The output clusters are mostly used for electron reconstruction and photon reconstruction. Due to the fixed size of the sliding window, a precise energy calibration is allowed.

The sliding-window algorithm consists of three steps. In the first step, the calorimeter is divided into grids of elements with size of $\Delta\eta \times \Delta\phi = 0.025 \times 0.025$, denoted as tower. The next step is to look for the seed of a cluster. In this step, a window with fixed size of 3×5 towers is moved across the calorimeter to find the local maximum window that is above a certain threshold [128][129], and the position of the seed is searched inside this window according to the energies in each cell. The final step is to fill the cluster with cells, where cells are assigned to clusters by taking all cells within a rectangle centered on a layer-dependent seed position. For electrons, the size of the cluster is 3×7 in the barrel and 5×5 in the endcap. In the barrel region, since the electron trajectory is curved by the magnetic field in ϕ direction, the size of cluster is lager in ϕ direction to contain most of the energy. In the endcap region, since the effect of the magnetic field is weaker, the shape of the cluster is defined as square.

Topological algorithm groups cells where the energy deposited is significant comparing to the noise. This algorithm can efficiently suppress the noise by setting the threshold as a function of calorimeter noise. The output of the topological algorithm is named as Topo Clusters, which are used in jet reconstruction and missing energy reconstruction.

The topological algorithm consists of two steps: cluster maker and cluster splitter. In cluster maker, the algorithm first calculate signal to noise ratio (s/n ratio) for all cells. If s/n ratio of a cell is higher than the predefined seed threshold T_{seed}, it is added to the seed list. The cells in the seed list are then ordered in descending order of s/n ratio. Starting from the cell with highest s/n ratio, topological algorithm associates the adjacent cells to the seed cells as neighbors. If an adjacent cell's s/n ratio is larger than the neighbor threshold $T_{neighbor}$, it is counted as a neighbor cell of the seed. Once all seeds have been processed, the neighbors are considered as a new seed list. This neighbor finding procedure is repeated until no neighbors can be found. After the iterative neighbor finding procedure, the seed cells and their neighbors are then converted into clusters. However, the output cluster from cluster maker is usually very large, especially in the endcap region and the forward region. The cluster splitter is designed to identify and separate individual particles in one cluster. The splitter algorithm searches for the local maximum cells with energy > 500 MeV, exceeding energy than all neighbors, and having at least four neighbors inside the parent cluster. These local maximum cells are taken as the seed of new isolated clusters, which grows again iteratively as described above. In splitter procedure, the shared cells are assigned to one of the adjacent clusters based on the energy of the clusters, as well as the distance between the cells and cluster centers.

3.4 Electron Reconstruction and Identification

Electrons are long lived charged particles that leave tracks in the inner detector, and deposit energy in the electromagnetic calorimeter. Since electron's momentum and energy can be precisely measured by the inner detector and calorimeter, it

plays an important role for many physics processes generated at ATLAS. Since this analysis only uses electrons with $|\eta| < 2.47$, the electron reconstruction in forward region is not discussed.

3.4.1 Electron Reconstruction

Electron reconstruction is based on tracks from inner detector, and clusters built by sliding-window algorithm from electromagnetic (EM) calorimeter. An electron candidate in ATLAS can be described as a cluster in EM calorimeter in association with a inner detector track pointing at it. Clusters for electrons are required to have at least 3 GeV of deposited transverse energy, with a size of 3×7 towers in the barrel region and 5×5 towers in the endcap region. The associated tracks are required to have transverse momentum $p_T > 0.5$ GeV, which are then extrapolated from the last measured point to the middle layer of the electromagnetic calorimeter. The η and ϕ of the extrapolated impact points are used to compare with the η and ϕ values of the center of the cluster. The track is considered to be associated with the track if the distance between the impact point and cluster center fulfill the requirement of $|\Delta\eta| < 0.05$ and $|\Delta\phi| < 0.1$. The higher threshold for $|\Delta\phi|$ is to account for the bremsstrahlung effect in bending direction. If there are more than one track associated with a cluster, the track with more hit points in silicon detector and smaller $\Delta R = \sqrt{\Delta\eta^2 + \Delta\phi^2}$ is favored. If there is no track associated with the cluster, the cluster is considered as an unconverted photon. A converted photon can be distinguished by the presence of a pair of close-by tracks from a secondary vertex. More detailed discussion of electron reconstruction can be found in [128][129].

Energy Scale

The energy of electron is measured from the electromagnetic calorimeter. Corrections are applied to account for the energy deposited out of the cluster region, as well as the energy loss in front and beyond the electromagnetic calorimeter [130] [131]. The energy measured is calibrated to the electromagnetic (EM) scale, using test beam measurement. During the calibration, a fit to the di-electron invariant mass of $Z \to ee$ and $J/\Psi \to ee$ process is performed, which can significantly reduce the uncertainty of the energy scale. The corresponding calibration constants are derived as a function of η. Another physics process of $W \to e\nu$ is also used to compare the cluster energy measured in calorimeter and track momentum measured in inner detector. Uncertainties of the energy scale mainly come from mis-modeling of the material budget, as well as the fit procedures in the data driven method. The uncertainties for electrons with transverse energy $E_T > 20$ GeV are less than 1% in barrel region, and about 1% in the endcap region [129].

Energy Resolution

The relative energy resolution consist of three terms: sampling term, noise term, and a constant term. The sampling term can be written as (9-10)%/$\sqrt{E/\text{GeV}}$, mainly contributes to electrons with low transverse energy. This resolution is expected to be worse at larger $|\eta|$ region because of the large amount of material in that region. The noise term is (350 $\times$ cosh (η)) / (E/MeV) for 3 $\times$ 7 clusters. For electrons with high transverse momentum, the energy resolution decreases asymptotically to the constant term 0.7% [130].

3.4.2 Electron Identification

During the electron reconstruction, a variety of background processes may also be reconstructed as electrons, such as jets and converted photons. In order to select pure electrons, an identification procedure must be implemented to reject the background processes while keeping real electrons. This identification procedure makes use of many variables from both clusters and tracks, as well as the angular distance between them.

For 8 TeV data, a set of quality cuts are used to define different identification criteria with increasing electron purities: loose, medium, and tight, which have been particularly tuned to account for the large pile-up caused by high luminosity. The identification criteria are summarized below:

- **Loose**: Selection criteria for loose electron is based on the hadronic leakage and shower shape in the middle layer of electromagnetic calorimeter, which have highest selection efficiency and lowest background rejection rate.
- **Medium** : Medium electrons are selected on top of loose electrons, employing additional information from the first layer of electromagnetic calorimeter to reject photons from pion decays. Medium electrons also require additional track quality cuts and tighter match between clusters and tracks.
- **Tight** : In additional to the cuts in medium criteria, tighter electron identification requires a large fraction of high threshold hits in TRT to reject charged pions, as well as hits on inner layer of the pixel detector to further reject photons. In the end, tighter electron requires a much tighter match between clusters and tracks, compared to the medium electron.

Fig 3.1 shows the efficiencies and corresponding uncertainties for different criteria

as functions of transverse energy. More detailed information can be found in [132].

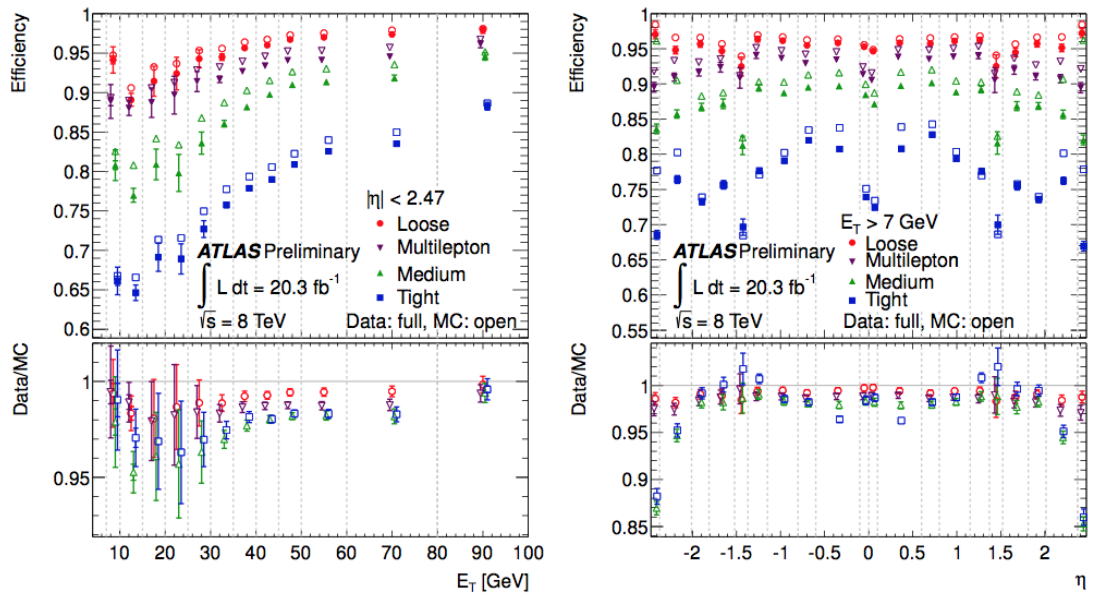

Figure 3.1: Identification efficiency in data as a function of E_T (left), η (right), compared to MC expectation for electrons from $Z \to ee$ decay. The lower panel shows the data-to-MC efficiency ratios. The data efficiency is derived from the measured data-to-MC efficiency ratios and the MC prediction for electrons from $Z \to ee$ decays. The uncertainties are statistical (inner error bars) and statistical+systematic (outer error bars). The dashed lines indicate the bins in which the efficiencies are calculated. [132]

For 7 TeV data, similar identification criteria are applied for electrons. Fig 3.2 shows the efficiency and corresponding uncertainties for different criteria as functions of transverse energy. Detailed description of the set of cuts are described in reference [133][134].

3.5 Muon Reconstruction and Identification

In principle, muon is the only particle that interacts with the Muon spectrometer. All other physics objects, such as electrons and jets, are stopped by the calorimeter. Therefore, the structure of ATLAS detector allows easy identification for muons.

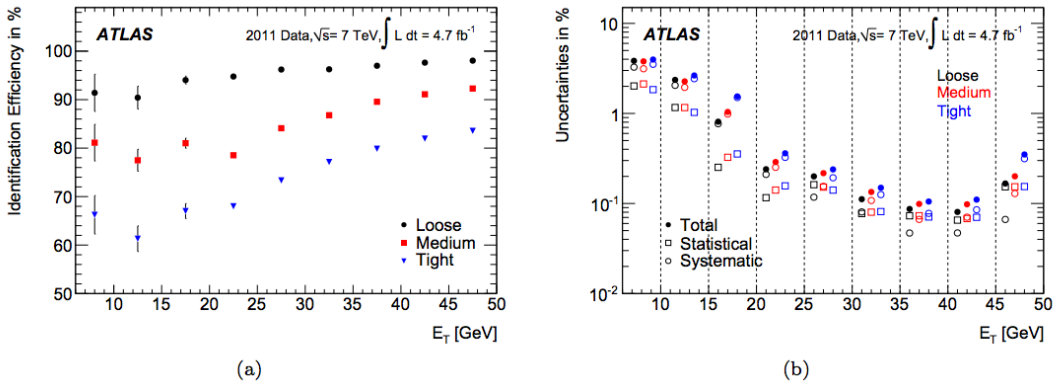

Figure 3.2: (a) Dependence of the combined identification efficiencies on the transverse energy of the probe for central electrons at $\sqrt{s} = 7$ TeV. Error bars correspond to the total uncertainties. (b) Decomposition of the total uncertainty into its statistical and systematic components. The three colors correspond to the three identification criteria (loose++, medium++, tight++) [133].

The curvature of muon tracks can also be precisely measured because of the long trajectory of muon in ATLAS detector, which leads to a precise measurement of muon momentum. Due to the low misidentifying rate of muons and the precise measurement of momentum, muons are considered as one of the most important final state objects in physics analysis.

Muons are reconstructed with four different algorithms [135] [136] [137]:

- **Stand Alone Muon :** For muons with $|\eta|$ <2.7, the muon spectrometer is capable of providing this independent reconstruction algorithm. The tracks reconstructed from the muon spectrometer are extrapolated to the interaction point to determine the track parameters, such as d_0 and z_0. In this algorithm, the minimal energy loss inside the calorimeter is taken into account.

- **Calorimeter Tagged Muon :** For muons with $|\eta| < 2.5$, the inner detector can provide an independent measurement for the tracks. If the track of muon candidate can match to a specific energy deposit in the calorimeters, a

Calorimeter Tagged Muon is reconstructed.

- **Segment Tagged Muon :** If the track of muon candidate mentioned above can match to a track segment in the muon spectrometer instead of a cluster, it can be reconstructed as a Segment Tagged Muon.

- **Combined Muon:** Combined Muons are built by combining tracks from muon spectrometer and tracks from the inner detector. This type of muon has the highest rejection power for fake muons, and the best momentum resolution.

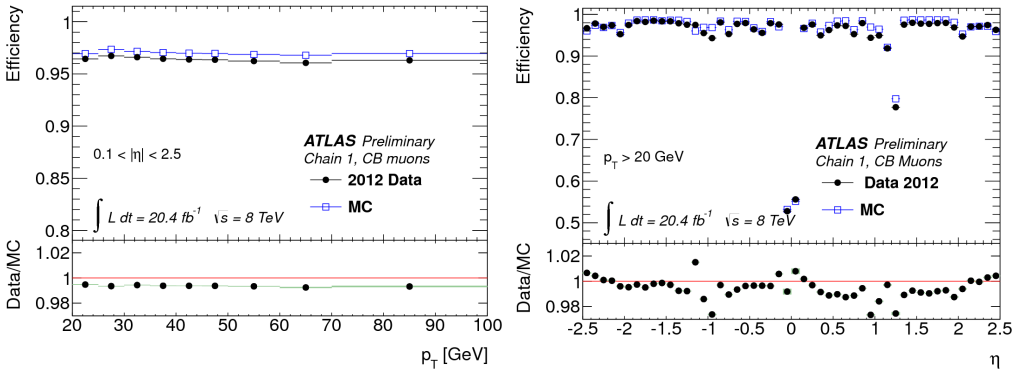

Figure 3.3: Muon reconstruction efficiency as a function of transverse momentum (Left) and the pesudo-rapidity (Right) from $Z \to \mu\mu$ tag-and-probe measurement. The ratio between data and MC shows a good agreement over the full p_T range and η range. [137]

Due to the high reconstruction efficiency and good identification efficiency, Combined Muons are used as final state muons in this analysis. Fig 3.3 shows the Combined muon reconstruction efficiency as functions of p_T and η. The significant drop at $|\eta|$ <0.1 is due to the service structures and the support structures, which make the muon spectrometer only partially available in that region. At 1.1< $|\eta|$ <1.3, the efficiency drops because some muon chamber were not installed in the time for data taking in 2012.

Momentum scale and resolution

Similar to electrons, muon momentum scale and resolution are studied using $Z \to \mu\mu$ processes. The momentum resolution ranges from 1.7% at central rapidity and for transverse momentum $p_T \simeq 10$GeV, to 4% at large rapidity and $p_T \simeq 100$ GeV. The momentum scale is known with an uncertainty of 0.05% to 0.2% depending on η [135].

3.6 Jet Reconstruction and Identification

Jet is a narrow cone of particles originating from the hadronization of a quark or a gluon, thus can be used as the experimental signature of a quark with high transverse energy. Jet plays an essential role in the analysis presented in this dissertation, where Higgs particle decays to a pair of bottom quarks, and the quarks hadronize to two b-jets.

3.6.1 Jet Reconstruction

In the analysis presented in this dissertation, the jets are reconstructed with anti-k_T algorithm [138], which takes Topo clusters as input, and merge them into jets basing on a distance variable $d_{i,j}$, defined as below:

$$d_{i,j} = min(p_{T,i}^{-2}, p_{T,j}^{-2}) \frac{\Delta R_{i,j}^2}{R^2} \tag{3.1}$$

In the equation above, the $d_{i,j}$ is the distance defined between two selected clusters,

$p_{T,i}$ and $p_{T,j}$ are the transverse momentums of clusters, $\Delta R_{i,j} = \sqrt{\Delta\phi^2 + \Delta\eta^2}$ is the angular distance between two clusters, and R is a constant number 0.4. Therefore, this algorithm is also specified as anti-k_T4. In jet reconstruction, the Topo clusters described in section 3.3 are ordered descendingly by p_T. The algorithm then iterates over clusters starting from the one with highest p_T, i, and try to merge it with the rest of the clusters, j. As long as $d_{i,j}$ is smaller than the $d_{Thres,i} = p_{T,i}^{-2}$, the cluster with smallest $d_{i,j}$ is merged into the cluster i. Once a new cluster is merged into cluster i, the two original clusters are replaced by the combined new cluster. The reconstruction of a jet is completed once there is no remaining cluster j to merge into it. The algorithm is then repeated for the remaining cluster with the highest p_T.

Anti-k_T algorithm has two main advantages. First, it is insensitive to the soft radiation processes, thus not allowing the jet properties, such as shower shape and jet energy, to be influenced by the low energy clusters. Second, it is insensitive to the collinear emission, which allows the reconstruction of one single jets instead of two even if the energy of the leading particle is changed after radiation [138].

Energy Scale and Resolution

The Topo clusters used to reconstruct jets are initially calibrated to the EM scale, which correctly measures the energy deposited in calorimeter through electromagnetic processes. However, Topo cluster also contains hadronic parts, which have different responses in the calorimeter. Therefore, the clusters are further calibrated to EM+JES scale to provide correct energy measurement [139], with an additional correction applied to account for the pileup influence in high instantaneous luminosity in 2012 [140, 141]. To further improve the energy calibration of jets, a Global Sequential (GS) calibration is applied based on the comparison between

the energy of reconstructed jets and truth jets in generator level [142].

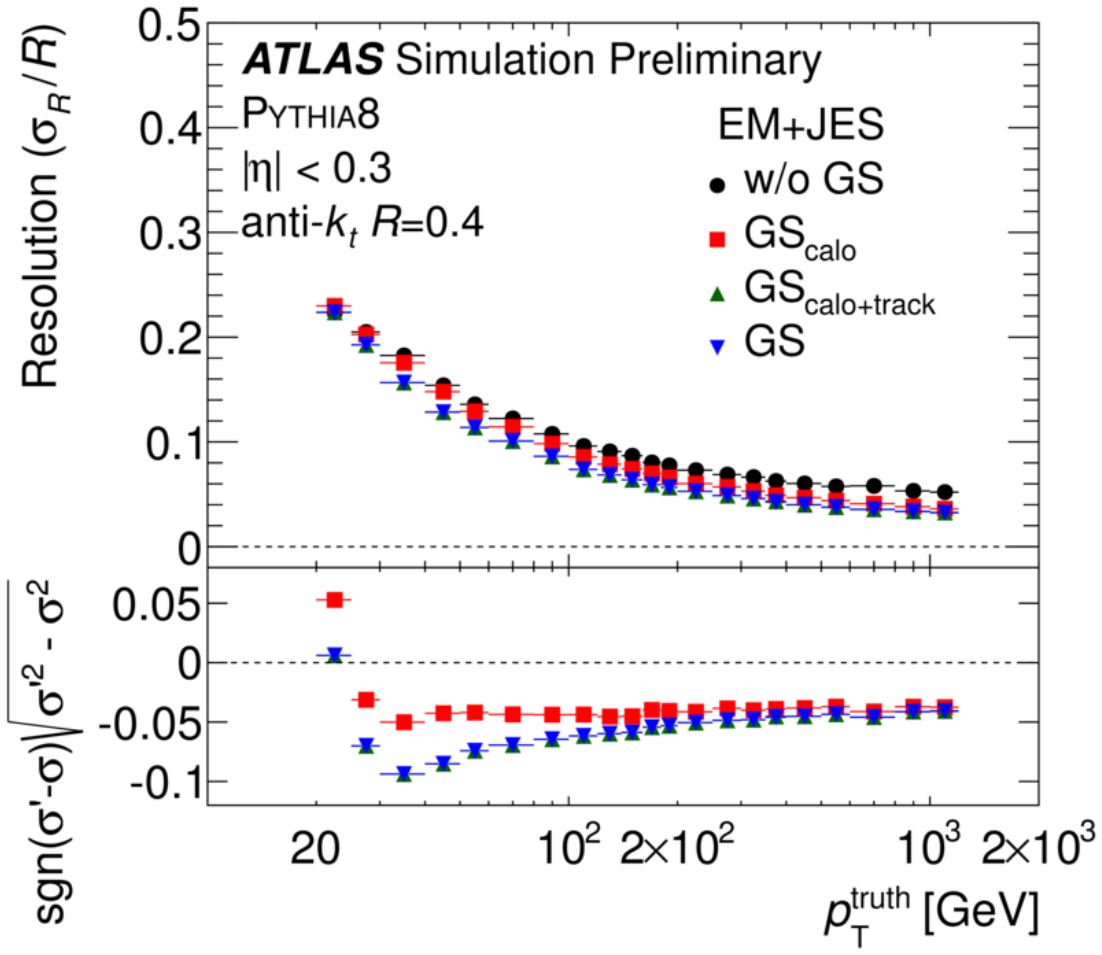

Figure 3.4: Jet transverse momentum resolution as a function of p_T^{truth} in the nominal PYTHIA8 Monte Carlo sample for $|\eta|$ <0.3. All jets are reconstructed with the anti-k_T algorithm with R=0.4 with and without GS Calibration.

3.6.2 B-jet Identification

A b-jet is a jet produced by the hadronization of a bottom quark or an anti-bottom quark. The analysis presented in this dissertation searches for Higgs decays to two b-jets. Due to the overwhelming multi-jet background in proton proton collision, an identification criteria with high efficiency for b-jet, as well as high rejection for non b-jets is essential for the success for this analysis. This identification criteria is also denoted as b-tagging.

Once a bottom quark is produced in the Higgs decay, it surrounds itself immediately with anti-quarks to form a b-hadron because of the color confinement. The life time of a b-hadron is $\simeq 1.5$ ps, which is relatively long compare to the top quarks. Convert the life time into distance, we have

$$d = \beta \times c \times \gamma \times \tau \tag{3.2}$$

For a b-hadron with 50 GeV energy, the decay length is about 5 mm, which means that the b-hadron travels $\simeq 5$ mm distance away from the interaction point before its decay. For the experimental perspective, a b-jet could be identified by reconstructing the tracks, whose impact parameters should be at mm level. If these tracks originating from b-hadron are used to reconstruct a vertex, it will be several mm away from the primary vertex, denoted as a secondary vertex.

As described above, the long life time of b-hadron is the most important characteristic for identification. Beside that, the mass of b-hadron is typically larger than others, which gives a greater angular spread to the resulting jet. These two features are exploited through various b-tagging algorithms [143] [144], as summarized

below:

- **IP3D**: IP3D algorithm is based on the significances of impact parameters of the tracks inside the jets. Since the tracks originate from a displaced secondary vertex, the impact parameters are expected to be large. This algorithm only uses information from a track, and Likelihood ratio technique is used to distinguish b-jets from other jets. Expected distributions from light quark and bottom quark are used to build b-jet hypothesis and light-jet (non-b-jet) hypothesis.

- **SV1** : SV1 algorithm is based on the significance of mass of b-hadron. This algorithm actually reconstructs the secondary vertex, and derives discriminating variable from it, such as invariant mass of tracks from this vertex, and fraction of momentum of the tracks originating from the secondary vertex with respect to all tracks inside the jet.

- **JetFitter** : In the JetFitter algorithm, a tertiary vertex where c-hadron (hadron that contains a c quark) decay to a s-hadron (hadron that contains a strange quark) is being searched. Since c-hadron and s-hadron all originate from the b-hadron, we can assume that the tertiary vertex and secondary vertex lies on the same path of flight. The discriminant is built on the fit of the flight path which goes through the primary vertex, secondary vertex, and the tertiary vertex.

The b-tagging algorithm used in this dissertation is MV1 [145, 146, 147], which combines the result of IP3D, SV1, and JetFitter, with an additional variation specially designed to increase the rejection for c-jets. The working point selected for this analysis have a b-tagging efficiency of 70% for b-jets, with rejection factor of 5 for c-jets, and 150 for light jets.

The performance of b-tagging algorithms, such as b-tagging efficiency and light jet rejections, has been measurement in several analysis. The b-tagging efficiency for example, can be measured in di-leptonic decay of $t\bar{t}$ events [148]. Fig 3.5 shows a comparison of measured b-tagging efficiencies in $t\bar{t}$ events for both data and MC samples. The ratio between the efficiencies are used as scale factors to account for the efficiency corrections in simulated events. The systematic uncertainties of b-tagging algorithm arises from the different hadronization models, PDFs and experimental uncertainties. The uncertainties of scale factor ranges from 6% at low p_T to about 2% at $p_T \simeq 140$ GeV. The uncertainties for rejection rate is measured from inclusive set of jets, with much larger uncertainties from 15% to 25% depending on p_T and η [149].

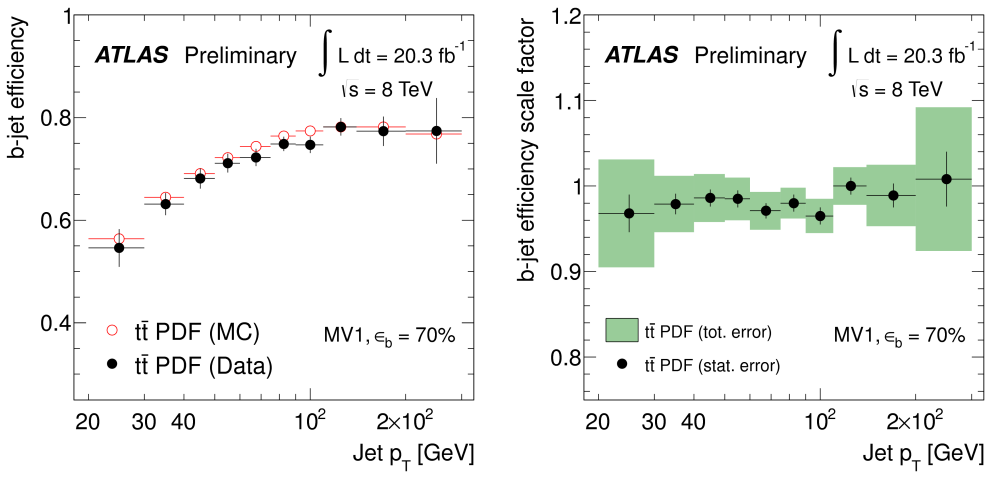

Figure 3.5: The measured b-tagging efficiency in di-leptonic decay of $t\bar{t}$ events as a function of p_T in both data and MC samples (Left), and the corresponding scale factors for work point with 70% efficiency for b-jets (Right). On the Left plot, the error bars on the data points represent the total statistical and systematic uncertainties. One the right plot, The statistical only (black lines) and total errors (green shaded region) are shown [148][149].

3.7 Missing Transverse Energy Reconstruction

Neutrinos provide important signatures for many interesting physics processes, such as the leptonic decay of W boson. Unfortunately, the neutrino can not be directly measured by the ATLAS detector since it interacts weakly with the detector material. However, an observable denoted as Missing Transverse Energy (also written as MET, or E_T^{miss}) can be used to quantify the transverse momentum vector in the transverse plane. Since the initial transverse momentum of the colliding partons are negligibly small, the total transverse momentum can be assumed to be 0. Using momentum conservation, the E_T^{miss} can be calculated from the following equation:

$$E_T^{miss} = -\sum E_T^e - \sum E_T^\gamma - \sum E_T^\tau - \sum E_T^{jets} - \sum E_T^\mu - \sum E_T^{SoftTerm} \quad (3.3)$$

In Eq 3.3, each term on the right side of the equation is the sum of transverse momentum of corresponding objects. The transverse momentum for each kind of objects are calibrated using corresponding energy scale. For example, electrons are calculated in EM scales, while jets are calculated in EM+JES scale. Since the reconstruction algorithms for physics objects are optimized for energetic particles, particles with low momentum are not included in the calculation, which may have a great impact on reconstruction of missing transverse energy because of their large multiplicity in proton-proton collision. To account for the low momentum particles, $E_T^{SoftTerm}$ is created from the clusters and tracks. Further detail of missing transverse energy reconstruction can be found in Ref [150, 151, 152].

CHAPTER 4

Analysis Overview

In 2012, the ATLAS and CMS experiments at the LHC reported the discovery of a new Higgs like particle with mass around 125 GeV. After that, more precise measurements have strengthened the hypothesis that the new particle is a Higgs boson. In ATLAS, different measurements have been performed in the bosonic decay channel of the new particle, where it decays to a pair of photons, a pair of Z bosons, or W bosons. Since Higgs particle is also predicted to decay to fermions in the Standard Model, it is essential to search for the evidence of Higgs decay to fermions, such as a pair of τ leptons, or a pair of bottom quarks. Evidence of Higgs decay to τ leptons has been found in both ATLAS and CMS in 2014 [12, 13]. This dissertation presents the search for $H \to b\bar{b}$ decay.

Although the predicted branching ratio of $H \to b\bar{b}$ decay in Standard Model is up to 58% at $m_H = 125$ GeV, an inclusive search for $H \to b\bar{b}$ is not feasible. This is due to the overwhelming background from the QCD process in proton proton collision. Instead, the associated production of Higgs boson with a vector boson can be used for the search. In spite of a small cross section, which is more than an order of magnitude smaller compared to the dominant gluon gluon fusion process,

the leptonic decay of the vector boson can be efficiently used for event triggering and background reduction.

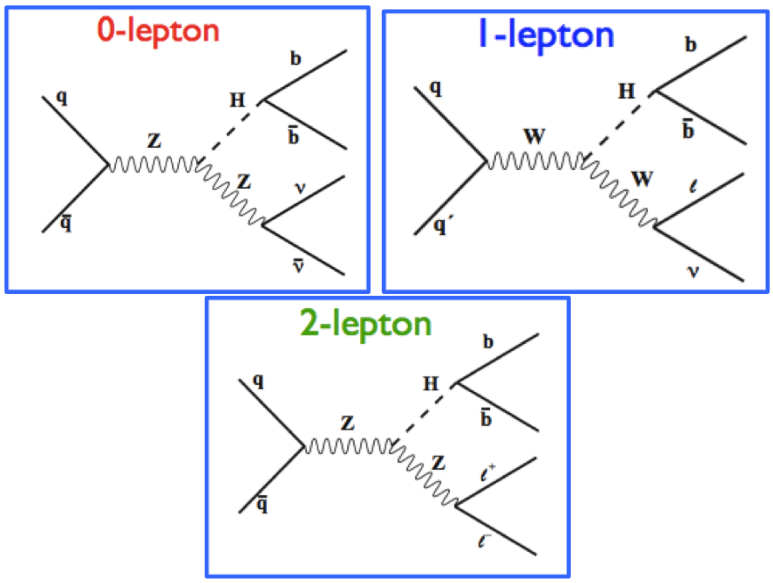

Figure 4.1: Feynman diagrams for different final states of Higgs produced in association with a vector boson (W/Z).

This analysis is performed in three individual channels, named zero lepton channel, one lepton channel, and two lepton channel, targeting different decay modes of the associated vector boson, corresponding Feynman diagrams are shown in Fig. 4.1.

- **Zero Lepton :** The zero lepton channel searches for events with zero charged leptons, targeting at $Z \to \nu\nu$ decay.
- **One Lepton :** The one lepton channel searches for events with one charged lepton(e or μ), targeting at $W \to l\nu$ decay.
- **Two Lepton :** The two lepton channel searches for events with two charged leptons(e^+e^- or $\mu^+\mu^-$), targeting at $Z \to ll$ decay.

In each channel, a b-tagging algorithm is used to identify the b-jets coming from $H \to b\bar{b}$ decay. To further improve the sensitivity, each channel is split into different

regions according to number of jets and the transverse momentum of vector boson with optimized topological and kinematic cuts applied in each region.

To obtain the final result, statistical analysis is performed to combine different categories in all three channels. The mass of two b-jets system is used as the main discriminating variable, and dedicated control regions are used to constrain the contribution from dominant background processes, such as $t\bar{t}$, W+jets, and Z+jets.

To validate the analysis, a measurement of cross section is performed on di-boson $(W/Z)Z$ production. The measurement is performed in same final states and with same event selections, with $H \to b\bar{b}$ replaced by $Z \to b\bar{b}$.

This dissertation includes a full analysis chain in one lepton channel, and the statistical combination of three decay channels. The work shown in this dissertation was published in July 2013 [153][154].

CHAPTER 5

Data Samples and Simulated Samples

This chapter describes the data samples used in this analysis, as well as the Monte Carlo simulated samples used for both signal and background processes. The Monte Carlo events are first generated at the same mass-of-center energy as the data, and then passed through a simulation procedure based on GEANT4 [155]. During simulation, most of the CPU time is used in calorimeter simulation because of the complicated geometry of calorimeter. In order to reduce the time spent in simulation, ATLFASTII (AFII) [156] is used instead of the full simulation for some of the MC samples. AFII uses a simplified model of the calorimeter, which can produce more than ten times of events with same CPU time, while still maintaining good performance. In the end, both data and MC are reconstructed by the same reconstruction algorithms.

In this chapter, section 5.1 discusses the set of data samples used in this analysis, while section 5.2 summaries the set of MC samples used.

5.1 Data Samples

The data samples used in this dissertation are collected by the ATLAS detector during the LHC Run 1 data taking in 2011 and 2012. The dataset collected in 2011 is produced with center-of-mass energy of $\sqrt{s} = 7$ TeV, while the dataset collected in 2012 is produced with $\sqrt{s} = 8$ TeV. For each dataset, events are selected according to a 'GoodRunList (GRL)' file, which ensures the data events were collected when the corresponding detectors were fully functional. The GRL files used in this analysis are listed below:

- **2011 :** data11_7TeV.periodAllYear.DetStatus-v36-pro10-02_CoolRunQuery-00-04-08_All_Good.xml
- **2012 :** data12_8TeV.periodAllYear.DetStatus-v61-pro14-02_DQDefects-00-01-00_PHYS_StandardGRL_All_Good.xml

The total integrated luminosity corresponding to the GRL is 4.7 fb^{-1} at $\sqrt{s} = 7$ TeV, and 20.3 fb^{-1} at $\sqrt{s} = 8$ TeV.

5.2 Simulated Samples

The simulated samples contain signal samples and background samples. Both signal and background samples are required to precisely describe the corresponding physics processes, while the background samples require much larger statistics, comparing to signal samples, to account for the much larger background cross sections.

5.2.1 Signal Samples

In signal samples, the events are generated with PYTHIA generator for both 7 TeV and 8 TeV, which are interfaced to PHOTOS [157] and TAUOLA [158] to account for the QCD final state radiation and the simulation of the τ decay. In VH decay, the associated vector boson decays to different flavors of leptons: e, μ, τ, and their corresponding neutrinos. In the one lepton analysis, only final states with electrons and muons are studied. The decay of vector boson to τ is also simulated to account for the small fraction of signal events where $\tau \to \nu_\tau + e + \bar{\nu_e}$, or $\tau \to \nu_\tau + \mu + \bar{\nu_\mu}$.

The signal samples are generated within Higgs mass range of 100 GeV $< m_H <$ 150 GeV, with an interval of 5 GeV. The cross sections for generated signal samples, as well as the corresponding uncertainties, are taken from Ref. [159], while the branching ratio of leptonic decay are taken from the Particle Data Group [160].

5.2.2 Background Samples

As mentioned in previous sections, large statistics is required for the background processes due to their large cross sections. In order to reduce the MC statistical uncertainty to be less than 5%, hundreds of millions simulated events are needed. To achieve this goal, the following attempts have been made:

- Collaborate with other working groups to produce common samples which can be shared between different groups.
- Use AFII simulation instead of full ATLAS simulation to reduce the CPU usage.
- Implement a number of filters on the final state objects to reduce the number of events simulated.

Process	Generator	$\sigma \times BR$	N_{events}
WH	PYTHIA 8.160		300K per mass
ZH	PYTHIA 8.160		300K per mass
$W \to \ell\nu$	SHERPA 1.4.1	10.97 nb	168M
$Z/\gamma* \to \ell\ell$	SHERPA 1.4.1		42M
$m_{\ell\ell} > 40$ GeV		1.24 nb	
$Z/\gamma* \to \nu\nu$	SHERPA 1.4.1		77M
$m_{\nu\nu} > 5$ GeV		6.71 nb	
WW	HERWIG 6.510	55.43 pb	10M
WZ	HERWIG 6.510		20M
$66 < m_{\ell\ell} < 116$ GeV		22.69 pb	
ZZ	HERWIG 6.510		7.5M
$66 < m_{\ell\ell} < 116$ GeV		7.697 pb	
Top-quark			
$t\bar{t}$	POWHEG	238.06 pb	75M
$t-$channel	ACER	87.76 pb	9M
$s-$channel	POWHEG	5.61 pb	6M
$Wt-$channel	POWHEG	22.37 pb	20M

Table 5.1: Monte Carlo generators used for modeling signal and background processes and the cross sections times branching ratio (BR) used to normalize the different processes at $\sqrt{s} = 8$ TeV. Branching ratios correspond to the decays shown.

VH analysis is a background dependent analysis. The signature of the signal is two b-tagged jets with high p_T plus the decay products of W/Z boson. The possible background processes for this analysis are: single top production, $t\bar{t}$ production, di-boson production, and W/Z + jets production. Table 5.1 and 5.2 summarizes the generators used for different background samples, the number of events produced for each sample, as well as the corresponding inclusive cross sections for these main background processes.

Process	Generator	$\sigma \times BR$
WH	PYTHIA 8.160	
ZH	PYTHIA 8.160	
$W \to \ell\nu$	SHERPA 1.4.1	10.46 nb
$Z/\gamma* \to \ell\ell$	SHERPA 1.4.1	
$m_{\ell\ell} > 40$ GeV		1.07nb
WW		
$WW \to \ell\nu qq$	HERWIG 6.510	46.23pb
WZ	HERWIG 6.510 , PYTHIA 6.001	
$66 < m_{\ell\ell} < 116$ GeV		18.0 pb
ZZ	HERWIG 6.510, PYTHIA 6.001	
$66 < m_{\ell\ell} < 116$ GeV		5.96 pb
Top-quark		
$t\bar{t}$	POWHEG	166.8 pb
$t-$channel	ACER	64.57 pb
$s-$channel	POWHEG	4.63 pb
$Wt-$channel	POWHEG	15.74 pb

Table 5.2: Monte Carlo generators used for modeling signal and background processes and the cross sections times branching ratio (BR) used to normalize the different processes at $\sqrt{s} = 7$ TeV. If there are two generators given, the second one is used to estimate systematic uncertainties.

CHAPTER 6

Object and Event Selection

This chapter describes the selection of physics objects in this analysis, as well as the strategy of event selection. The goal of VH analysis is to search for the Higgs boson produced in association with a vector boson. This chapter focuses on the objection selection and event selection in the one lepton channel, where the Higgs boson is produced in association with a W boson, and $W \to \ell + \bar{\nu_l}$. In the final state, the presence of a lepton and a neutrino is required for W decay, and 2 b-jets are required to account for the decay of Higgs boson.

In this chapter, section 6.1 provides the selections of physics objects, such as leptons and jets, while section 6.2 discusses the event selection imposed using the selected objects to distinguish signal events from background events.

6.1 Object Selection

The final physics objects used in one lepton channel include electrons, muons, jets, and missing transverse momentum. This section discusses the selection criteria for

each of them.

6.1.1 Lepton Selection

Based on the identification categories discussed in Chapter 3, three different lepton types are defined with increasing order of purity:

- **Loose :** Loose electrons used in this analysis are selected with kinematic cuts $E_T > 10$ GeV and $|\eta| < 2.47$, and required to pass the ATLAS LoosePP quality requirement [134].

  The selection of loose muons is a bit complicated comparing to electrons. In ATLAS, four types of muons are reconstructed, as mentioned in chapter 3. In general, only Combined Muons are used in this analysis. However, other muon types are also used in specific η regions to extend the acceptance. For example, Calo Tagged Muons are used in $|\eta| < 0.1$, where the supporting structure limited the acceptance of muon spectrometer, while Standalone Muons are used in $2.5 < |\eta| < 2.7$, where inner detector information is not available. Loose muons are selected with kinematic cuts $E_T > 10$ GeV and $|\eta| < 2.7$, and required to pass the Tight MuID criteria, as well as the MCP hit requirements in the Inner Detector, which are summarized below:

  - At least one hit on the b-layer of the pixel detector, if the track crosses an active layer.
  - At least one hit in the pixel detector.
  - At least four hits in the SCT detector.
  - At most two holes across the pixel or SCT detectors.
  - At least 6 TRT hits in region $0.1 < |\eta| < 1.9$, and the ratio of TRT outliers to hits must be less than 0.5.

Loose leptons are also required to pass the track isolation cuts and track quality cuts. The track isolation cut requires the sum of transverse momentum of tracks within a cone of $\Delta R < 0.2$ around the lepton (excluding the momentum corresponding to the lepton itself) to be less than 10% of the lepton momentum. The track impact parameter cuts are different for electrons and muons, loose electrons are required to have $d_0 < 0.1$ mm, while loose muons are required to have $z_0 < 10$ mm.

Medium : Medium leptons are selected from loose leptons with higher E_T cut of 25 GeV, while medium electrons are further required to pass the MediumPP requirement [134].

Tight : Tight leptons must satisfy the selection criteria for both loose and medium leptons, while tight electrons are further required to pass the TightPP requirement. In order to suppress the background processes, additional isolation cuts are applied to tight leptons. In calorimeter, the deposited energy around leptons in a cone of radius of $\Delta R < 0.3$ is required to be less than 7% (9% in 2011) of the lepton momentum. In the inner detector, the sum of transverse momentum of tracks within a cone of $\Delta R < 0.2$ around the lepton is required to be less than 4% (5% in 2011) of the lepton momentum.

6.1.2 Jet Selection

As described in chapter 3, jets used in this analysis are reconstructed using the anti-k_t algorithm with a radius parameter R = 0.4. In order to distinguish signal events and background events, two types of jets are defined:

- **Signal Jets :** Signal jets are defined to account for the jets comes from Higgs decay. The kinematic cuts for signal jets are $|\eta| < 2.5$ and $p_T > 20$

GeV to reduce the contribution from QCD events. To further suppress the background, the leading jet p_T is required to be larger than 45 GeV. In order to reduce the contribution from pile up events, a cut is placed on Jet Vertex Fraction (JVF), which is defined as the ratio of sum of p_T of tracks within the jet that originate from the primary vertex to the sum of p_T of all tracks within the jet. For signal jets, the requirement is $|JVF| > 0.5$ (0.75 for 2011) for jets with $p_T < 50$ GeV and $|\eta| < 2.4$. The cut is not applied to jets with $p_T > 50$ GeV because the jets from pile-up vertices usually have low p_T, and the cut-off at $|\eta| < 2.4$ ensures that the tracks can be fully reconstructed by the inner detector.

- **Veto Jets :** Veto jets are selected to reject the events with additional hadronic activities, such as semileptonic decay of $t\bar{t}$. These jets are defined as jets with $p_T > 30$ GeV, and within η region $2.5 < |\eta| < 4.5$. Events with veto jets are vetoed.

Jets selected in this analysis are labeled with different flavors. A jet is labeled as a b-jet if there is a b hadron within a cone of $|\Delta R| < 0.4$ around the jet axis. Non b-jets are labelled as c-jets if there is a c hadron within the same cone region. Non b/c-jets are labelled as τ jets if there is a τ lepton within the same cone region. All other jets are labelled as light jets.

6.1.3 MET and MPT

The leptonic decay of W boson produces a lepton and a lepton neutrino. To account for the lepton neutrino, large missing transverse energy is required in the final state. In addition, a cut is placed on track-based missing transverse momentum (p_T^{miss} or MPT) to ensure the presence of the neutrino. p_T^{miss} is calculated from the

vector sum of the transverse momenta of the inner detector tracks with $p_T > 0.5$ GeV and $\eta < 2.5$. The tracks are required to satisfy a set of quality cuts:

- $|d_0| < 1.5$
- $|z_0 sin\theta| < 1.5$
- At least 5 SCT hits.
- At least 1 pixel hit.

6.1.4 Overlapping Objects Removal

Physics objects selected in previous sections sometimes overlap with each other, which causes difficulties in object identification between electrons and muons, as well as double counting the energy deposited in the calorimeter as both lepton and jets. Therefore, an overlap removal procedure is developed to remove these ambiguities. The overlap removal criteria is based on the angular distance ΔR between overlapping objects, applied in the following order:

- Remove the signal jet within Δ R < 0.4 of loose electrons with $p_T > 15$ GeV.
- Muons within Δ R < 0.4 of jets is treated as un-isolated muons, and thus removed.
- Remove loose electrons with $p_T < 15$ GeV and Δ R < 0.4 to a jet.
- Remove loose electrons with Δ R < 0.2 to a loose muon.

6.1.5 B-jet Tagging

As described in previous chapters, the MV1 tagging algorithm is used to distinguish b-jets from other flavor of jets, the output of which is a network based discriminant w. A higher w value indicates that the jet is more likely to be a b-jet. In this analysis, a working point with 70% efficiency is selected, the corresponding rejection factor is 5 for c-jets, and 150 for light jets.

Direct Tagging and Truth Tagging

Given the powerful rejection of the b-tagging algorithm, a large majority of events are discarded by the b-tagging algorithm during selection. Therefore, it is almost impossible to have a reliable background template with enough statistics after requiring two b-tagged jets. In order to reduce the statistical uncertainty of these background template, a method known as "truth tagging" is developed. Not like the "direct tagging" method, which simply applies b-tagging selection to the signal jets, the "truth tagging" method does not reject any jet, but parameterizes the c-jet and light jet tagging efficiency as a function of p_T and η. The efficiency map is then used to calculate the probability for a jet to pass the b-tagging selection, which is assigned to the jet as a weight. With this method, a background template with small statistical uncertainty can be built.

The truth tagging method is applied to V+light jets, V+c-jets, and WW samples when requiring two b-tagged jets.

The direct tagging method is applied to all samples when requiring no b-tagged jet or one b-tagged jet, and b-jet dominate samples when requiring two b-tagged jets.

6.2 Event Selection

The following section describes how selected physics objects are used to categorize events into signal regions and control regions. The signal region is used to search for the signal events, while the control region is background dominant region, mainly used to investigate and constrain the background processes. The trigger used to select events are discussed in 6.2.1, while the event selection strategies are provided in 6.2.2.

6.2.1 Triggers

In one lepton channel, the lepton from the W decay can be efficiently used as the trigger object. In order to increase the acceptance, the events are selected with unprescaled single lepton triggers with lowest p_T threshold.

The trigger used in 2012 are listed below:

- **Electron:** EF_e24vhi_medium1 or EF_e60_medium1

- **Muon:** EF_mu24i_tight or EF_mu36_tight

The name of trigger indicates the cuts applied to the trigger object, taking EF_e24vhi_medium1 for example, EF means trigger at event filter level, e24 means p_T threshold of 24 GeV for electrons, vh means veto of hadronic leakage, i refers to the track based isolation cut, and medium1 means a set of cuts which are similar to the medium electron identification criteria.

6.2.2 Topological Cuts and Kinematic Cuts

After trigger selections, further kinematic requirements and topological cuts are placed in each channel to discriminate signal events from the background events. In all three channels, events are required to have exactly two b-tagged jets. In the one lepton channel, exactly one tight lepton is required and events with additional loose leptons will be vetoed. Kinematic cuts are further placed on the missing transverse energy and transverse mass ($m_T^W = \sqrt{(}2 \times p_T(\ell) \times p_T(\nu) \times (1 - cos(\phi(\ell) - \phi(\nu)))))$ [163] to select events consistent with a W boson. Since the produced Higgs bosons are mostly boosted, the signal to background ratio increases with p_T of W boson. Therefore, the one lepton channel is further divided into several regions of p_T^W to increase the sensitivity. In each region, kinematic cuts on E_T^{miss} and m_T^W are adjusted to enhance the signal, and additional topological cuts are placed on ΔR between two signal jets to suppress the backgrounds. The cuts are summarized in Table 6.1

p_T^W / GeV	0-90	90-120	120-160	160-200	>200
Δ R (j_1,j_2)	0.7-3.4	0.7-3.0	0.7-2.3	0.7-1.8	<1.4
E_T^{miss} / GeV	> 25				> 50
m_T^W / GeV	40-120			< 120	

Table 6.1: Topological cuts applied to one lepton channel in each p_T^W bin.

As shown in Table 6.1, the topological cuts are carefully adjusted in each p_T^W region. In the low p_T^W region, where QCD has a large contribution, a lower cut is placed on m_T^W to reject QCD events, which was then removed in high p_T^W regions to increase the acceptance. For the same reason, the cut on E_T^{miss} was also increased from 25 GeV to 50 GeV in highest p_T^W region. In order to reduce the $t\bar{t}$ background, an upper cut on ΔR is placed in every p_T^W region, which is tighter in the high p_T^W region where Higgs are more boosted. The lower cut on ΔR is meant to reduce the QCD background, which was removed in the high p_T^W region to increase the

acceptance.

The signal region in this analysis is defined by requiring 2 b-tagged signal jets with leading jet $p_T > 45$ GeV. In order to increase the acceptance, one additional signal jet is allowed. The signal region is then divided into two categories with respect to number of jets. There are a 2 jets signal region and a 3 jets signal region. In the 3 jets signal region, the 2 b-tagged jets must be leading jets.

Control regions are defined for specific background processes, like W + c-jets and W + light jets. By relaxing the requirement on the 2 b-tagged jets, the 0-tag and 1-tag regions are defined, where there are exactly 0 or 1 b-tagged jet respectively. The 0-tag and 1-tag control regions can be used to constrain the normalization of W+jets background processes, and study the invariant mass distribution for the leading jets. The 3 jets signal region is also a top enriched region, which is described as the top control region in this dissertation.

In the 0 lepton channel and 2 lepton channel, the definition of signal region and control region are almost the same as in the 1 lepton channel. In the 0 lepton channel, due to the overwhelming QCD background in the low p_T^V bins, the signal region and background regions are only divided in 3 p_T^V bins starting from 120 GeV. In the 2 lepton channel, an additional top control region is defined by requiring two signal leptons with different flavors, whose invariant mass are outside the Z mass shell (40 GeV $< m_{ll} <$ 83 GeV or $m_{ll} >$ 99 GeV), and dropping the cut on MET. This top control region is not only for the 2 lepton channel, but also used for the 1 lepton channel and 0 lepton channels.

6.3 Acceptance

This section provides the signal and background acceptances. The numbers shown in table 6.2 and 6.3 correspond to the yield for each MC samples in the di-jet mass range 80 GeV $< m_{jj} <$ 150 GeV after all event selections has been applied. The numbers are obtained with normalization to the given cross sections of the corresponding MC simulations.

p_T^W /GeV	2b-jets, 2jets					2b-jets, 3jets				
	0-90	90-120	120-160	160-200	> 200	0-90	90-120	120-160	160-200	> 200
Zl	1.96 ± 0.89	0.16 ± 0.07	0.03 ± 0.01	0.02 ± 0.01	0.01 ± 0.00	0.58 ± 0.29	0.07 ± 0.03	0.02 ± 0.01	0.01 ± 0.01	0.01 ± 0.00
Zcl	3.24 ± 0.66	0.33 ± 0.08	0.07 ± 0.02	0.04 ± 0.01	0.01 ± 0.00	1.38 ± 0.42	0.13 ± 0.08	0.03 ± 0.03	0.03 ± 0.01	0.02 ± 0.01
Zcc	21.6 ± 0.92	0.28 ± 0.12	0.08 ± 0.04	0.06 ± 0.03	0.04 ± 0.02	1.20 ± 0.72	0.22 ± 0.11	0.08 ± 0.04	0.05 ± 0.03	0.04 ± 0.02
Zbl	3.33 ± 1.32	0.18 ± 0.09	0.00 ± 0.00	0.00 ± 0.00	0.00 ± 0.00	1.05 ± 0.79	0.44 ± 0.22	0.03 ± 0.03	0.03 ± 0.01	0.01 ± 0.00
Zbb	20.25 ± 1.96	2.70 ± 0.32	0.93 ± 0.15	0.63 ± 0.16	0.13 ± 0.04	12.78 ± 2.76	2.05 ± 0.48	0.41 ± 0.29	0.30 ± 0.15	0.21 ± 0.06
Wl	22.18 ± 10.87	3.17 ± 1.57	1.16 ± 0.57	0.46 ± 0.23	0.41 ± 0.21	6.81 ± 3.48	1.06 ± 0.55	0.44 ± 0.27	0.21 ± 0.10	0.21 ± 0.10
Wcl	101.80 ± 29.09	14.55 ± 4.25	5.13 ± 1.53	2.00 ± 0.61	1.20 ± 0.38	32.07 ± 10.74	4.99 ± 1.71	2.05 ± 0.73	0.85 ± 0.33	0.72 ± 0.29
Wcc	105.55 ± 43.47	16.74 ± 7.01	6.99 ± 2.98	3.10 ± 1.35	3.76 ± 1.74	40.85 ± 18.96	6.49 ± 3.00	3.22 ± 1.54	1.79 ± 0.87	2.09 ± 1.05
Wbl	26.10 ± 10.06	4.29 ± 1.73	1.67 ± 0.74	0.76 ± 0.31	0.51 ± 0.21	17.10 ± 10.53	1.92 ± 1.95	1.03 ± 0.82	0.29 ± 0.25	0.74 ± 0.39
Wbb	341.90 ± 29.26	60.60 ± 5.95	25.95 ± 2.66	10.88 ± 1.47	8.96 ± 1.36	125.31 ± 27.97	23.61 ± 5.36	10.73 ± 2.83	6.62 ± 1.68	5.78 ± 1.48
stopWt	43.44 ± 6.20	11.37 ± 1.32	6.02 ± 0.98	2.05 ± 0.45	1.86 ± 0.47	62.34 ± 8.45	16.05 ± 2.78	8.78 ± 1.36	3.98 ± 0.84	3.61 ± 0.61
stop st	283.77 ± 30.85	43.58 ± 5.19	11.52 ± 1.46	2.49 ± 0.34	0.57 ± 0.40	167.13 ± 21.95	25.94 ± 3.83	6.32 ± 0.89	1.09 ± 0.30	0.73 ± 0.13
ttbar	643.01 ± 92.03	199.46 ± 26.30	84.84 ± 10.10	19.69 ± 2.71	5.72 ± 1.07	1649.78 ± 218.31	367.19 ± 42.68	141.05 ± 15.73	44.12 ± 5.60	18.90 ± 3.91
multijet	212.79 ± 6.38	12.44 ± 2.11	3.61 ± 1.01	3.13 ± 1.31	1.12 ± 0.62	5.93 ± 1.79	0.59 ± 0.20	0.27 ± 0.11	0.24 ± 0.12	0.09 ± 0.05
WW	4.69 ± 1.14	0.64 ± 0.17	0.39 ± 0.14	0.19 ± 0.06	0.20 ± 0.07	2.22 ± 0.72	0.25 ± 0.10	0.15 ± 0.06	0.08 ± 0.04	0.11 ± 0.09
WZ	44.54 ± 5.28	6.98 ± 0.91	4.87 ± 0.64	2.77 ± 0.33	2.14 ± 0.37	10.00 ± 2.94	2.23 ± 0.85	1.84 ± 0.52	1.26 ± 0.37	1.16 ± 0.36
Sum of bkg	1860.73 ± 162.16	377.47 ± 36.36	153.26 ± 15.40	48.28 ± 5.15	26.63 ± 3.59	2136.53 ± 245.58	453.25 ± 48.92	176.45 ± 18.75	61.05 ± 7.41	34.41 ± 5.57
Signal (WtH)	7.88 ± 0.74	1.81 ± 0.20	1.31 ± 0.13	1.01 ± 0.11	0.98 ± 0.12	2.13 ± 0.24	0.60 ± 0.07	0.55 ± 0.05	0.43 ± 0.04	0.50 ± 0.06
data	2030	414	159	40	33	2286	463	211	54	40

Table 6.2: Event yields of data, signal and different background channels in 2-jets and 3-jets signal region in 1 lepton channel for 7 TeV data. Only statistical uncertainty is included in the table. The signal sample are generated with Higgs boson mass $m_H = 125$ GeV.

p_T^W /GeV	2b-jets, 2jets				2b-jets, 3jets			
	0-90	90-120	120-160	> 200	0-90	90-120	120-160	160-200	> 200
Zl	11.98± 4.43	0.91 ± 0.33	0.19 ± 0.07	0.10 ± 0.04	0.03 ± 0.01	3.52 ± 1.24	0.39 ± 0.14	0.09 ± 0.06	0.05 ± 0.02	0.03 ± 0.01
Zcl	18.42 ± 4.60	1.76 ± 0.48	0.36 ± 0.10	0.17 ± 0.04	0.06 ± 0.02	7.09 ± 2.00	0.92 ± 0.25	0.23 ± 0.08	0.12 ± 0.04	0.05 ± 0.02
Zcc	12.53 ± 4.95	1.94 ± 0.76	0.44 ± 0.18	0.31 ± 0.15	0.10 ± 0.04	6.82 ± 3.00	1.14 ± 0.55	0.52 ± 0.23	0.23 ± 0.12	0.12 ± 0.06
Zbl	9.68 ± 3.97	1.70 ± 0.81	0.89 ± 0.36	0.01 ± 0.00	0.17 ± 0.09	7.42 ± 5.66	0.52 ± 0.64	0.33 ± 0.16	0.40 ± 0.17	0.00 ± 0.00
Zbb	128.91 ± 10.91	20.06 ± 2.31	4.40 ± 0.91	2.29 ± 0.41	0.82 ± 0.52	83.89 ± 18.27	11.97 ± 2.78	3.78 ± 1.19	1.50 ± 0.50	1.13 ± 0.40
Wl	113.33 ± 45.97	15.02 ± 6.24	5.26 ± 2.17	2.17 ± 0.91	1.94 ± 0.80	34.68 ± 13.41	5.29 ± 2.28	2.14 ± 0.88	1.00 ± 0.39	1.02 ± 0.40
Wcl	490.80 ± 122.63	66.57 ± 16.96	22.23 ± 5.57	8.56 ± 2.15	5.14 ± 1.29	152.17 ± 38.83	23.71 ± 6.24	9.28 ± 2.44	4.16 ± 1.12	3.27 ± 0.87
Wcc	462.44 ± 184.09	71.33 ± 27.95	27.75 ± 10.90	11.92 ± 4.62	14.22 ± 5.56	173.09 ± 76.29	28.82 ± 12.83	13.19 ± 5.88	6.60 ± 2.92	9.14 ± 4.00
Wbl	135.29 ± 47.32	18.64 ± 6.77	10.24 ± 3.65	3.58 ± 1.34	2.44 ± 1.03	77.58 ± 47.64	11.82 ± 7.16	5.25 ± 2.81	2.36 ± 1.66	2.53 ± 1.75
Wbb	1776.16 ± 118.38	301.37 ± 21.85	124.12 ± 13.14	53.79 ± 5.41	50.47 ± 6.67	666.54 ± 143.83	119.64 ± 27.83	59.59 ± 13.00	32.64 ± 7.80	34.72 ± 8.21
stopWt	221.70 ± 38.89	61.16 ± 8.04	27.76 ± 4.20	17.26 ± 2.44	5.10 ± 1.36	333.01 ± 46.85	72.05 ± 13.54	49.03 ± 9.02	30.55 ± 5.23	24.34 ± 4.50
stop st	1457.79 ± 121.40	231.32 ± 18.31	65.67 ± 6.66	12.73 ± 1.66	4.33 ± 0.80	881.31 ± 108.03	144.55 ± 18.66	35.27 ± 7.01	7.95 ± 1.23	4.05 ± 0.59
ttbar	3299.71 ± 391.26	1016.74 ± 99.17	421.25 ± 40.61	99.09 ± 10.64	30.35 ± 5.04	8562.69 ± 1007.54	2017.06 ± 199.25	756.45 ± 78.47	219.90 ± 24.58	97.31 ± 17.91
multijet	1278.08 ± 385.34	64.21 ± 22.14	12.25 ± 5.03	4.65 ± 2.40	0.77 ± 0.48	221.73 ± 66.85	11.06 ± 3.81	2.76 ± 1.13	1.07 ± 0.55	0.36 ± 0.23
WW	16.21 ± 3.55	2.64 ± 0.51	1.57 ± 0.33	0.69 ± 0.23	0.77 ± 0.37	6.65 ± 1.31	1.41 ± 0.27	0.77 ± 0.18	0.28 ± 0.10	0.58 ± 0.38
VZ	201.45 ± 22.31	32.89 ± 3.32	21.01 ± 3.07	12.75 ± 3.89	11.39 ± 7.32	45.41 ± 5.52	10.20 ± 0.92	8.08 ± 1.27	5.99 ± 2.00	5.85 ± 3.75
Sum of bkg	9634.46 ± 789.78	1908.27 ± 142.24	745.38 ± 63.19	230.09 ± 20.47	128.11 ± 16.27	11263.59 ± 1115.42	2460.55 ± 223.05	946.76 ± 93.52	314.81 ± 32.42	184.50 ± 25.33
Signal (WlvH)	39.04 ± 3.03	8.95 ± 0.68	6.01 ± 0.50	5.36 ± 0.52	5.56 ± 0.64	11.89 ± 0.85 ± 3.25 ± 0.33	2.73 ± 0.31	2.67 ± 0.29	3.33 ± 0.35	
data	11077	2084	833	250	148	12661	2754	974	333	198

Table 6.3: Event yields of data, signal and different background channels in 2-jets and 3-jets signal region in 1 lepton channel for 8 TeV data. Only statistical uncertainty is included in the table. The signal sample are generated with Higgs boson mass $m_H = 125$ GeV.

CHAPTER 7

Background Estimation and Modeling

The VH analysis is a background dominated analysis. After the complete event selection, the ratio of signal to background is less than 5% even in the most sensitive signal region. Therefore, it is essential to correctly estimate and model the background processes.

The possible sources of backgrounds are :

- **Lepton misidentification :** In case of jets misidentified as electrons, QCD events could be selected as signal events.
- **Miss tag of c/light jets :** In case of c-jets or l-jets mis-tagged as b-jets. W+l and W+c events could be selected as signal events.
- **Same final state objects :** In principle, processes with same final states can not be distinguished, such as W+bb, or WZ with Z $\rightarrow$ bb.
- **Undetected additional final state objects :** A $t\bar{t}$ event could decay to

2 b-jets and 2 W bosons. If one of the lepton from a W-boson decay falls out of the acceptance region, the observed final state is same as the signal. Such $t\bar{t}$ events can not be distinguished.

Besides the backgrounds listed above, there are some other backgrounds with negligible contributions to the one lepton channel, such as Z+jets, WW, etc. Most of the Z+jets events are discarded by the lepton veto, while the WW events are rejected by requiring two b-jets, since W boson can not decay to two quarks with same flavor.

In order to enhance specific background processes and allow for their study, various background control regions are defined in this analysis. Section 7.1 discusses the control regions for different backgrounds, such as the 0-tag and 1-tag regions for W+jets modeling, the QCD enriched region, and the $t\bar{t}$ control region. After that, detailed informations about background modeling and estimation are provided. Section 7.2 is for multi-jets background, Section 7.3 is for W+jets background, Section 7.4 briefly discusses the modeling of Z+jets, and section 7.5 focuses on the $t\bar{t}$ background.

7.1 Control Regions

This section briefly discusses the selection cuts and background contribution in each control region, as well as the background mis-modeling observed.

7.1.1 0-Tag Control Region

The 0 Tag region has exactly the same selection cuts as the signal region, except for requiring 0 b-tagged jet rather than 2 b-tagged jets. This region is dominated by W+light jets events (W+l), and with its high statistics makes it an excellent phase space to detect the discrepancy between data and simulation.

Fig. 7.1 shows the m_{jj} distributions in 0-tag region for 1 lepton channel in different p_T^W bins. The distributions are without any corrections, which indicates a reasonable agreement between data and background. However, the distribution of other variables, p_T^W for example, shows a clear evidence of mis-modeling, as shown in Fig. 7.2. This discrepancy is then recovered by the $\Delta\phi$ correction and p_T^W correction, as discussed in section 7.3.

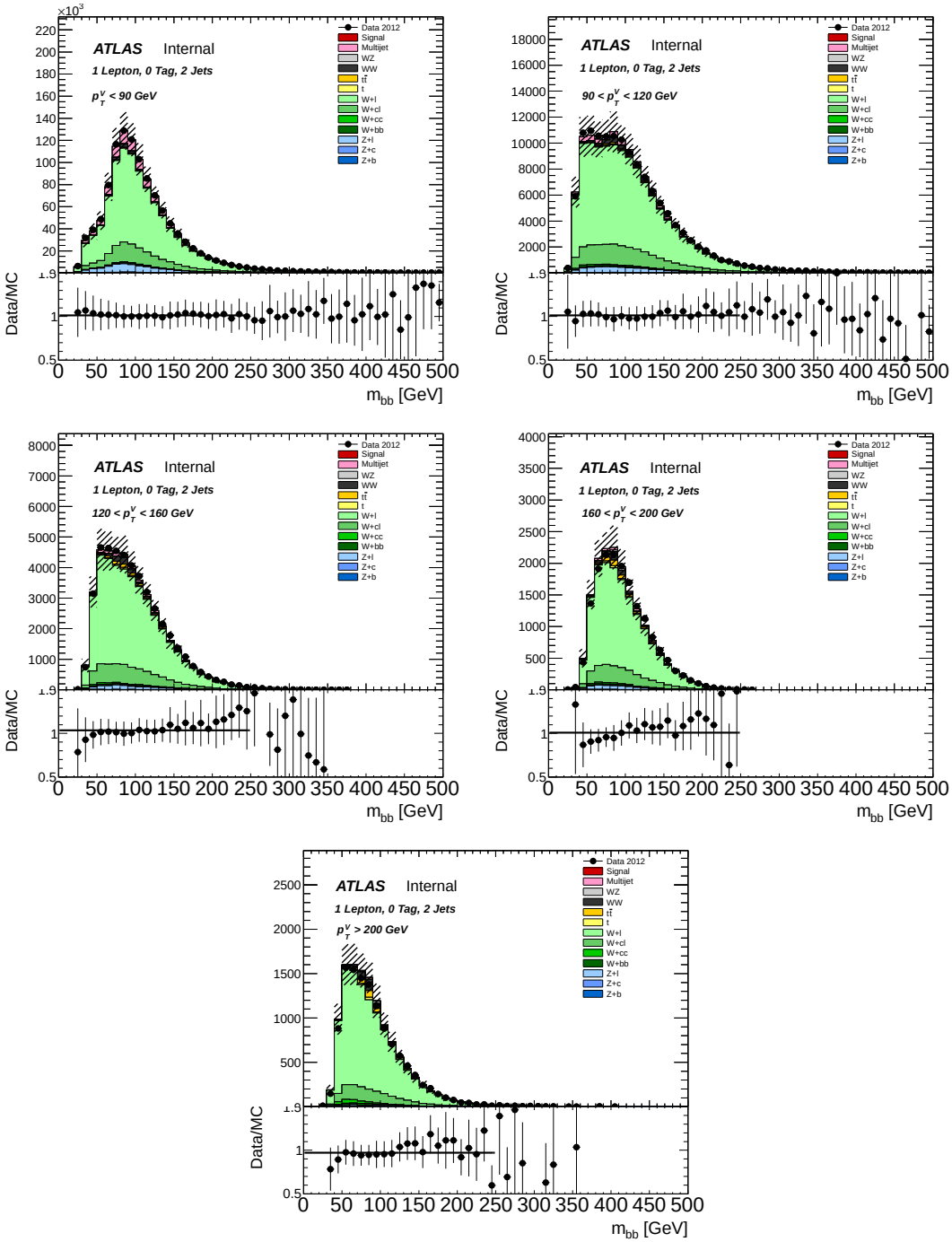

Figure 7.1: Distribution of m_{jj} in different p_T^W bins in 2 jets 0-tag region in 1 lepton channel with 8 TeV data.

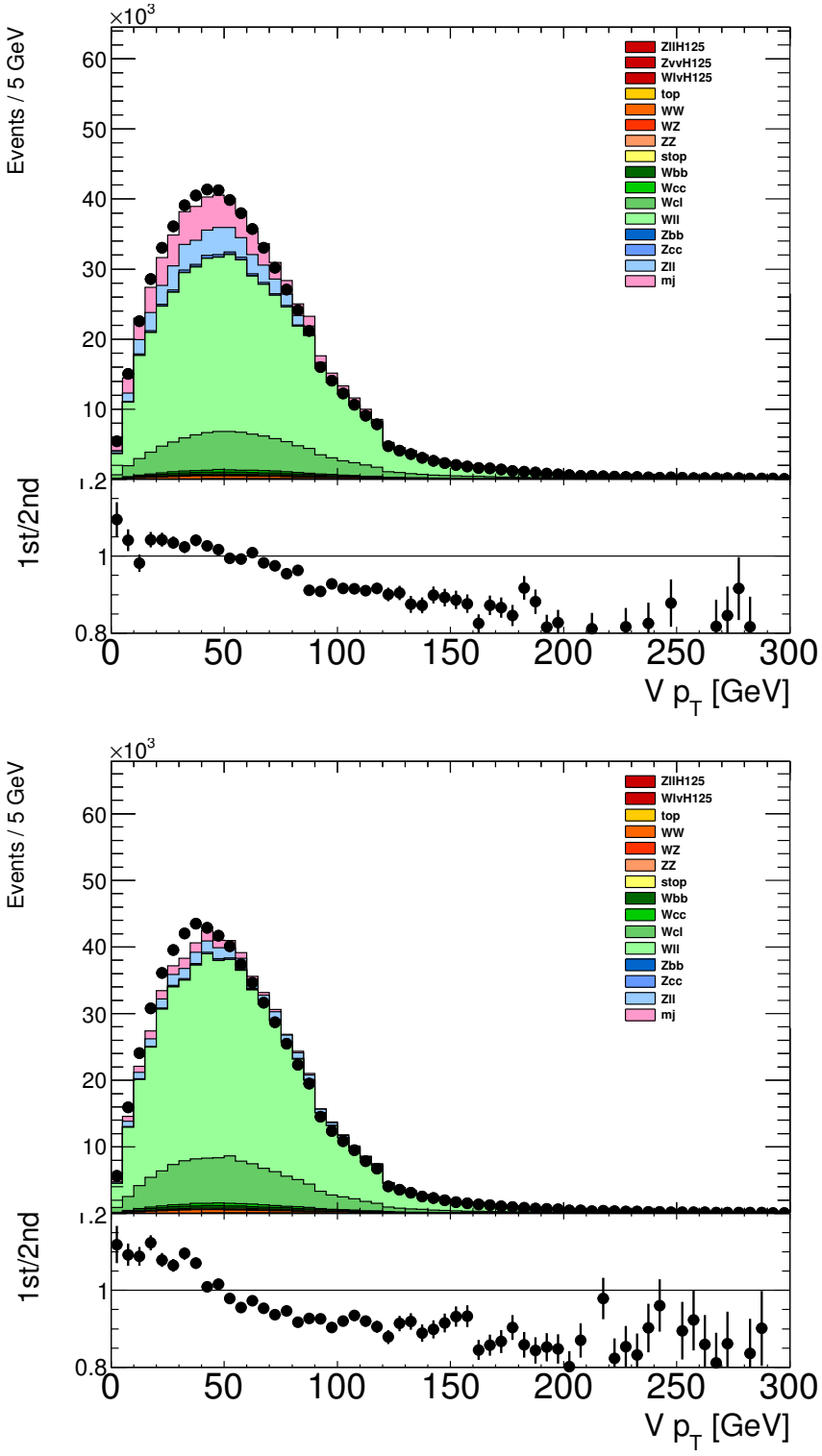

Figure 7.2: Distribution of p_T^V in 0-tag region for 1 lepton channel with 8 TeV data for electron (left) channel and muon (right) channel.

7.1.2 1-Tag Control Region

The 1-tag control region is again identical to the signal region, except the events are required to have exactly 1 b-tagged jet instead of 2. The requirement of 1 b-tagged jet discards a large fraction of $W+l$ background. Therefore, the dominate background in this region is $W+c$ and $W+b$, as shown in Fig. 7.3. Similar to 0 Tag control region, mis-modeling in p_T^W is also observed. Fig 7.4 shows the distribution of p_T^W in 1-tag region before any correction.

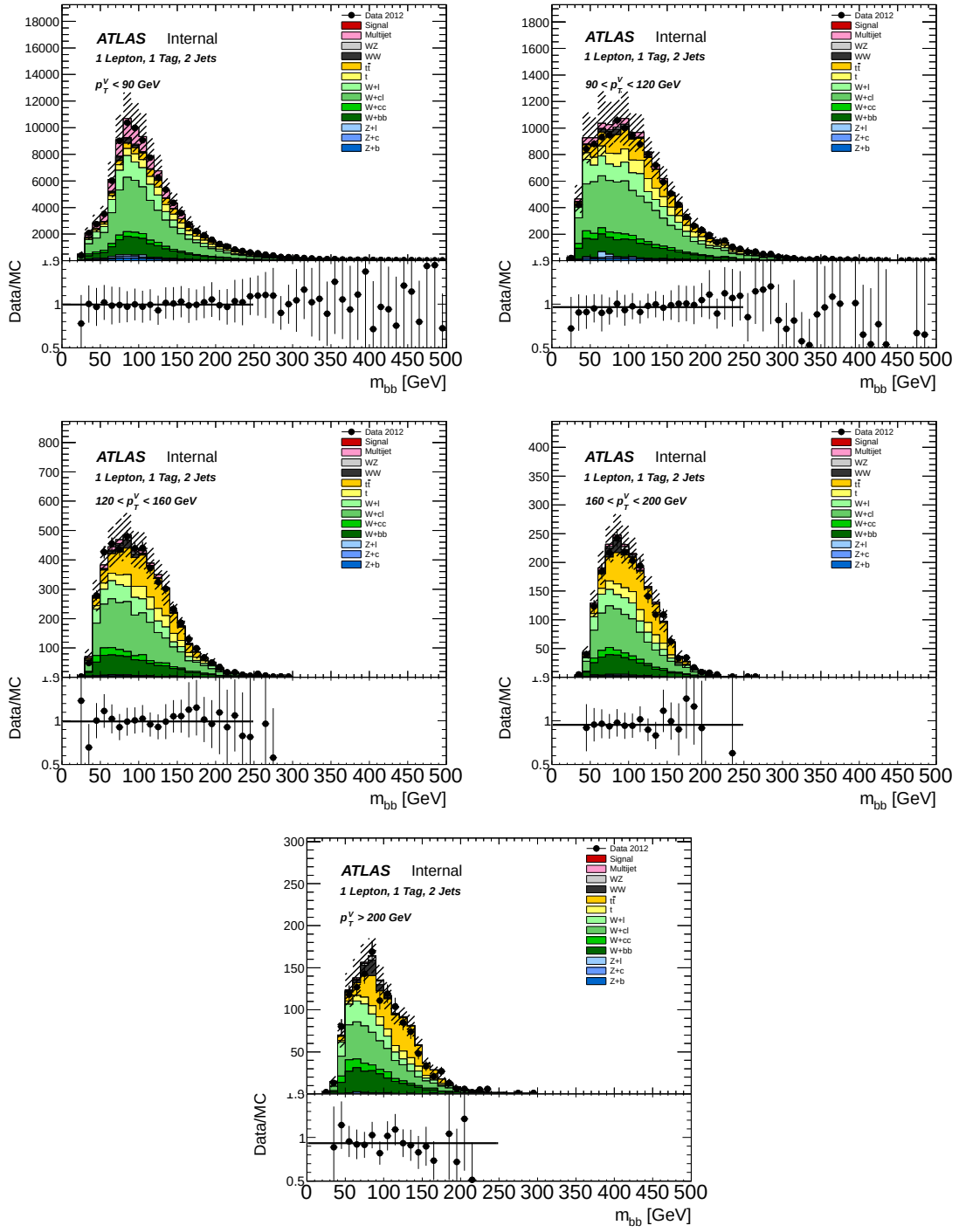

Figure 7.3: Distribution of m_{jj} in different p_T^W bins in 2 jets 1-tag region in 1 lepton channel with 8 TeV data.

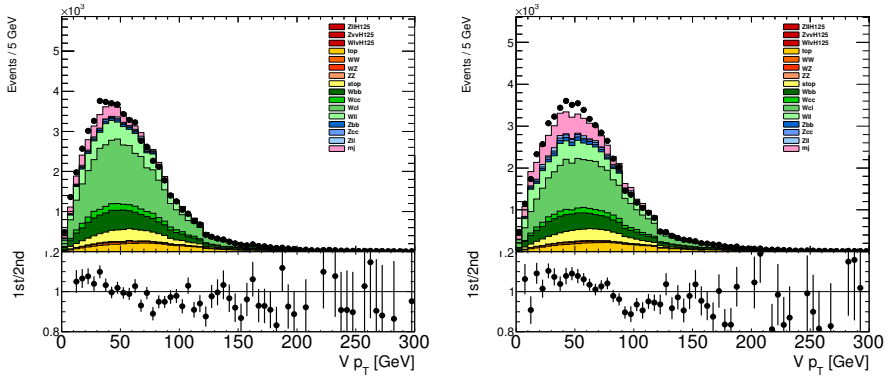

Figure 7.4: Distribution of p_T^V in 1-tag region for 1 lepton channel with 8 TeV data for electron (left) channel and muon (right) channel.

7.1.3 $t\bar{t}$ Control Region

In order to study the $t\bar{t}$ background, several control regions are defined. In the one lepton channel, the $t\bar{t}$ control region is also one of our signal regions, where 2 b-tagged jets and one addition jet is required. One additional control region is defined by requiring 2 signal lepton with different flavors, and $m_{ll} > 40$ GeV($e\mu$ region). The purity of $t\bar{t}$ events in 3 jets 2-tag region is about 90%, while the $e\mu$ top control region has a purity of nearly 100%.

Fig 7.5 shows the m_{bb} distribution in 3 jets 2-tag control region, and Fig 7.6 show the m_{bb} distribution in $e\mu$ top control region.

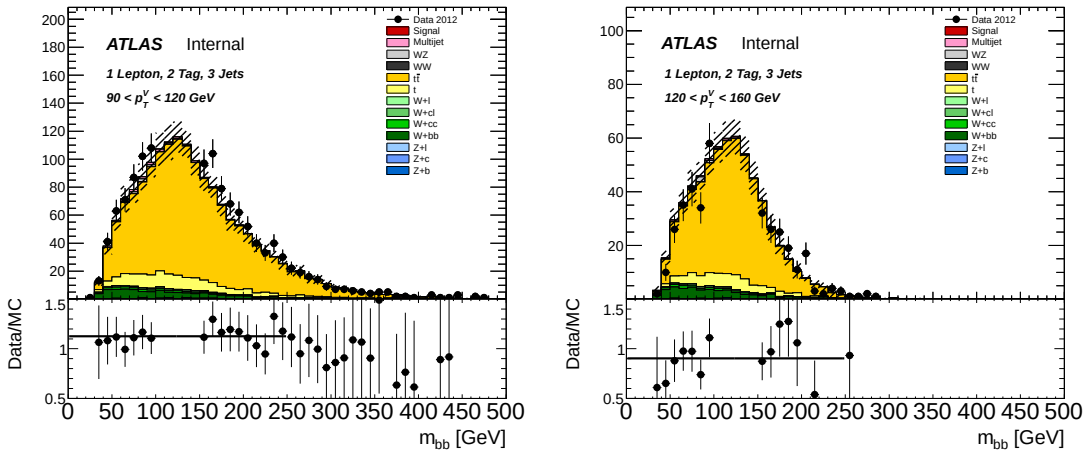

Figure 7.5: Distribution of m_{jj} in two p_T^W bins in 2-tag 3jets region in 1 lepton channel with 8 TeV data.

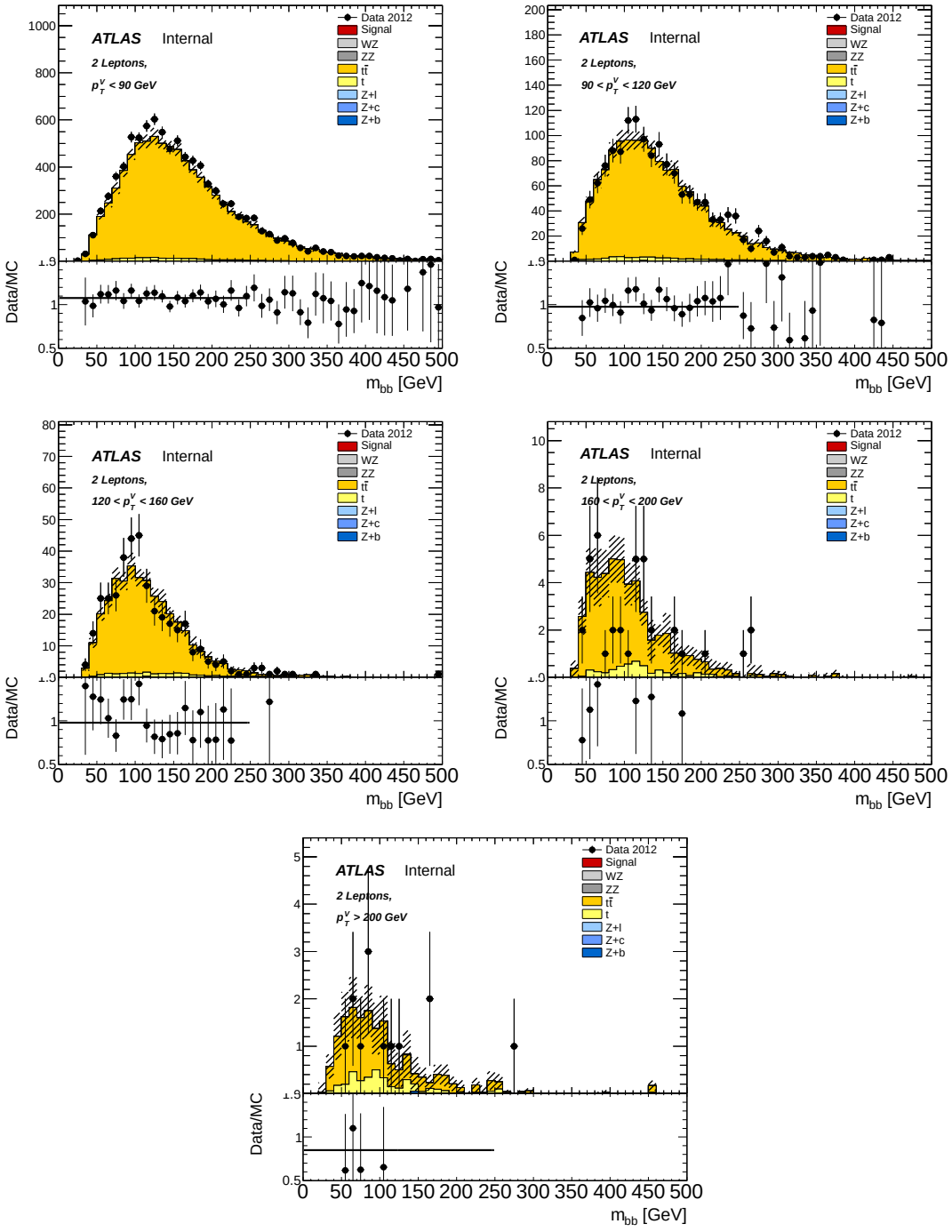

Figure 7.6: Distribution of m_{jj} in five p_T^Z bins in $e\mu$ top control region with 8 TeV data.

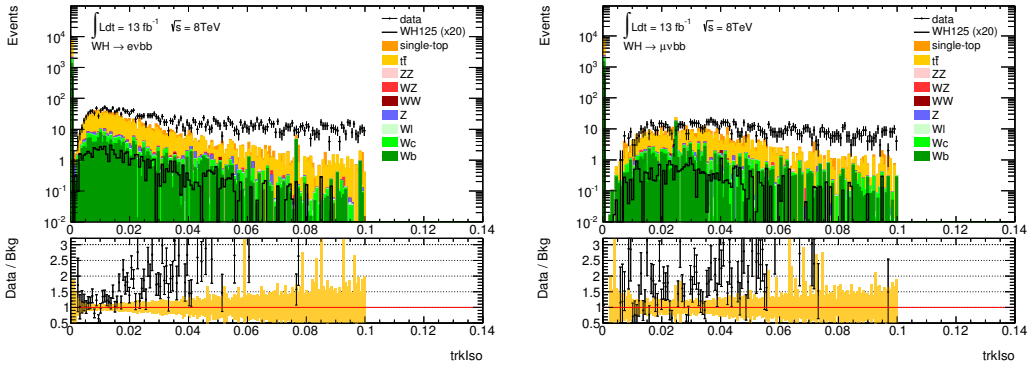

(a) electron (b) muon

Figure 7.7: This plots show the track isolation distributions of the electrons and the muons with 8 TeV data. The black dots in this plots are data points, while the colorful bands are for different background processes. The gap between data and MC samples are multi-jets event.

7.2 Multi-jets background

In one lepton channel, the normalization scale factor and the shape distribution of multi-jets background are derived using a data-driven method. A multi-jets template is created by reversing the track isolation cut of the lepton candidates, and loosening the lepton identification criteria from tight to medium. The normalization scale factor is then measured from the fit to data.

The isolation cut for signal electron is $trk_{iso} < 0.04$. By reversing the cut, we should have $trk_{iso} > 0.04$. However, there is one more cut on track isolation when passing through electron EF trigger, $trk_{iso} < 0.1$. Therefore, the isolation cut used to select multi-jets template is actually $0.04 < trk_{iso} < 0.1$. Although the isolation cut from trigger reduces the statistic, it helps to select the multi-jets events which are more signal like. The distributions of track isolation and calorimeter isolation are shown in Fig 7.7 and 7.8. In these plots, the gap between data and MC samples are multi-jets events with $0.04 < trk_{iso} < 0.1$.

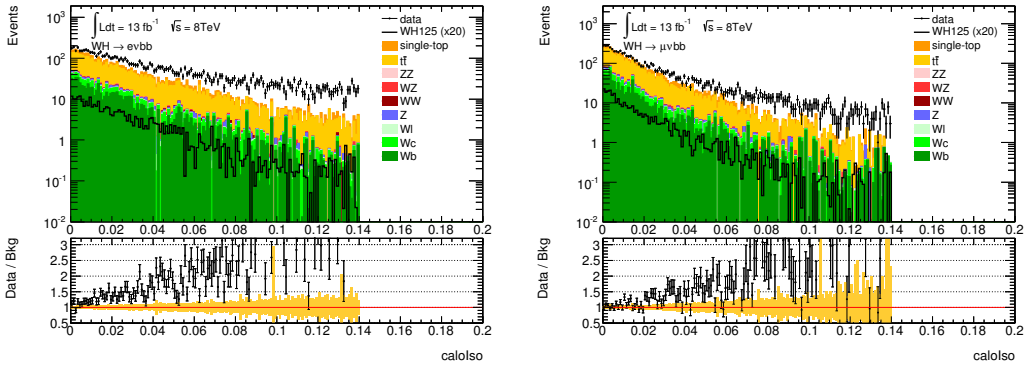

(a) electron (b) muon

Figure 7.8: The plots show the calorimeter isolation distributions of the electrons and the muons with 8 TeV data. The black dots in this plots are data points, while the colorful bands are for different background processes. The gap between data and MC samples are multi-jets event.

In this way, a multi-jets enriched region is defined by requiring medium lepton plus inverse track isolation cut. The multi-jets template can then be derived from this region by subtracting all the other background contributions from data, with assumption that all other background are correctly described by MC samples. However, a conserved systematic uncertainty will be used to cover the uncertainty caused by this assumption.

With this template, the normalization of the multi-jets background in each region is obtained by a χ^2 fit of the m_T^W distribution. During the fit, the shape for the multi-jets background uses the template we just derived, while the shape for the other background processes use templates derived from simulation. The normalization scale factor of multi-jets is floating in the fit. Fig. 7.9 shows the χ^2 fit of the m_T^W distribution in signal region, while Fig. 7.10 shows the χ^2 fit of the m_T^W distribution in 0 tag region and 1 tag region. In 0 tag region and 1 tag region, the high statistic provides accurate fit result for the multi-jets normalization.

The normalization scale factor derived from χ^2 fit of the m_T^W distribution are

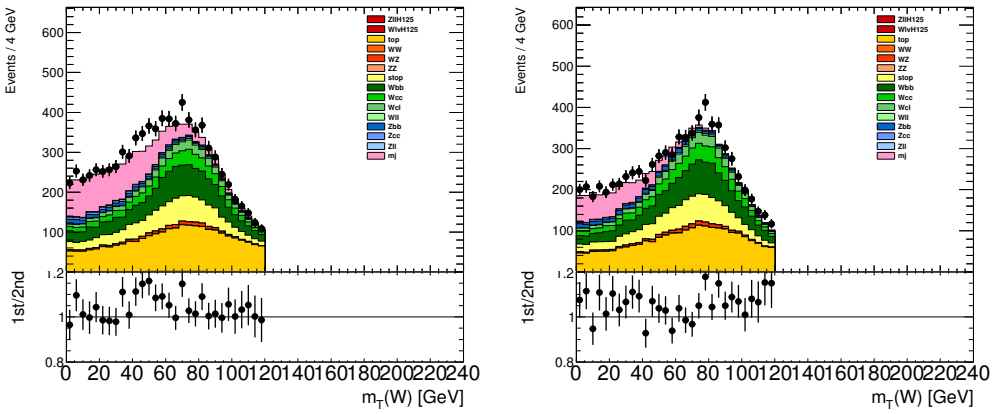

(a) electron (b) muon

Figure 7.9: The result of the χ^2 fit of the m_T^W distribution in signal region. The plot on the left is for electron channel, while the plot on the right is for muon channel. The pink color is the multi-jets background, the template of which comes from multi-jets control region.

then applied to other distributions, such as $\Delta\phi$, m_{jj}, etc. Fig 7.11 shows the m_{jj} distribution in signal region and 1 tag control region. From the plot, good agreement between data and the estimated background can be observed.

Given the good agreement observed in the sidebands of signal regions and in all of the control regions, a conservative uncertainty of 30% is assigned to the normalization of multi-jets background to account for the uncertainty from the fit. Since the template is extracted from a region with different isolation cuts than the signal region, a systematic is estimated by studying the variation with different track isolation cuts, as shown in Fig 7.12. To further validate the shape systematics of the multi-jets template, several additional checks are performed. The nominal multi-jets template is compared with other templates extracted from other regions, such as regions with inverted E_T^{miss} and m_T^W cut. The systematic is also estimated separately in low p_T^W region and high p_T^W region to check the consistency in different p_T^W regions. All the checks show consistency with the estimated uncertainty on

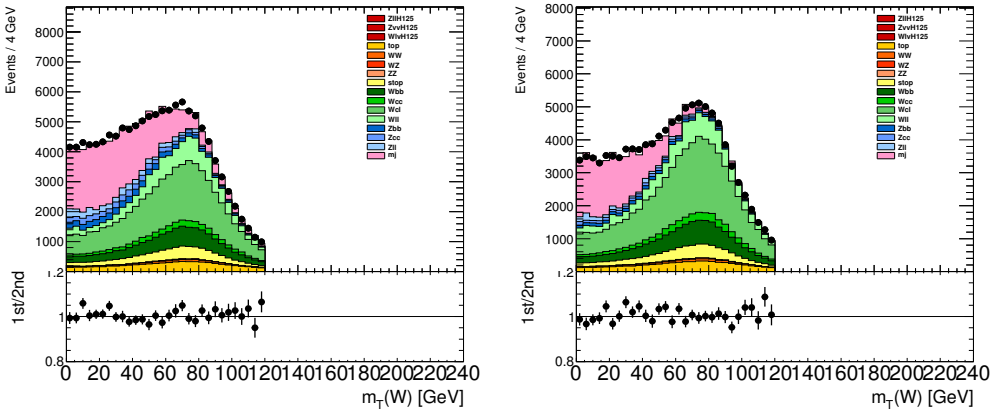

(a) electron (b) muon

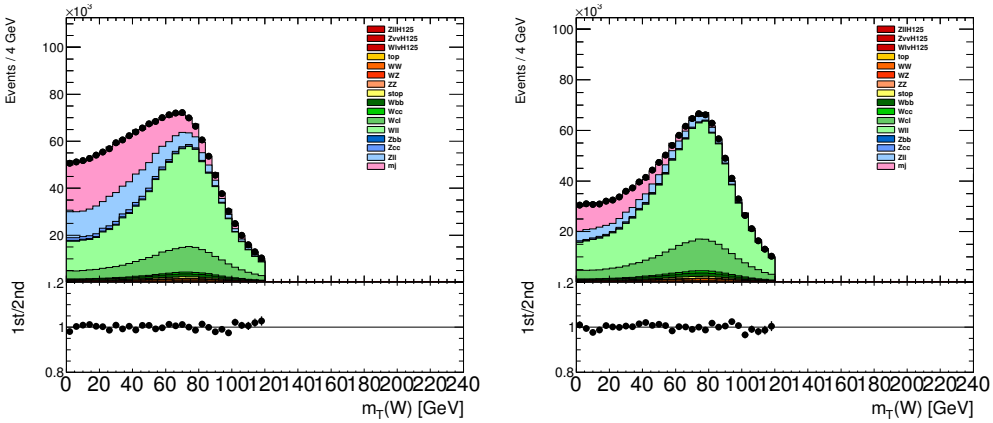

(c) electron (d) muon

Figure 7.10: (Top) The result of the χ^2 fit of the m_T^W distribution in 1 tag control region. The plot on the left is for electron channel, while the plot on the right is for muon channel. (Bottom) The result of the χ^2 fit of the m_T^W distribution in 0 tag control region. The pink color is the multi-jets background, whose template comes from multi-jets control region.

multi-jets template.

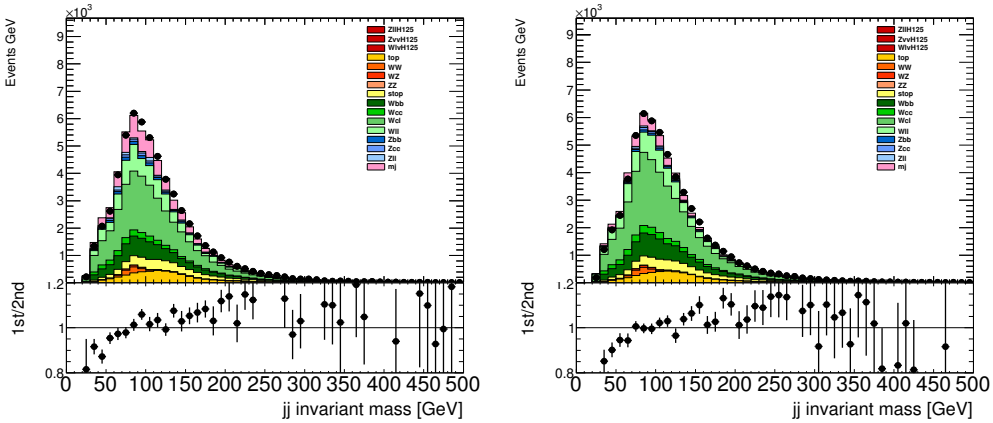

(a) electron (b) muon

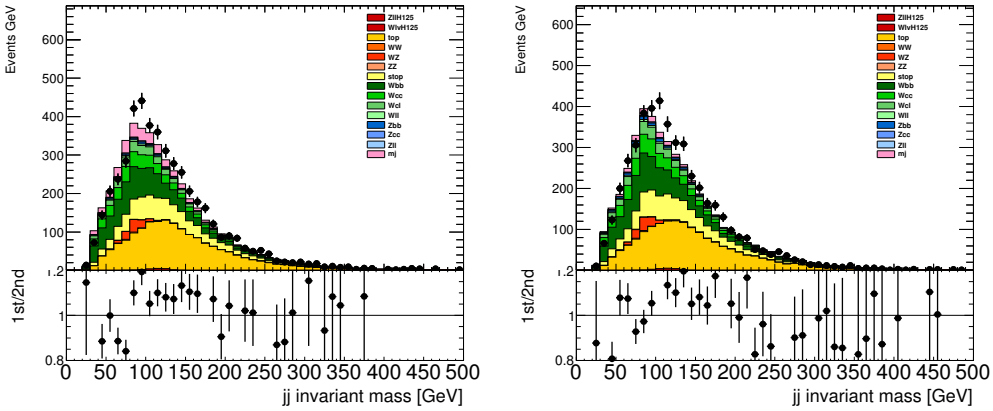

(c) electron (d) muon

Figure 7.11: The m_{jj} distribution in the 1-tag regions (top) and in the 2-tag signal region (bottom), for electrons (left) and muons (right). The normalization of multi-jets background is derived from χ^2 fit of the m_T^W distribution. The observed discrepancy is from the mis-modeling of W+jets samples, which is discussed in section 7.3.

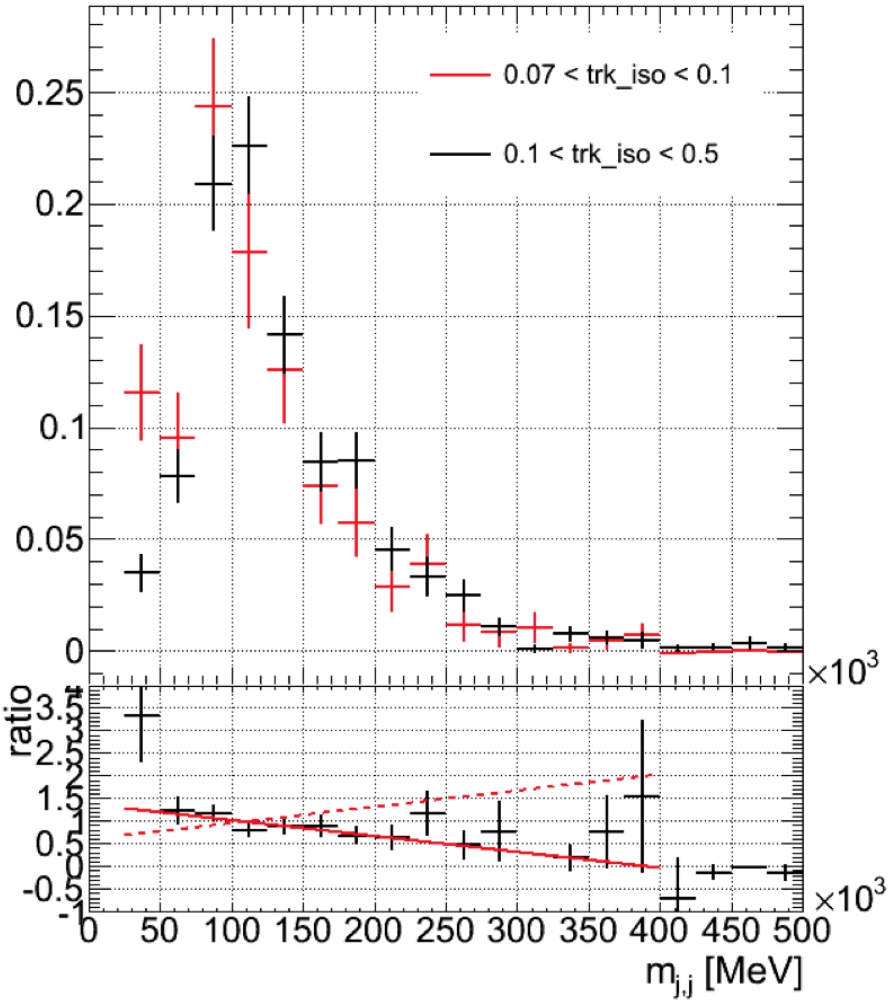

Figure 7.12: Comparison of the multi-jets templates extracted with different track isolation cuts

7.3 W+jets Background

The W+jets background is one of the main backgrounds in this analysis, the shape information is obtained from Monte Carlo samples using Sherpa as generator, while the normalization is derived from a fit to the data. In both 0-tag and 1-tag control region, mis-modeling has been observed. This section describes the mis-modeling of W+jets, as well as the corrections applied. Section 7.3.1 focuses on the correction on $\Delta\phi$ distribution, and Section 7.3.2 discusses an additional correction on the p_T^W distribution.

7.3.1 $\Delta\phi$ Correction

In the 0-tag region, where W+jets is dominant, a discrepancy is observed for many variables between data and simulated events, which indicates mis-modeling of the MC samples generated with the Sherpa generator. Similar mis-modeling is observed with other generators, as well as in other control regions for both electron channel and muon channel. Since the muon channel contains much less multi-jets events compared to the electron channel, similar behavior between two channels indicate that this mis-modeling is not due to multi-jet background. The discrepancy of $\Delta\phi$ and p_T^W is shown in Fig. 7.13, while the discrepancy of other variables, such as m_{jj}, MET, and ΔR, are shown in Fig 7.14.

After checking the correlation between different variables, the discrepancy between data and simulated events can be reduced by correcting only the mis-modeling of $\Delta\phi$. Therefore, the mis-modeling is manifested as a ratio between data and MC across the range of $\Delta\phi$ between $-\pi$ and π. The 0-tag region is used to evaluate the ratio for $\Delta\phi$ correction because of its high statistic. During the evaluation, all

the other backgrounds except W+jets are considered to be well described by MC samples. With this assumption, the mis-modeling ratio is calculated by subtracting all the other background from the data, and then divided by the W+jets MC simulation. The ratio is fitted with a quadratic polynomial to derive an expression versus $\Delta\phi$. Since the $\Delta\phi$ correction is a shape only correction, it is scaled to keep the same normalization before and after the correction. The derived correction scale factor is shown in Fig 7.15.

With $\Delta\phi$ applied to the simulated sample, the agreement between data and simulation improves for almost all variables. Fig. 7.16 shows the improvement of $\Delta\phi$ and p_T^W distribution in 0-tag region after $\Delta\phi$ correction. Fig 7.17 shows the improvement for other variables, such as m_{jj}, MET, and ΔR, in the same control region. The improvement of $\Delta\phi$ and p_T^W in 1-tag control region is shown by comparing Fig. 7.18 and Fig. 7.20, while the improvement of other variables in 1 tag control region are shown by comparing 7.19 and 7.21. The overall improvement in different control regions are summarized in Fig 7.22.

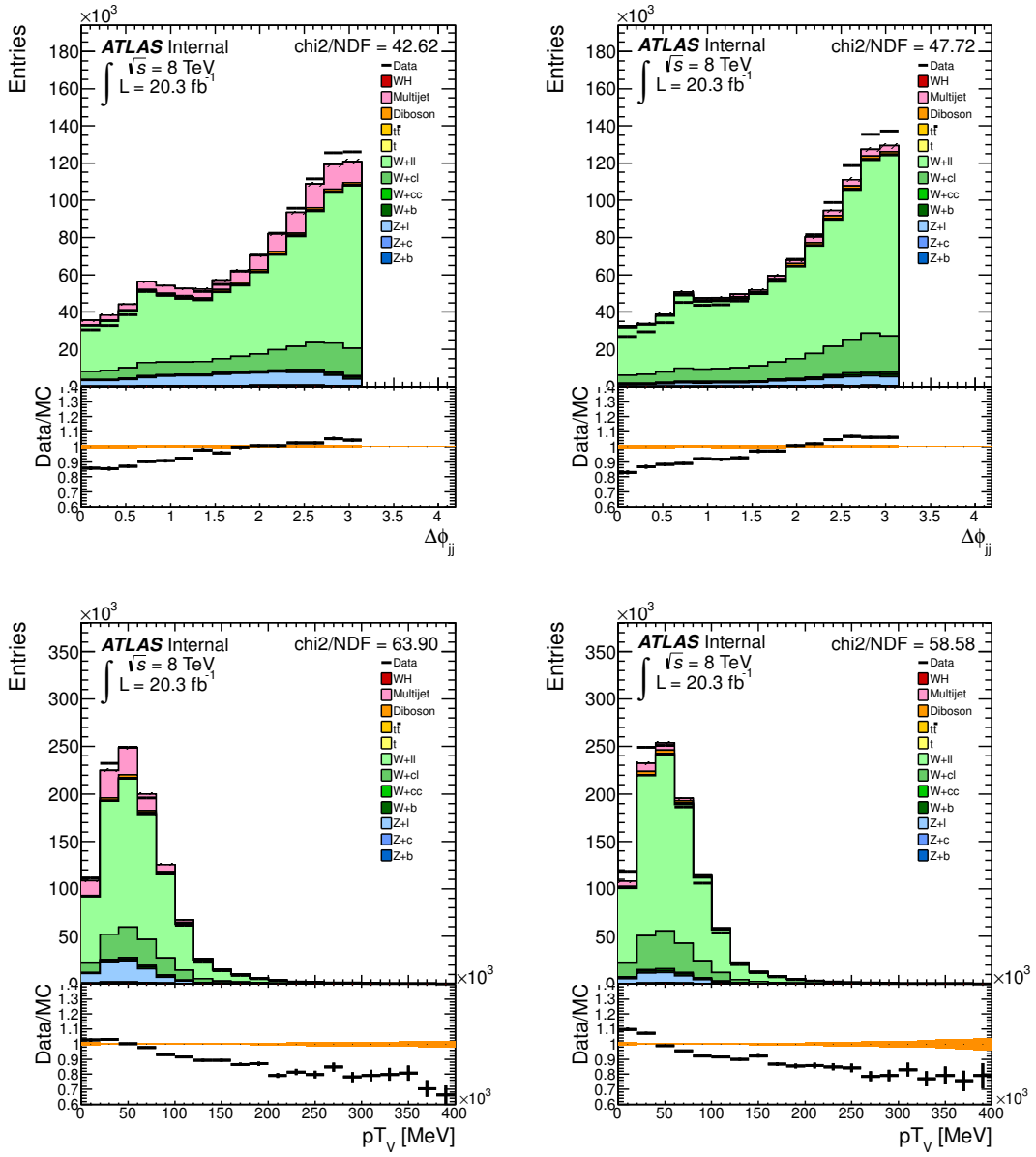

Figure 7.13: Distributions of $\Delta\phi$ and p_T^W with the 1-lepton selection in the 0-tag bin. On the left, the electron channel, on the right, the muon channel.

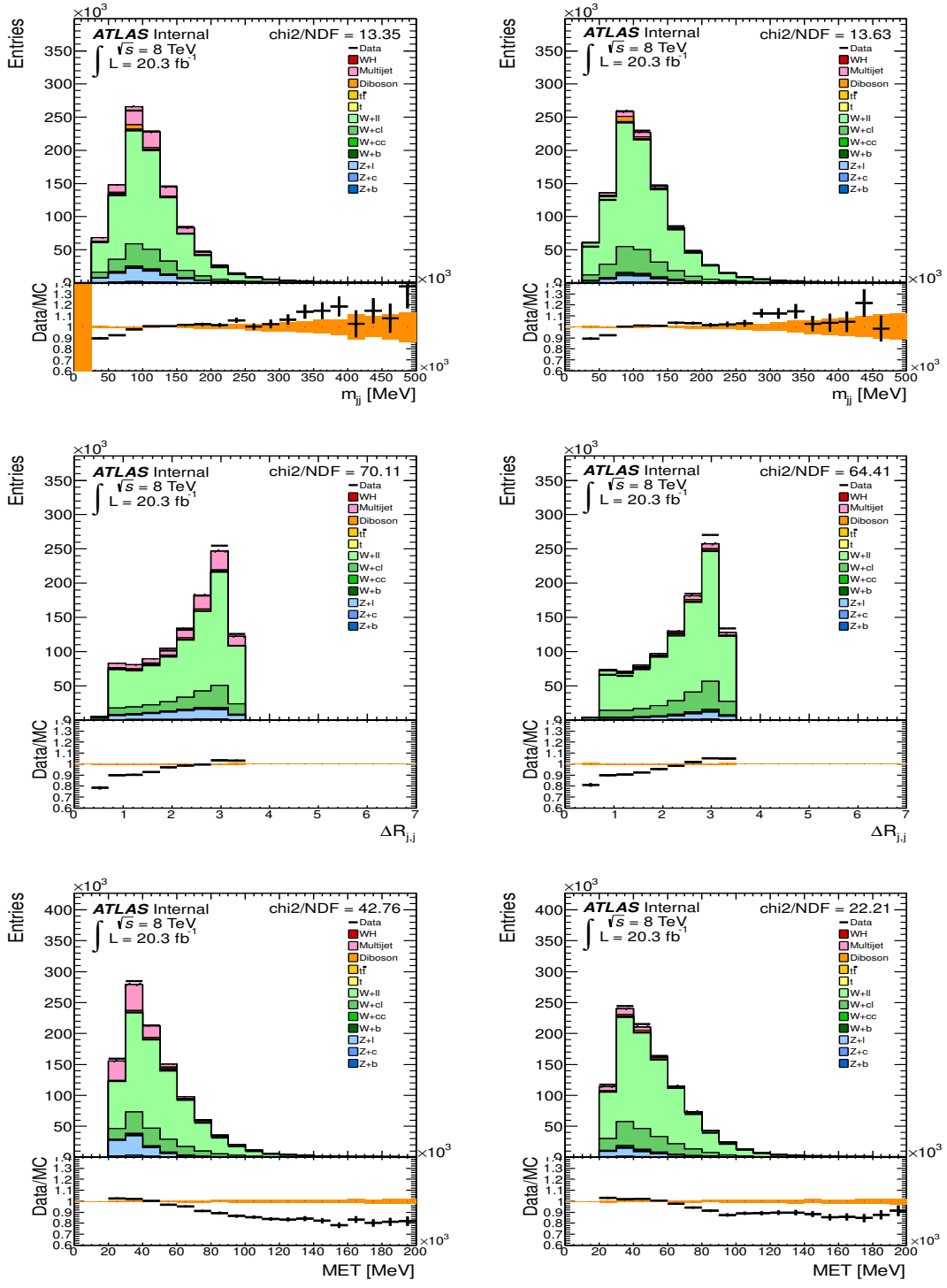

Figure 7.14: The 8 TeV 1-lepton channel - 0 tag region before applying the $\Delta\phi$ correction. Distributions of m_{jj}, ΔR, MET, for electron events (left) and muon events (right)

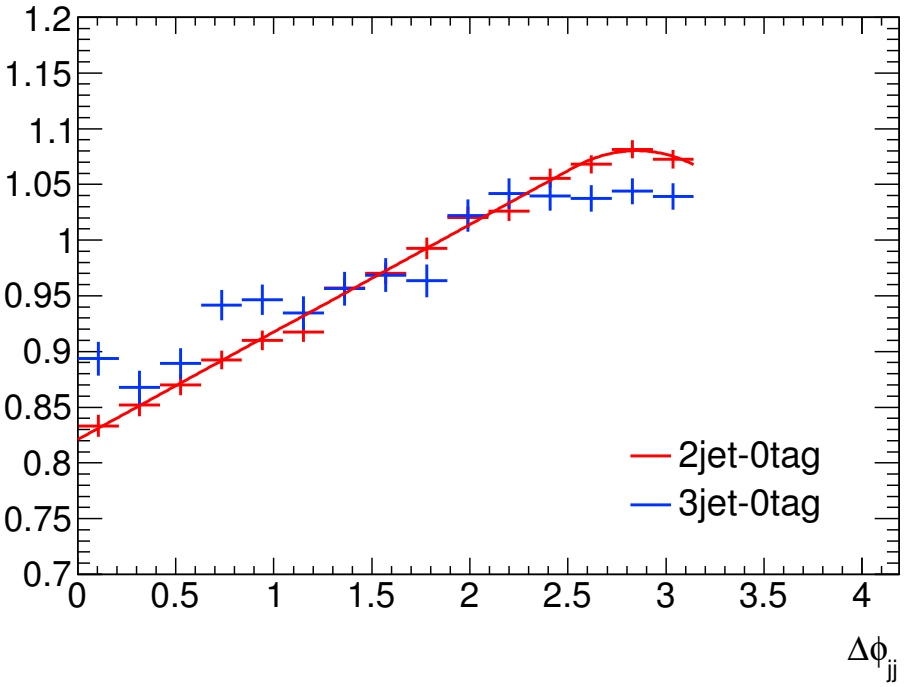

Figure 7.15: The $\Delta\phi$ correction factors calculated for W+jets as a function of $\Delta\phi$.

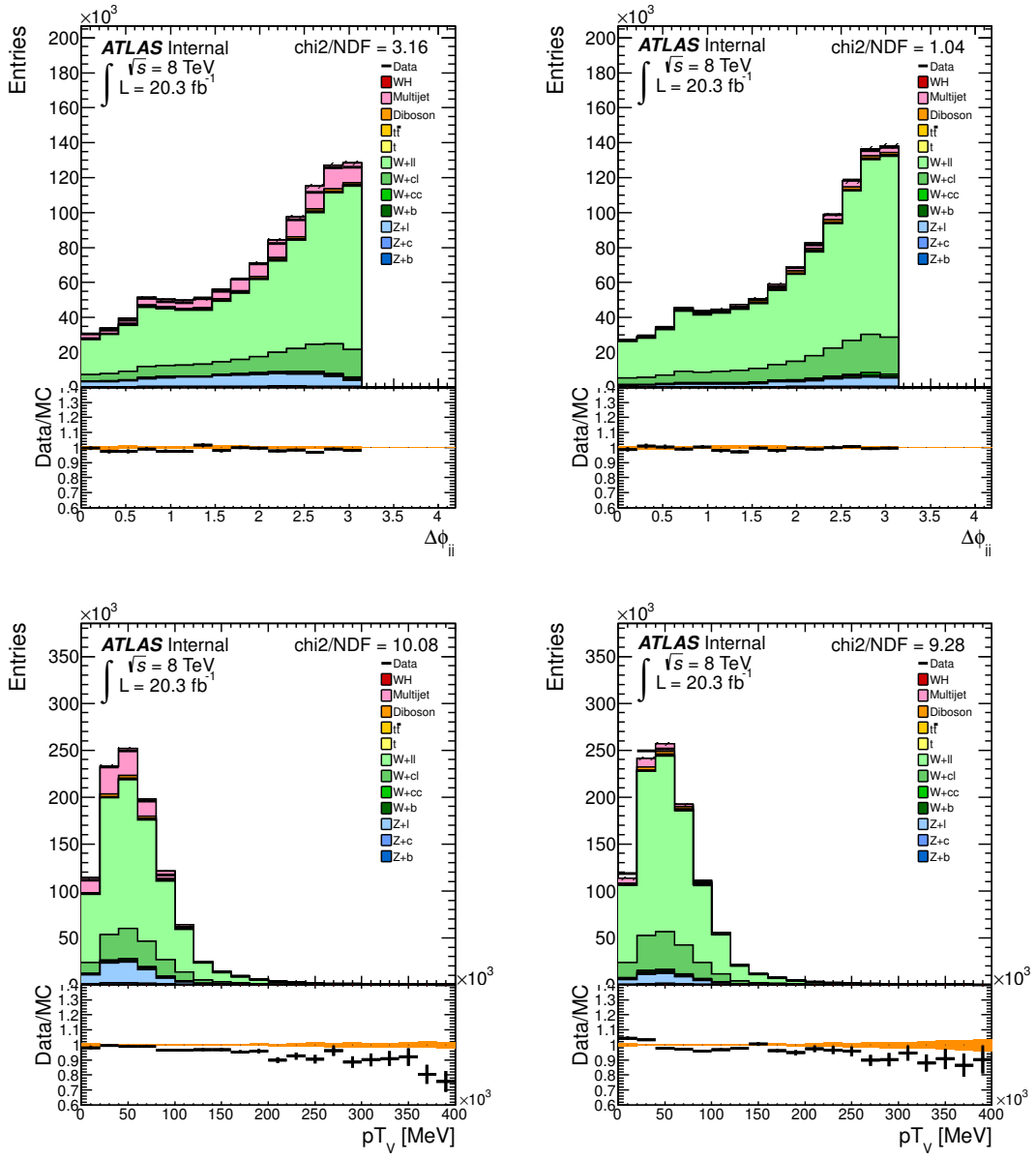

Figure 7.16: Distributions of $\Delta\phi$ and p_T^W with the 1-lepton selection in the 0-tag bin after applying the $\Delta\phi$ correction. The electron channel is on the left and the muon channel is on the right.

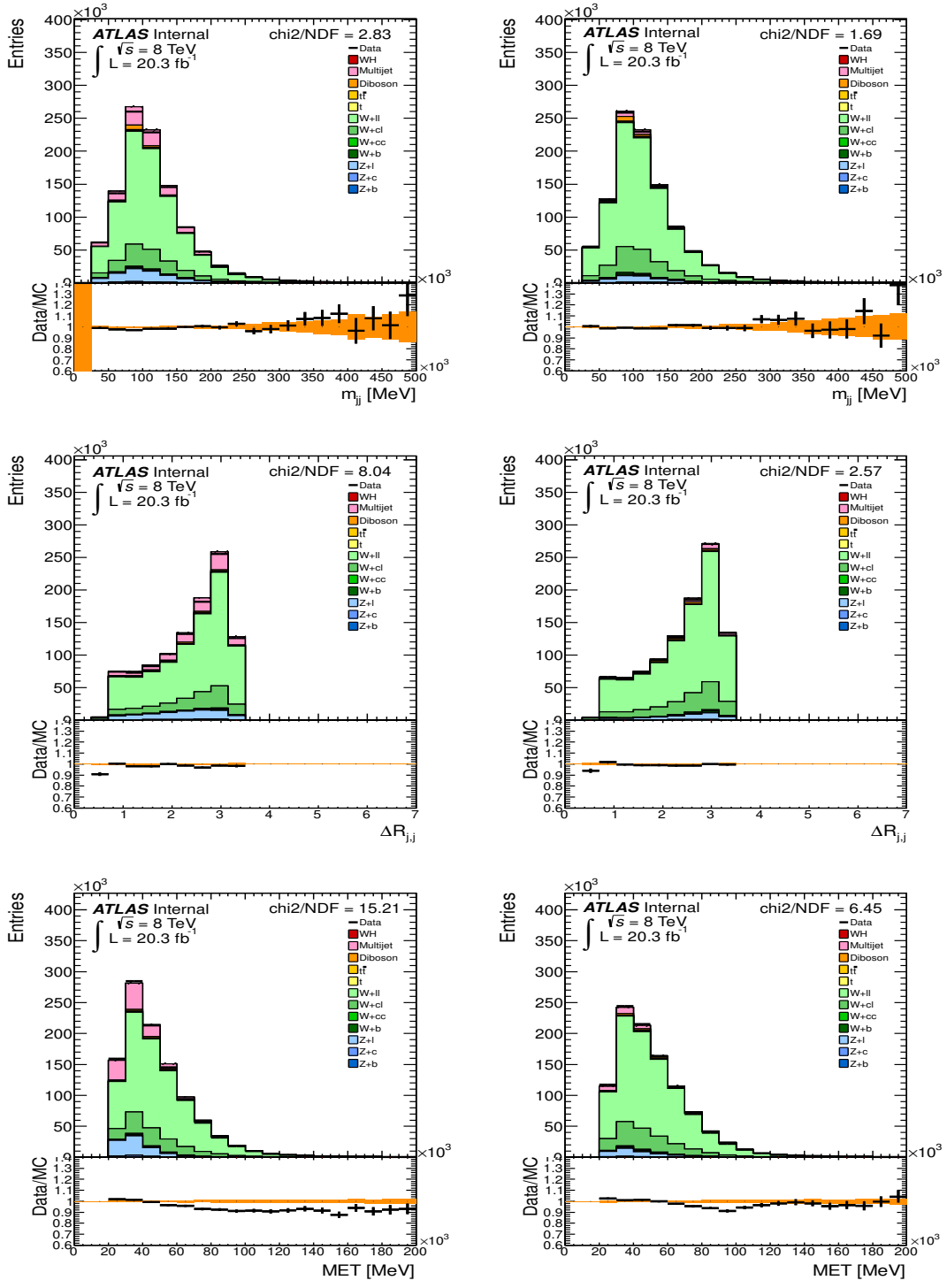

Figure 7.17: The 8 TeV 1-lepton channel - 0 tag region after applying the $\Delta\phi$ correction. Distributions of m_{jj}, ΔR, MET, for electron events (left) and muon events (right)

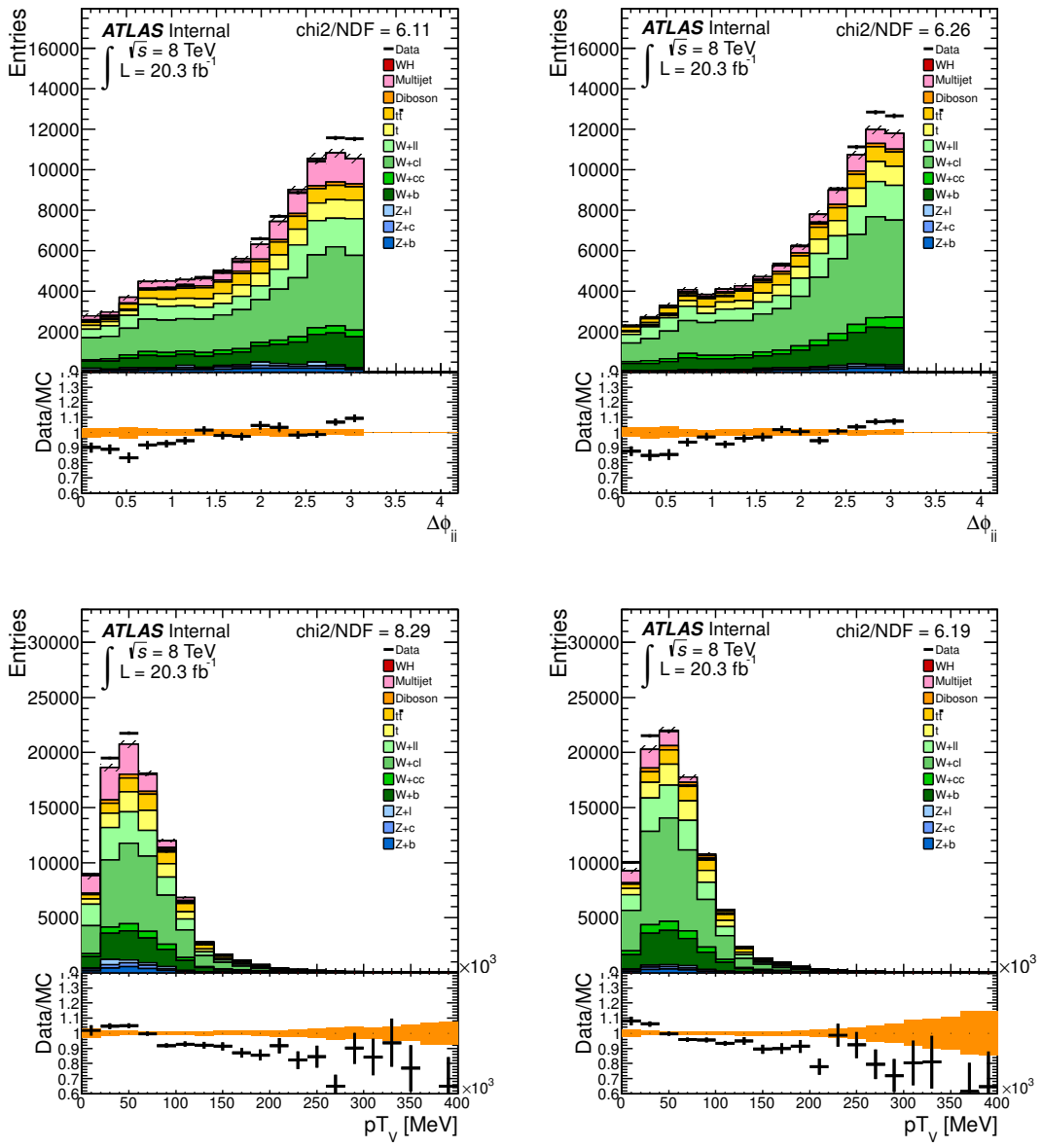

Figure 7.18: Distributions of $\Delta\phi$ and p_T^W with the 1-lepton selection in the 1-tag bin before applying the $\Delta\phi$ correction. The electron channel is on the left and the muon channel is on the right.

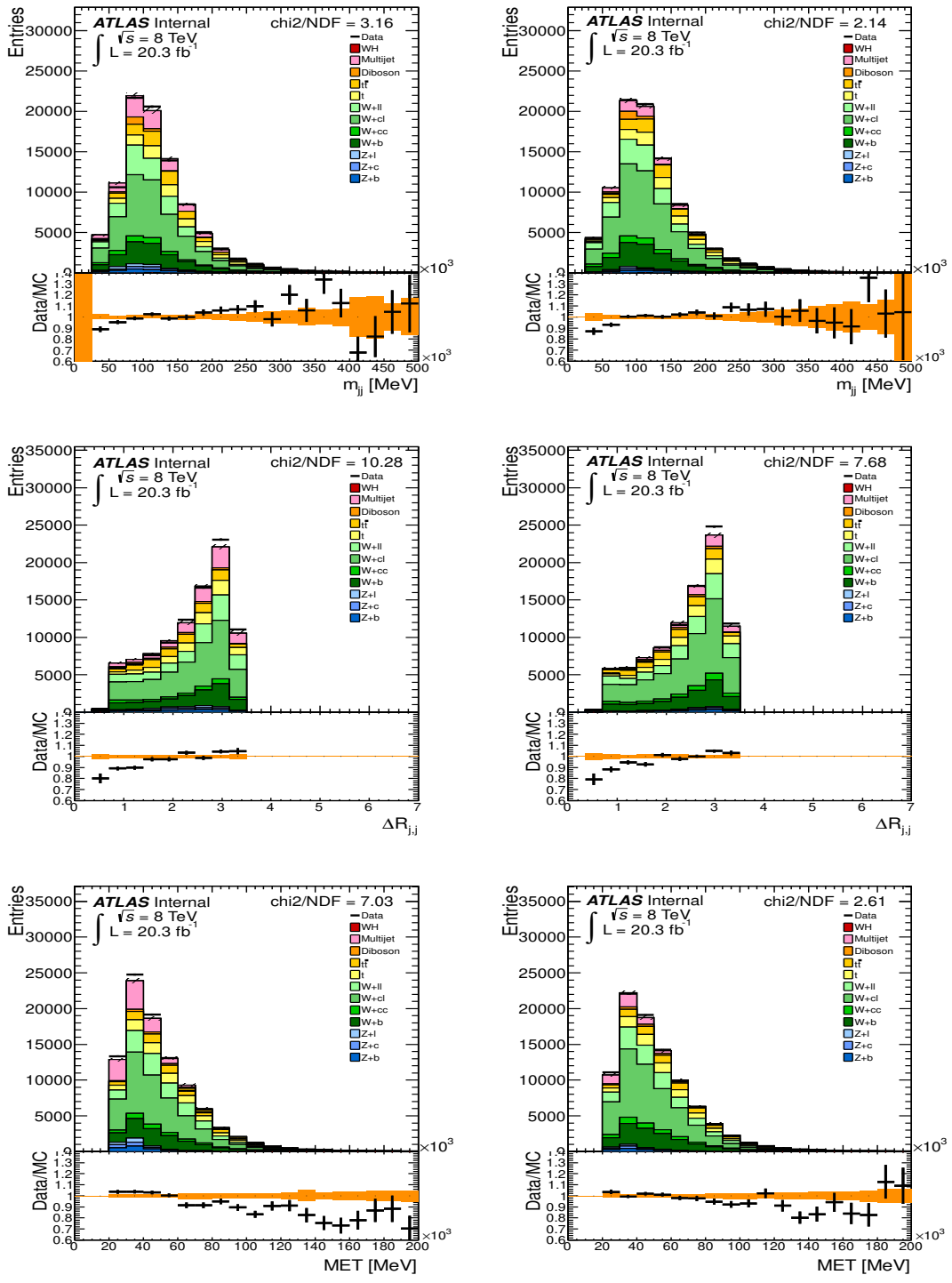

Figure 7.19: The 8 TeV 1-lepton channel - 1 tag region before applying the $\Delta\phi$ correction. Distributions of m_{jj}, ΔR, MET, for electron events (left) and muon events (right)

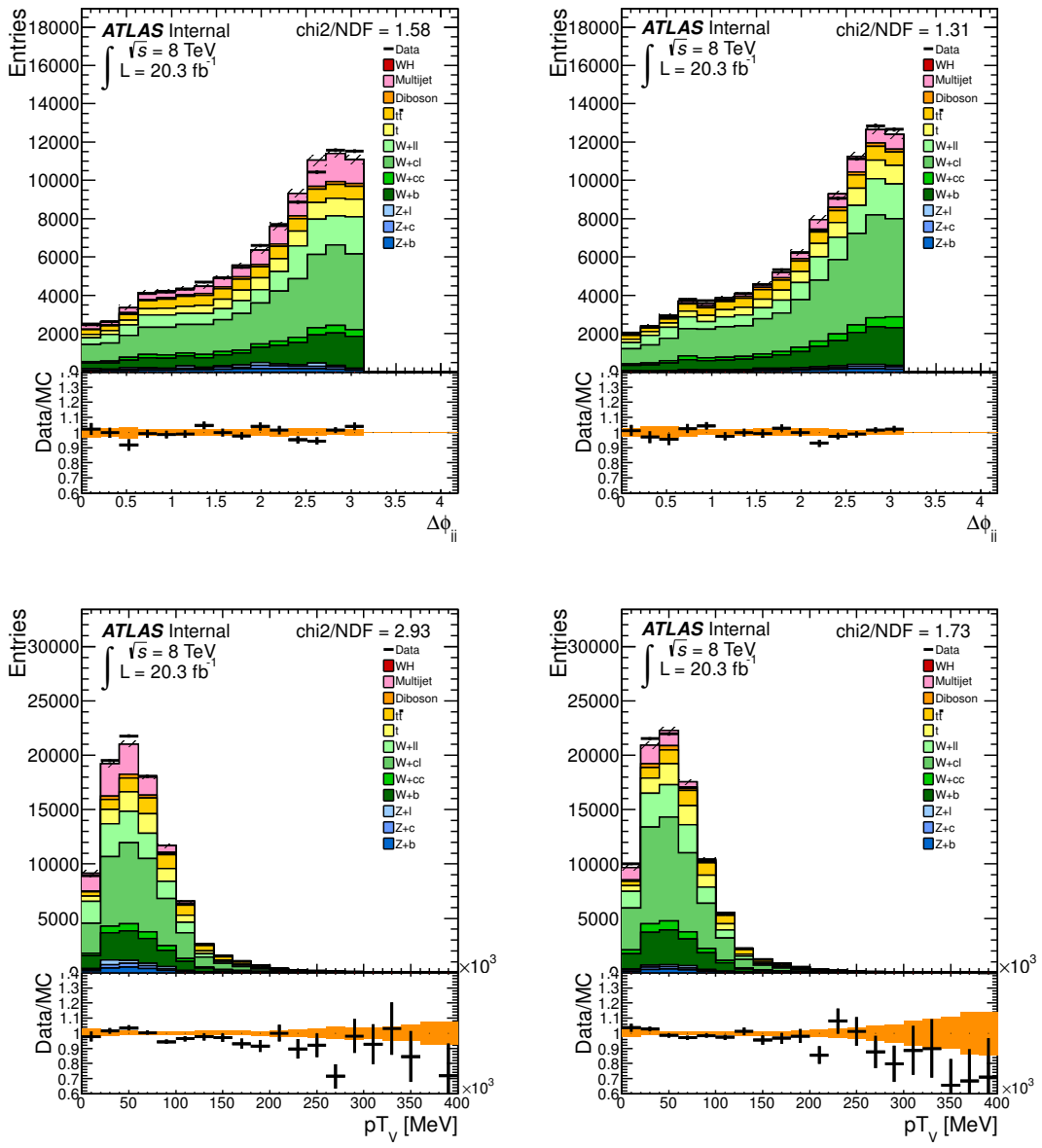

Figure 7.20: Distributions of $\Delta\phi$ and p_T^W with the 1-lepton selection in the 1-tag bin after applying the $\Delta\phi$ correction. The electron channel is on the left and the muon channel is on the right.

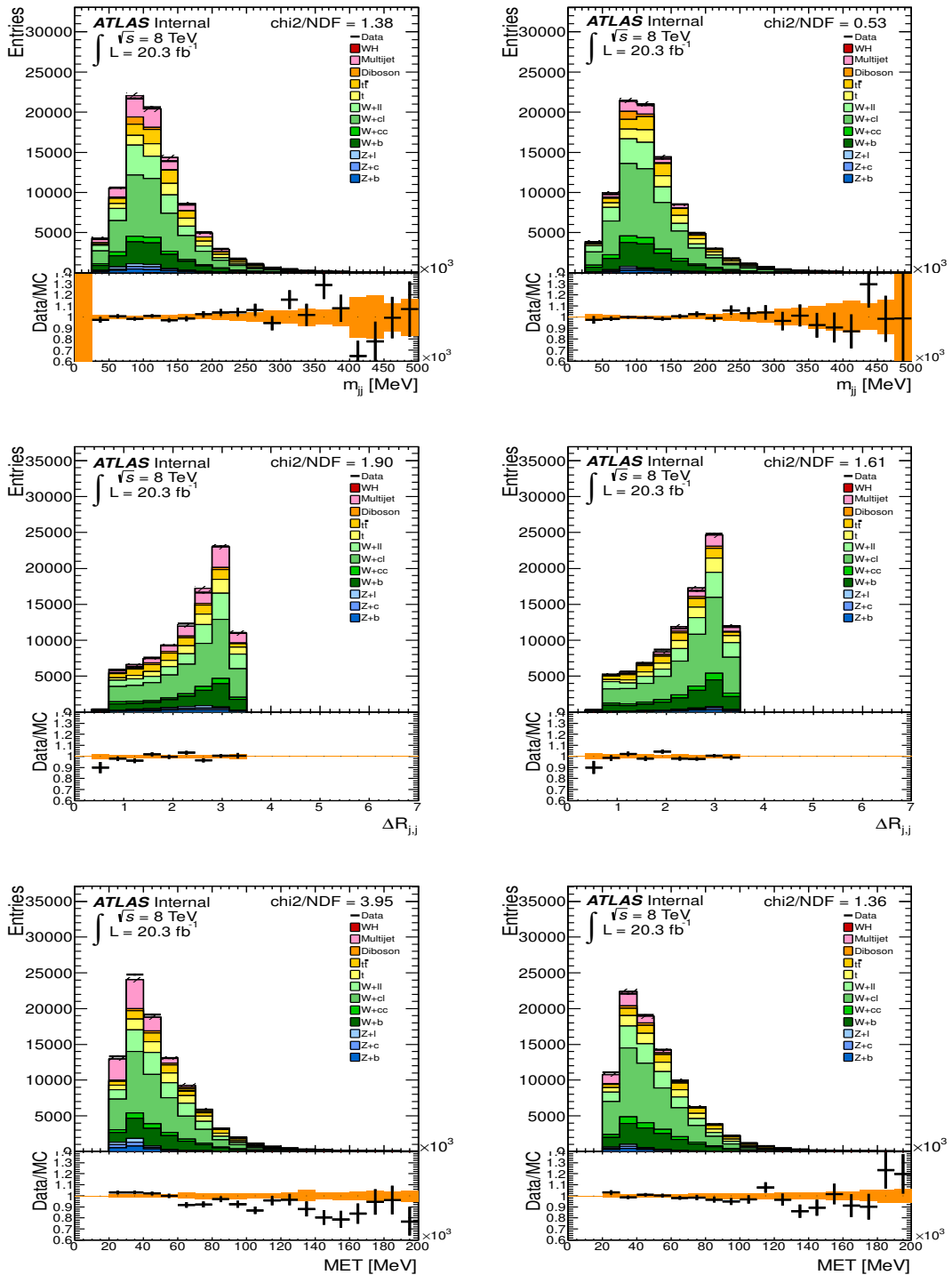

Figure 7.21: The 8 TeV 1-lepton channel - 1 tag region after applying the $\Delta\phi$ correction. Distributions of m_{jj}, ΔR, MET, for electron events (left) and muon events (right)

(a) 1-lepton Electron, 0 b-tag

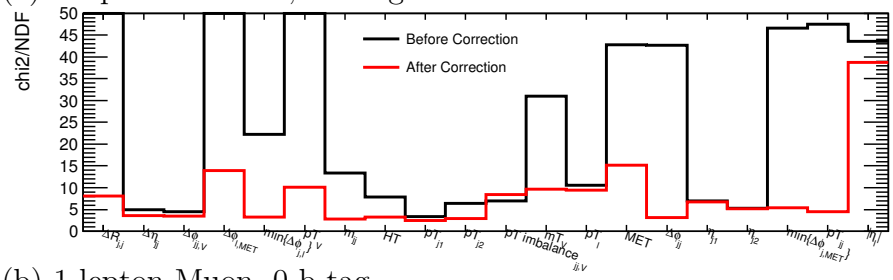

(b) 1-lepton Muon, 0 b-tag

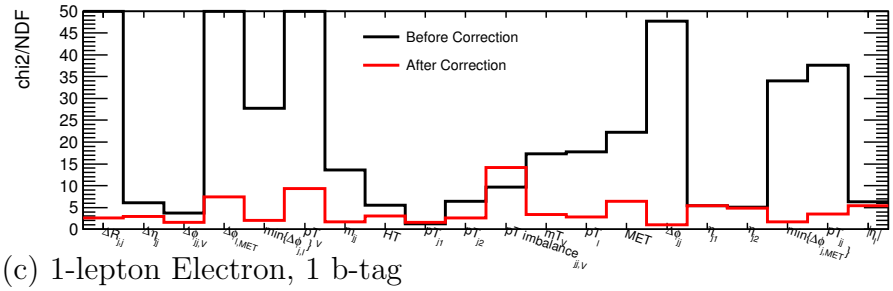

(c) 1-lepton Electron, 1 b-tag

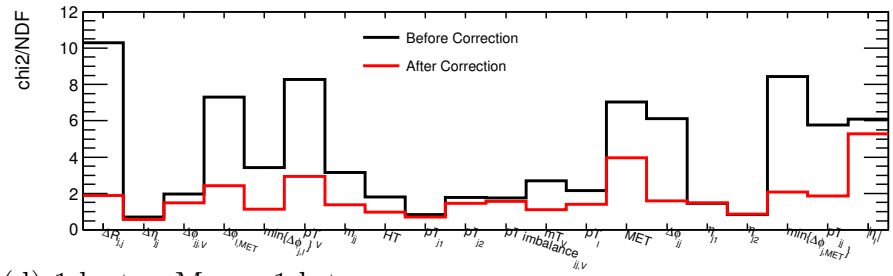

(d) 1-lepton Muon, 1 b-tag

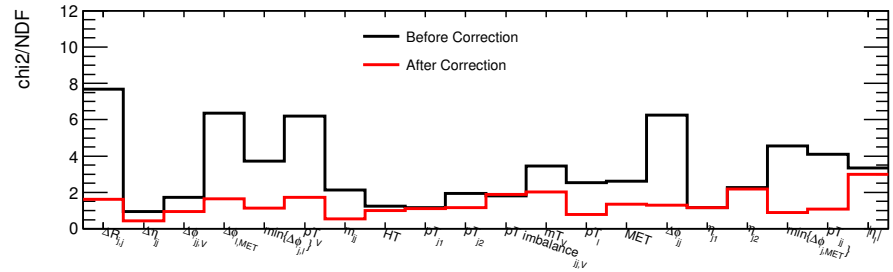

Figure 7.22: Chi2/NDF values for a number of kinematic variables with the 1-lepton selection before $\Delta\phi$ correction (black), and after (red). (a) Electron 0 b-tag control region, (b) Muon 0 b-tag control region, (c) Electron 1 b-tag control region, and (d) Muon 1 b-tag control region.

7.3.2 p_T^W correction

After applying the $\Delta\phi$ correction, a residual mis-modeling of p_T^W distribution still exists in the two highest p_T^W bins, as shown in Fig. 7.23. Due to the small effect of the mis-modeling, no correction is made, but an additional systematic uncertainty is assigned to the normalization of W+jets sample in the highest two p_T^W bins. The systematic assigned to the second highest p_T^W bin is 2%, and 4% for the highest p_T^W bin.

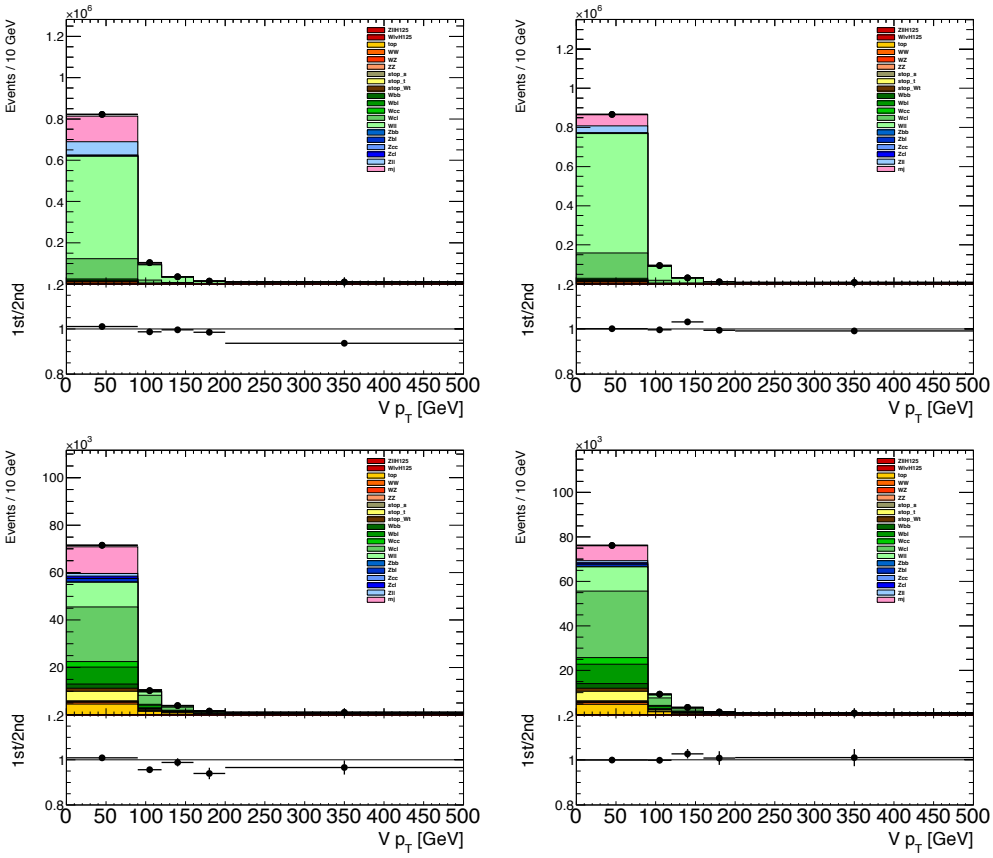

Figure 7.23: p_T^W distribution in 0 tag region (Top) and 1 tag region (Bottom) after $\Delta\phi$ correction, the plots on the left is for electron channel, while the plot on the right is for muon channel.

7.4 Z+jets Background

The Z+jets and W+jets backgrounds are described using the same MC generator, and have similar performance. This section briefly summarizes the the $\Delta\phi$ correction and p_T^Z correction in Z+jets background.

7.4.1 $\Delta\phi$ and p_T^Z Correction

$\Delta\phi$ mis-modeling is also observed in Z+jets background, but less severe. Similar to the W+jets sample, $\Delta\phi$ correction is applied to the Z+jets background. The scale factor is derived from Z+jets control region, where all the other backgrounds are considered to be well described by the simulation. With this assumption, the $\Delta\phi$ distribution of Z+jets background in data is obtained by subtracting all the other background, which is then divided by the $\Delta\phi$ distribution from MC events. The scale factor is shown in Fig. 7.24. The improvement of the $\Delta\phi$ and p_T^Z distributions are shown in Fig. 7.25 and Fig. 7.26.

After applying the $\Delta\phi$ correction, no significant mis-modelling is observed in p_T^Z distribution. Therefore, no correction is applied.

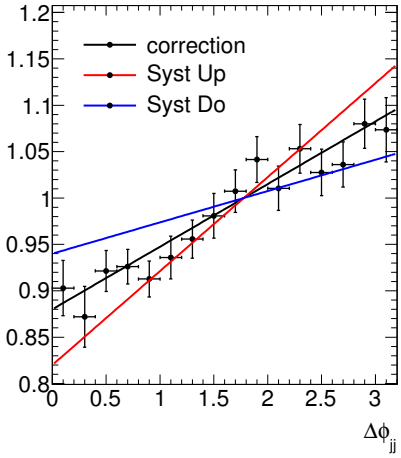

Figure 7.24: The $\Delta\phi$ correction functions calculated for Z+jets as a function of $\Delta\phi$.

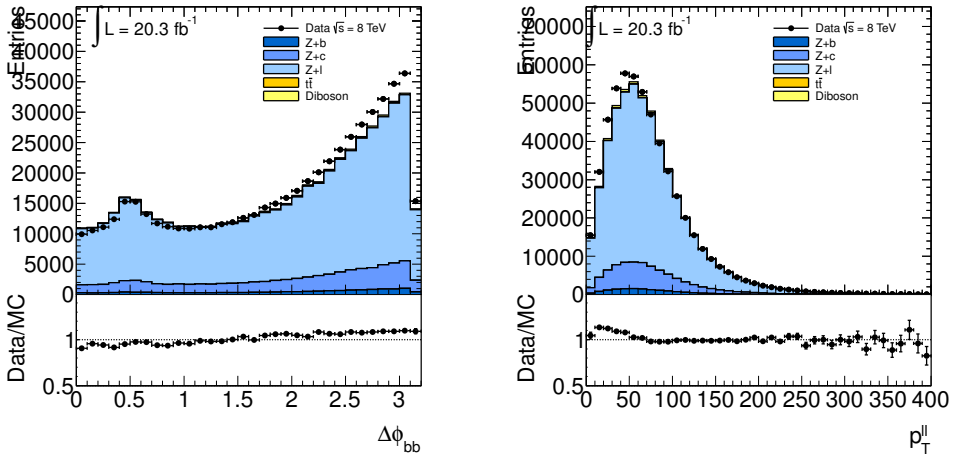

Figure 7.25: Distributions of $\Delta\phi$ between two signal jets and p_T^Z in 0 tag region before applying the $\Delta\phi$ correction.

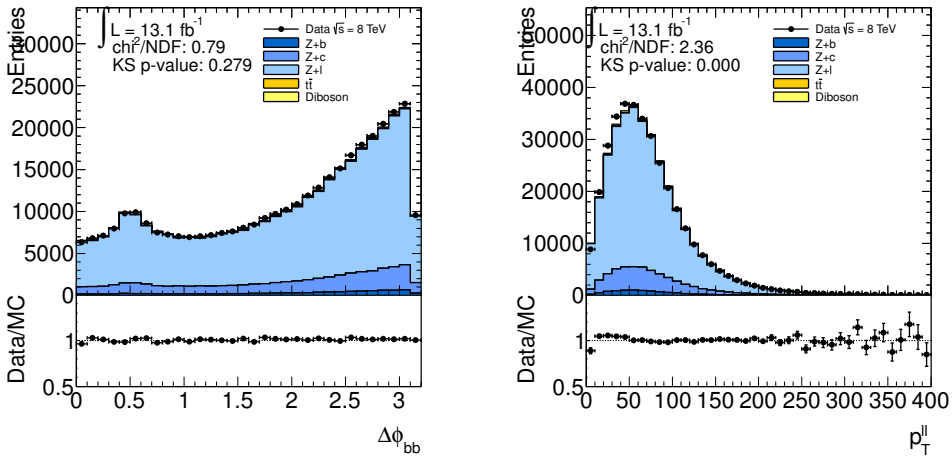

Figure 7.26: Distributions of $\Delta\phi$ between two signal jets and p_T^Z in 0 tag region after applying the $\Delta\phi$ correction.

7.5 Top background

As described in the previous sections, several control regions are used to study the $t\bar{t}$ background. As shown in Fig. 7.27, no $\Delta\phi$ mis-modeling is observed. However, the Powheg-Pythia generator still cannot fully describe the $t\bar{t}$ background, especially in the high p_T^V region. Similar mis-modeling is also observed in the $t\bar{t}H$ analysis. The differential cross section measurement of $t\bar{t}$ process further indicates a mis-modeling originating from p_T distribution of top quarks.

In order to obtain the correction function for top p_T distribution, comparisons are made between data and simulated samples with various generators. Fig 7.28 shows the comparison and ratio between data and MC samples, and the correction function is summarized in Table 7.1 [154].

The correction function in Table 7.1 is obtained in 7 TeV, which can be extrapolated to 8 TeV without any corrections. Fig 7.29 shows the top p_T distribution for both 7 TeV and 8 TeV. In the plot on the left, the mean of top p_T is shifted by 1.8% in 8 TeV comparing to 7 TeV. After scaling the 1.8% in 7 TeV MC sample, good agreement can be observed between 7 TeV and 8 TeV data. Since the 1.8% shift is negligible for top p_T correction, no further correction is needed when extrapolating from 7 TeV to 8 TeV.

Table 7.1: The event weight for the top p_T correction from the unfolding measurement. The uncertainties from the measurement [154].

top p_T(GeV)	0-50	50-100	100-150	150-200	200-250	250-350	350-
Weight	$1.051^{+0.088}_{-0.083}$	$1.029^{+0.028}_{-0.026}$	$0.999^{+0.038}_{-0.038}$	$0.976^{+0.049}_{-0.054}$	$0.915^{+0.057}_{-0.068}$	$0.830^{+0.067}_{-0.073}$	$0.753^{+0.116}_{-0.116}$

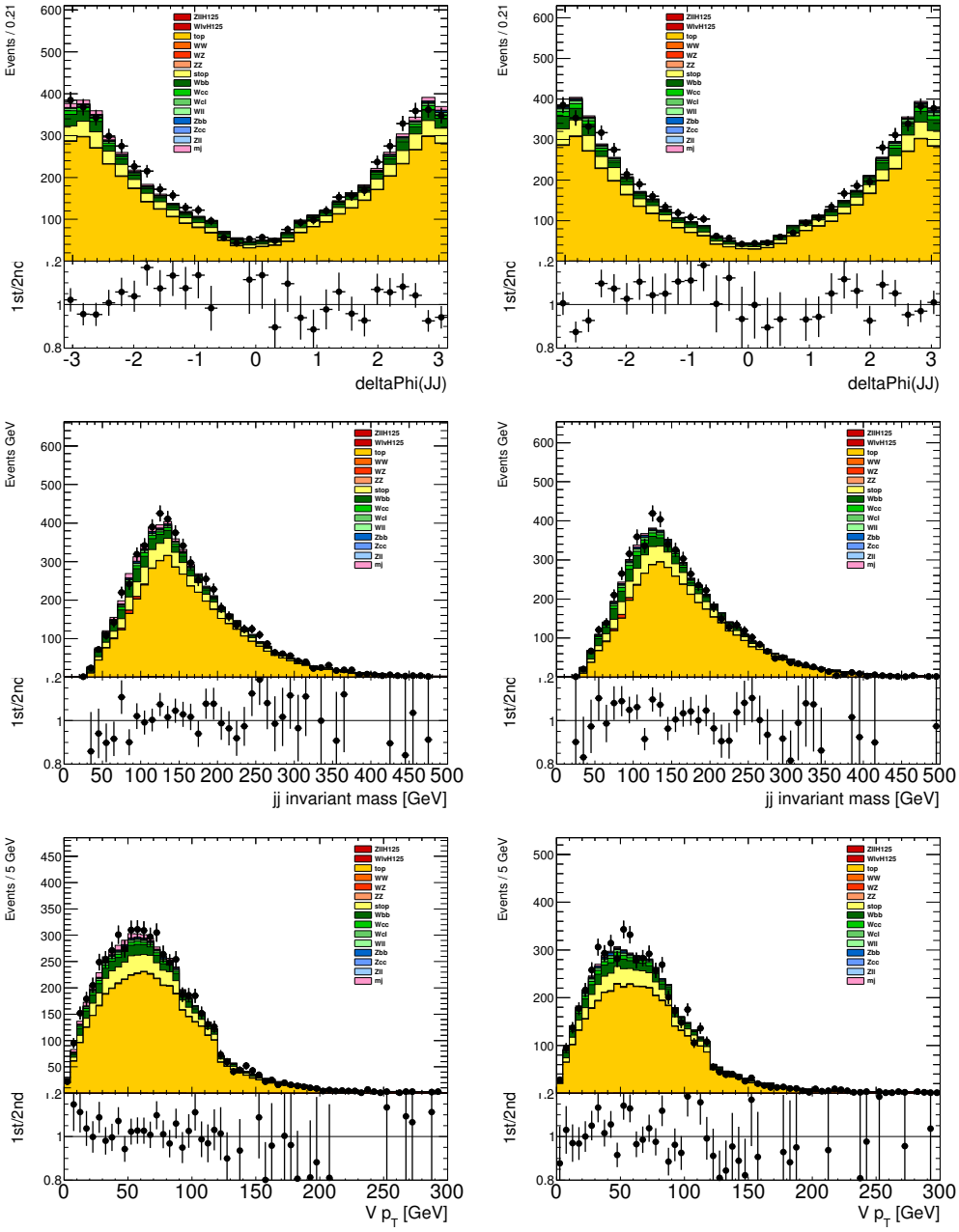

Figure 7.27: The 8 TeV 1-lepton channel - Top control region with 3 jets. Distributions of $\Delta\phi$, m_{jj}, and p_T^W for electron events (left) and muon events (right).

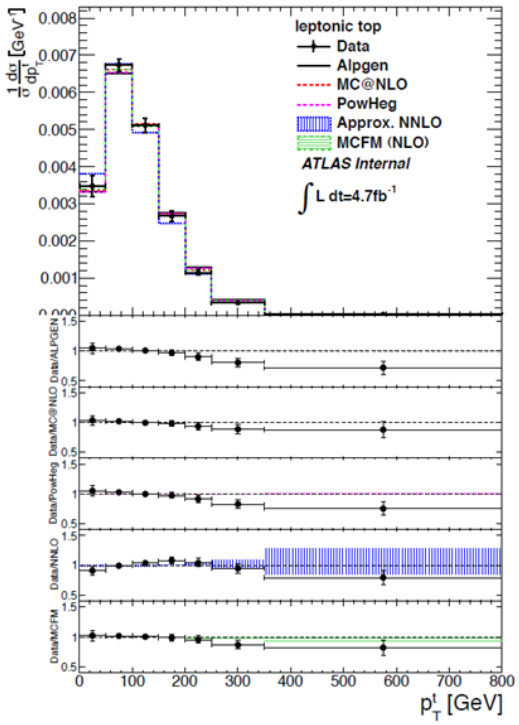

Figure 7.28: The unfolded top p_T differential cross section with 7 TeV dataset.

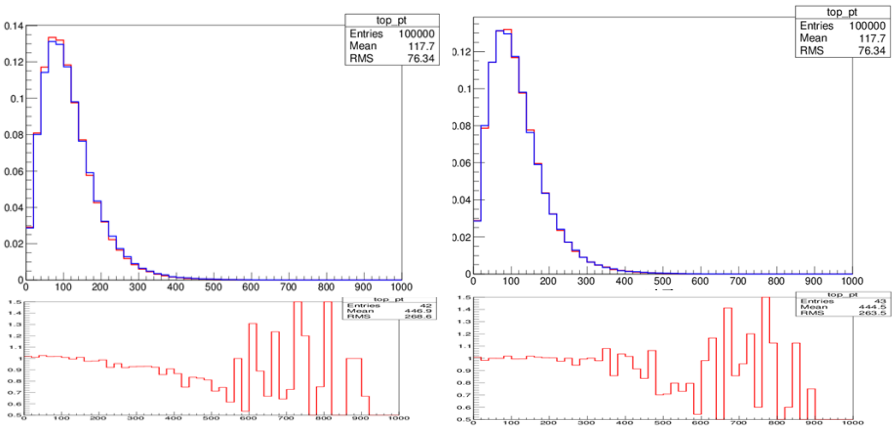

Figure 7.29: (On the left) The comparison of top p_T between 7 TeV (Red histogram) and 8 TeV (blue histogram). (On the right) Same comparison after scaling 1.8% in top p_T in the 7 TeV MC sample [154].

CHAPTER 8

Systematic Uncertainties

This section discusses the source of systematic uncertainties in this analysis, which can be grouped in three categories: experimental systematic uncertainties, background modeling systematic uncertainties, and theoretical uncertainties on signal processes. In the statistical treatment, each uncertainty is treated as a physically-motivated nuisance parameter. Section 8.1 discusses the experimental systematics in this analysis, and section 8.2 focuses on the uncertainties in background modeling. At the end, section 8.3 provides the theoretical uncertainties in signal processes.

8.1 Experimental Uncertainties

Experimental uncertainties are usually related to detector effects, the majority of which are estimated by dedicated measurements in ATLAS, while the rest are developed as part of this analysis. The most relevant uncertainties in this analysis are uncertainties on the b-tagging efficiencies and jet energy scales, along with minor uncertainties on the luminosity measurement, trigger efficiency and

reconstruction of final state objects.

8.1.1 Luminosity and Pile-up Uncertainties

Section 2.2.6 presented the measurement of integrated luminosity in ATLAS experiment. The uncertainty on the integrated luminosity for the 2012 dataset is $\pm$ 2.8%, and $\pm$ 1.8% for the 2011 dataset. The method to derive the uncertainty is described in [117, 118]. The luminosity uncertainties are applied to both signal and background processes that are estimated from Monte Carlo simulation.

Besides the uncertainty on luminosity, an additional uncertainty is applied to this analysis to account for the effect of pile-up, which introduces a 2% shape variation on the m_{jj} distribution.

8.1.2 Electron Specific Uncertainties

Uncertainties are estimated for the electron triggering process, as well as electron reconstruction and identification.

The uncertainty on the electron trigger is evaluated using the tag-and-probe method. The corresponding uncertainty is less than 1%. Therefore no separate nuisance parameter is assigned for the trigger efficiency.

The uncertainty on the electron reconstruction comes from energy and momentum scale, which is referred as **SysElecResol**, with negligible effect on the analysis.

The uncertainty on the electron identification efficiency is also evaluated using tag-and-probe method around the Z boson mass peak. The uncertainties is denoted as **SysElecEffic**, and it is smaller than 1%.

In addition, the uncertainty on the electron isolation is denoted as **SysLepIso**, which is also evaluated using the tag-and-probe method, with value of less than 1%.

8.1.3 Muon Specific Uncertainties

Similar to electron, the muon specific uncertainties are related to trigger, reconstruction, identification and cuts on isolation. Tag-and-probe method are used to evaluate the corresponding uncertainties.

The uncertainty on the muon trigger is negligible, thus no nuisance parameter is assigned to it.

The uncertainty on the muon reconstruction are evaluated separately for inner detector and muon spectrometere, referred to **SysMuonEResolID** and **SysMuonEResolMS**. The effect of these uncertainties is also negligible.

The uncertainties on the muon identification is less than 1%, the associated nuisance parameter is **SysMuonEffic**.

Since the uncertainties on the muon isolation is very small, it is combined with the isolation uncertainty of electron, the associated nuisance parameter is **SysLepIso**.

8.1.4 Jet Specific Uncertainty

The experimental uncertainties related to the jets are uncertainties on jet energy scale (JES), jet energy resolution (JER), and the cut efficiency of jet vertex fraction (JVF).

Jet Energy Scale Uncertainty

Uncertainty on jet energy scale (JES) is one of the leading uncertainties in this analysis. The detailed discussion of JES and its corresponding uncertainty can by found in [139, 140, 141, 142]. In this analysis, the total uncertainties has been broken down into a large number of nuisance parameters, which are summarized below:

- **54 uncertainties for the various in-situ jet energy scale calibration studies.** The in-situ JES analyses includes balance studies with different physics objects, such as Z+jets, photon+jets, and multi-jets. The uncertainties from these balance studies originate from three main sources: differences between MC generators, such as Alpgen, Herwig, and Pythia; differences between selection, calibration, and modeling of different physics objects, such as Z boson, photon, and multi-jet system; and statistical uncertainties of samples used in calibration. These uncertainties are combined into 7 nuisance parameters: **SysJetModel1-4** accounting for physics modeling, and **SysJetStat1-3** accounting for the statistical uncertainties.

- **Two uncertainties for η inter-calibration.** The systematic uncertainty on η inter-calibration arises from the potential mis-modeling of additional radiation that may affect the p_T and η of the di-jet system. The associated nuisance parameter are **SysJetEtaModel** and **SysJetEtaStat**.

- **Four uncertainties for pile-up effects.** Most of pile-up related uncertainties are dependent on the average number of interactions per bunch crossing and the number of primary vertices in the event, the associated nuisance parameters are **JetMu**, **JetNPV**, **JetPilePt**. In addition, one uncertainty is dependent on the energy density of the event, with an associated nuisance

parameter **JetPileRho**.

- **One uncertainty for additional b-jet energy scale uncertainty.** This uncertainty is to account for the detector response to b-jets. Since the final states objects in this analysis include two b-jets, the b-jets energy scale becomes an important source of uncertainty, the associated nuisance parameter is **SysJetFlavB**. To evaluate this uncertainty, different MC simulations are used to study the detector response to b-jet. The corresponding variation is between 1% and 2%.

- **One uncertainty for the non-closure term of the Monte Carlo simulations.** Various of MC samples are used when evaluating the jet energy scale. This uncertainty is to account for the differences in the jet response between different MC samples. The associated nuisance parameter is **SysJetNonClos**.

- **One uncertainty for the effect of close-by jets.** In this analysis, the jet energy scale is derived with isolated jets. However, non-isolated jets may have a different response comparing to isolated jets. This uncertainty accounts for the difference in response between isolated jets and non-isolated jets. The associated nuisance parameter for this uncertainty is **SysJetCloseby**, with a negligible effect to this analysis.

- **Two uncertainties for flavor composition and response.** The background processes in this analysis consists of jets with different flavors. These two uncertainties account for the difference of flavor composition and their corresponding responses between different MC samples. The jet flavor composition is the fraction of light-quark and gluon initiated jets presented in the sample, while the jet flavor response is calorimeter response to these two type of jets. The different calorimeter responses results in a specific jet energy

scale for the specific MC sample. The associated nuisance parameters are **SysJetFlavComp** and **SysJetFlavResp**, the total uncertainty is about 4%.

- **One uncertainty for jets with $p_T > 1$ TeV.** The corresponding nuisance parameter (**SysJetHighPt**) is derived by treating the jets as superpositions of single-particle energy deposits rather than summed clusters. In this analysis, the effect of this uncertainty is negligible.

Overall, the systematic uncertainty on JES ranges from 3% at 20 GeV to 1% for 1 TeV jet. The sources listed above are accounted for by varying each source by the value of its uncertainty and recalculating the observables in the signal region. In the final statistical treatment, each source of systematic are considered as uncorrelated Gaussian constrained nuisance parameters.

Jet Energy Resolution Uncertainty

In this analysis, the jet energy resolution is found to be well described by the simulated samples. The range of jet energy resolution is about 25% at 20 GeV, and about 5% at 1 TeV. The relative systematic uncertainty on jet energy scale is evaluated from the differences in resolution between data and MC. The associated nuisance parameter for this analysis is **JetEResol**, and the corresponding effect to this analysis is derived by smearing the jet p_T according to a gaussian distribution centered at 1, with a width equal to the true resolution plus the value of relative uncertainty given by the p_T and η of the jet.

Jet Vertex Fraction Uncertainty

The associated nuisance parameter for jet vertex fraction (JVF) uncertainty is **SysJetJVF**. The method used to determine the size of this uncertainty is provided by the JetEtMiss group. For a given JVF cut, the corresponding efficiency is different from data and MC. To calculate the uncertainty, the value of JVF cut is varied up and down to create two additional cuts, which can be used to simulate the JVF cut efficiency discrepancy between data and MC. These two additional cuts are then propagated through the analysis chain to determine the change on the m_{bb} distribution. The corresponding value for this uncertainty is about 1%.

8.1.5 B-tagging Uncertainty

In this analysis, the b-tagging efficiencies are calibrated separately for jets with different flavors, such as b-jets, c-jets and light jets. These calibrations are then applied as MC to data scale factors, which depend on the jet p_T and η. The uncertainties of these scale factors are corresponding to the statistical and systematic uncertainties of the calibration.

Different nuisance parameters are created for jets with different flavors. For b-jets, totally 7 (10) nuisance parameters are used to model the p_T dependence of the b-tagging efficiency for 2012 (2011) data, named as **SysBtagBXEffic**, where X is from 0 to 6 in 2012, and from 0 to 9 in 2011. For c-jets, 6 (5) nuisance parameters are used to account for the possible p_T dependence, named as **SysBtagCXEffic**, where X is from 0 to 5 (4) in 2012 (2011). For light-jet, a single nuisance parameter named **SysBtagLEffic** is used.

8.1.6 MET Specific Uncertainty

MET (E_T^{miss}) is calculated from the vectorial sum of all detected physics objects, like electron, muons, taus, photons, jets and clusters of calorimeter cells not associated to the objects above. Therefore, all the systematic uncertainties on the reconstructed objects are propagated to the MET calculation. In addition, the uncertainties of the scale (**METScaleSoftTerms**) and resolution (**METResoSoftTerms**) of the energy in calorimeter clusters which are not associated with reconstructed objects also contribute to the total uncertainties. The "SoftTerm" uncertainties affect the low E_T^{miss} region more than other regions.

8.2 Background Modeling Uncertainties

The following section discusses the non-experimental systematics that account for the uncertainties on background modeling, which include shape systematic on m_{bb} and p_T^V distributions, 3 jets to 2 jets ratio, etc.

8.2.1 W+jets Modeling Uncertainty

The nuisance parameter associated with the uncertainty of the distribution of m_{bb} is **SysWMbb** for W+light jets samples, and **SysWbbMbb** for W+heavy flavor jets. The distribution of m_{bb} can be affected by several sources of systematic uncertainties:

- **Uncertainty from $\Delta\phi$ correction.** In one lepton channel, the mis-modeling of W+jets observed in 0-tag control region is corrected through a reweighting of the $\Delta\phi$ distribution. One systematic uncertainty is assigned to account

for the impact of this reweighting on the m_{bb} distribution. The value of this uncertainty is evaluated by scaling the $\Delta\phi$ corrections up and down by 50% (100%) of the original correction value for W+light jets (W+heavy flavor jets), and taking the full differences between the resulting m_{bb} shape and the norminal m_{bb} shape. The uncertainty on $\Delta\phi$ mainly comes from the normalization of multi-jets background. To account for this uncertainty, the multi-jets background has been both removed and doubled to recalculate the $\Delta\phi$ correction. In both cases, the change of $\Delta\phi$ is much smaller than the 50% (100%) of uncertainty we assigned to it. Therefore, the systematic uncertainty we assigned for $\Delta\phi$ is quite conservative. The effect of multi-jet background variation on the $\Delta\phi$ correction is shown on Fig. 8.1.

Uncertainty from MC generator. To evaluate the m_{bb} shape uncertainty from different MC samples, a generator level comparison is performed between Sherpa, Powheg, and MC@NLO. Fig 8.2 shows the comparison between different MC samples before and after the $\Delta\phi$ correction. The ratio between Sherpa and MC@NLO is taken as a function of m_{bb}, **SysWbbMbb** = p0 + p1 $\times$ m_{bb}/[MeV] with p0= 0.88 $\pm$ 0.03, and p1 = (1.2 $\pm$ 0.3) $\times$ 10^{-3}.

Beside the uncertainty on the m_{bb} shape, an additional systematic is defined to account for the uncertainty on the normalization ratio between 3 jets region and 2 jets region. This uncertainty is derived by comparing the ratio between various MC samples, such as Sherpa, Alpgen, Powheg, etc. From the comparison between all these samples, the largest difference is taken as the uncertainty. For W+light jets sample, the uncertainty is taken as 10%, while for W+heave flavor jets samples, the uncertainty is taken as 20%.

Finally, one systematic uncertainty is assigned to the fractions of W+bl, W+bb and W+cc events in W+hf jets samples. Since the fractions will change for each category

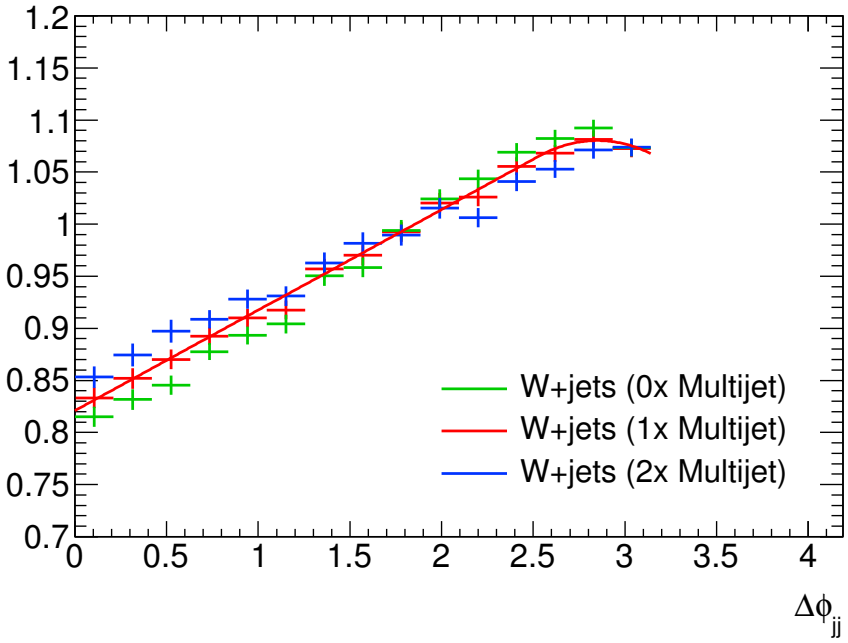

Figure 8.1: Recalculation of the $\Delta\phi$ correction in 1 lepton channel with multijet contribution varied up and down by 100%.

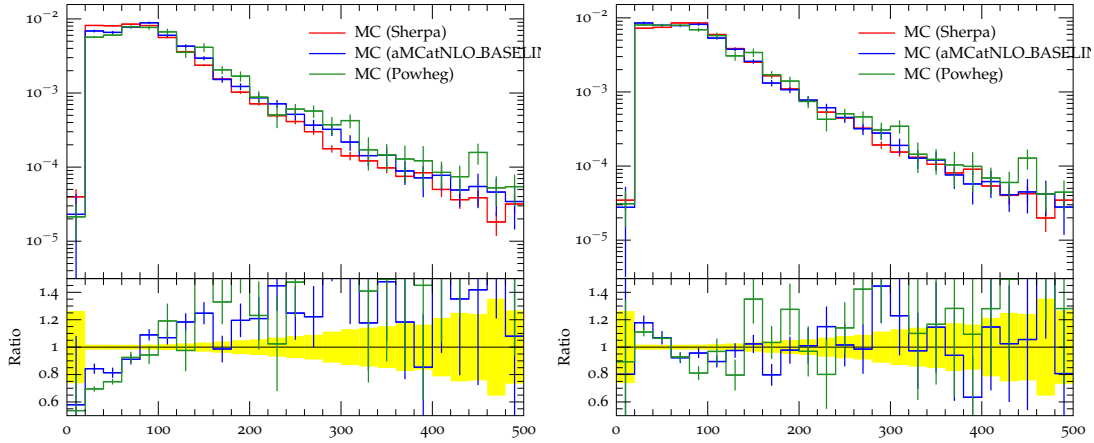

(a) m_{bb} distribution

(b) m_{bb} reweighted distribution

Figure 8.2: Comparison of m_{bb} shape between different MC samples. The ratio shown are calculated with respect to Sherpa. The plot on the left is before $\Delta\phi$ correction, while the plot on the right is after $\Delta\phi$ correction.

and is not necessarily well determined in MC sample, the W+hf contribution is allowed to float with an uncertainty. This uncertainty is evaluated with the W+bb sample at generator level, resulting in a value of 30% on the fractions. For the W+cl sample and W+l sample, they are allowed to float independently.

8.2.2 Z+jets Modeling Uncertainty

Since Z+jets has a negligible contribution to one lepton channel, the modeling uncertainty of Z+jets is not considered.

8.2.3 $t\bar{t}$ Modeling Uncertainty

To account for the systematics uncertainties in the m_{bb} shape, p_T^W distribution, and 3 jets to 2 jets ratios, detailed study is performed on $t\bar{t}$ background modeling by comparing different MC samples. The baseline Powheg $t\bar{t}$ sample is compared to MC@NLO Alpgen predictions. During the comparison, the effect of initial and final state radiation was investigated with dedicated samples, and the impact of parton shower was also studied by comparing with Powheg interfaced with Herwig and Powheg interfaced with a different Pythia tune.

Fig. 8.3 shows the comparison of the m_{bb} shape between different MC samples, and the corresponding ratio to the baseline prediction. During the comparison, the largest variation is obtained as corresponding uncertainty. So we have **SysTopMbb** = p0 + p1 $\times$ m_{bb}/[MeV], with p0 = 1.05 $\pm$ 0.02, and p1 = (-3.4 $\pm$ 1.2) $\times$ 10^{-7}.

Fig. 8.4 shows the ratio of events in 3 jets region and 2 jets region from different MC samples. By comparing these distributions, a 5% uncertainty is assigned on the normalization of $t\bar{t}$ background in 3 jets region (**SysTop3JNorm**).

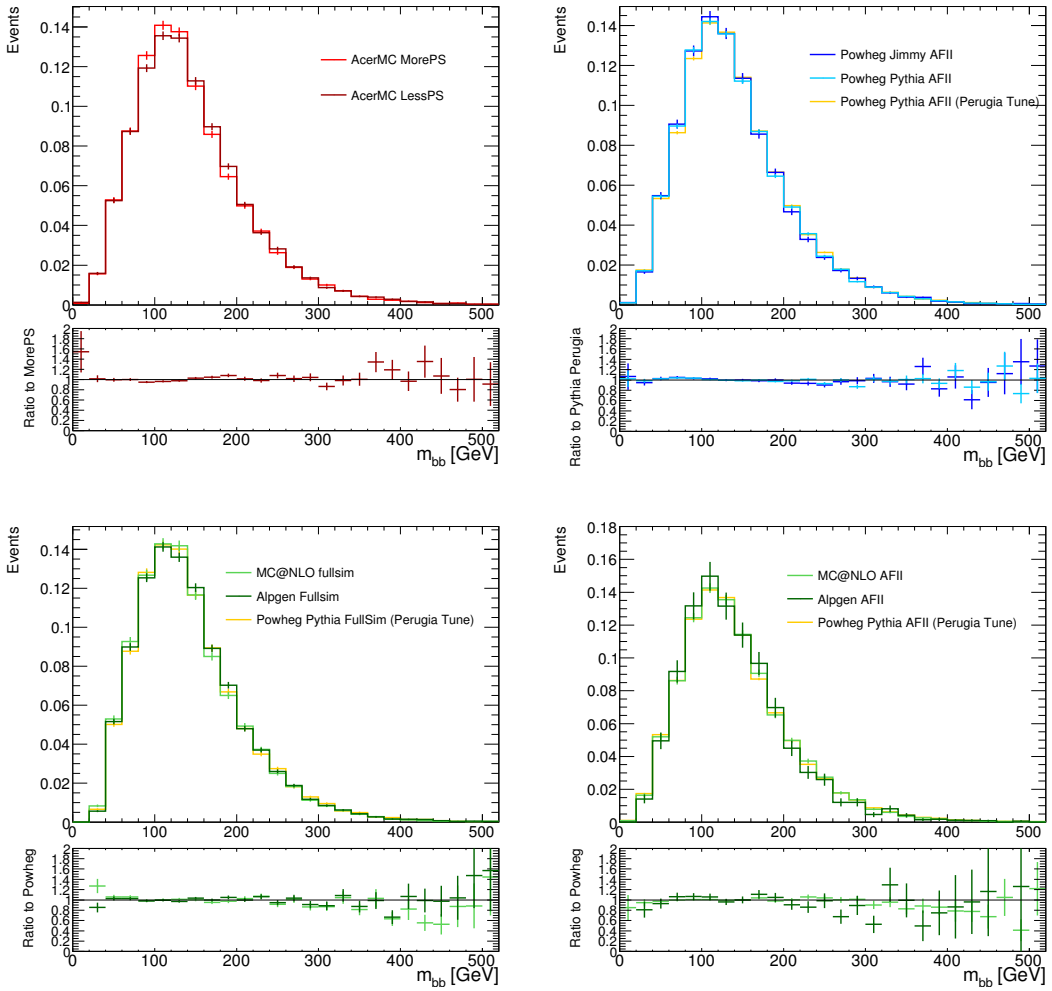

Figure 8.3: Comparison of m_{bb} distribution between different $t\bar{t}$ MC samples.

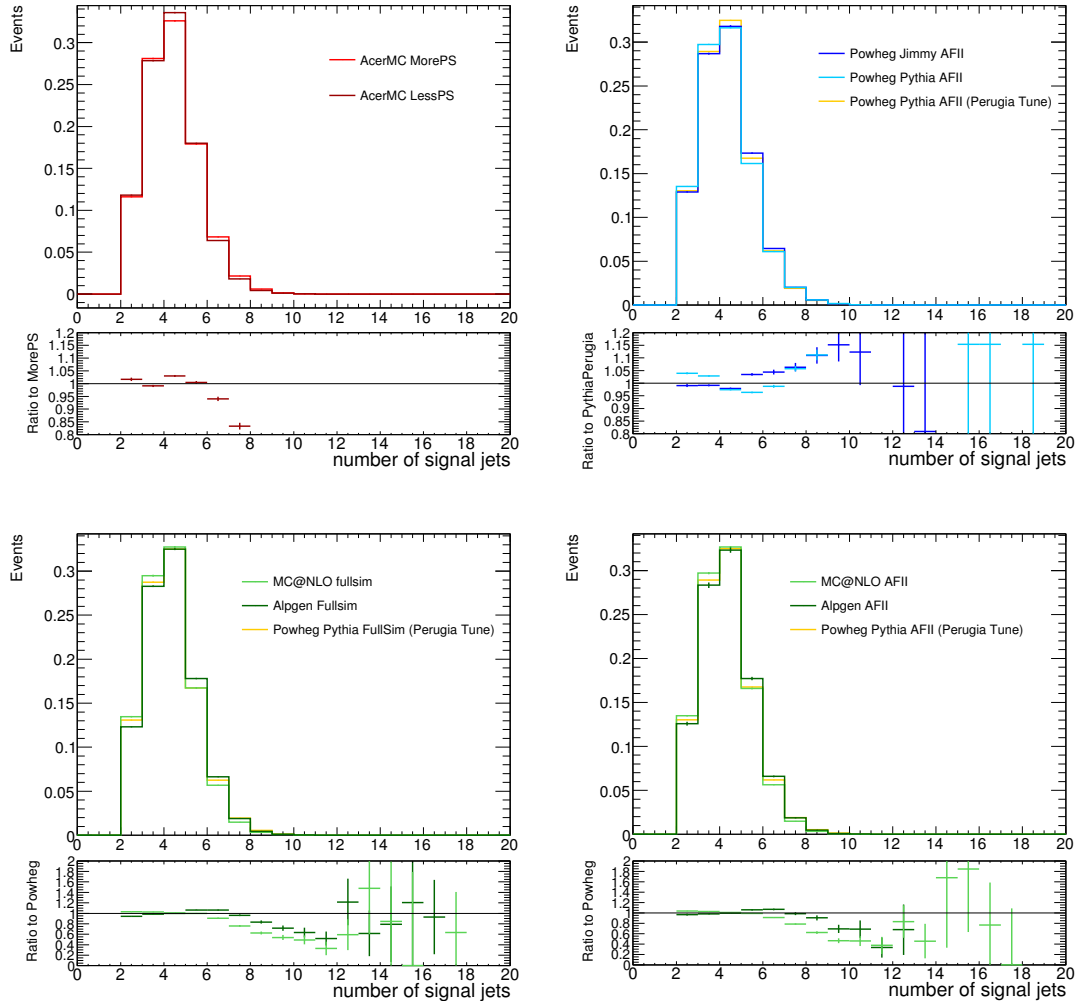

Figure 8.4: Comparison of distribution of number of jets between different $t\bar{t}$ MC samples.

Finally, an additional top p_T systematic is assigned to $t\bar{t}$ modeling as **SysTopPt**, which is defined as half of the top p_T correction.

8.2.4 Single-top Modeling Uncertainty

The single-top background has three channels: Wt-, t-, and s-channels, with corresponding uncertainties on the normalization of 7%, 4% and 4%, respectively.

The modeling uncertainty is also split into the Wt-, t-, and s-channels. In each channel, systematic uncertainties were considered on m_{bb} shape, p_T^W shape and the ratio of events between 3 jets region and 2 jets region. The systematics were estimated by comparing different MC generators.

For m_{bb} shape uncertainty, t and s channels are combined together because of low statistics. The corresponding uncertainty is taken from t channel, since it has much larger uncertainties comparing to s channel.

The p_T^W shape uncertainty is estimated by comparing MC samples. In each p_T^W bin, a systematic uncertainty of $< 5\%$ is assigned.

The uncertainty on 3 jets to 2 jets ratio is also derived by comparing different MC samples. Uncertainties of 13%, 9%, and 9% are assigned to the 2 jets to 3 jets extrapolation for Wt-, t-, and s-channels respectively.

Fig. 8.5 shows the m_{bb} comparison in one lepton channel. Fig 8.6 shows the p_T^W distributions for different MC samples. The distributions of number of jets in each single top channel are shown in Fig. 8.7, from which the uncertainty on 3 jets to 2 jets ratio is derived.

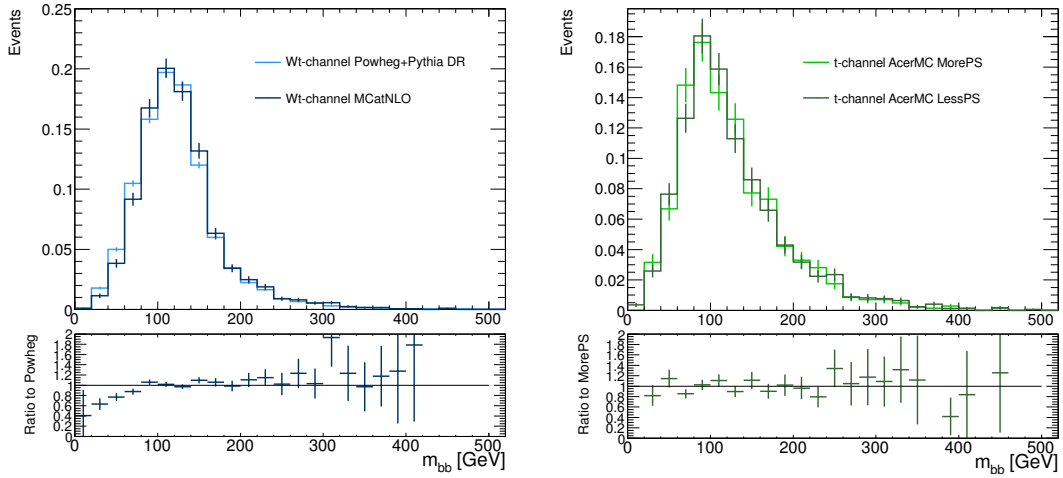

(a) Wt-channel

(b) t-channel

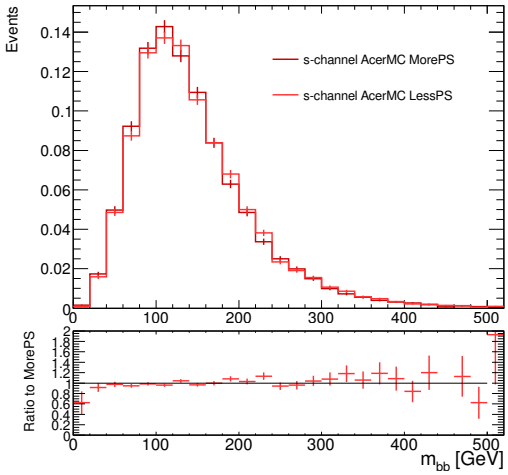

(c) s-channel

Figure 8.5: Distribution of m_{bb} in each single top sample from different MC samples. Blue lines is for Wt channel, green line is for t channel, red line is for s channel.

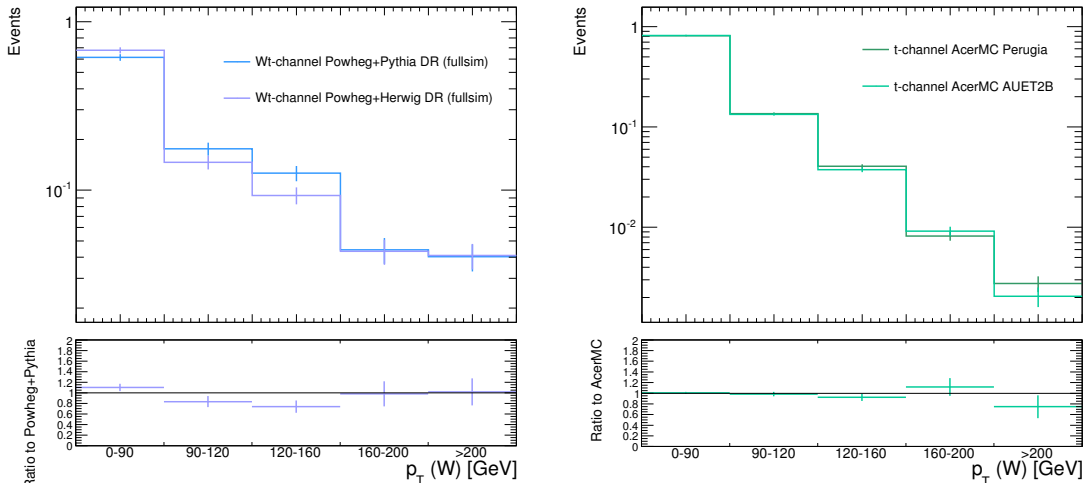

(a) Wt-channel (b) t-channel

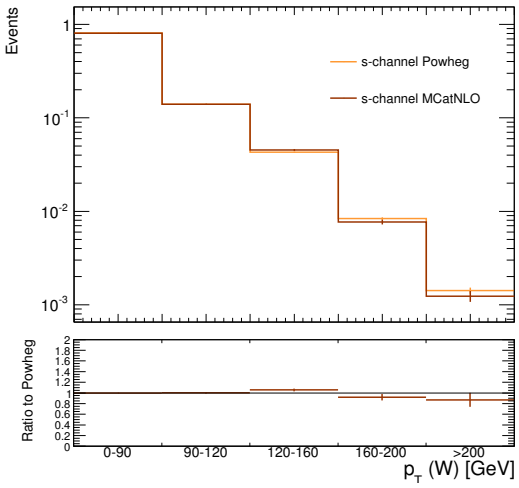

(c) s-channel

Figure 8.6: Distribution of p_T^W in each single top sample from different MC samples. Blue lines is for Wt channel, green line is for t channel, red line is for s channel.

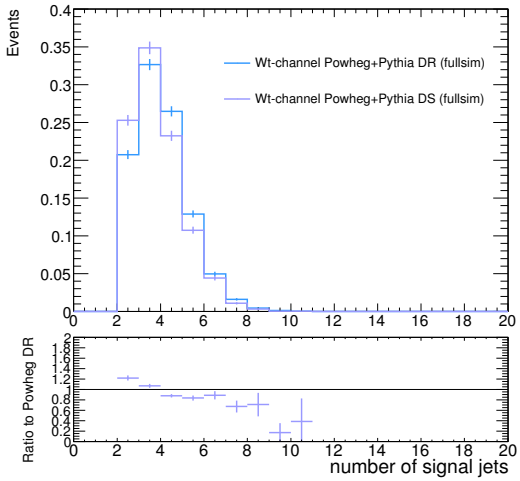

(a) *Wt*-channel

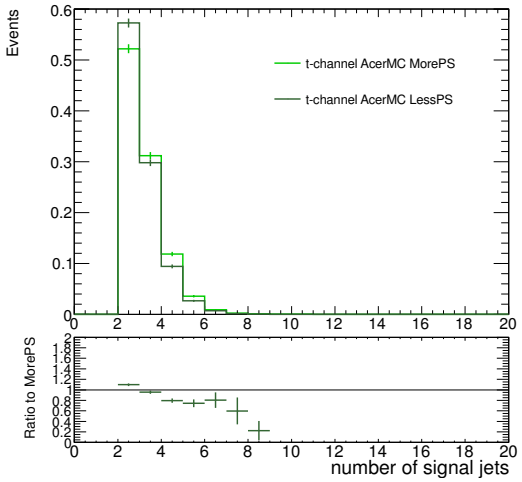

(b) *t*-channel

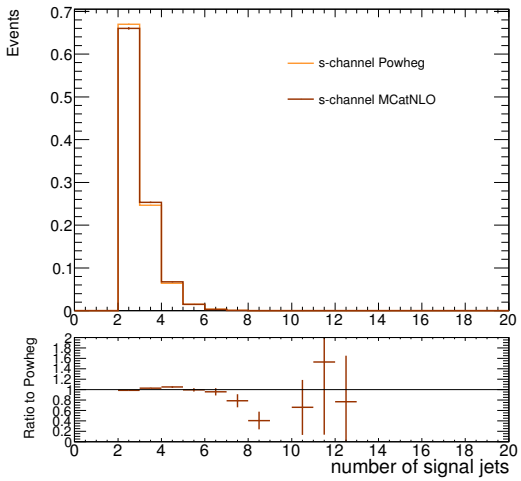

(c) *s*-channel

Figure 8.7: Distribution of the number of jets in each single top sample from different MC samples. Blue lines is for Wt channel, green line is for t channel, red line is for s channel.

8.2.5 Di-boson Modeling Uncertainties

Since the di-boson process has exactly the same final state as the signal process, it is one of the irreducible background sources in one lepton analysis. Di-boson production contains three different processes : WZ, WW, and ZZ. In the one lepton channel, the dominant di-boson process is WZ production with $Z \to b\bar{b}$ and $W \to \ell\nu$. Uncertainties on di-boson modeling are evaluated by comparing MC samples with different generators. As a result, a p_T^W uncertainty of 5-60% is applied for different p_T^W bins, and a 5-7% normalization uncertainty is applied to the total cross section.

8.3 Signal Modeling Uncertainties

The uncertainties on signal modeling contains the uncertainty on branching ratio of Higgs decay to $b\bar{b}$, and uncertainties on inclusive cross section of Higgs boson at $\sqrt{s} = 7$ TeV and 8 TeV.

For the branching ratio of Higgs decay to $b\bar{b}$, the relative uncertainty varies from 2.5% to 4.3% in the m_H range from 115 GeV to 135 GeV. The associated nuisance parameter is **SysTheoryHbbBr**, with 3.3% uncertainty when $m_H = 125$ GeV.

The uncertainties on the inclusive Higgs production cross section can be divided into normalization scale uncertainties and PDF uncertainties, with associated nuisance parameters **SysTheoryWHScale** and **SysWHPDF**, respectively. The normalization scale uncertainty is calculated to be of the order or 0.5%, and the PDF uncertainty is about 3.5%.

CHAPTER 9

Global Fit

The goal of this analysis is to determine the compatibility between data and the Standard Model prediction of the VH process. To achieve this goal, a fit is performed globally for the combination of zero lepton channel, one lepton channel, and two lepton channel.

The global fit employs a binned likelihood function $\mathscr{L}(\mu, \theta)$ constructed as product of Poisson probability terms. In this fit, the parameter of interest is defined as the normalized signal strength parameter, μ, which is the ratio of cross section times branching ratio measured in time to the cross section times branching ratio predicted by the Standard Model.

$$\mu = \frac{\sigma \times BR}{\sigma_{SM} \times BR_{SM}} \tag{9.1}$$

The dependence of the signal and background predictions on systematic uncertainties is described by the nuisance parameters, θ, which is parametrised by

either Gaussian or log-normal priors or left free without any priors. Therefore, the expected number of events for signal and background processes can be described as functions of θ. The test statistics is then constructed as :

$$q_\mu = -2ln\frac{\mathscr{L}(\mu, \hat{\hat{\theta}}_\mu)}{\mathscr{L}(\hat{\mu}, \hat{\theta})} \tag{9.2}$$

In Eq. 9.2, $\hat{\hat{\theta}}_\mu$ are nuisance parameter values that maximise the likelihood for a given μ, while $\hat{\mu}$ and $\hat{\theta}$ are the parameters that maximise the likelihood with a constrain that $0 \leq \hat{\mu} \leq \mu$. This test statistic is then used to evaluate the compatibility between the background only model and observed data, as well as to determine the exclusion intervals derived with the CL_s method[161, 162].

The global fit is performed in both signal regions and control regions, which allows a direct evaluation of normalization scale factors for some of the background processes. The high statistic in control region can also helps constraining the experimental uncertainties, such as JES and JER.

The fit to determine the compatibility between data and the Standard Model prediction of VH process is denoted as Higgs fit. In addition, another fit with same model is performed as validation, by measuring the cross section of Standard Model di-boson process: WZ/ZZ with Z $\rightarrow b\bar{b}$.

Section 9.1 provides the input to the fit, and section 9.2 discusses the fit model used in this global fit. In the end, section 9.3 presents the fit result.

9.1 Global Fit Input

The global fit is performed in both signal regions and control regions in three channels. Therefore, the input to the fit contains information from many regions, as summarized in Table 9.1.

Channel	2T2J	2T3J	1T2J	1T3J	Top $e\mu$
Requirement	2 jets, 2 b-tagged	3 jets, 2 b-tagged	2 jets, 1 b-tagged	3 jets, 1 b-tagged	$e+\mu$+2 b-tagged jets
0 lepton	3 × (N+S)	3 × (N+S)	3 × N	3 × N	-
1 lepton	7 × (N+S)	5 × (N+S)	5 × N	5 × N	-
2 lepton	5 × (N+S)	5 × (N+S)	5 × N	5 × N	5 × N

Table 9.1: Number of regions entering the global fit. N+S stands for a region where both m_{bb} shape information and normalization information enters the global fit. N labels a region where only normalization information enters the global fit.

As shown in table 9.1, both number of events and the m_{bb} shape information are used for regions with 2 b-tagged jets, while in 1 b-tagged region, only number of events are used in the fit. In one lepton channel 2J signal region, there are two additional regions for events with $p_T^W > 160$ GeV with E_T^{miss} trigger selections. These two regions contain small number of events, and have small impact to the final result.

In each region, there are numerous background processes and signal processes, as summarized in table 9.2

	sub processes
VH Signal	WH, ZH
W+jets	W+light, W+cl, W+cc, W+bl, W+bb
Z+jets	Z+light, Z+cl, Z+cc, Z+bl, Z+bb
Top pair	$t\bar{t}$
Di-boson	WW, WZ, and ZZ
Single top	Wt channel, t channel, s channel
Multi jet	Multi-jets

Table 9.2: Signal and background processes included in global fit.

As a result, there are totally 59 regions entering the global fit. Among these regions, 31 of them only provide normalization information, while the rest of them provide both m_{bb} shape information and normalization information. In each region, there are 18 background processes and VH signal processes.

Each signal and background process is associated by various systematic uncertainties. Therefore, a large amount of nuisance parameters are included in the global fit. The nominal value of nuisance parameters are described in chapter 8. After performing the fit, the value of nuisance parameters will be changed, which could be evaluated by checking the pulls of each parameter, and used as a symptom of a physics mis-modeling. Beside the nominal value, the error on each nuisance parameter can also be changed after the fit. Before the fit, the error is usually $\pm$ 1σ deviation of the nominal value. The error after the fit can indicate an initial underestimate or overestimate of the uncertainty.

9.2 Global Fit Model

9.2.1 Free Parameters

In order to determine the normalization scale factors for some of the backgrounds, their corresponding nuisance parameter are floated freely as a free parameter in the fit. The free parameters are scale factors for $t\bar{t}$, W+cl, W+hf, Z+cl, Z+hf, and multijet. Here cl indicates a c-jet plus a light jet, while hf indicates a mixture of heavy flavor jets components, which contains a b-jet plus a light jet (bl), two c-jets (cc), and two b-jets (bb). In order to account for the mis-modeling of relative ratios between W/Z+hf samples (bl, cc, and bb), an additional nuisance parameter is assigned for each component with a gaussian prior. The multijet background is

included only in one lepton channel, its floating normalisation scale factor is set to be uncorrelated between each b-tag and jet multiplicity region. In 2 b-tag 3 jets region, since the contribution of multijet background is only 2%, its normalization is fixed to its nominal value with a 50% log-normal prior. In 1 b-tag 3 jets region, the normalization is fixed to nominal value in 7 TeV dataset only for the same reason.

9.2.2 Nuisance Parameters

Splitting Nuisance Parameter

For each systematic uncertainty described in chapter 8, there is one associated nuisance parameter. However, some of the systematic uncertainties are further divided in the fit model to account for the differences between processes and regions, which lead to more than one nuisance parameters.

The uncertainty on jet flavor composition and response represents the uncertainty on quarks-gluons fraction. Since the flavor composition are different for different processes, this uncertainty is de-correlated between different MC samples. According to quarks-gluons fraction of the jets, the MC processes can be grouped into four categories: W+jets, Z+jets, top (contains both single top and $t\bar{t}$) and signal like (di-boson plus VH signal), each of which holds one flavor composition nuisance parameter.

The uncertainty on top p_T is split into three nuisance parameters, one for two lepton channel, one for the 2jets region in 0 and 1 lepton channels, and one for the 3 jets region in both 0 and 1 lepton channels.

The uncertainty on $\Delta\phi$ correction are decorrelated across 2jets regions and 3jets

regions and different flavor compositions (W/Z+l,W/Z+c,W/Z+b). Therefore, totally 12 nuisance parameters for on $\Delta\phi$ correction.

In order to account for the different jet flavor composition in different regions, the uncertainty on m_{bb} shape is also split. The jet flavor composition is shown in table 9.3 and table 9.4. In the high p_T^V regions in 1 lepton channel, the two jets selected as b-jets contains a large contribution of bc, which is consistent with what happened in 0 lepton channel, where only 3 high p_T^V bins are used. In the two low p_T^V regions in 1 lepton channel, the contributions of bc jets becomes very small. In 2 lepton channel, the contribution of bc jets are negligible. Therefore, the uncertainty on m_{bb} shape is split into 5 nuisance parameters, one for 2 lepton channel, two for the first two p_T^V bins in 1 lepton channel discriminating 2jets regions and 3jets regions, two for the rest of p_T^V bins in 0 and 1 lepton channels discriminating 2jets regions and 3jets regions.

Multi-jets related nuisance parameters only exist in 1 lepton channel, and de-correlated across b-tag and jet multiplicities.

All the di-boson systematics are un-correlated across WW, WZ, and ZZ, expect for the uncertainty on 3 jets to 2 jets ratio, which is 25%.

All the other systematics except the ones mentioned above are correlated across different processes, channels, p_T^V bins, jet multiplicities and b-tag multiplicities.

Pruning Nuisance Parameters

VH analysis is divided into various control regions and signal regions. Limited statistic in each region results in systematic templates with large fluctuations, which introduce large noise to the fit. To reduce the noise from low statistic, following treatment is performed on nuisance parameters.

		$t\bar{t}$ flavor composition in different p_T^V (GeV) bins				
		0-90	90-120	120-160	160-200	>200
0 lepton channel	bb			81%	59%	24%
	bc			14%	32%	62%
1 lepton channel	bb	88%	88%	82%	59%	22%
	bc	9%	10%	14%	33%	64%
2 lepton channel	bb	99.2%	99.2%	98.6%	94.7%	92.6%
	bc	0.5%	0.6%	0.8%	2.9%	7.4%

Table 9.3: $t\bar{t}$ flavor composition in 2jets 2 b-tagged region in all three channels for 8 TeV dataset

		$t\bar{t}$ flavor composition in different p_T^V (GeV) bins				
		0-90	90-120	120-160	160-200	>200
0 lepton channel	bb			72%	45%	12%
	bc			22%	46%	74%
1 lepton channel	bb	83%	79%	68%	37%	12%
	bc	14%	17%	27%	52%	74%
2 lepton channel	bb	97.4%	97.5%	96.3%	92.9%	83.4%
	bc	1.6%	1.2%	2.4%	4.7%	12.2%

Table 9.4: $t\bar{t}$ flavor composition in 3jets 2 b-tagged region in all three channels for 8 TeV dataset

- Reduce the statistical fluctuations by rebinning. The bins are merged in m_{bb} distribution until the nominal distribution has less than 5% statistical uncertainty.

- Separate normalization uncertainty from shape variations. The normalization is taken into account as a log-normal prior, while the shape variation is considered as a gaussian prior. In the fit model, the shape variations has not effect to the event yield. Fig 9.1 shows the decomposition of systematic uncertainty into a normalisation uncertainty and a shape uncertainty.

- Uncertainties with less than 0.5% variation in event yield is neglected.

- Uncertainties are also neglected if both up and down variation have the same sign.

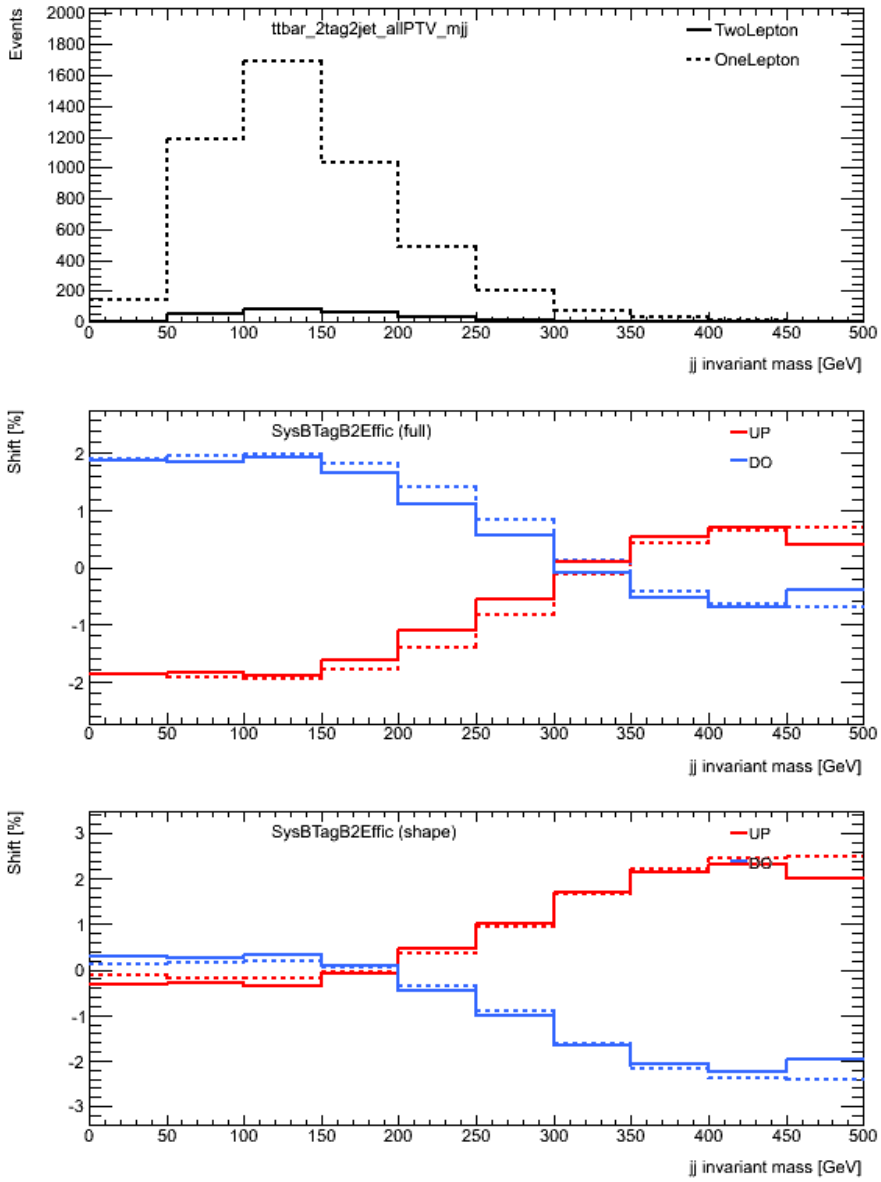

Figure 9.1: The decomposition of a systematic uncertainty into a normalization uncertainty and a shape uncertainty. The uncertainty is a b-tagging uncertainty in the 3rd p_T^V bin of 2 jets 2 b-tagged region for $t\bar{t}$ background. The normalization uncertainty is 1.76%.

9.2.3 Combination of 7 TeV and 8 TeV data

It is important to appropriately correlate systematics when combining the datasets with different center of mass energies. In general, the systematic uncertainties evaluated using different methods or different MC samples should be un-correlated.

Among experimental systematics, all systematics related with lepton are treated as correlated uncertainties between 7 and 8 TeV. Systematics related with E_T^{miss} are de-correlated between 7 and 8 TeV, as well as the systematics related to the b-tag efficiencies. For the systematics related with JES, it depends on the method that is used when evaluating them. The JES uncertainties that are correlated between 7 TeV and 8 TeV are : **JetStaX**, **JetMixedX**, **JetHighPt**, **JetEtaModel**, **JetMu**, **JetNPV**, **JetNonClosure**, **JetFlavResp**, **JetFlavComp**, **JetFlavB**. All other JES uncertainties are treated as un-correlated systematics between 7 and 8 TeV.

For the modeling systematics uncertainties, such as the ones on top p_T correction and $\Delta\phi$ correction, they are all set as correlated between two datasets.

9.3 Global Fit Result

This section provides the result of global fit for a Higgs boson with mass 125 GeV. The outcome from the fit is grouped into three categories: post fit yields in all three channels, nuisance parameter pulls and correlations, and post fit m_{bb} distributions in 2-btag region.

9.3.1 Post Fit Yields

This section provides the post fit yields in the 2 b-tag regions for 0 lepton, 1 lepton and 2 lepton channels. Table 9.5 provides the post fit values of the background scale factors that floats freely during the fit. Table 9.6 and 9.7 shows the post fit yields in 2T2J region and 2T3J region for 0 lepton channel. Table 9.8 and 9.9 shows the post fit yield in 2T2J region and 2T3J region for 1 lepton channel, table 9.10 shows the post fit yield in 2T2J region with E_T^{miss} trigger for 1 lepton channel. Table 9.11 and 9.12 shows the post fit yield in 2T2J region and 2T3J region for 2 lepton channel.

Backgrounds	2011	2012	2011 + 2012
W+cl	1.8±0.22	0.97±0.16	1.05±0.14
W+hf	1.13±0.26	0.76±0.15	0.90±0.15
Z+cl	0.92±0.53	1.14±0.38	0.89±0.48
Z+hf	1.27±0.12	1.25±0.08	1.30±0.07
$t\bar{t}$	1.14±0.08	1.11±0.06	1.12±0.05
multijet 1T2J 2011	0.20±0.44	-	0.59± 0.40
multijet 2T2J 2011	0.74±0.35	-	0.95 ±0.24
multijet 1T2J 2012	-	0.89±0.21	0.94± 0.17
multijet 1T3J 2012	-	1.16±0.26	1.28±0.19
multijet 2T2J 2012	-	0.98±0.13	0.97±0.13

Table 9.5: Background normalization scale factors derived from the fit.

	ZeroLepton , 2T2J		
	$120 < p_T^V < 160$ GeV	$160 < p_T^V < 200$ GeV	$p_T^V > 200$ GeV
Zl	5.46±1.57	1.66±0.47	1.51±0.43
Zcl	12.82±6.98	3.82±2.06	2.87±1.55
Zcc	42.47±12.93	11.77±3.56	12.99±3.95
Zbl	22.92±6.00	8.01±2.10	4.62±1.22
Zbb	509.47±20.19	134.71±5.63	91.71±4.65
Wl	10.05±2.40	1.84±0.48	0.91±0.24
Wcl	23.93±3.11	4.41±0.62	2.07±0.31
Wcc	19.40±5.51	5.48±1.55	5.88±1.70
Wbl	6.74±2.11	1.43±0.46	0.80±0.25
Wbb	84.36±12.87	22.94±3.41	19.24±2.92
StopWt	11.90±1.03	3.60±0.37	0.99±0.11
Stopst	45.07±2.45	5.68±0.39	0.83±0.13
ttbar	253.90±11.03	40.80±2.05	10.84±0.86
mulitjet	10.76±12.61	2.37±0.00	1.60±0.00
WW	1.38±0.24	0.35±0.07	0.49±0.08
ZZ	36.14±4.82	16.78±1.99	15.21±1.36
WZ	14.71±2.58	4.85±0.86	3.99±0.72
Bkg	1111.49±21.76	270.50±5.47	176.54±5.12
ZvvH125	1.72±5.88	0.96±3.27	1.03±3.52
WlvH125	0.45±1.52	0.19±0.65	0.15±0.52
ZllH125	–	–	–
Signal	2.17±7.40	1.15±3.91	1.18±4.04
data	1142	286	175

Table 9.6: The post fit yield in zero lepton 2T2J regions for both 7 and 8 TeV.

	ZeroLepton , 2T3J		
	$120 < p_T^V < 160$ GeV	$160 < p_T^V < 200$ GeV	$p_T^V > 200$ GeV
Zl	1.41±0.38	0.52±0.14	0.55±0.15
Zcl	3.71±2.00	1.42±0.76	1.33±0.71
Zcc	11.06±3.37	4.29±1.33	5.65±1.71
Zbl	6.91±1.67	2.83±0.73	1.97±0.48
Zbb	127.69±6.35	48.47±2.43	38.54±2.20
Wl	2.47±0.61	0.58±0.15	0.37±0.10
Wcl	7.62±1.26	1.86±0.32	1.08±0.20
Wcc	6.94±2.13	2.09±0.64	2.27±0.70
Wbl	2.79±0.97	0.69±0.27	0.50±0.18
Wbb	32.42±5.98	9.80±1.89	7.83±1.51
StopWt	12.37±1.24	3.89±0.41	2.81±0.31
Stopst	21.04±2.20	3.50±0.57	0.49±0.06
ttbar	274.64±7.97	55.79±2.02	15.85±0.98
mulitjet	7.07±9.56	1.27±0.00	0.78±0.00
WW	0.57±0.20	0.20±0.09	0.13±0.09
ZZ	5.50±2.80	2.94±2.37	3.60±0.88
WZ	3.84±1.92	1.09±0.84	0.94±0.24
Bkg	528.06±13.26	141.22±3.41	84.70±2.59
ZvvH125	0.45±1.53	0.28±0.94	0.36±1.23
WlvH125	0.15±0.50	0.05±0.16	0.04±0.15
ZllH125	–	–	–
Signal	0.59±2.03	0.32±1.09	0.40±1.38
data	570	131	88

Table 9.7: The post fit yield in zero lepton 2T3J regions for both 7 and 8 TeV.

	OneLepton , 2T2J				
	$p_T^V < 90$ GeV	$90 < p_T^V < 120$ GeV	$120 < p_T^V < 160$ GeV	$160 < p_T^V < 200$ GeV	$p_T^V > 200$ GeV
Zl	11.94±3.09	0.93±0.23	0.18±0.05	0.11±0.03	0.03±0.01
Zcl	18.95±10.18	1.78±0.96	0.35±0.19	0.17±0.09	0.05±0.03
Zcc	15.34±4.67	2.34±0.71	0.56±0.17	0.37±0.12	0.13±0.04
Zbl	14.72±3.98	1.90±0.54	0.99±0.25	0.01±0.00	0.15±0.06
Zbb	191.33±8.49	28.77±1.73	6.97±0.55	3.67±0.27	1.39±0.16
Wl	105.70±30.38	14.00±4.05	4.96±1.41	2.04±0.58	1.80±0.51
Wcl	579.54±92.52	78.98±12.20	26.66±3.99	10.11±1.50	6.01±0.91
Wcc	578.68±165.13	90.51±25.57	35.25±9.99	15.05±4.26	17.57±5.02
Wbl	114.71±37.46	17.21±5.57	8.70±2.79	3.01±0.97	2.00±0.65
Wbb	1846.10±295.25	315.96±46.67	131.50±19.15	56.79±8.31	51.70±7.55
StopWt	271.88±25.41	68.92±5.73	34.64±2.94	17.00±1.53	11.25±1.09
Stopst	1721.02±103.11	271.35±13.35	77.04±4.27	16.35±1.16	5.97±0.62
ttbar	4730.92±185.16	1448.20±51.00	602.97±23.18	143.85±6.65	48.11±3.98
mulitjet	2623.00±328.27	118.24±27.24	21.65±6.57	10.48±4.06	2.10±1.01
WW	21.30±3.08	3.11±0.56	1.87±0.33	0.85±0.17	0.88±0.17
ZZ	11.25±1.09	1.40±0.21	0.52±0.09	0.20±0.03	0.07±0.01
WZ	240.79±22.28	38.71±6.81	25.13±4.40	15.06±2.66	13.28±2.40
Bkg	13097.16±117.31	2502.31±34.28	979.95±18.05	295.10±6.65	162.50±7.08
ZvvH125	–	–	–	–	–
WlvH125	8.15±27.84	1.92±6.54	1.31±4.48	1.12±3.81	1.17±3.99
ZllH125	0.23±0.77	0.03±0.11	0.01±0.04	0.01±0.03	0.01±0.02
Signal	8.38±28.61	1.95±6.65	1.32±4.52	1.12±3.83	1.18±4.02
data	13107	2498	992	290	181

Table 9.8: The post fit yield in one lepton 2T2J regions for both 7 and 8 TeV.

	OneLepton , 2T2J				
	$p_T^V < 90$ GeV	$90 < p_T^V < 120$ GeV	$120 < p_T^V < 160$ GeV	$160 < p_T^V < 200$ GeV	$p_T^V > 200$ GeV
Zl	3.87±0.93	0.39±0.09	0.10±0.03	0.06±0.01	0.03±0.01
Zcl	7.30±3.90	0.92±0.49	0.21±0.11	0.11±0.06	0.05±0.03
Zcc	8.31±2.54	1.26±0.42	0.60±0.18	0.32±0.10	0.16±0.05
Zbl	12.64±4.34	1.17±0.43	0.40±0.11	0.45±0.11	0.01±0.00
Zbb	121.20±5.90	17.05±1.01	4.91±0.48	2.55±0.24	1.61±0.17
Wl	34.72±9.09	5.35±1.45	2.16±0.58	0.99±0.27	1.01±0.28
Wcl	193.08±31.32	29.48±4.88	11.76±2.00	5.37±0.94	4.18±0.77
Wcc	197.90±59.73	31.26±9.41	14.73±4.47	7.61±2.32	9.87±3.02
Wbl	72.61±27.29	10.25±3.67	4.62±1.65	2.06±0.75	2.52±0.92
Wbb	633.62±118.76	110.83±20.07	55.04±10.05	28.94±5.37	31.31±5.88
StopWt	418.75±43.19	100.91±9.63	54.81±5.30	30.63±3.10	26.32±2.80
Stopst	1069.59±113.82	170.09±17.51	44.57±4.94	9.16±1.05	4.67±0.57
ttbar	11661.35±248.80	2664.00±49.25	1004.25±22.05	305.95±9.63	146.40±7.72
mulitjet	878.55±189.21	45.01±12.41	11.73±4.02	5.05±2.15	1.51±0.78
WW	8.18±2.21	1.48±0.44	0.85±0.30	0.31±0.14	0.43±0.33
ZZ	4.28±1.16	0.48±0.17	0.33±0.17	0.11±0.09	0.05±0.01
WZ	48.19±14.81	9.54±3.10	6.97±3.47	4.85±3.74	5.96±1.49
Bkg	15374.13±122.19	3199.47±34.99	1218.02±19.17	404.52±9.59	236.09±8.34
ZvvH125	–	–	–	–	–
WlvH125	2.35±8.02	0.65±2.22	0.57±1.96	0.54±1.84	0.67±2.29
ZllH125	0.15±0.50	0.02±0.08	0.01±0.04	0.01±0.04	0.01±0.03
Signal	2.50±8.53	0.67±2.30	0.58±2.00	0.55±1.88	0.68±2.32
data	15380	3217	1185	387	238

Table 9.9: The post fit yield in one lepton 2T3J regions for both 7 and 8 TeV.

	OneLepton MET , 2T2J	
	$160 < p_T^V < 200$ GeV	$p_T^V > 200$ GeV
Zl	0.01 ± 0.00	0.00 ± 0.00
Zcl	0.03 ± 0.02	0.01 ± 0.01
Zcc	0.03 ± 0.01	0.01 ± 0.00
Zbl	-	-
Zbb	0.39 ± 0.13	0.27 ± 0.03
Wl	0.20 ± 0.06	0.18 ± 0.05
Wcl	1.03 ± 0.17	0.63 ± 0.10
Wcc	1.42 ± 0.42	1.77 ± 0.53
Wbl	0.43 ± 0.14	0.19 ± 0.06
Wbb	5.23 ± 0.82	5.37 ± 0.81
StopWt	1.51 ± 0.19	1.10 ± 0.15
Stopst	1.29 ± 0.12	1.00 ± 0.09
ttbar	14.00 ± 0.70	5.66 ± 0.47
mulitjet	0.66 ± 0.32	0.50 ± 0.31
WW	0.10 ± 0.02	0.09 ± 0.02
ZZ	0.06 ± 0.01	0.01 ± 0.00
WZ	1.44 ± 0.25	1.38 ± 0.25
Bkg	27.81 ± 0.91	18.15 ± 0.95
ZvvH125	-	-
WlvH125	0.09 ± 0.32	0.14 ± 0.47
ZllH125	0.00 ± 0.00	0.00 ± 0.00
Signal	0.09 ± 0.32	0.14 ± 0.47
data	30	16

Table 9.10: The post fit yield in one lepton 2T2J regions with MET trigger for both 7 and 8 TeV.

	TwoLepton , 2T2J				
	$p_T^V < 90$ GeV	$90 < p_T^V < 120$ GeV	$120 < p_T^V < 160$ GeV	$160 < p_T^V < 200$ GeV	$p_T^V > 200$ GeV
Zl	17.00±4.97	2.86±0.84	1.11±0.32	0.30±0.09	0.28±0.08
Zcl	41.04±22.58	7.34±4.05	2.75±1.52	0.74±0.41	0.56±0.31
Zcc	132.53±40.63	24.35±7.37	9.77±2.91	2.40±0.71	2.65±0.79
Zbl	78.79±20.72	15.39±4.03	5.75±1.49	1.84±0.49	1.20±0.31
Zbb	1788.79±58.95	368.94±12.56	138.78±5.30	28.98±1.40	19.94±1.01
Wl	–	–	–	–	–
Wcl	–	–	–	–	–
Wcc	–	–	–	–	–
Wbl	–	–	–	–	–
Wbb	–	–	–	–	–
StopWt	9.56±0.91	2.67±0.22	0.65±0.06	0.12±0.01	–
Stopst	0.59±0.04	-	0.02±0.00	-	–
ttbar	428.62±8.29	72.96±1.64	15.77±0.63	1.04±0.05	–
mulitjet	–	–	–	–	–
WW	–	-	–	-	–
ZZ	98.35±9.03	17.43±2.48	9.67±1.29	4.31±0.52	4.21±0.43
WZ	–	-	–	-	–
Bkg	2595.28±42.89	511.93±9.71	184.26±4.38	39.73±1.31	28.85±1.05
ZvvH125	–	–	–	–	–
WlvH125	–	-	–		–
ZllH125	2.24±7.65	0.55±1.88	0.43±1.48	0.22±0.75	0.22±0.77
Signal	2.24±7.65	0.55±1.88	0.43±1.48	0.22±0.75	0.22±0.77
data	2567	517	167	50	24

Table 9.11: The post fit yield in two lepton 2T2J regions for both 7 and 8 TeV.

	TwoLepton , 2T2J				
	$p_T^V < 90$ GeV	$90 < p_T^V < 120$ GeV	$120 < p_T^V < 160$ GeV	$160 < p_T^V < 200$ GeV	$p_T^V > 200$ GeV
Zl	12.72±3.72	2.44±0.71	1.13±0.33	0.36±0.11	0.38±0.11
Zcl	31.44±17.18	6.34±3.48	2.86±1.57	0.93±0.51	0.84±0.46
Zcc	79.00±24.20	17.05±5.15	8.21±2.46	2.57±0.76	3.72±1.11
Zbl	74.17±18.97	14.78±3.74	6.16±1.59	2.42±0.60	0.69±0.21
Zbb	1060.49±42.04	223.33±8.80	106.39±4.67	28.79±1.38	26.28±1.45
Wl	–	–	–	–	–
Wcl	–	–	–	–	–
Wcc	–	–	–	–	–
Wbl	–	–	–	–	–
Wbb	–	–	–	–	–
StopWt	6.20±0.66	1.67±0.17	0.45±0.05	0.14±0.02	0.11±0.02
Stopst	0.60±0.10	0.00±0.00	–	–	–
ttbar	290.50±14.65	52.61±2.75	13.21±0.69	0.73±0.07	0.25±0.02
mulitjet	–	–	–	–	–
WW	–	–	–	–	–
ZZ	34.82±9.26	6.66±2.19	4.14±2.11	1.84±1.48	2.33±0.58
WZ	–	–	–	–	–
Bkg	1589.95±31.65	324.89±6.93	142.57±3.97	37.77±1.67	34.60±1.51
ZvvH125	–	–	–	–	–
WlvH125	–	–	–	–	–
ZllH125	1.01±3.46	0.31±1.06	0.24±0.81	0.13±0.45	0.14±0.49
Signal	1.01±3.46	0.31±1.06	0.24±0.81	0.13±0.45	0.14±0.49
data	1599	308	157	35	33

Table 9.12: The post fit yield in two lepton 2T3J regions for both 7 and 8 TeV.

9.3.2 Pulls and Correlations for Nuisance Parameters

During the global fit, the value of each nuisance parameter may vary from the nominal value, and the corresponding error may also be constrained by fit if the data can actually provides a tighter constraint than what we assumed before the fit. Besides that, correlations may be observed between the nuisance parameters that were assumed to be un-correlated.

This section provides the pulls and correlations of nuisance parameters. Fig 9.2 shows the pulls of all nuisance parameters used in this analysis for both 7 and 8 TeV. Due to the large number of nuisance parameters in the fit, it is inconvenient to put them all in one plot. Fig 9.3 to 9.6 breaks down the full set of uncertainties into four groups: b-tagging uncertainties, jet energy scale, modeling nuisance parameters and floating normalization. Fig 9.7 shows all nuisance parameters that have a correlation above 25% with at least one other nuisance parameter. The plots are made for 7 and 8 TeV fit separately, and the combination of 7+8 TeV.

This section also summaries the most important systematic uncertainties in this analysis with 8 TeV dataset. Table 9.13 and 9.14 shows the sizes of systematic uncertainties before the fit on background processes and signal processes. Table 9.15 and 9.16 shows the sizes of systematic uncertainties after the fit on background processes and signal processes. In these table, the uncertainties are grouped into board categories, like b-tagging related ones, c-tagging related ones, etc. The values shown in the table are averaged over all p_T^V intervals in each category, the total error is obtained by adding the individual components in quadrature in each p_T^V interval, and then averaging. The values are evaluated in a mass region from 110 GeV to 130 GeV in 2 b-tag regions.

In the end, the impact on the Higgs signal strength $\hat{\mu}$ of the nuisance parameters

is shown in Fig 9.8.

Uncertainties [%]	0 lepton	1 lepton	2 lepton
b-tagging	4.19	3.74	4.4
c-tagging	3.63	4.56	2.33
light tagging	1.88	1.4	2.01
Jet/Pile-up/E_T^{miss}	6.09	6.45	6.73
Lepton	0.55	1.66	1.54
Top modelling	1.74	3.05	0.38
W modelling	1.45	1.83	0
Z modelling	4.39	0.09	10.14
Single-top modelling	0.32	0.7	0.03
Diboson	0.34	0.15	0.77
Multijet	0.49	0.8	0
Luminosity	2.77	2.68	2.8
Total	10.53	10.39	14.81

Table 9.13: A summary of the sizes of the components of the systematic uncertainties on the total estimated **background** yield after full selection for the three channels at 8 TeV. The uncertainties are shown as a percentage and grouped into broad categories. They are averaged over all p_T^V intervals in each category. The total error is obtained by adding the individual components in quadrature in each p_T^V interval, and then averaging. The numbers are evaluated in the 110 GeV - 130 GeV mass region for 2T2J region and 2T3J region.

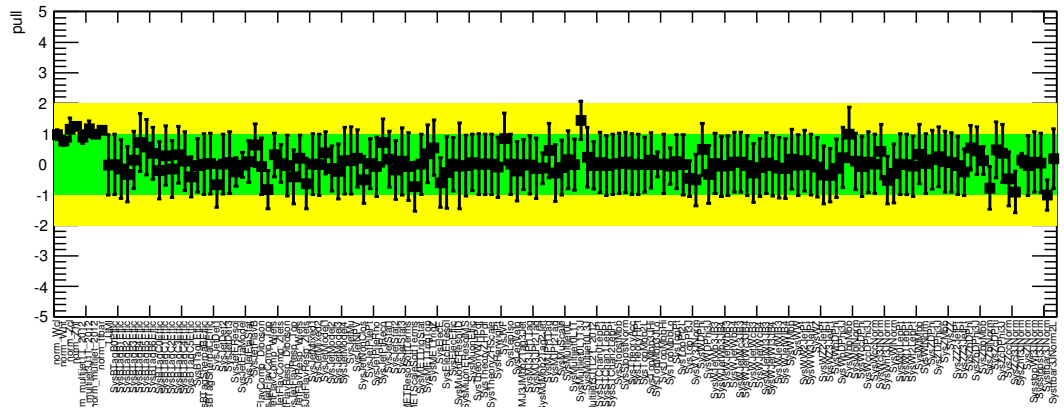

(a) 8 TeV

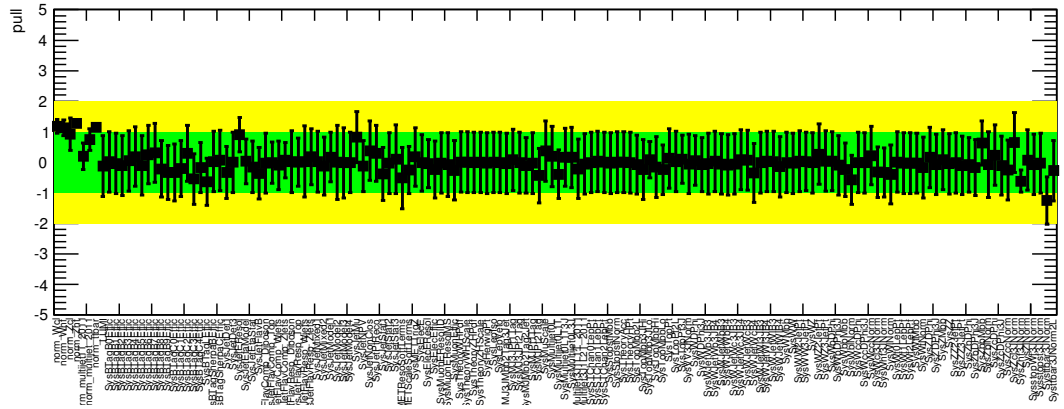

(b) 7 TeV

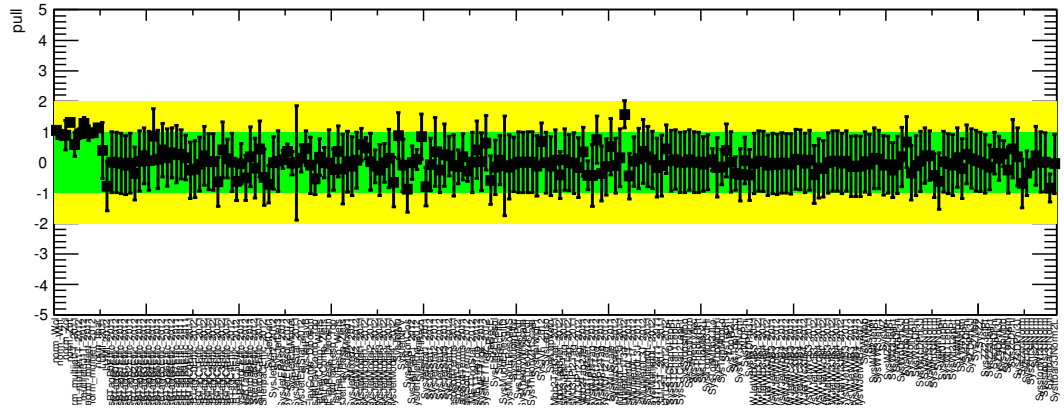

(c) 7+8 TeV

Figure 9.2: Pulls of all nuisance parameters for both 7 and 8 TeV.

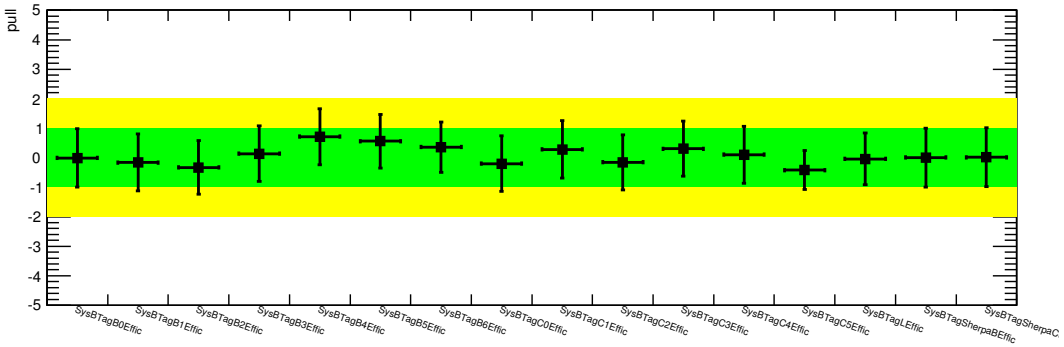

(a) 8 TeV

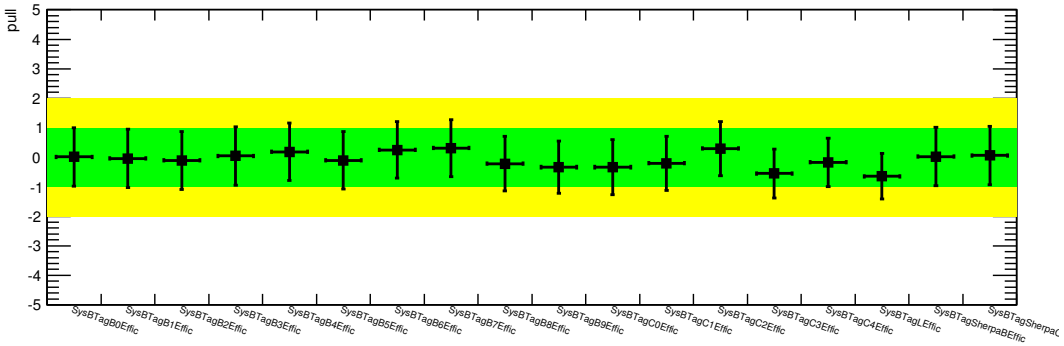

(b) 7 TeV

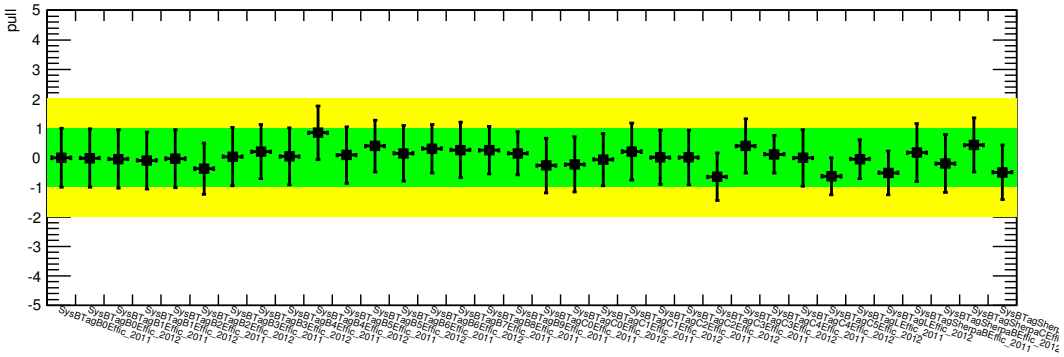

(c) 7+8 TeV

Figure 9.3: Pulls of b-tagging related nuisance parameters for both 7 and 8 TeV.

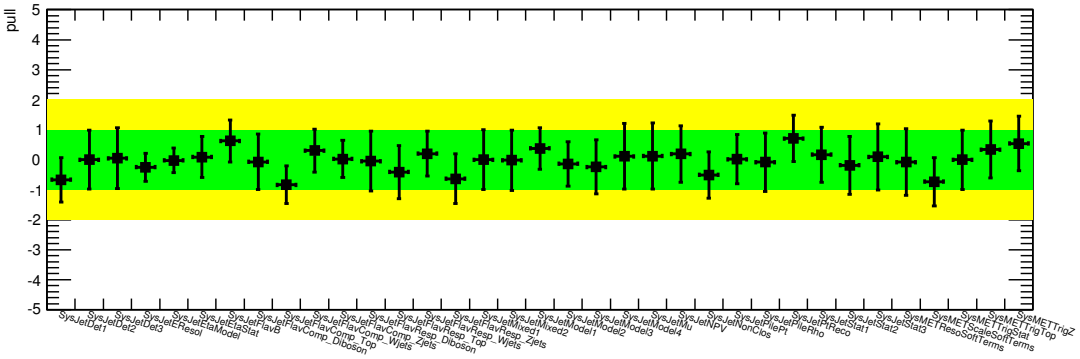

(a) 8 TeV

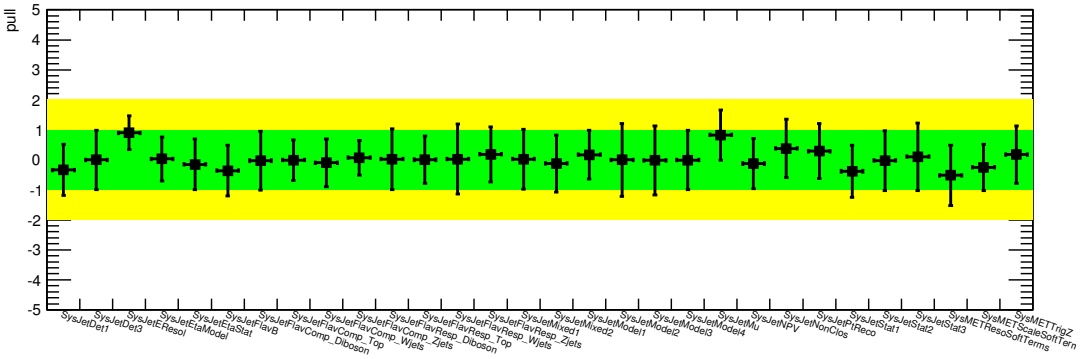

(b) 7 TeV

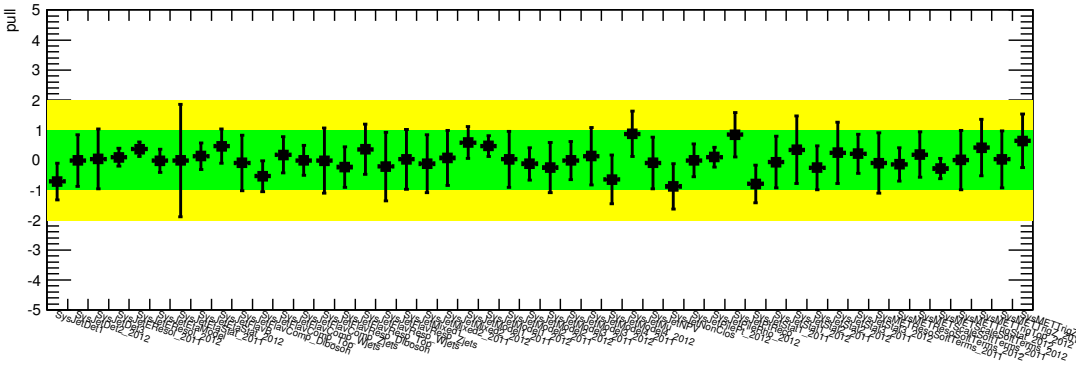

Figure 9.4: Pulls of JES related nuisance parameters for both 7 and 8 TeV.

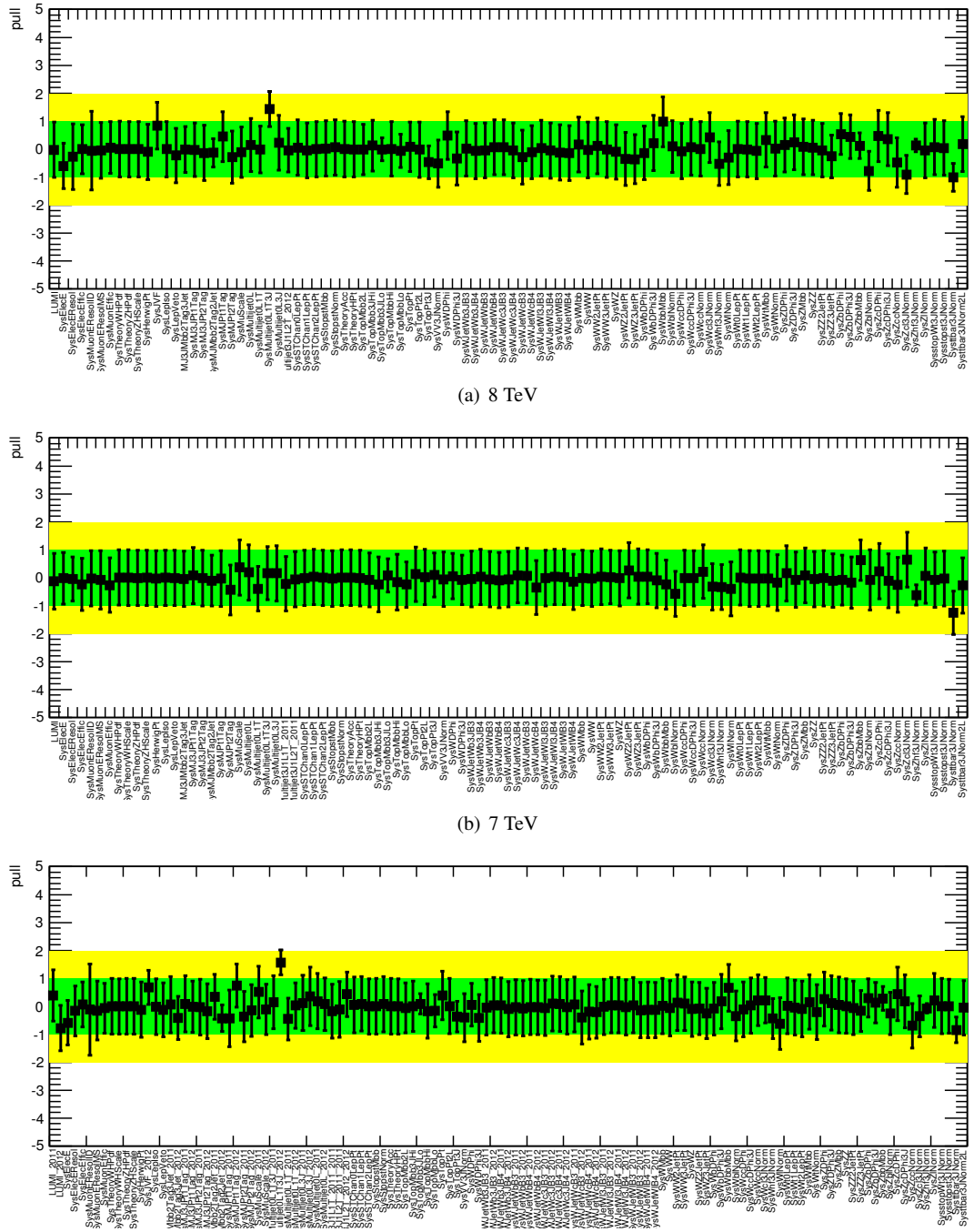

(a) 8 TeV

(b) 7 TeV

(c) 7+8 TeV

Figure 9.5: Pulls of modeling uncertainties for both 7 and 8 TeV.

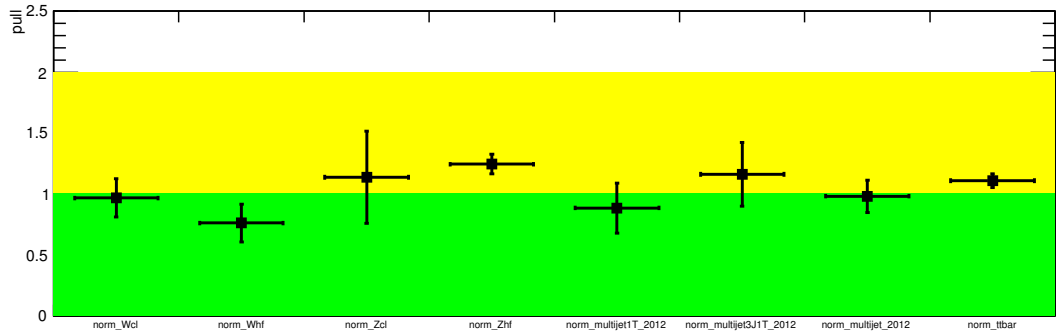

(a) 8 TeV

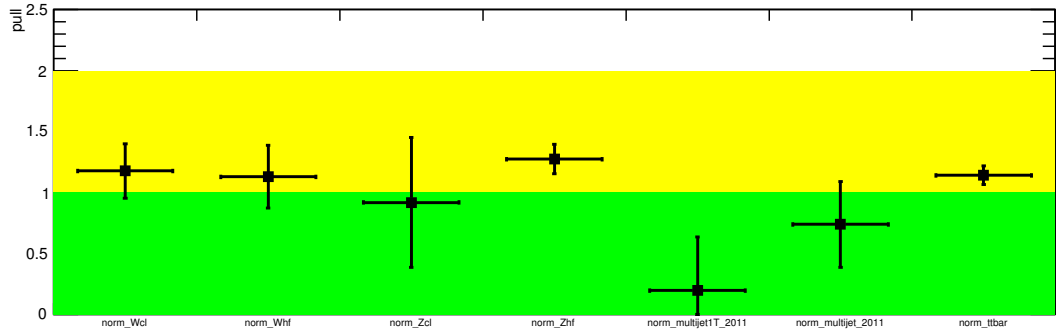

(b) 7 TeV

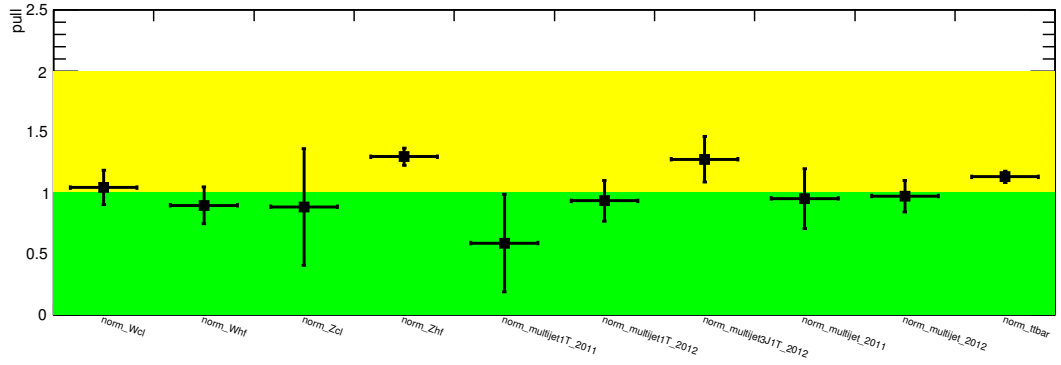

(c) 7+8 TeV

Figure 9.6: Pulls of normalization uncertainties for both 7 and 8 TeV.

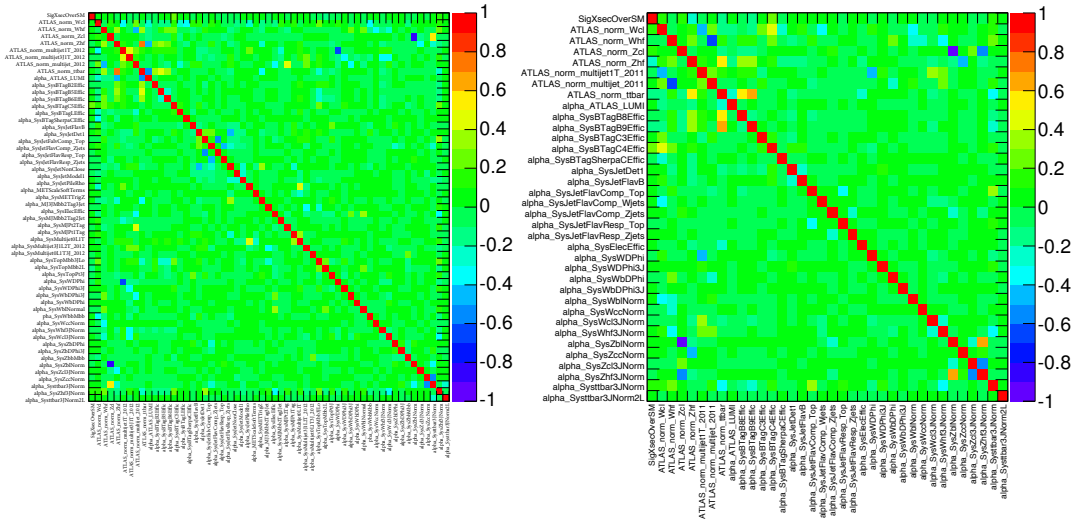

(a) 8 TeV

(b) 7 TeV

(c) 7+8 TeV

Figure 9.7: Correlation between the nuisance parameters in 7 TeV fit, 8 TeV fit, and the combined fit for both 7 and 8 TeV. Only nuisance parameters with more than 25% correlation are shown.

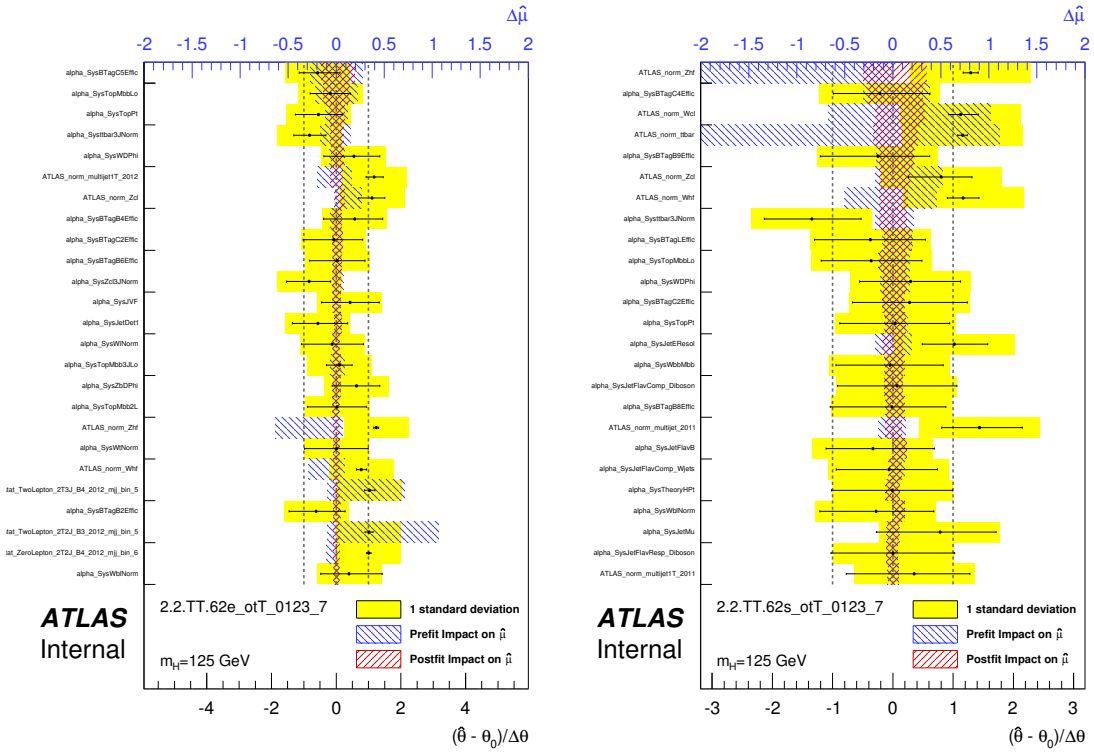

Figure 9.8: Impact of the nuisance parameters on $\hat{\mu}$ in decreasing order of post fit effect. Only the most significant nuisance parameters in terms of impact on $\hat{\mu}$ are shown in the plot. The x axis at the bottom shows the number of standard deviations from the nominal input value of each nuisance parameter. The dashed vertical lines indicate the ± 1 band. The x axis at the top in blue represents the fractional variation on $\hat{\mu}$ caused by each of the nuisance parameters on the y axis. Around each pull point both post (in black) and pre-fit (in solid yellow) one sigma errors are shown, highlighting the eventual constraints. The blue hatched areas represent the fractional variation on $\hat{\mu}$ caused by the pre-fit value of the nuisance parameters on the y axis. The red hatched areas, instead show the post-fit effect.

Uncertainties [%]	0 lepton	1 lepton	2 lepton
b-tagging	5.57	5.47	5.3
c-tagging	0.02	0.03	0.03
light tagging	0.07	0.08	0.06
Jet/Pile-up/E_T^{miss}	8.29	8.96	6.53
Lepton	0	1.73	1.27
VH p_T-dependence	2.04	2.15	2
VH theory scale	1.35	0.03	1.6
VH theory PDF	3.01	3.43	3.5
VH acceptance	10	10	10
Luminosity	2.8	2.8	2.8
Total	15.01	15.76	14.22

Table 9.14: A summary of the sizes of the components of the systematic uncertainties on the **signal** yield for $m_H = 125$ GeV after full selection for the three channels at 8 TeV. The dominant signal process is shown for the 1-lepton and 2-lepton channels, while for the 0-lepton channel both the ZH and WH signals are shown. The uncertainties are shown as a percentage and grouped into broad categories. They are averaged over all p_T^V intervals in each category. The total error is obtained by adding the individual components in quadrature in each p_T^V interval, and then averaging. The numbers are evaluated in the 110-130 GeV mass region for the 2-btag region.

Uncertainties [%]	0 lepton	1 lepton	2 lepton
b-tagging	2.87	2.52	3.08
c-tagging	2.08	2.78	1.28
light tagging	1.22	0.99	1.18
Jet/Pile-up/E_T^{miss}	2.59	2.78	2.63
Lepton	0.51	1.25	1.25
Top modelling	1.63	3.14	0.49
W modelling	1.38	2.35	0
Z modelling	2.51	0.07	4.61
Single-top modelling	0.28	0.67	0.02
Diboson	0.26	0.13	0.51
Multijet	0.53	0.64	0
Luminosity	2.31	2.23	2.33
Total	2.96	3.18	3.83

Table 9.15: A summary of the sizes of the components of the systematic uncertainties on the total estimated **background** yield after full selection and fitting for the three channels at 8 TeV. The uncertainties are shown as a percentage and grouped into broad categories. They are averaged over all p_T^V intervals in each category. The total error is obtained by adding the individual components in quadrature in each p_T^V interval, and then averaging. The numbers are evaluated in the 110 - 130 GeV mass region for the 2-btag region.

Uncertainties [%]	0 lepton	1 lepton	2 lepton
b-tagging	3.71	3.68	3.57
c-tagging	0.02	0.02	0.02
light tagging	0.05	0.06	0.05
Jet/Pile-up/E_T^{miss}	3.83	3.73	2.65
Lepton	0	1.3	1.03
VH p_T-dependence	2.04	2.15	2
VH theory scale	1.34	0.03	1.6
VH theory PDF	3	3.43	3.5
VH acceptance	10	10	10
Luminosity	2.33	2.33	2.33
Total	12.24	12.4	12.09

Table 9.16: A summary of the sizes of the components of the systematic uncertainties on the **signal** yield for $m_H = 125$ GeV after full selection and fitting for the three channels at 8 TeV. The dominant signal process is shown for the 1-lepton and 2-lepton channels, while for the 0-lepton channel both the ZH and WH signals are shown. The uncertainties are shown as a percentage and grouped into broad categories. They are averaged over all p_T^V intervals in each category. The total error is obtained by adding the individual components in quadrature in each pVT interval, and then averaging. The numbers are evaluated in the 110 - 130 GeV mass region for the 2-btag region.

9.3.3 Post Fit m_{bb} Distributions

This section provides the m_{bb} distribution used in the final step of the analysis to test the possible presence of Higgs signal. Normalization scale factor derived from fit has been has been applied to the following background processes : $t\bar{t}$, multi-jets, W+hf, W+cl, W+hf and Z+cl. The normalization of other backgrounds are constrained by corresponding uncertainties, as discussed in previous sections.

Fig 9.9 and 9.10 shows the m_{bb} distribution for 0 lepton channel using 8 TeV dataset. Fig 9.11 and 9.12 are for 1 lepton channel, and Fig 9.9 and 9.10 are for the 2 lepton channel. In the plots, the background expectation before global fit is indicated with dashed blue line, and background expectation after fit is indicated with dashed red line. Dashed band in the plots indicates the uncertainties after global fit. The Higgs signal is normalized to the result of the fit. In general, good agreement has been observed between data and MC within the systematic uncertainties. There seems to be small discrepancy between data and MC at low m_{bb} in 0 lepton channel, but no significant problems were found after careful investigation.

Similar plots are made using 7 TeV dataset, Fig 9.15 and 9.16 shows the m_{bb} distribution for 0 lepton channel. Fig 9.17 and 9.18 are for 1 lepton channel, and Fig 9.15 and 9.16 are for the 2 lepton channel.

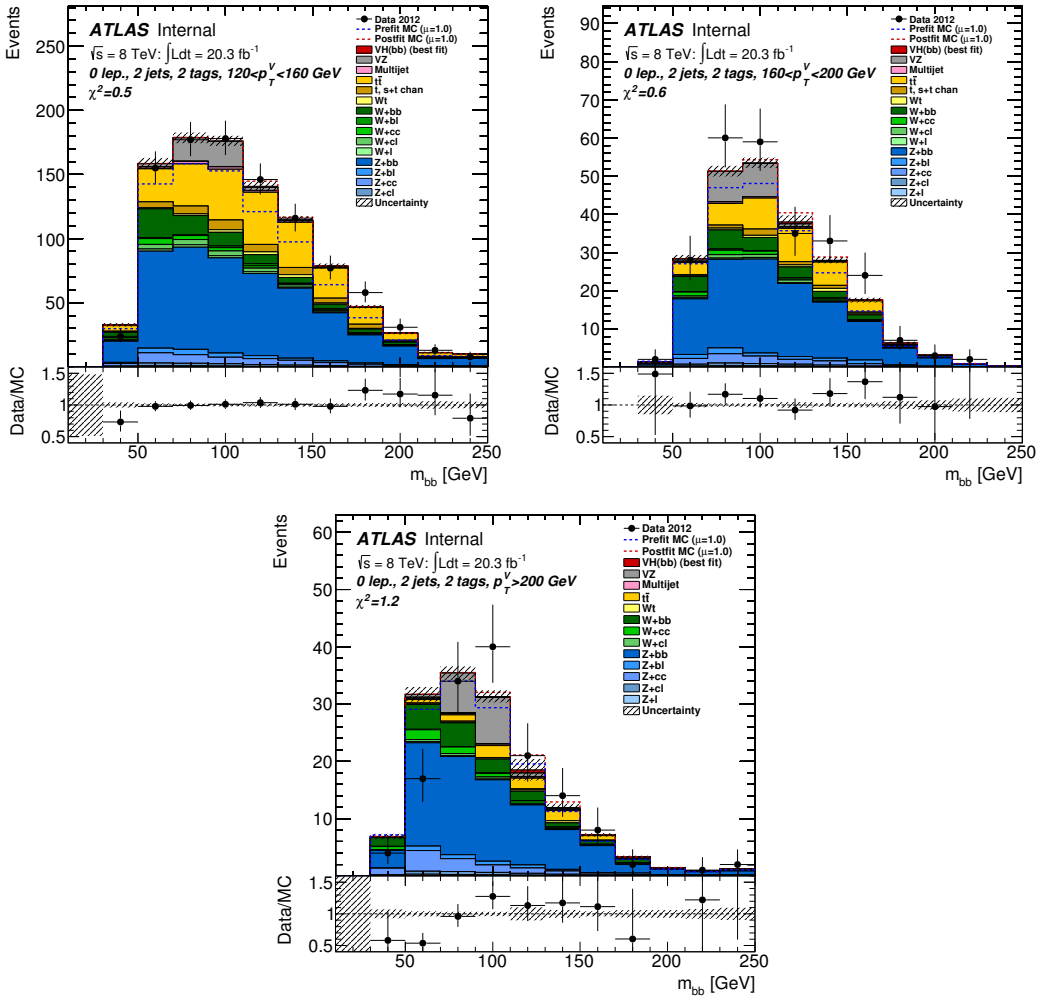

Figure 9.9: Post fit m_{bb} distributions in 0 lepton 2T2J region with 8 TeV dataset.

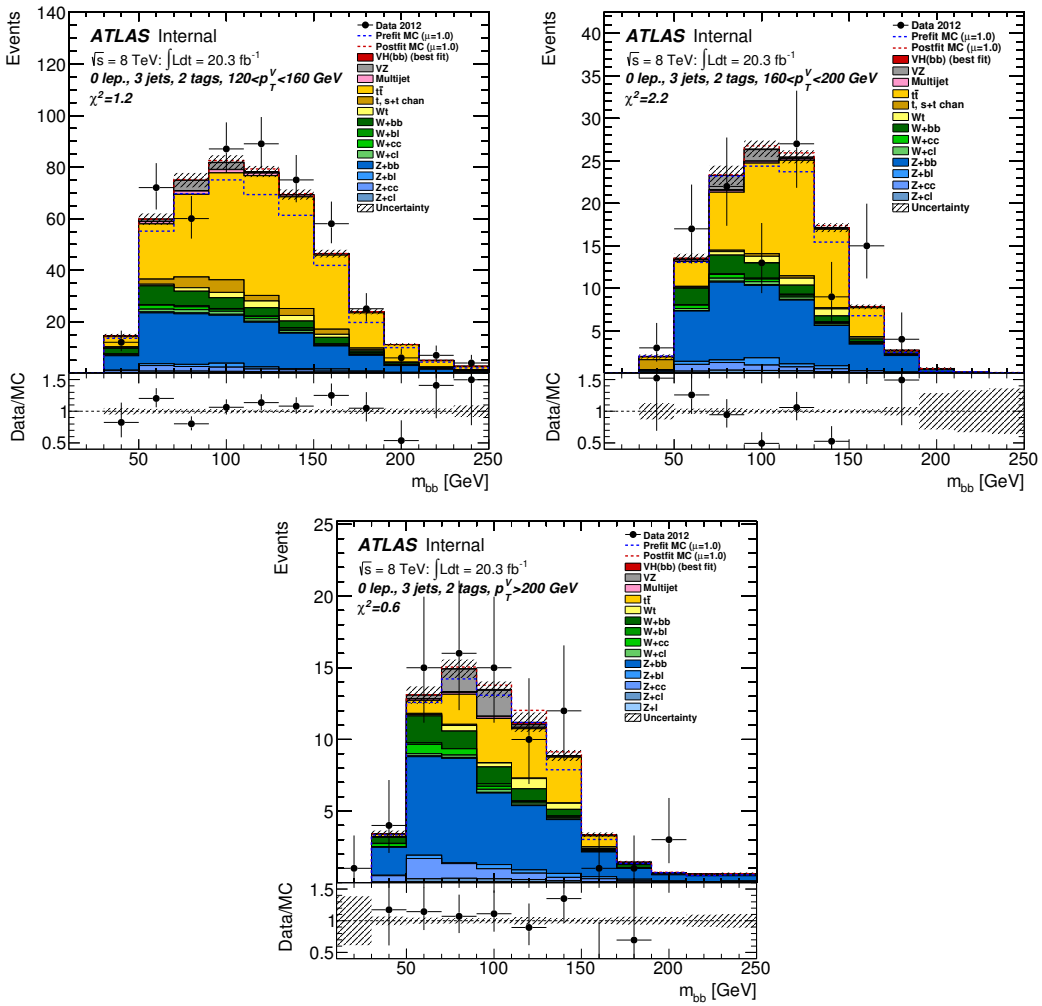

Figure 9.10: Post fit m_{bb} distributions in 0 lepton 2T3J region with 8 TeV dataset.

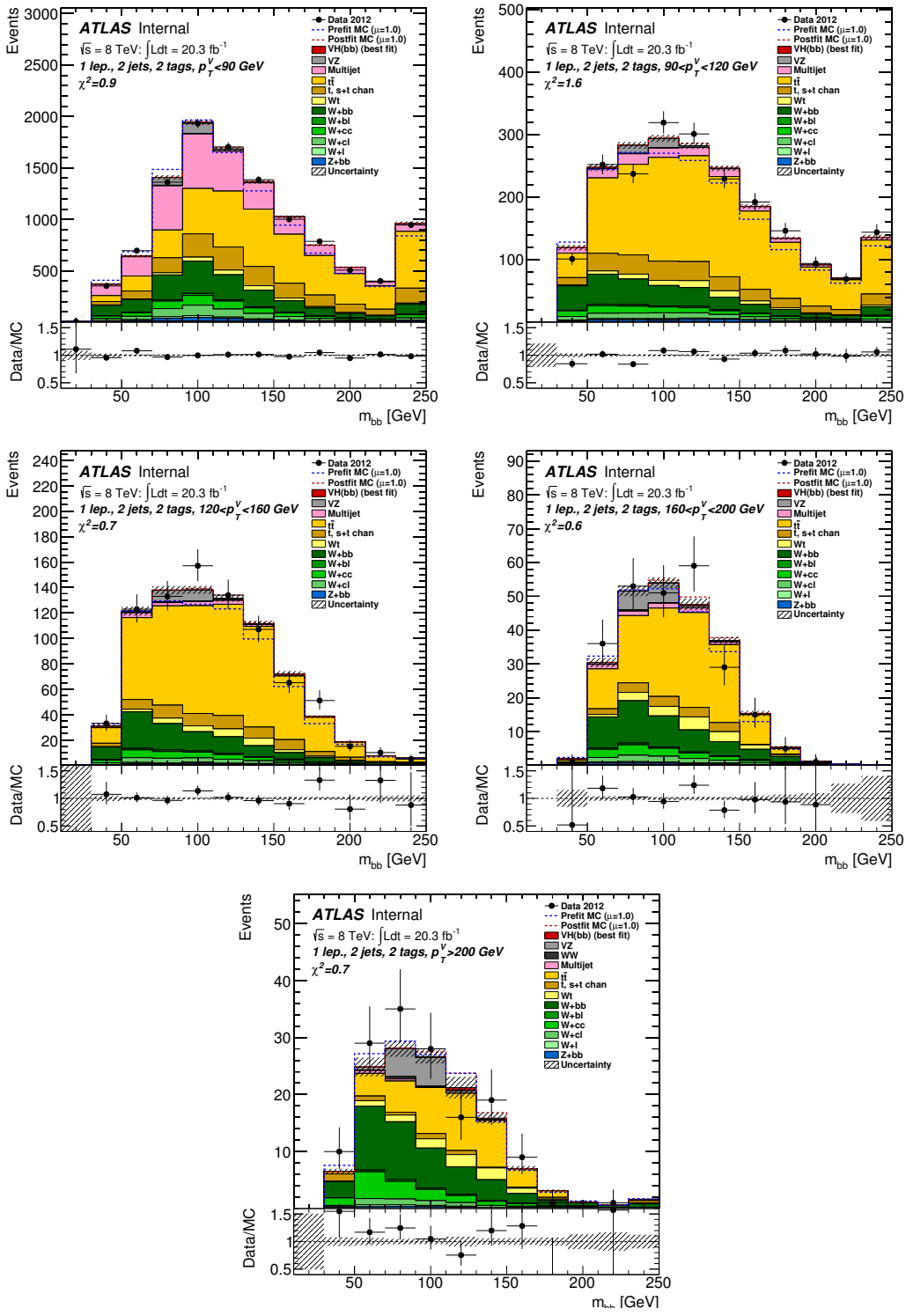

Figure 9.11: Post fit m_{bb} distributions in 1 lepton 2T2J region with 8 TeV dataset.

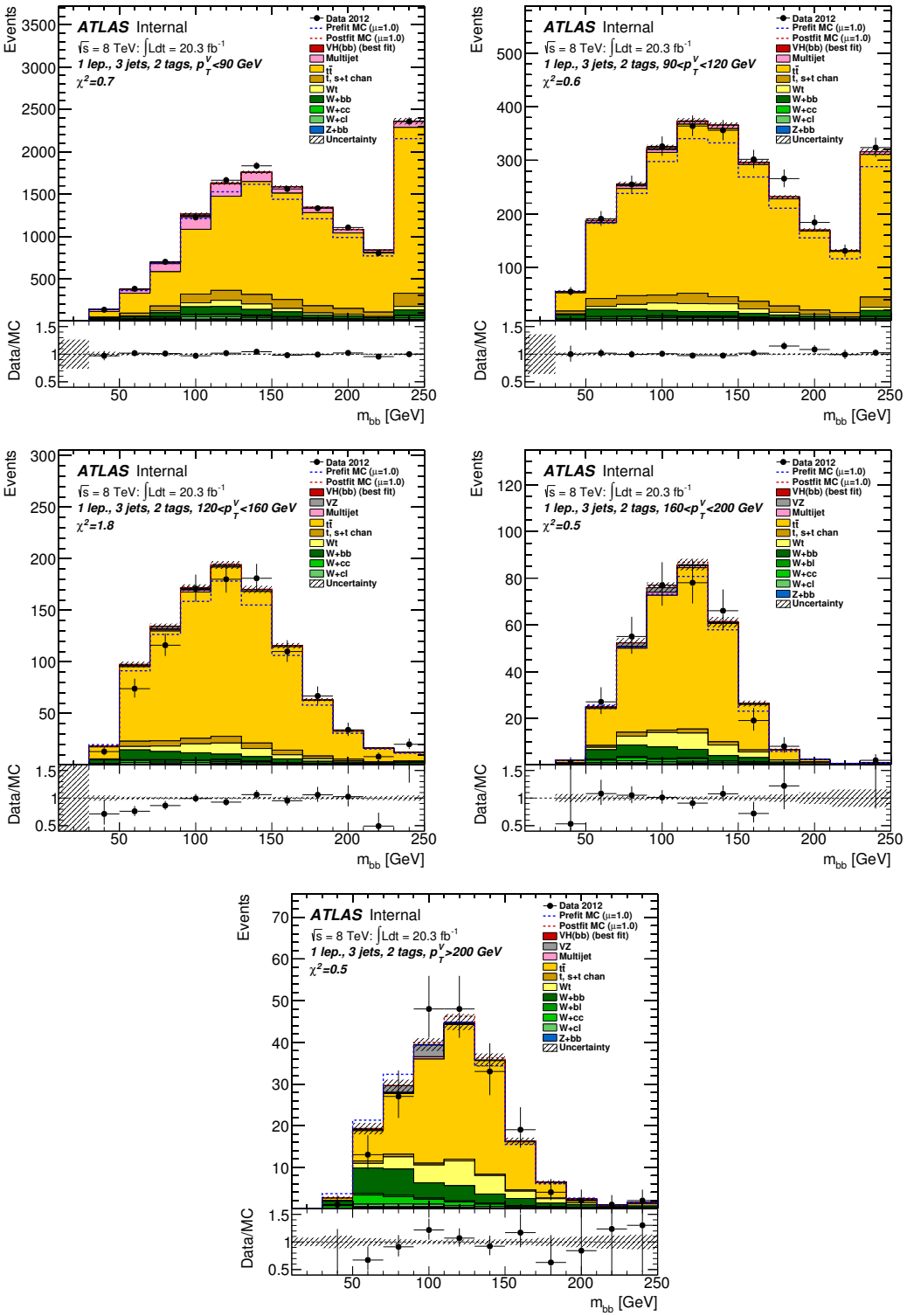

Figure 9.12: Post fit m_{bb} distributions in 1 lepton 2T3J region with 8 TeV dataset.

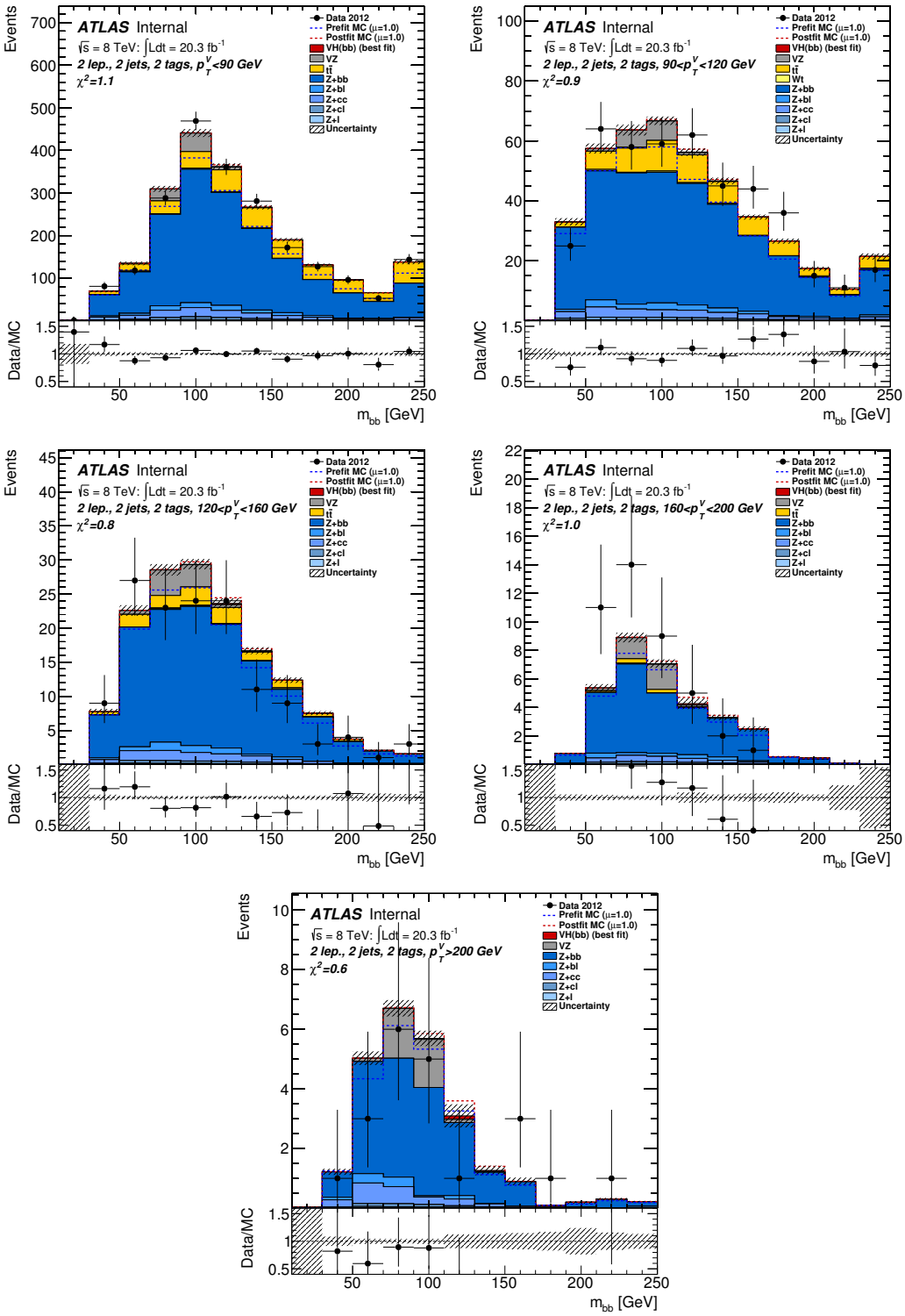

Figure 9.13: Post fit m_{bb} distributions in 2 lepton 2T2J region with 8 TeV dataset.

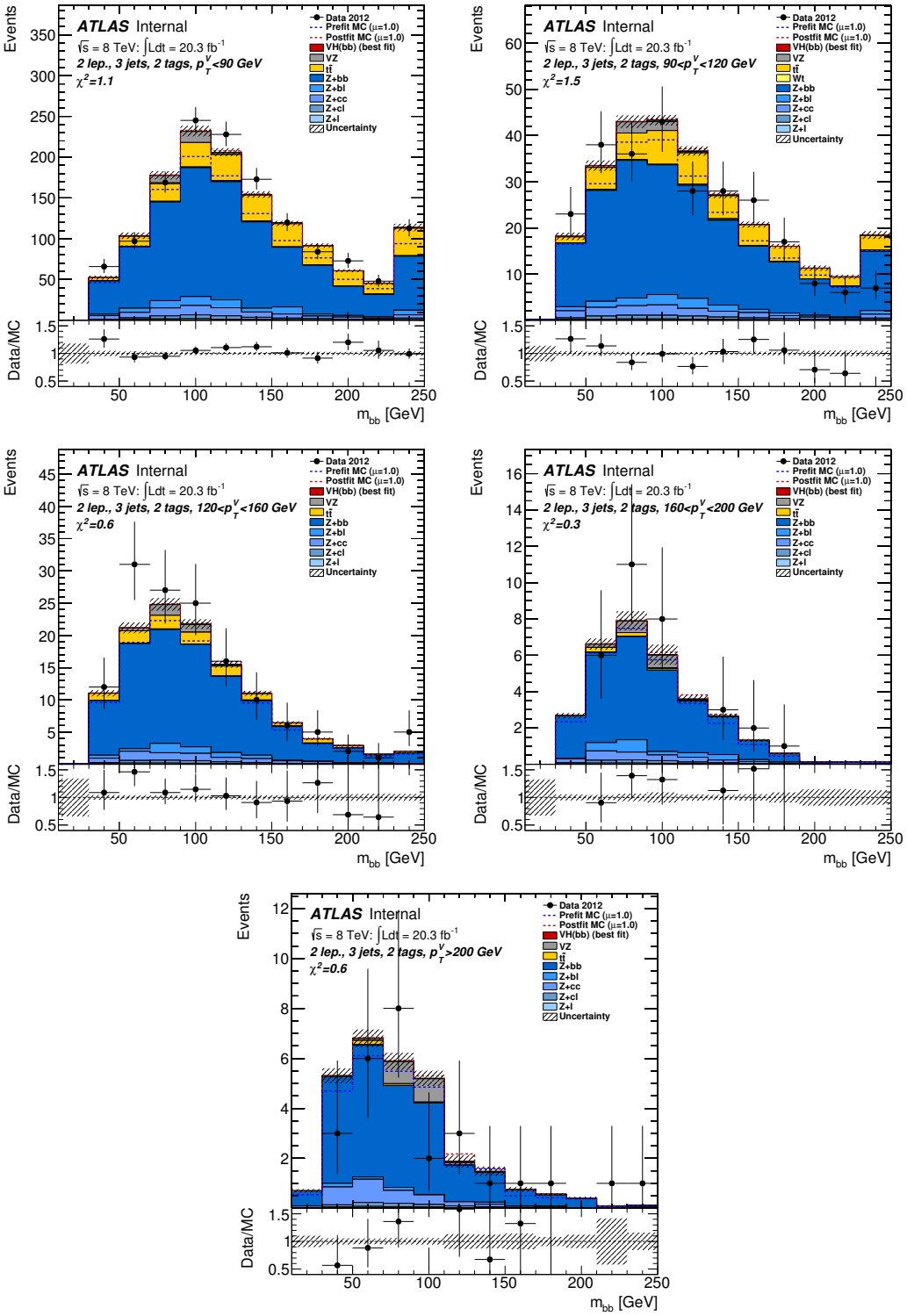

Figure 9.14: Post fit m_{bb} distributions in 2 lepton 2T3J region with 8 TeV dataset.

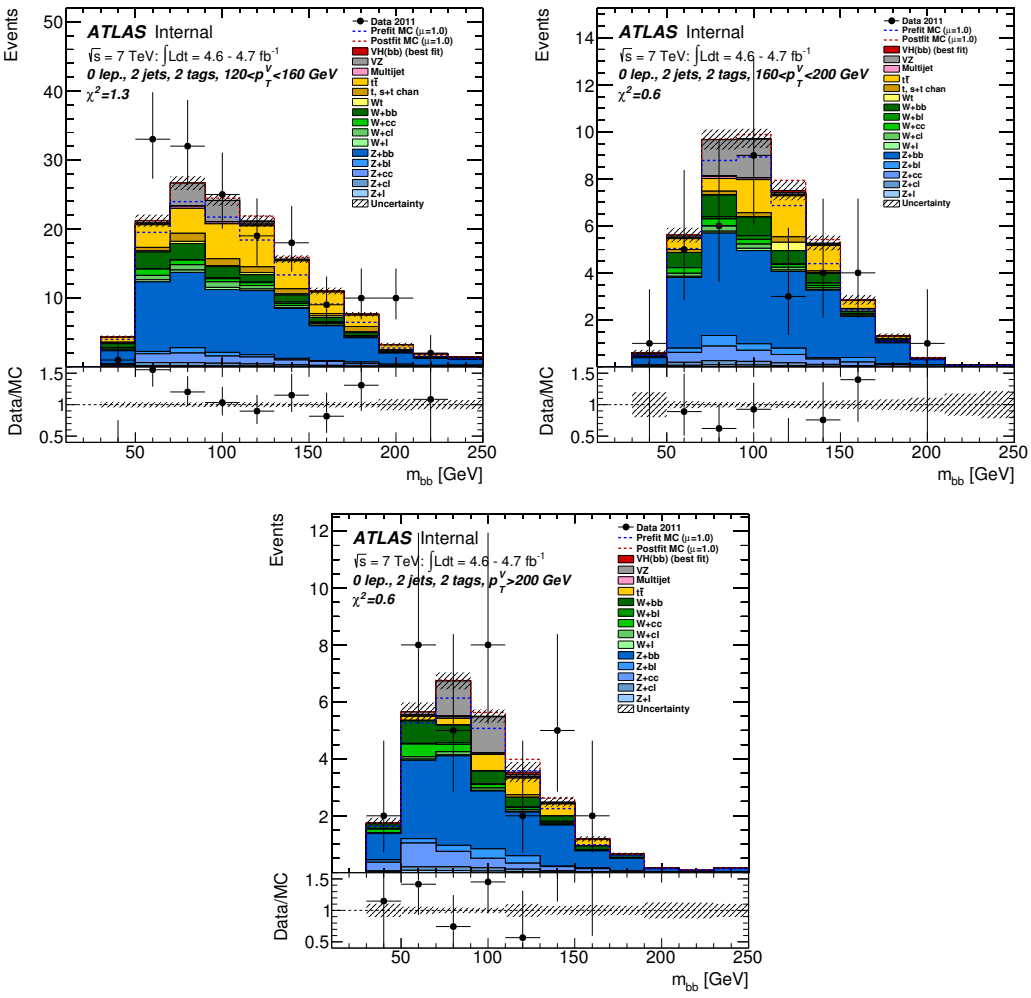

Figure 9.15: Post fit m_{bb} distributions in 0 lepton 2T2J region with 7 TeV dataset.

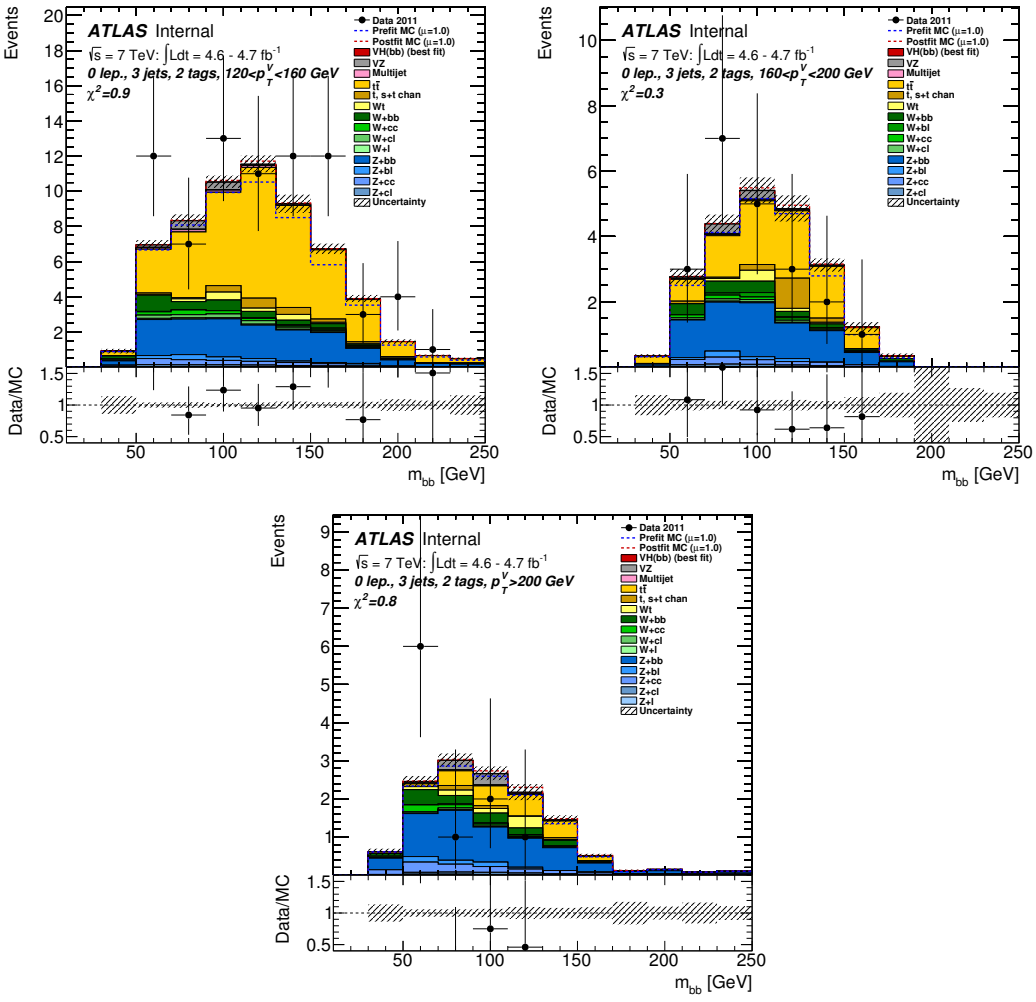

Figure 9.16: Post fit m_{bb} distributions in 0 lepton 2T3J region with 7 TeV dataset.

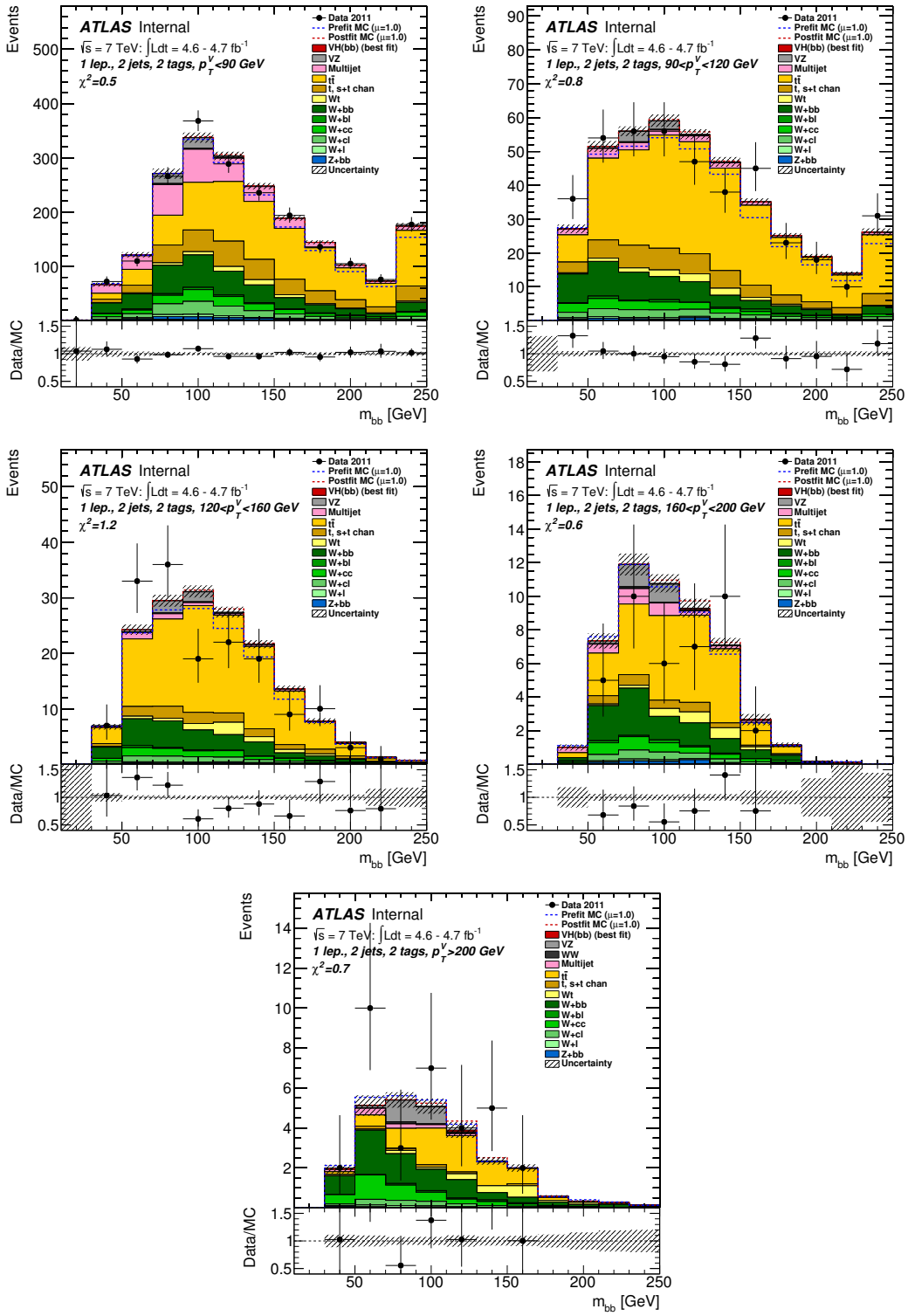

Figure 9.17: Post fit m_{bb} distributions in 1 lepton 2T2J region with 7 TeV dataset.

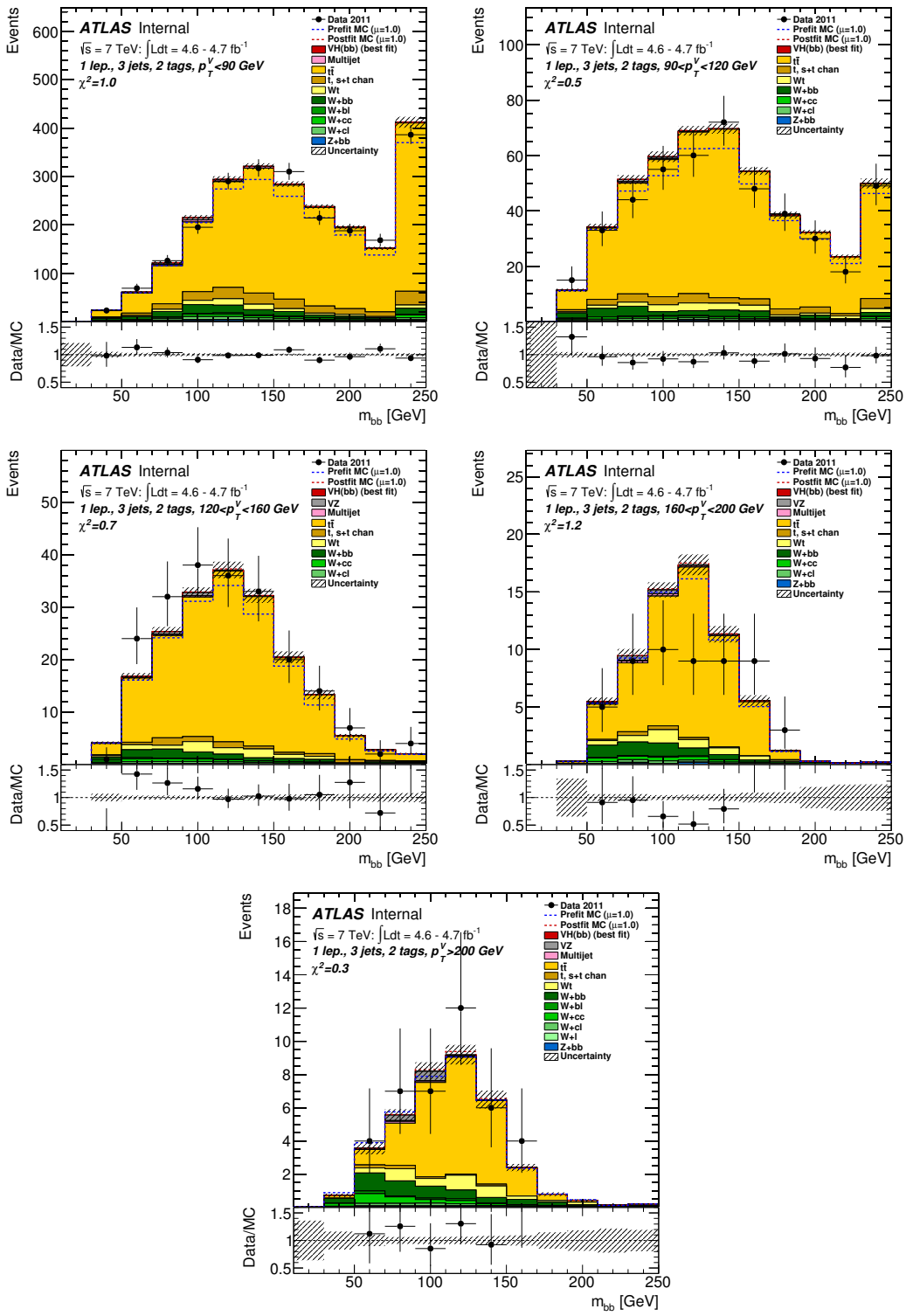

Figure 9.18: Post fit m_{bb} distributions in 1 lepton 2T3J region with 7 TeV dataset.

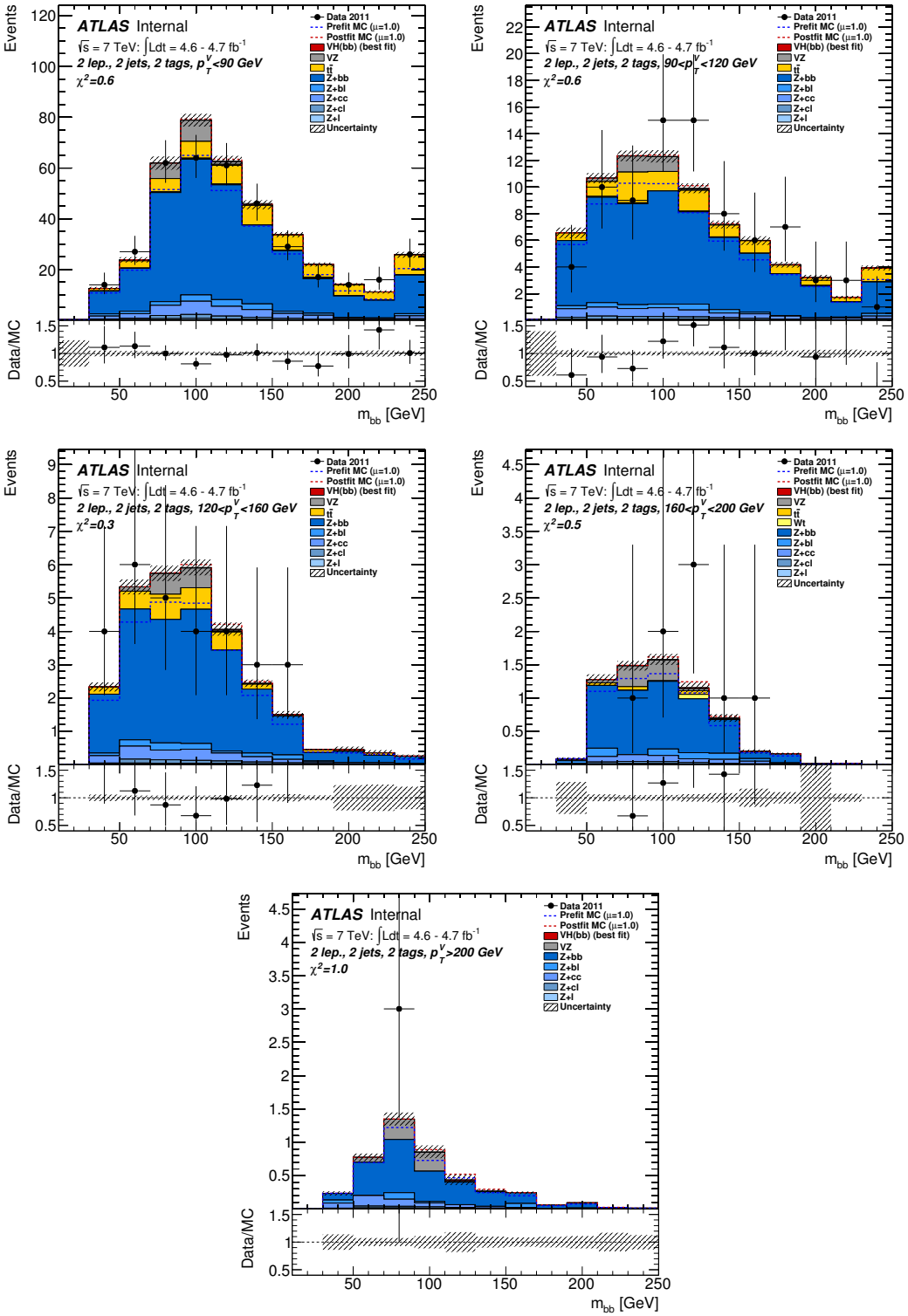

Figure 9.19: Post fit m_{bb} distributions in 2 lepton 2T2J region with 7 TeV dataset.

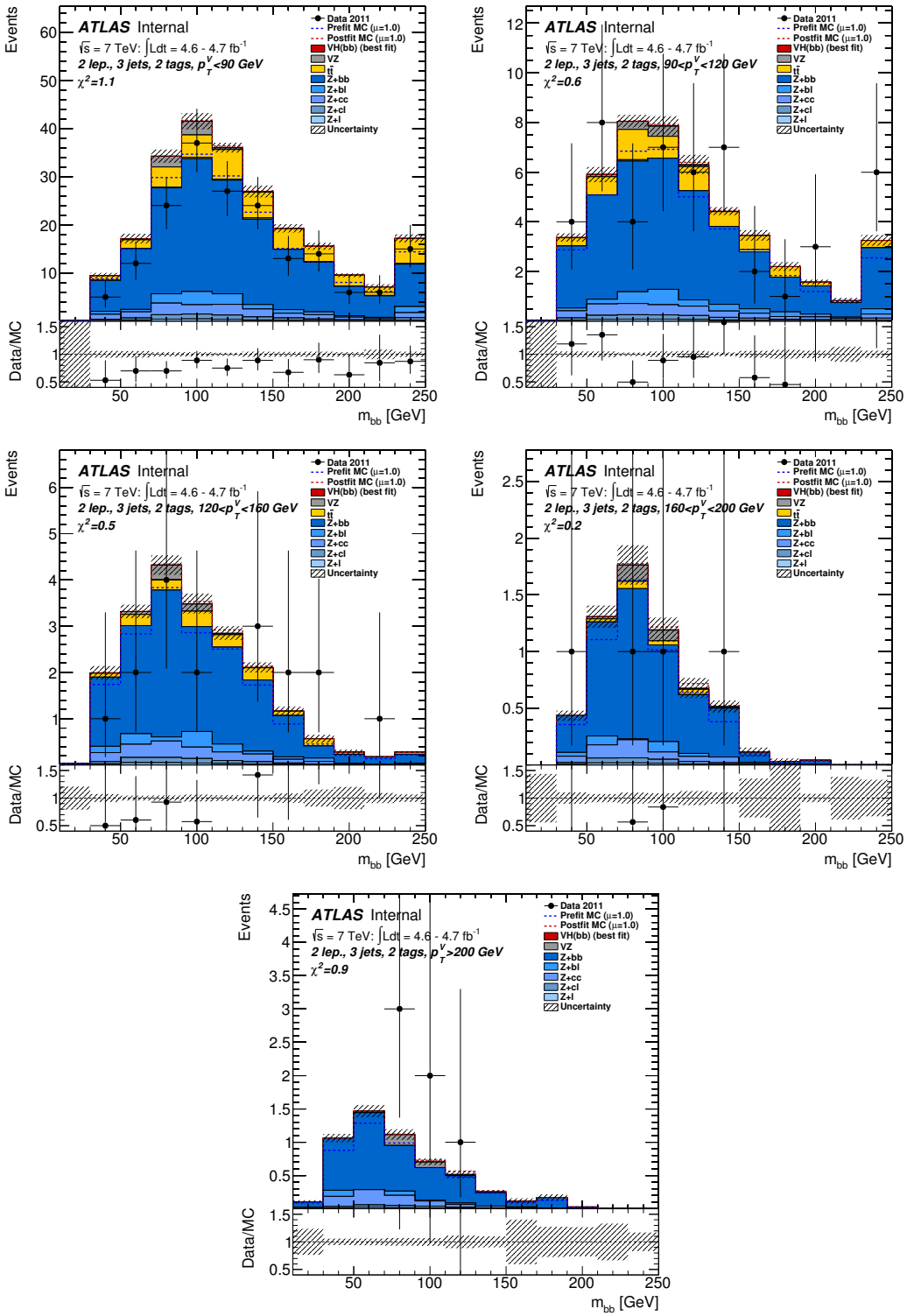

Figure 9.20: Post fit m_{bb} distributions in 2 lepton 2T3J region with 7 TeV dataset.

CHAPTER 10

Results and Summary

This chapter presents the validation procedure for the statistical treatment used in this analysis, as well as the result of the search for VH production with $H \to b\bar{b}$.

Section 10.1 describes the validation procedure through measurement of diboson production, section 10.2 presents the final result on VH search. In the end, section 10.3 summarizes this dissertation.

10.1 Diboson Fit

Diboson production (WZ/ZZ) with Z boson decaying to a pair of b-quarks has a very similar final state comparing to VH (WH/ZH) production, where Higgs boson also decays to a pair of b-quarks. The cross section of diboson production is about 5 times larger than VH signal, and the distribution of p_T^Z and m_{bb} is close to the Higgs signal region. Therefore, the observation of the diboson can be taken as a powerful validation of the statistical model presented in Chapter 9. During validation, a separate fit was performed to measure the cross section of

diboson production, named "diboson fit". Since the main purpose of diboson fit is validation, same input file as Higgs search is used.

In diboson fit, the VH process is included as a background, normalized to the predicted Standard Model cross section. Meanwhile, the normalization scale factor of diboson process is left floating freely in the fit. This scale factor is the diboson signal strength, denoted as μ_D. Fig. 10.1 shows the post fit m_{bb} distribution after subtracting all backgrounds events except diboson and Higgs events. From the plot, an excess of data near the mass of Z boson is observed. Fig. 10.2 shows the diboson signal strength obtained in 0 lepton channel, 1 lepton channel, 2 lepton channel, and the combination of all three channels. For each channel, the fit was performed with 7 TeV dataset, 8 TeV dataset, and the combination of 7 and 8 TeV dataset. Since the input are different for each case, the scale factors will be different for each case. Therefore the results will also be different between different channels and different datasets. For example, the combined μ_D is higher than μ_D from each single channel with 7 TeV dataset. This effect is more significant for result from 0 lepton only. The reason is there is little constraints for the backgrounds in 0 lepton channel.

The result of diboson fit from each channel agrees with Standard Model expectation. After combining the 0, 1, 2 lepton channels with 7+8 TeV dataset, the measured μ_D is 0.93 ± 0.21, which agrees with the Standard Model expectation of $\mu_D = 1$.

10.2 Higgs Result

After validation of the statistical treatment, we can now proceed to finalize the result of Higgs search. In Higgs search, the diboson contribution is constrained to

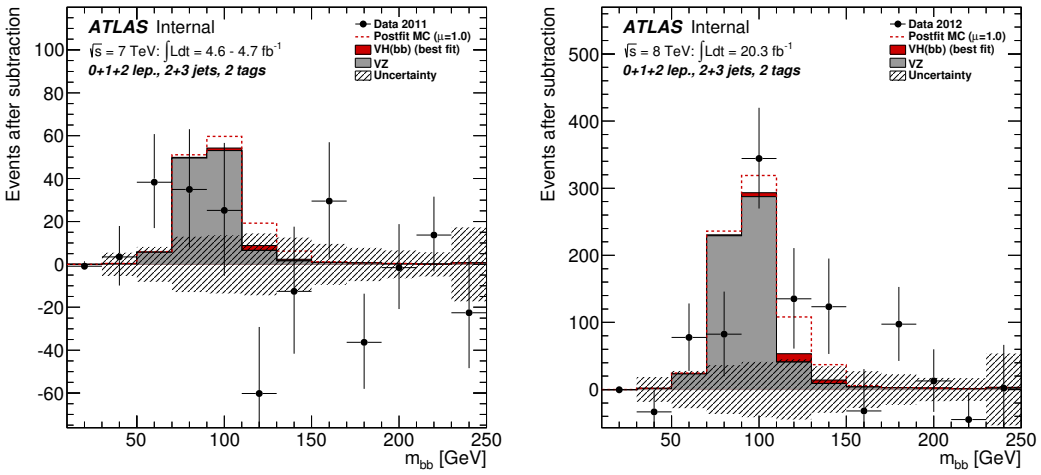

(a) 7 TeV

(b) 8 TeV

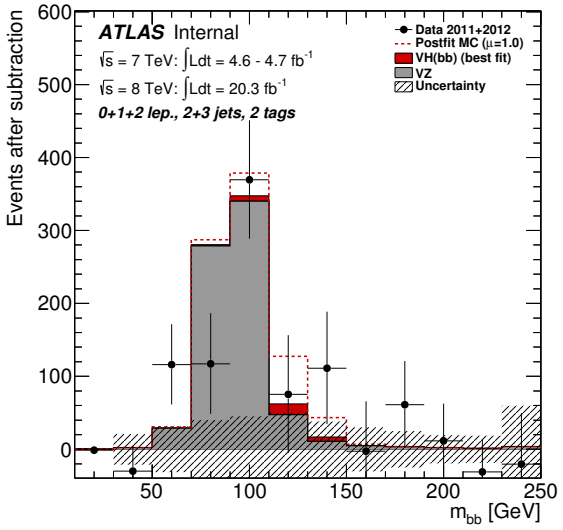

(c) 7+8 TeV

Figure 10.1: The m_{bb} distribution in data after subtracting all background events except the events from diboson process and Higgs process.

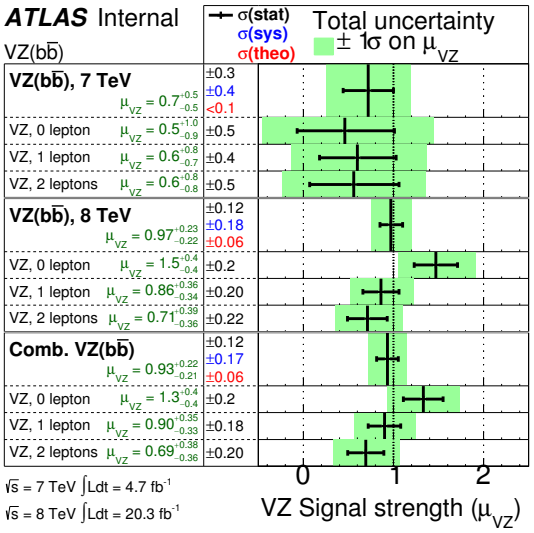

(a) independent fits

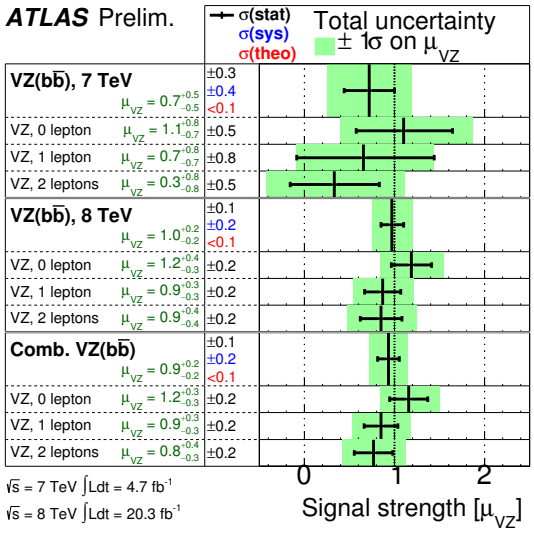

(b) independent fits

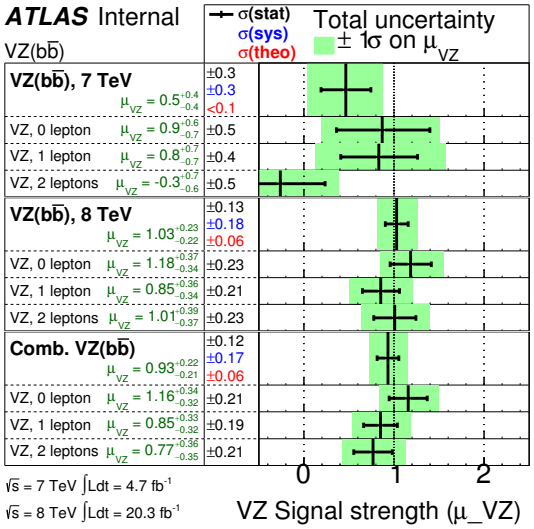

(c) independent fits

Figure 10.2: The measured value of μ_D for 0, 1, 2 lepton channels separately and the combination of all 3 channels. The measurement is performed for 7 TeV (a), 8 TeV (b), and 7+8 TeV together.

its Standard Model expectation with corresponding uncertainty, while the Higgs signal strength, μ, is allowed to float as a free parameter. Section 10.2.1 presents the upper limit of Higgs search, as well as the value of $p0$. Section 10.2.2 presents the signal strength measured in this analysis.

10.2.1 Upper Limit and $p0$

The 95% confidence level upper limits on the Higgs boson production cross section are shown in Fig 10.3. No significant excess is observed. When combining 7 TeV and 8 TeV together, the observed limit for $m_H = 125$ GeV is 1.4 times the Standard Model expectation, to be compared to an expected limit of 1.3 in the absence of signal. If the fit is restricted to 7 TeV only, the observed limit is 2.0 times the Standard Model expectation, while the expected limit is 3.3. For 8 TeV dataset only, the observed limit is 1.9 times the Standard Model expectation, while the expected limit is 1.3 with the absence of signal.

The local $p0$ value is shown in Fig. 10.4 as a function of Higgs boson mass m_H. At $m_H = 125$ GeV mass point, the observed $p0$ is 0.36, to be compared to an expectation of 0.05 in the presence of a SM Higgs boson with that mass.

10.2.2 Signal Strength

The fitted signal strength values are shown in Fig. 10.5 for all three channels separately and combined together. Combining all three channels with 7+8 TeV dataset, the measured signal strength is found to be $\mu = 0.2 \pm 0.5(\text{stat.}) \pm 0.4(\text{syst.})$. To visualize the statistical significance of the excess, Fig 10.6 shows the m_{bb} distribution all channels and categories combined, with each category weighted by the corresponding signal to background ratio.

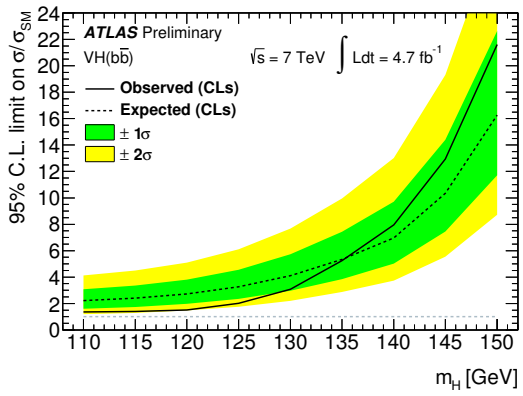

(a) $\sqrt{s} = 7$ TeV

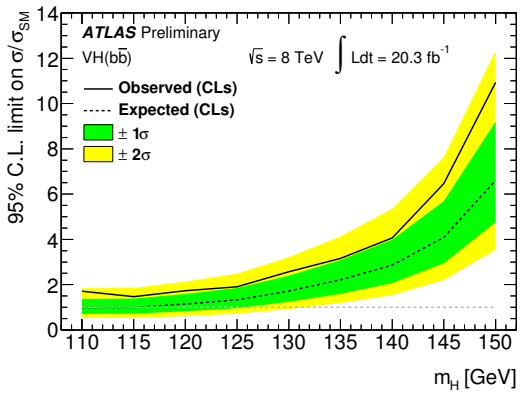

(b) $\sqrt{s} = 8$ TeV

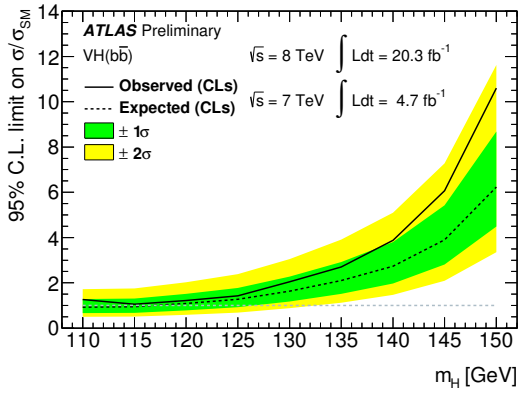

(c) Combination

Figure 10.3: Expected (dashed) and observed (solid) 95% confidence level upper limits as a function of m_H for all three channel combined together for 7 TeV, 8 TeV, and the combination of 7+8 TeV.

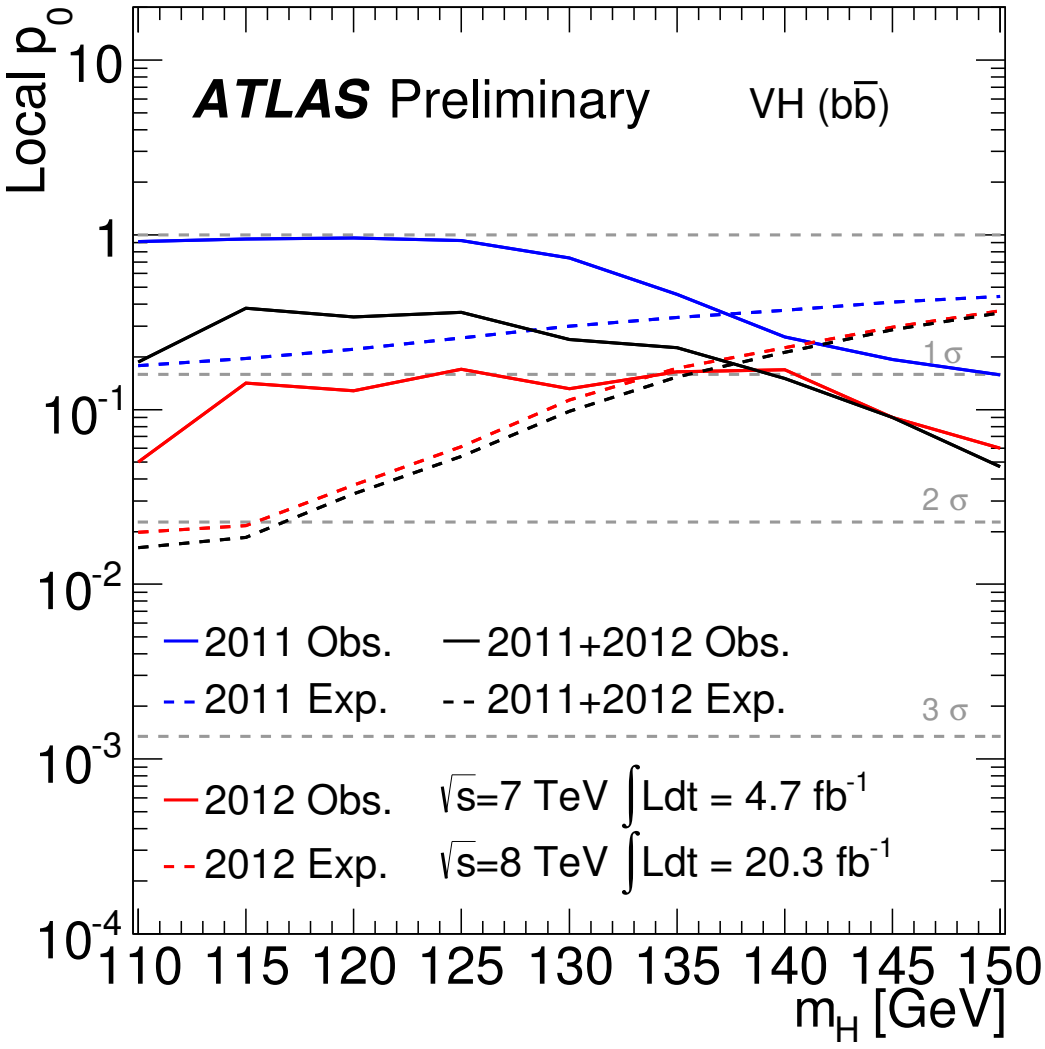

Figure 10.4: The observed (solid) and expected (dashed) local $p0$ as a function of the Higgs boson mass for 7 TeV, 8 TeV, and the combination.

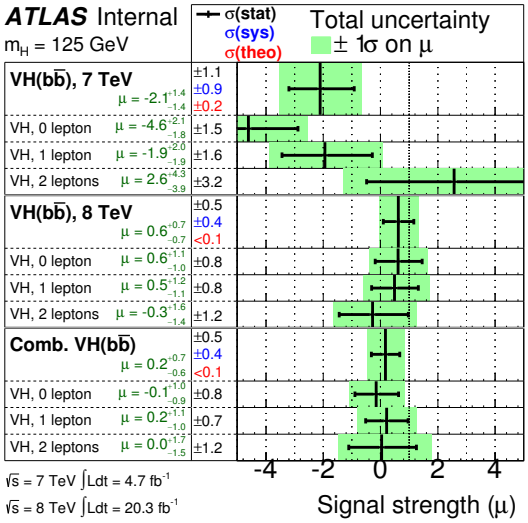

(a) independent fits

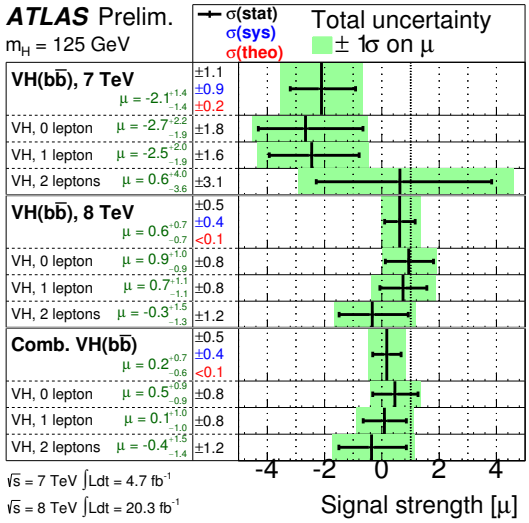

(b) independent fits

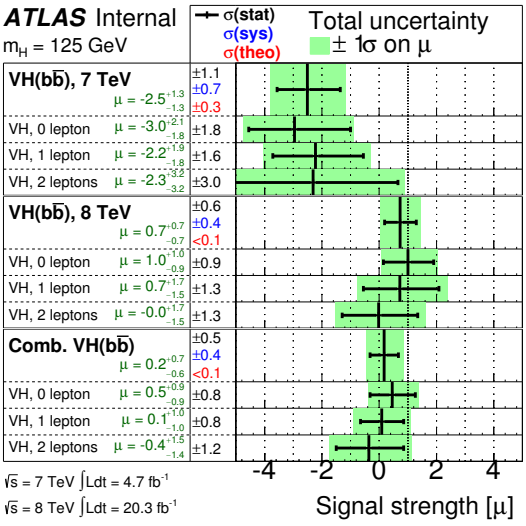

(c) independent fits

Figure 10.5: The measured value of signal strength μ for 0, 1, 2 lepton channels separately and the combination of all 3 channels. The measurement is performed for 7 TeV (a), 8 TeV (b), and 7+8 TeV together.

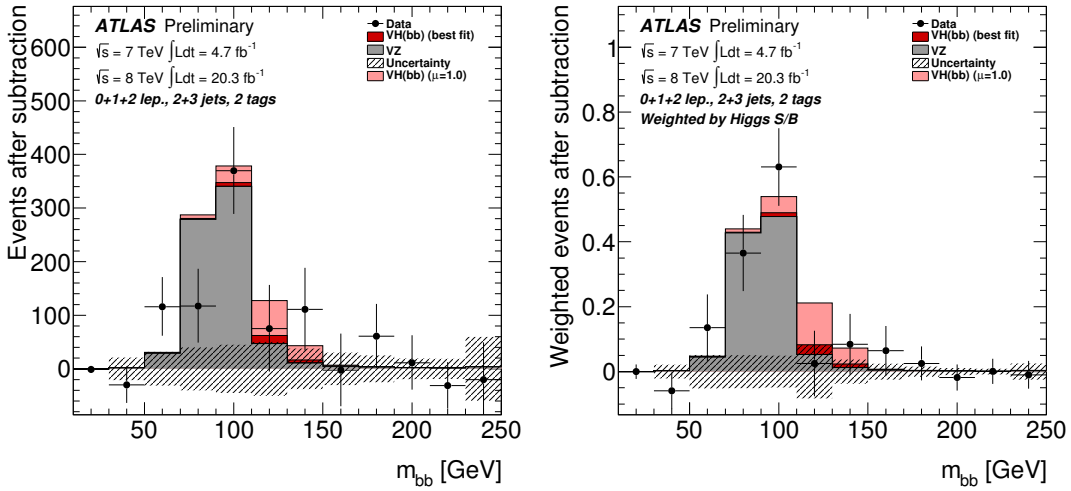

Figure 10.6: The m_{bb} distribution in data after subtraction of all backgrounds except for the diboson processes and for the associated WH and ZH production of a SM Higgs boson with $m_H = 125$ GeV (left). Also shown is the m_{bb} distribution where the contributions from all channels, p_T^V intervals, and data taking periods are summed weighted by their respective values of signal over background ratio (right). The backgrounds are evaluated according to the results of the global Higgs-boson fit. The Higgs boson signal contribution is shown both with its fitted signal strength (indicated as "best fit") and as expected for the SM cross section (indicated as $\mu = 1.0$). The size of the combined statistical and systematic uncertainty on the fitted background is indicated by the hashed band.

10.3 Summary

This dissertation describes the search that has been performed on the Stand Model Higgs boson produced in association with a W or Z boson, where Higgs boson decays to a pair of b quarks. In the analysis, three decay channels of associated lepton have been considered: $Z \to \nu\nu$, $W \to l\nu$, $Z \to ll$. The dataset used in this analysis corresponds to the integrated luminosity of 4.7 fb^{-1} at 7 TeV and 20.3 fb^{-1} at 8 TeV, recorded by the ATLAS detector during LHC Run 1. This analysis has been performed in different categories based on number of leptons, number of jets, number of b-jets, and the transverse momentum of the associated vector boson.

In this analysis, no significant excess of Higgs boson signal is observed. For $m_H = 125$ GeV, a 95% confidence level upper limit of 1.4 times the Standard Model expectation has been set on the cross section times branching ratio for VH production with $H \to b\bar{b}$, comparing to the expected limit of 1.3 in the absence of signal. The measured signal strength for Higgs boson signal is $\mu = 0.2 \pm 0.5$(stat.) $\pm$ 0.4 (syst.).

APPENDIX A

Analysis Update

VH analysis is updated in 2014 with further optimized cuts and multivariate analysis. The observed (expected) deviation from the background only hypothesis corresponds to a significance of 1.4 (2.6) standard deviations and the ratio of the measured signal yield to the Standard Model expectation is found to be $\mu = 0.52 \pm 0.32(\text{stat.}) \pm 0.24(\text{syst.})$ [164].

Bibliography

[1] ATLAS Collaboration, *The ATLAS Experiment at the CERN Large Hadron Collider,* Journal of Instrumentation 3 (2008) no. 08, S08003.

[2] CMS Collaboration, *The CMS experiment at the CERN LHC,* Journal of Instrumentation 3 (2008) no. 08, S08004.

[3] L. Evans and P. Bryant, *LHC Machine* JINST, vol. 3, p. S08001, 2008

[4] ATLAS Collaboration, *Observation of a new particle in the search for the Standard Model Higgs boson with the ATLAS detector at the LHC,* Physics Letters B 716 (2012) no. 1, 1 – 29.

[5] CMS Collaboration, *Observation of a new boson at a mass of 125 GeV with the CMS experiment at the LHC,* Physics Letters B 716 (2012) no. 1, 30 – 61.

[6] ATLAS Collaboration, *Observation and study of the Higgs boson candidate in the two photon decay channel with the ATLAS detector at the LHC* ATLAS-CONF-2012-168

[7] CMS Collaboration, *Observation of the diphoton decay of the Higgs boson and measurement of its properties* arXiv:1407.0558

[8] ATLAS Collaboration, *Measurements of Higgs boson production and couplings in the four-lepton channel in pp collisions at center-of-mass energies of 7 and 8 TeV with the ATLAS detector,* Physics Letters B 738 (2014) 234-253

[9] CMS Collaboration, *Measurement of the properties of a Higgs boson in the four-lepton final state* Phys. Rev. D 89 (2014) 092007

[10] ATLAS Collaboration, *Observation and measurement of Higgs boson decays to WW^* with ATLAS at the LHC,* arXiv:1412.2641

[11] CMS Collaboration, *Measurement of Higgs boson production and properties in the WW decay channel with leptonic final states* JHEP 01 (2014) 096

[12] ATLAS Collaboration, *Evidence for the Higgs-boson Yukawa coupling to tau leptons with the ATLAS detector,* arXiv:1501.04943

[13] CMS Collaboration, *Evidence for the 125 GeV Higgs boson decaying to a pair of τ leptons* doi:10.1007/JHEP05(2014)104.

[14] A. Salam, *Weak and electromagnetic interactions,* Proc. of the 8th Nobel Symposium on 'Elementary particle theory, relativistic groups and analyticity', Stockholm, Sweden, 1968, edited by N. Svartholm, p.367-377

[15] S. Weinberg, *A model of leptons,* Phys. Rev. Lett. 19 (1967) 1264-1266

[16] S. L. Glashow, *Partial symmetries of weak interactions,* Nucl. Phys. 22 (1961) 579-588.

[17] M. Kobayashi; T. Maskawa, *CP-Violation in the Renormalizable Theory of Weak Interaction,* Progress of Theoretical Physics 49 (2): 652–657.

[18] Fermilab, *Discoveries at Fermilab – Discovery of the Bottom Quark,* Press release. Fermilab. 7 August 1977.

[19] CDF Collaboration, *Observation of Top Quark Production in pp Collisions with the Collider Detector at Fermilab,* Physical Review Letters 74 (14): 2626–2631.

[20] F. Englert and R. Brout, *Broken symmetry and the mass of gauge vector mesons,* Phys. Rev. Lett. 13 (1964) 321–323

[21] P. Higgs, *Broken symmetries, massless particles and gauge fields,* Physics Letters 12 (1964) 132–133

[22] P. W. Higgs, *Broken symmetries and the masses of gauge bosons,* Phys. Rev. Lett. 13 (1964) 508–509

[23] G. S. Guralnik, C. R. Hagen, and T. W. B. Kibble, *Global conservation laws and massless particles,* Phys. Rev. Lett. 13 (1964) 585–587

[24] P. W. Higgs, *Spontaneous symmetry breakdown without massless bosons* Phys. Rev. 145 (1966) 1156

[25] T. W. B. Kibble, *Symmetry breaking in non-Abelian gauge theories* Phys. Rev. 155 (1967) 1554

[26] Fermilab, *The science of matter, space and time* Fermilab, Office of Science, United States Department of Energ

[27] Particle Data Group, *Review of Particle Physics (RPP),* Chin.Phys. C38 (2014) 090001

[28] A. Salam and J. C. Ward, *On A Gauge Theory OF Elementary Interactions,* Nuovo Cim.,vol. 19, pp. 165–170, 1961

[29] S. Glashow, *Partial Symmetries of Weak Interactions,* Nucl.Phys., vol. 22, pp. 579–588,1961

[30] A. Salam and J. C. Ward, *Electromagnetic and weak interactions,* Phys.Lett., vol. 13,pp. 168–171, 1964.

[31] S. Weinberg, *A model of leptons,* Phys. Rev. Lett., vol. 19, pp. 1264–1266, Nov 1967.

[32] C. N. Yang and R. L. Mills, *Conservation of isotopic spin and isotopic gauge invariance,* Phys. Rev., vol. 96, pp. 191–195, Oct 1954.

[33] J. Schwinger, *A theory of the fundamental interactions,* Annals of Physics, 2, 407-434, 1957

[34] T. D. Lee and C. N. Yang, *Possible nonlocal effects in μ decay,* Phys. Rev., vol. 108, pp. 1611–1614, Dec 1957

[35] G. Arnison et al, *Experimental Observation of Isolated Large Transverse Energy Electrons with Associated Missing Energy at $\sqrt{s}$ = 540-GeV,* Phys.Lett., vol. B122, pp. 103–116,1983.

[36] M. Banner et al, *Observation of Single Isolated Electrons of High Transverse Momentum in Events with Missing Transverse Energy at the CERN pp Collider,* Phys.Lett., vol. B122, pp. 476–485,1983.

[37] G. Arnison et al, *Experimental Observation of Lepton Pairs of Invariant Mass Around 95-GeV/c^2 at the CERN SPS Collider* Phys.Lett., vol. B126, pp. 398–410, 1983

[38] P. Bagnaia et al., *Evidence of $Z^0 \to e^+e^-$ at the CERN pp Collider* Phys.Lett., vol. B129, pp. 130–140, 1983

[39] H. Yukawa, *On the Interaction of Elementary Particles,* Prog. Theor. Phys. Supplement (1955) 1 1-10

[40] R. P. Feynman, *The Behavior of Hadron Collisions at Extreme Energies in Special Relativity and Quantum Theory,* vol. 33 of Fundamental Theories of Physics, pp. 289–304. Springer Netherlands, 1988.

[41] Bjorken, J.D, *Asymptotic Sum Rules at Infinite Momentum,* Physical Review, vol. 179, Issue 5, pp. 1547-1553

[42] D. J. Gross and F. Wilczek, *Ultraviolet behavior of non-abelian gauge theories* Phys.Rev. Lett. 30 (1973) 1343–1346.

[43] G. Altarelli and G. Parisi, *Asymptotic freedom in parton language,* Nucl.Phys.B 126 (1977) 298.

[44] J. C. Collins, D. E. Soper, and G. F. Sterman, *Factorization of Hard Processes in QCD,* Direct. High Energy Phys. 5 (1988) 1–91

[45] S. Bethke *Experimental Tests of Asymptotic Freedom,* Prog.Part.Nucl.Phys.58:351-386,2007

[46] V. Gribov and L. Lipatov, *Deep inelastic e-p scattering in perturbation theory,* Sov.J.Nucl.Phys. 15 (1972) 438–450.

[47] Y. L. Dokshitzer, *Calculation of the structure functions for deep inelastic scattering and e^+e^- annihilation by perturbation theory in quantum chromodynamics.* Sov.Phys.JETP 46 (1977) 641–653.

[48] H.-L. Lai et al., *New parton distributions for collider physics,* Phys. Rev. D 82 (2010) 074024, arXiv:1007.2241 [hep-ph]

[49] A. D. Martin, W. J. Stirling, R. S. Thorne, and G. Watt, *Parton distributions for the LHC,* Eur. Phys. J. C 63 (2009) 189–285, arXiv:0901.0002 [hep-ph]

[50] R. D. Ball et al., *Impact of heavy quark masses on parton distributions and LHC phenomenology,* Nucl. Phys. B 849 (2011) 296–363, arXiv:1101.1300 [hep-ph]

[51] ATLAS Collaboration, *Summary plots from the ATLAS Standard Model physics group* ATLAS SM physics group

[52] H. M. Georgi, S. L. Glashow, M. E. Machacek, and D. V. Nanopoulos, *Higgs bosons from two gluon annihilation in proton proton collisions,* Phys. Rev. Lett. 40 (1978) 692

[53] Michael Spira, *QCD Effects in Higgs Physics* Fortsch.Phys. 46 (1998) 203-284

[54] Abdelhak Djouadi, *The Anatomy of Electro-Weak Symmetry Breaking. I: The Higgs boson in the Standard Model* Phys.Rept.457:1-216,2008

[55] The ATLAS Collaboration, *Detector and physics performance technical design report,* CERN/LHCC/99-14/15, 1999

[56] R. Raitio and W. W. Wada, *Higgs boson production at large transverse momentum in QCD,* Phys. Rev. D19 (1979) 941.

[57] Z. Kunszt, *Associated production of heavy Higgs boson with top quarks,* Nucl. Phys. B247 (1984) 339

[58] S. Dawson and R. Kauffman, *QCD corrections to Higgs boson production: nonleading terms in the heavy quark limit,* Phys.Rev., vol. D49, pp. 2298–2309, 1994

[59] A. Djouadi, M. Spira, and P. Zerwas, *Production of Higgs bosons in proton colliders: QCD corrections* Phys.Lett., vol. B264, pp. 440–446, 1991

[60] D. Graudenz, M. Spira, and P. M. Zerwas, *QCD corrections to higgs-boson production at proton-proton colliders* Phys. Rev. Lett., vol. 70, pp. 1372–1375, Mar 1993

[61] M. Spira, A. Djouadi, D. Graudenz, and P. Zerwas, *Higgs boson production at the LHC,* Nucl.Phys., vol. B453, pp. 17–82, 1995

[62] R. V. Harlander, *Virtual corrections to $gg \to H$ to two loops in the heavy top limit,* Phys.Lett., vol. B492, pp. 74–80, 2000

[63] S. Catani, D. de Florian, and M. Grazzini, *Higgs production in hadron collisions: Soft and virtual QCD corrections at NNLO,* JHEP, vol. 0105, p. 025, 2001

[64] R. V. Harlander and W. B. Kilgore, *Soft and virtual corrections to Higgs production at next-to-next-to-leading order* Phys. Rev. D, vol. 64, p. 013015, Jun 2001

[65] R. V. Harlander and W. B. Kilgore, *Next-to-next-to-leading order higgs production at hadron colliders* Phys. Rev. Lett., vol. 88, p. 201801, May 2002

[66] S. Dittmaier et al, *Handbook of LHC Higgs Cross Sections: 1. Inclusive Observables,* arXiv:1101.0593 [hep-ph]

[67] M. Ciccolini, A. Denner, and S. Dittmaier, *Strong and electroweak corrections to the production of Higgs + 2-jets via weak interactions at the LHC,* Phys. Rev. Lett., vol. 99, p. 161803, 2007

[68] M. Ciccolini, A. Denner, and S. Dittmaier, *Electroweak and QCD corrections to Higgs production via vector-boson fusion at the LHC,* Phys. Rev., vol. D77, p. 013002, 2008.

[69] K. Arnold et al., *VBFNLO: A Parton level Monte Carlo for processes with electroweak bosons* Comput. Phys. Commun., vol. 180, p. 1661, 2009

[70] T. Han and S. Willenbrock, *QCD correction to the $pp \to WH$ and ZH total cross sections,* Phys. Lett., vol. B273, p. 167, 1991.

[71] O. Brein, A. Djouadi, and R. Harlander *NNLO QCD corrections to the Higgs-strahlung processes at hadron colliders,* Phys. Lett., vol. B579, p. 149, 2004

[72] M. Ciccolini, S. Dittmaier, and M. Kramer, *Electroweak radiative corrections to associated WH and ZH production at hadron colliders,* Phys. Rev., vol. D68, p. 073003, 2003

[73] W. Beenakker et al., *Higgs radiation off top quarks at the Tevatron and the LHC,* Phys. Rev. Lett., vol. 87, p. 201805, 2001.

[74] W. Beenakker et al., *NLO QCD corrections to ttH production in hadron collisions,* Nucl. Phys., vol. B653, p. 151, 2003.

[75] S. Dawson, L. Orr, L. Reina, and D. Wackeroth, *Next-to-leading order QCD corrections to pp $\to$ t$\bar{t}$h at the CERN Large Hadron Collider* Phys. Rev., vol. D67, p. 071503, 2003.

[76] S. Dawson, C. Jackson, L. Orr, L. Reina, and D. Wackeroth, *Associated Higgs production with top quarks at the large hadron collider: NLO QCD corrections* Phys. Rev., vol. D68, p. 034022, 2003.

[77] J.R.Ellis,M.K.Gaillard,andD.V.Nanopoulos, *A Phenomenological Profile of the Higgs Boson,* Nucl.Phys., vol. B106, p. 292, 1976.

[78] B. W. Lee, C. Quigg, and H. Thacker, *The Strength of Weak Interactions at Very High Energies and the Higgs Boson Mass,* Phys.Rev.Lett., vol. 38, pp. 883–885, 1977.

[79] B. W. Lee, C. Quigg, and H. B. Thacker, *Weak interactions at very high energies: The role of the higgs-boson mass,* Phys. Rev. D, vol. 16, pp. 1519–1531, Sep 1977.

[80] E.A. Paschos. *Electroweak theory.* Cambridge University Press, 2007.

[81] William J. Marciano, Cen Zhang, Scott Willenbrock, *Higgs Decay to Two Photons,* arXiv:1109.5304

[82] A. Djouadi, J. Kalinowski, and M. Spira, *HDECAY: A Program for Higgs boson decays in the Standard Model and its supersymmetric extension, Comput.Phys.Commun.* 108 (1998) 56–74, [hep-ph/9704448].

[83] M. Spira, *QCD effects in Higgs physics,* Fortsch.Phys. 46 (1998) 203–284, [hep-ph/9705337].

[84] A. Bredenstein, A. Denner, S. Dittmaier, and M. Weber, *Precise predictions for the Higgs-boson decay $H \to WW/ZZ \to 4$ leptons,* Phys.Rev. D74 (2006) 013004, [hep-ph/0604011].

[85] A. Bredenstein, A. Denner, S. Dittmaier, and M. Weber, *Radiative corrections to the semileptonic and hadronic Higgs-boson decays $H \to WW/ZZ \to 4$ leptons,* JHEP 0702 (2007) 080, [hep-ph/0611234].

[86] LEP Working Group for Higgs boson searches, ALEPH Collaboration, DELPHI Collaboration, L3 Collaboration, OPAL Collaboration, *Search for the standard model Higgs boson at LEP,* Phys.Lett. B565 (2003) 61–75, [hep-ex/0306033].

[87] CDF Collaboration, D0 Collaboration, *Higgs Boson Studies at the Tevatron,* Phys.Rev. D88 (2013) 052014, [arXiv:1303.6346].

[88] ATLAS Collaboration *ATLAS Higgs Search Update,* atlas news

[89] ATLAS Collaboration, *Evidence for the spin-0 nature of the Higgs boson using ATLAS data,* Phys.Lett. B726 (2013) 120–144, [arXiv:1307.1432].

[90] CMS Collaboration, *Measurement of the properties of a Higgs boson in the four-lepton final state* arXiv:1312.5353.

[91] ATLAS Collaboration, *Measurements of Higgs boson production and couplings in diboson final states with the ATLAS detector at the LHC,* Phys. Lett. B 726 (2013) 88

[92] CMS Collaboration, *Combination of standard model Higgs boson searches and measurements of the properties of the new boson with a mass near 125 GeV,* .CMS-PAS-HIG-13-005

[93] ATLAS Collaboration *Measurement of the Higgs boson mass from the $H \rightarrow$ and $H \rightarrow ZZ \rightarrow 4l$ channels with the ATLAS detector using 25 fb^{-1} of pp collision data,* arXiv:1406.3827.

[94] CMS Collaboration *Precise determination of the mass of the Higgs boson and studies of the compatibility of its couplings with the standard model,* CMS-PAS-HIG-14-009.

[95] ATLAS Collaboration, *ATLAS detector and physics performance : Technical Design Report, 1, tech. rep.,* CERN, 1999. ATLAS-TDR-014, CERN-LHCC-99-014.

[96] ATLAS Collaboration, *ATLAS detector and physics performance : Technical Design Report, 2, tech. rep.,* CERN, 1999. ATLAS-TDR-015, CERN-LHCC-99-015.

[97] ATLAS Collaboration, *Studies of the performance of the ATLAS detector using cosmic-ray muons,* Eur. Phys. J. C71 (2011) 1593.

[98] CMS Collaboration, *CMS technical proposal, tech. rep.,* CERN, 1994. CERN-LHCC-894-38.

[99] CERN *Aerial view image of CERN's LHC taken in 2008.* CERN website

[100] ALICE Collaboration, *ALICE: Technical proposal for a Large Ion collider Experiment at the CERN LHC , tech. rep.,* CERN, 1997. CERN-LHCC-95-71.

[101] LHCb Collaboration, *LHCb technical proposal, tech. rep.,* CERN, 1998. CERN-LHCC-98-004.

[102] CERN *Proton injector for the LHC at CERN,* CERN website

[103] ATLAS Collaboration, *ATLAS inner detector: Technical Design Report, 1, tech. rep.,* CERN, Geneva, 1997. CERN-LHCC-97-016.

[104] ATLAS Collaboration, *ATLAS inner detector: Technical Design Report, 2, tech. rep.,* CERN, Geneva, 1997. CERN-LHCC-97-017.

[105] ATLAS Collaboration, *ATLAS pixel detector electronics and sensors,* JINST 3 (2008) P07007.

[106] ATLAS Collaboration *The barrel modules of the ATLAS semiconductor tracker,* Nucl. Instrum. Meth. A568 (2006) 642–671.

[107] ATLAS Collaboration *The ATLAS semiconductor tracker end-cap module,* Nucl. Instrum. Meth. A575 (2007) 353–389.

[108] ATLAS Collaboration *The silicon microstrip sensors of the ATLAS semiconductor tracker,* Nucl. Instrum. Meth. A578 (2007) 98–118.

[109] ATLAS Collaboration, *The ATLAS Transition Radiation Tracker (TRT) proportional drift tube: design and performance,* JINST 3 (2008) P02013.

[110] ATLAS Collaboration, *The ATLAS TRT Barrel Detector,* JINST 3 (2008) P02014.

[111] ATLAS Collaboration, *The ATLAS TRT end-cap detectors,* JINST 3 (2008) P10003.

[112] A. Yamamoto et al., *Progress in ATLAS central solenoid magnet,* IEEE T.Appl. Supercond., 10:353, 2000.

[113] ATLAS Collaboration, *ATLAS calorimeter performance technical design report.* CERN-LHCC-96-040,CERN, Geneva

[114] ATLAS Collaboration, *Liquid argon calorimeter technical design report.* CERN-LHCC-96-041

[115] ATLAS Collaboration, *Tile calorimeter technical design report.* CERN-LHCC-96-042,CERN, Geneva

[116] ATLAS Collaboration, *ATLAS Muon Spectrometer Technical Design Report.* CERN, Geneva, 1997. CERN-LHCC-97-22, ATLAS-TDR-10

[117] ATLAS Collaboration, *Improved luminosity determination in pp collisions at* $\sqrt{s}$ *= 7 TeV using the ATLAS detector at the LHC,* Eur. Phys. J. C (2013) 73:2518

[118] ATLAS Collaboration, *Preliminary Luminosity Determination in pp Collisions at* $\sqrt{s}$ *= 8 TeV using the ATLAS Detector in 2012,* ATL-COM-LUM-2012-013, CERN, 2012

[119] James Stirling, *PARTON LUMINOSITY AND CROSS SECTION PLOTS,* W.J. Stirling, private communication

[120] R. Achenbach et al. , *The ATLAS Level-1 calorimeter trigger,* The ATLAS Level-1 Calorimeter Trigger

[121] R. Hauser, *The ATLAS Data Acquisition and High Level Trigger Systems: Experience and Upgrade Plans,* ATL-DAQ-PROC-2012-073.

[122] ATLAS Collaboration, *Luminosity public result,* ATLAS twiki

[123] ATLAS Collaboration, *ATLAS Computing: Technical Design Report,* CERN-LHCC-2005-022.

[124] Cornelissen, T ; Elsing, M ; Fleischmann, S ; Liebig, W ; Moyse, E ; Salzburger, A (ed.) *Concepts, Design and Implementation of the ATLAS New Tracking (NEWT)* ATL-COM-SOFT-2007-002

[125] ATLAS Collaboration, *Performance of the ATLAS Inner Detector Track and Vertex Reconstruction in the High Pile-Up LHC Environment,* ATLAS-CONF-2012-042.

[126] ATLAS Collaboration, *Performance of primary vertex reconstruction in proton- proton collisions at* $\sqrt{s}$ *= 7 TeV in the atlas experiment.* ATLAS-CONF-2010-069

[127] W. Lampl, S. Laplace, D. Lelas, P. Loch, H. Ma, S. Menke, S. Rajagopalan, D. Rousseau, S. Snyder, and G. Unal,
Calorimeter Clustering Algorithms: Description and Performance ATL-LARG-PUB-2008-00

[128] ATLAS Collaboration, *Electron reconstruction and identification efficiency measurements with the ATLAS detector using the 2011 LHC proton-proton collision data,* Eur. Phys. J. C (2014) 74:2941

[129] The ATLAS Collaboration, *Improved electron reconstruction in ATLAS using the Gaussian Sum Filter-based model for bremsstrahlung,* ATLAS-CONF-2012-047

[130] ATLAS Collaboration, *Electron and photon energy calibration with the ATLAS detector using LHC Run 1 data,* Eur. Phys. J. C (2014) 74: 3071

[131] ATLAS Collaboration, *Electron performance measurements with the ATLAS detector using the 2010 LHC proton-proton collision data* Eur. Phys. J. C72 (2012) 1909

[132] ATLAS Collaboration, *Electron efficiency measurements with the ATLAS detector using the 2012 LHC proton-proton collision data.* ATLAS-CONF-2014-032

[133] ATLAS Collaboration, *Electron reconstruction and identification efficiency measurements with the ATLAS detector using the 2011 LHC proton-proton collision data,* Eur. Phys. J. C (2014) 74:2941

[134] ATLAS Collaboration, *Electron performance measurements with the ATLAS detector using the 2010 LHC proton-proton collision data.* Eur. Phys. J C72 (2012) 1909

[135] ATLAS Collaboration, *Measurement of the muon reconstruction performance of the ATLAS detector using 2011 and 2012 LHC proton-proton collision data,* Eur.Phys.J. C74 (2014) 3130

[136] ATLAS Collaboration, *Muon Reconstruction Efficiency and Momentum Resolution of the ATLAS Experiment in Proton-Proton Collisions at* $\sqrt{s} = 7$ *TeV in 2010,* Eur. Phys. J. C (2014) 74:3034

[137] ATLAS Collaboration, *Preliminary results on the muon reconstruction efficiency, momentum resolution, and momentum scale in ATLAS 2012 pp collision data,* ATLAS-CONF-2013-088.

[138] M. Cacciari, G. P. Salam, and G. Soyez. *The anti-kt jet clustering algorithm.* HEP, 04:063, 2008.

[139] ATLAS Collaboration, *Jet energy measurement with the ATLAS detector in proton-proton collisions at* $\sqrt{s} = 7$ *TeV* Eur. Phys. J. C, 73 3 (2013) 2304

[140] ATLAS Collaboration, *Jet-area-based pile-up subtraction,* ATLAS Twiki

[141] G.P. Salam M. Cacciari., *Pileup subtraction using jet areas,* Phys. Lett. B, 119, 2008.

[142] ATLAS Collaboration, *Jet global sequential corrections with the ATLAS detector in proton-proton collisions at* $\sqrt{s} = 8$ *TeV* ATLAS-CONF-2015-002

[143] ATLAS Collaboration, *Calibration of b-tagging using dileptonic top pair events in a combinatorial likelihood approach with the ATLAS experiment,* ATLAS-CONF-2014-004

[144] ATLAS Collaboration, *A new inclusive secondary vertex algorithm for b-jet tagging in ATLAS* Journal of Physics: Conference Series, 119(3):032032, 2008.

[145] ATLAS Collaboration, *b-jet tagging calibration on c-jets containing D^{*+} mesons* ATLAS-CONF-2012-039

[146] ATLAS Collaboration, *Measurement of the Mistag Rate with 5 fb^{-1} of Data Collected by the ATLAS Detector* ATLAS-CONF-2012-040

[147] ATLAS Collaboration, *Measurement of the b-tag Efficiency in a Sample of Jets Containing Muons with 5 fb^{-1} of Data from the ATLAS Detector* ATLAS-CONF-2012-043

[148] ATLAS Collaboration, *Calibration of b-tagging using dileptonic top pair events in a combinatorial likelihood approach with the ATLAS experiment,* ATLAS-CONF-2014-004

[149] ATLAS Collaboration, *Calibration of the performance of b-tagging for c and light-flavour jets in the 2012 ATLAS data,* ATLAS-CONF-2014-046

[150] ATLAS Collaboration, *Performance of Missing Transverse Momentum Reconstruction in ATLAS studied in Proton-Proton Collisions recorded in 2012 at 8 TeV* ATLAS-CONF-2013-082

[151] ATLAS Collaboration, *Performance of Missing Transverse Momentum Reconstruction in Proton-Proton Collisions at 7 TeV with ATLAS* Eur. Phys. J. C72(2012) 1844

[152] ATLAS Collaboration, *Performance of Missing Transverse Momentum Reconstruction in ATLAS with 2011 Proton-Proton Collisions at $\sqrt{s}$ = 7 TeV* ATLAS-CONF-2012-101

[153] ATLAS Collaboration, *Search for the $b\bar{b}$ decay of the Standard Model Higgs boson in associated (W/Z)H production with the ATLAS detector.* ATLAS-CONF-2013-079

[154] ATLAS Collaboration, *Search for the Standard Model Higgs boson in associated production with a vector boson and decaying to bottom quarks with the ATLAS detector,* ATL-COM-PHYS-2013-465

[155] GEANT4 Collaboration, *GEANT4: A Simulation toolkit.* Nucl.Instrum.Meth. A506 (2003) 250–303.

[156] ATLAS Collaboration, *Atlfast ii.* https://twiki.cern.ch/twiki/bin.viewauth/atlas/atlfastii

[157] Piotr Golonka and Zbigniew Was, *PHOTOS Monte Carlo: A Precision tool for QED corrections in Z and W decays.* Eur.Phys.J., C45:97–107, 2006.

[158] Z.Was, *TAUOLA the library for τ lepton decay, and KKMC/KORALB/KORALZ/... status report* Nucl. Phys. B, Proc. Suppl. 98, 96 (2001).

[159] LHC Higgs Cross Section Working Group, S. Dittmaier, C. Mariotti, G. Passarino, and R. Tanaka (Eds.), *Handbook of LHC Higgs Cross Sections: 1. Inclusive Observables.* arXiv:1101.0593 [hep-ph].

[160] K. e. a. Nakamura, *Review of particle physics.* J. Phys. G.

[161] A. L. Read, *Presentation of search results: The CL(s) technique,* J.Phys. G28 (2002) 2693–2704.

[162] G. Cowan et al, *Asymptotic formulae for likelihood-based tests of new physics,* Eur. Phys. J. C71(2011) 1554, arXiv:1007.1727 [physics.data-an].

[163] B. Abbott, M. Abolins, B.S. Acharya, et.al *A Measurement of the W Boson Mass,* Phys.Rev.D58:092003,1998

[164] ATLAS Collaboration, *Search for the $b\bar{b}$ decay of the Standard Model Higgs boson in associated (W/Z)H production with the ATLAS detector,* JHEP01(2015)069, arXiv:1409.6212 [hep-ex]